MULTISCALE EFFECTS IN PLASMA MICROTURBULENCE

Dissertation

zur Erlangung des Doktorgrades
Dr. rer. nat.
der Fakultät für Naturwissenschaften
der Universität Ulm

vorgelegt von

Tobias Görler

aus

Witten

Ulm 2009

Amtierender Dekan bei der Eröffnung des Promotionsverfahrens:	Prof. Dr. Peter Bäuerle
Amtierender Dekan beim Abschluss des Promotionsverfahrens:	Prof. Dr. Axel Groß
Erstgutachter:	apl. Prof. Dr. Frank Jenko
Zweitgutachter:	Prof. Dr. Peter Reineker
Drittgutachter:	Prof. Dr. Steven Cowley
Tag der Promotion:	16. Dezember 2009

Abstract

Microinstabilities are one of the key physics problems on the way to efficient power plants based on nuclear fusion. They cause anomalous heat and particle transport which significantly degrades the plasma confinement quality, thus preventing self-sustaining plasma burning in present-day experiments. However, due to their complex dynamics and highly nonlinear character, it is impossible to solve the underlying equations of turbulent systems analytically—a problem which is also well known in several other physics research fields, e.g. aerodynamics. Theoretical descriptions and predictions are therefore typically based on numerical simulations. Here, the multitude of involved space and time scales may cause problems since the parameters required for a numerical treatment – e.g., the grid resolutions – often turn out to be infeasible for computations. However, if scales are clearly separated – as it is the case in magnetically confined fusion plasmas – multiscale approaches allow for a reduction of the problem under investigation to the relevant domain of interest. In this context, gyrokinetics is well-established as one of the most powerful theoretical descriptions. It serves as a basis for the plasma turbulence code GENE which numerically solves the modified Vlasov-Maxwell system of equations and which is used throughout this work.

During this thesis project, the GENE code has been significantly extended. While previous versions were restricted to a local approximation and therefore only able to describe a small part of a fusion plasma, it is now possible to consider radial temperature and density profiles as well as corresponding variations of the magnetic geometry. The inclusion of these additional macroscopic scales is essential for the investigation of non-local effects. The according modifications of the equations underlying the GENE code as well as the changes in the numerical schemes are discussed in detail, and successful tests of the new code to several scenarios and benchmarks are presented. Furthermore, first implementations of heat sources and sinks terms are introduced.

Another part of this work deals with coupled microturbulence on different space and time scales which are not affected by the gyrokinetic approximation. Traditionally, much of the heat transport and thus the confinement degradation in fusion experiments is attributed to ion temperature gradient (ITG) or trapped electron mode (TEM) driven turbulence which predominantly exhibits wavelengths of the order of the ion gyroradius. However, several recent theoretical and experimental findings indicate significant contributions originating from the considerably smaller electron scales which are predicted

by naïve models to be negligible. The high potential relevance of small-scale turbulence even in the presence of large-scale turbulence for future fusion experiments and power plants motivated several simulations covering both ion and electron spatial and temporal scales self-consistently. Due to the associated enormous computational effort, the multiscale investigations performed in the course of this work represent one of the first such attempts worldwide. It is found that for realistic ion heat (and particle) flux levels and in the presence of unstable ETG modes, there tends to be a scale separation between electron and ion thermal transport. In contrast to the latter, the former may exhibit substantial or even dominant small-scale contributions. Furthermore, it is investigated in which way this behavior is reflected in several experimentally accessible quantities, including frequency or density spectra.

Zusammenfassung

Auf dem Weg zur technischen Energiegewinnung durch Kernfusionsreaktionen mittels magnetisch eingeschlossener Plasmen bilden kleinskalige Fluktuationen eine der zentralen physikalischen Problemstellungen. Der durch sie verursachte anomale Transport reduziert die Qualität des Einschlusses derart, dass ein eigenständiges Plasmabrennen in heutigen Experimenten nicht möglich ist. Wie auch aus anderen Bereichen der Physik, bspw. der Aerodynamik, bekannt, sind die Grundgleichungen turbulenter Systeme aufgrund ihrer komplexen Dynamik und ihres hochgradig nichtlinearen Charakters nur in wenigen Spezialfällen analytisch lösbar. Theoretische Beschreibungen und Vorhersagen beruhen daher in der Regel auf numerischen Simulationen. Hierbei ist allerdings die Vielzahl involvierter Raum- und Zeitskalen problematisch, da die für eine numerische Behandlung benötigten Parameter, bspw. die Gitterauflösung, in der Praxis nicht anwendbar sind. Liegen allerdings, wie bei magnetisch eingeschlossenen Plasmen, deutlich von einander abgegrenzte Skalen vor, kann mit Hilfe von Multiskalentheorien eine Reduktion des vorliegenden Problems auf den eigentlich relevanten Bereich vorgenommen werden. Eine der bedeutendsten theoretischen Beschreibungen dieser Art ist die Gyrokinetik. Sie bildet die Grundlage für den in dieser Arbeit verwendeten GENE-Code, der die modifizierten Vlasov-Maxwell Gleichungen numerisch löst.

Diese Software wurde im Rahmen der vorliegenden Dissertation bedeutend erweitert. Während frühere Versionen auf eine lokale Näherung beschränkt waren und somit nur einen kleinen Teil eines Fusionsplasmas beschreiben konnten, werden nun radiale Temperatur- und Dichteprofile sowie Änderungen der Geometrie berücksichtigt. Diese Aufnahme zusätzlicher makroskopischer Skalen erlaubt nun die Untersuchung nichtlokaler Effekte. Hierfür notwendige Modifikationen der GENE-Grundgleichungen, bzw. der Normierung derselbigen, sowie der numerischen Verfahren werden ausführlich diskutiert und die erfolgreiche Anwendung des neuen Codes auf diverse Testfälle präsentiert.

Ein weiterer Teil der Arbeit beschäftigt sich mit gekoppelter Mikroturbulenz auf verschiedenen Raum- und Zeitskalen, die auch in der reduzierten, gyrokinetischen Beschreibung auftreten können. Traditionell wird ein Großteil des Wärmetransports und damit der Einschlussverminderung u.a. auf Ionentemperatur-Gradienten (ITG) oder gefangene Elektronen (TEM) getriebene Turbulenz zurückgeführt, die vorwiegend Wellenlängen im Bereich des Ionengyroradius aufweist. In jüngster Zeit haben sich jedoch immer mehr Anzeichen für signifikante Beiträge von den deutlich kleineren Elektronenskalen gefun-

den, die in einfachen Modellen als vernachlässigbar erachtet wurden. Die hohe Relevanz der Frage, ob und unter welchen Umständen diese Elektronentemperatur-Gradienten (ETG) getriebene Turbulenz bei gleichzeitiger Anwesenheit von großskaliger Turbulenz bedeutende Transportbeiträge liefert, erfordert numerische Untersuchungen, bei denen sowohl die Elektronen- als auch die Ionen-Skalen selbstkonsistent in Raum und Zeit behandelt werden. Da der hierfür benötigte Rechenaufwand enorme Ausmaße annimmt, gehören die im Rahmen dieser Arbeit durchgeführten Multiskalensimulationen zu den weltweit ersten Repräsentanten dieser Art. Anhand dieser wird gezeigt, dass die kurzwellige Elektronenskalenturbulenz bei realistischen Ionenwärmeflüssen durchaus einen signifikanten Anteil des Elektronenwärmetransports verursachen kann, so dass eine Skalentrennung gegenüber dem Ionenwärmetransport auftritt, der weiterhin auf langwellige Beiträge beschränkt bleibt. Darüber hinaus werden die Einflüsse der ETG Moden auf experimentell beobachtbare Größen wie Dichte- und Frequenzspektren untersucht.

Contents

Chapter 1

Introduction

This chapter aims at providing the main motivations for studying multiscale effects in plasma turbulence. For this purpose, an understanding of fusion energy research, plasma physics, and turbulence effects is developed first.

1.1 Fusion energy

A growing world population and industrialization led to dramatically increased energy demands during the 20th century. For instance, the worldwide primary energy consumption rose by almost 70% over the last twenty years, cf. Fig. 1.1. Although some

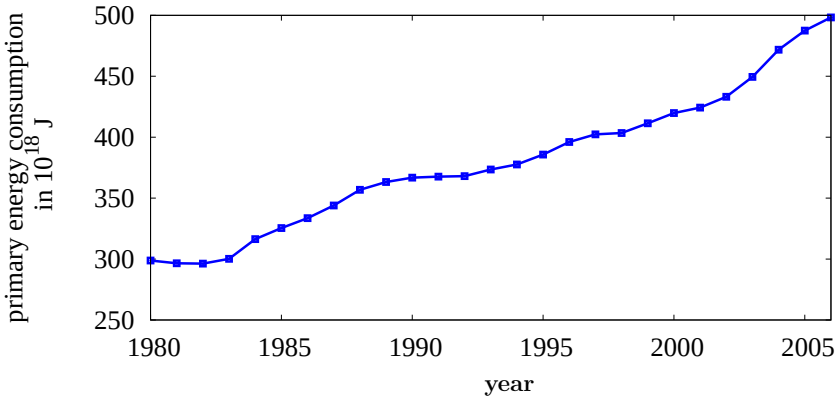

Figure 1.1: Worldwide primary energy consumption in 10^{18} J. Source: Energy Information Administration (Dec 2008).

studies expect a saturation of the global population in the 21st century, and political programs aim at saving energy, a further increase is expected [1]. In this context, it can be seen as an unfortunate coincidence that most of the current energy production is based on the burning of fossil fuels like coal, oil, or gas. During recent decades, a close relation between this kind of energy production and global warming became more and more evident. Furthermore, fossil fuels are finite and therefore become expensive once easily accessible sources are exhausted.

Triggered by these developments, scientists are attempting to improve present or develop new alternative energy producing technologies. Currently, fission plants and regenerative energy sources are possible choices for the near-to-intermediate future. However, the former suffer from potentially uncontrollable chain reactions and the unsolved problem of nuclear waste disposal while the latter depend on local conditions as, for instance, sufficient water, wind, or sunshine duration, and require significantly optimized energy storage systems than currently at hand. Another possibility is to imitate the most obvious energy supplier—the sun. Until 1929, when Atkinson and Houtermans [2] suggested fusion of light atoms to be the energy generating mechanism in sun-like stars, no satisfactory explanation was available on how the sun provided its energy. Five years later, particle accelerator experiments by Oliphant, Harteck, and Rutherford [3] proved the general possibility of such reactions. Complementarily, a model for heavier stars has been developed in the late 1930s by Weizsäcker [4] and Bethe [5].

Since then, people were electrified by the idea of employing a similar reaction in power plants on Earth. However, the nuclear cross sections of the proton-proton-chain or the Bethe-Weizsäcker-cycle reactions are too small to be used in terrestrial devices. Hence, the most probable fusion reaction for technically achievable temperatures, namely the deuterium-tritium-fusion,

$$ {}^{2}_{1}\mathrm{H} + {}^{3}_{1}\mathrm{H} \rightarrow {}^{4}_{2}\mathrm{He} + {}^{1}_{0}\mathrm{n} + 17.59\,\mathrm{MeV}, \tag{1.1} $$

is favored instead. The heavy hydrogen isotope deuterium accounts for approximately 0.015% of all naturally occurring hydrogen in the oceans on earth and can be extracted by enrichment and distillation processes. And while the radioactive isotope tritium does not accumulate over geological timescales due to its relatively short half-life of about 12.3 years, it can be produced by neutron activation of lithium which constitutes 0.006% of the lithosphere. Current estimates based on the present-day energy consumption predict at least several 10,000 years until those deposits are exhausted [6]. This perspective, together with the enormous energy generation per process – compared to typical chemical reactions, an increase of more than a factor of a million is achieved in nuclear fusion reactions – constitutes the main argument for fusion research, even if both the fundamental scientific and the technological barriers are much higher than in conventional power plants.

One obvious complication in this context is given by the Coulomb repulsion. Only if the deuterium and tritium nuclei are able to overcome the corresponding potential barrier, they come close enough to let the attractive nuclear force induce a fusion reaction. Although quantum mechanics, in particular the tunneling effect, corrects the classically required kinetic energies by a significant factor, on the order of 100 keV are necessary (on average) to facilitate sufficiently high D-T-fusion rates.

1.2 Magnetic confinement fusion

One promising candidate for the realization of fusion based power plants is magnetic confinement fusion. Here, both fusion fuels are heated to high temperatures of about 100 million K, i.e. average kinetic energies of around 10 keV. A large fraction of the high energy tail of the Maxwellian distribution is then clearly exceeding the potential barrier, and fusion reactions are sufficiently frequent. However, any contact with surrounding reaction chamber walls should be minimized in order to avoid surface erosion and impurity generation.

For this purpose, a basic property of extremely hot matter proves helpful. At such high temperatures, a large fraction of the deuterium-tritium mixture is found to be in plasma state which is a partially or fully ionized gas obeying the quasi-neutrality condition, $|\sum_\sigma q_\sigma n_\sigma| \ll e n_e$. Here, q_σ is the charge and n_σ the density of the σth particle species with σ running over all present species, e the elementary charge and n_e the electron density. Maxwell's equations then describe a possible influence of electromagnetic fields on the particle motion. Given, for instance, a strong and homogeneous magnetic field, motions perpendicular to the magnetic field line are restricted to gyrations due to the Lorentz force. Along the field lines, however, particles can still move without any constraint. Early linear, e.g. cylindrical, fusion devices thus employed magnetic field inhomogeneities to create a mirror force which reflects a significant particle fraction at both ends. Unfortunately, this kind of trapping appears to be most inefficient for highly energetic particles with large velocities along the magnetic field so that the particle and energy confinement remains unsatisfactory. An alternative approach is to connect both ends, therefore creating a toroidal device and avoiding the corresponding losses. However, the magnetic field lines themselves must not be purely toroidal but need a poloidal component, as well, in order to balance outwardly directed drifts which would emerge otherwise [6]. In case of an irrational number of toroidal turns per poloidal turn, a single helically-wound field line spans an entire toroidal surface which is often called flux surface.

Based on the technical realization, two different concepts, the tokamak and the stellarator, are distinguished. The latter employs a complex coil geometry, see Fig. 1.2(b), to generate the desired helically twisted field lines. In tokamaks, however, field coils are only used to provide the toroidal magnetic field. The poloidal component is created by a toroidal plasma current which is induced by applying the transformer principle, with the plasma itself as a secondary winding. This design is thus much easier to realize and, moreover, possesses an intrinsic plasma heating through the plasma current. However, in the absence of elaborate additional current driving mechanisms, it can only be operated in a pulsed regime due to the transformer principle, a problem which is not present in stellarators. Therefore, both concepts are still under investigation and further

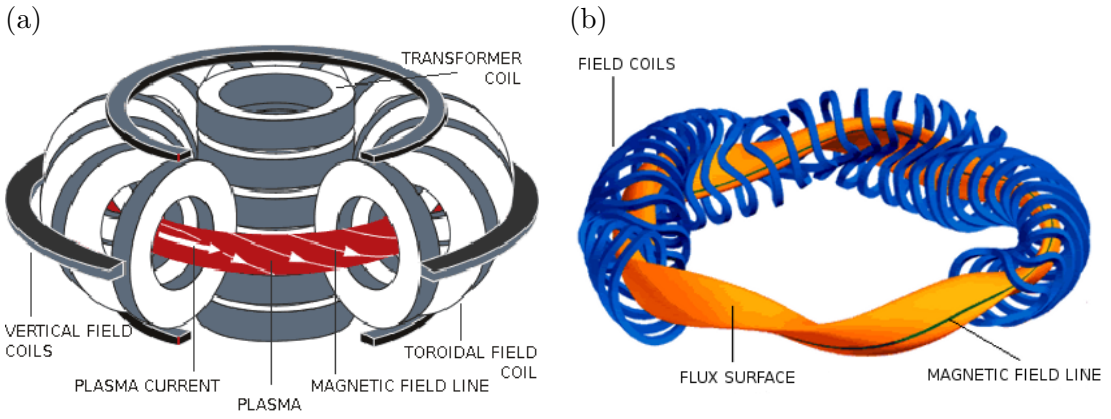

Figure 1.2: Schematic illustration of the two main concepts for magnetic confinement fusion devices: the tokamak (a) and the stellarator (b). Source: IPP

developed.

The next step on the way towards a fusion power plant is expected to be taken by the ITER tokamak [7] which is designed to reach breakeven, i.e. produce more power than is required to compensate for power losses. The underlying theoretical framework for such predictions is based on the Lawson criterion [8] which relates power losses due to convection and radiation to the power input. For self-sustaining plasmas, a corresponding power balance yields

$$nT\tau_E > 3 \times 10^{21} \frac{\mathrm{keV\,s}}{\mathrm{m}^3}, \tag{1.2}$$

see e.g. Ref. [6], for deuterium-tritium mixtures with density n. Here and in the following, a popular definition in plasma physics, $k_B T \to T$, is applied, thus measuring temperatures in units of energy. The third quantity, τ_E, denotes the energy confinement time, specifying the time scale on which energy can be retained in a plasma. For typical parameters of $T \approx 10 - 20\,\mathrm{keV}$ and $n \approx 10^{20}\,\mathrm{m}^{-3}$, it needs to be of the order of several seconds to allow for a self-sustaining plasma burning. Present-day experiments like ASDEX Upgrade typically exhibit $\tau_E \lesssim 0.2\,\mathrm{s}$ [9].

These findings clearly disagree with early theoretical predictions based on collision-induced cross-field transport. Classically, the only remaining transport mechanism perpendicular to flux surfaces is induced by particle collisions. The characteristic perpendicular length scale of gyrating particles with mass m in a magnetic field B_0 would then be on the order of a thermal gyroradius $\rho_{th} = v_T/\Omega$. Here, $v_T = (2T/m)^{1/2}$ denotes the thermal velocity and $\Omega = |q|\,B_0/(mc)$ the Larmor frequency in cgs units with the speed of light c. A random walk model, considering in addition a frequency ν for collisions among particles of the same species, would predict a thermal diffusivity $\chi \sim \rho_{th}^2 \nu$. For tokamaks with minor radius a, an associated confinement time $\tau_E \sim a^2/\chi$ can be esti-

mated which would amount to several hours, thus clearly exceeding the experimental findings. However, such an argument does not include magnetic field inhomogeneities. Taking this feature into account leads to the more sophisticated, neoclassical transport theory. Here, magnetic drift effects introduce new and larger length scales, leading to higher transport levels. Although examples exist where the ion heat transport appears to be neoclassical, it is usually underestimated. With respect to particle and electron heat transport, neoclassical theory fails to predict the correct levels by at least one order of magnitude.

At present, it is widely accepted that small scale instabilities, i.e. instabilities on scales of the order of the Larmor radius, are responsible for so-called anomalous transport. They are driven by the unavoidable density and temperature gradients occurring in fusion devices. Over the distance of about one meter, for instance, the temperature drops from the required central value of about 100 million K to several hundred K at the vessel walls. The theoretical understanding of the microinstabilities and associated turbulent fluctuations is therefore a crucial point on the way to optimized fusion devices. In the context of this work, contributions to this effort are the development of a new tool for the numerical simulation of plasma microturbulence and the investigation of turbulent features on separated space and time scales. However, before entering into a corresponding discussion, some details on plasma modeling shall be given.

1.3 Plasma modeling

Theories of plasmas are based on several mathematical models which can be subdivided into the following classes:

- **Single particle description**
  This type of model describes the motion of individual particles. Therefore it cannot handle self-consistent fields and is only valid if strong external fields are imposed. Furthermore, it is only applicable in the case of very dilute plasmas. However, a single particle description is probably the best choice to explain the aforementioned gyration in strong and homogeneous magnetic fields. In the non-relativistic limit, which can be assumed for fusion plasmas, the force balance equation reads, in the absence of electric fields,

$$m\dot{\mathbf{v}} = \frac{q}{c}\mathbf{v} \times \mathbf{B}_0. \tag{1.3}$$

  By considering an orthogonal coordinate system $(\hat{\mathbf{e}}_x, \hat{\mathbf{e}}_y, \hat{\mathbf{e}}_z)$ with $\hat{\mathbf{e}}_z = \mathbf{B}_0/B_0$, it can easily be shown that

$$\ddot{v}_{x,y} = -\Omega^2 \, v_{x,y} \tag{1.4}$$

which describes an oscillatory motion or gyration with Larmor frequency Ω. Here and in the following, dots indicate time derivatives.

- **Kinetic description**
  Instead of treating each particle individually, it often proves advantageous to describe the evolution of a phase space distribution $f_\sigma(\mathbf{x}, \mathbf{v})$ for each particle species σ in the presence of self-consistently derived electromagnetic fields. For this purpose, the so-called Vlasov equation [10],

$$\frac{\mathrm{d}f}{\mathrm{d}t} = \frac{\partial f}{\partial t} + \dot{\mathbf{x}} \cdot \frac{\partial f}{\partial \mathbf{x}} + \dot{\mathbf{v}} \cdot \frac{\partial f}{\partial \mathbf{v}} = 0 \tag{1.5}$$

  has to be solved which is coupled to Maxwell's equations. Although being one of the most fundamental plasma descriptions, it is typically only used in simplified versions due to its high dimensionality and complexity. In the presence of highly separable scales, for instance, perturbative techniques may be applied to reduce the number of dimensions.

- **Plasma fluid models**
  The velocity space distribution can be replaced by its moments if time scales are considered where collisional effects induced a thermalization of the plasma and kinetic effects as, for instance, Landau damping become negligible. However, in order to keep the complexity low, the system of equations for the macroscopic quantities like temperature, density, fluid velocity, etc. is truncated by applying appropriate approximations to the highest desired velocity space moment. The remaining continuum description in real space then bears an obvious resemblance to usual fluid models, with the inclusion of electromagnetic fields being the striking difference. If local charge neutrality is assumed, the plasma is treated as a one-component fluid. This model, usually referred to as magnetohydrodynamics (MHD), has been successfully applied e.g. to determine the magnetic field configuration in the presence of a specific set of field coils. For this purpose, stationary solutions are typically required which further simplify the set of equations. In the ideal, i.e. non-resistive, limit, they contain the following constraint

$$\nabla p_0 = \frac{1}{c} \mathbf{j}_0 \times \mathbf{B}_0 \tag{1.6}$$

  which relates the thermal plasma pressure p_0 to the plasma current density $\mathbf{j}_0$ and the magnetic field $\mathbf{B}_0$. Here and in the following, the index 0 indicates equilibrium quantities if not stated otherwise. Based on Eq. (1.6), it is obvious that the equilibrium pressure is constant on flux surfaces, a feature which will be utilized in a later chapter.

Of course, no claim of completeness is made for this list, and the main ideas have been presented only briefly. For a more detailed and comprehensive description, the reader may consult, for instance, Refs. [11, 12].

Turbulence studies being applied to magnetically confined fusion plasmas are usually based on kinetic descriptions since collisions only play a subdominant role in these hot and dilute plasmas.

1.4 Multiple scales in plasma microturbulence

Apparently, various space and time scales are involved in the description of magnetically confined plasmas. The characteristic length scales, for instance, include the electron gyroradius on the submillimeter range as well as correlation lengths on the order of several meters along a magnetic field line. With respect to the time scales, fast dynamics – like the high-frequency Larmor gyration – have to be considered, as well as the comparably large energy confinement time scale.

However, multiscale techniques allow for the definition of subsets of scales which can approximatively be investigated separately. For instance, the aforementioned turbulent fluctuations are much faster than the energy confinement time but slow compared to the gyrofrequencies. In addition, they typically exhibit small relative amplitudes. For the prediction of anomalous transport, it is therefore quite common to consider constant mean values on the one hand, and special models reducing the description of the gyromotion on the other. The kinetic theory – chosen due to the weak collisionality emerging in hot and dilute fusion plasmas – is therefore replaced by the so-called gyrokinetic theory which will be discussed in more detail in the next chapter.

But even in the reduced model, several scales can occur. On the macroscopic side, these are the temperature and density gradients which can be modified even by small amplitude fluctuations, as can now be observed with a newly developed tool presented in this thesis. On the other hand, various turbulence types exist which may be distinguished by means of their characteristic wave numbers and frequencies. Three prominent examples which will be addressed in this work are the ion temperature gradient (ITG) driven mode, the trapped electron mode (TEM), and the electron temperature gradient (ETG) mode. While the first two types are typically found on space-time scales attributed to the ion dynamics, the ETG mode resides on electron scales. Obviously, the question arises whether both turbulence scales can be treated independently. Furthermore, the significance of ETG modes for heat transport fluxes is currently a controversial issue. Namely, mixing length estimates predicting negligible contributions have recently been challenged by new theoretical and experimental findings. A clarification along these line is desparately needed since future fusion devices will exhibit a strong electron heating caused by the α particles which are generated in a fusion reaction, see Eq. (1.1).

A corresponding discussion of these two topics constitutes another main part of this thesis. Due to the complexity of the underlying equations, it will be based on numerical simulations. Although a highly parallelized and optimized code is at hand, a self-consistent coverage of the involved ion and electron space and time scales requires an enormous computational effort. The simulations which will be presented in this work are therefore amongst the first few which have been performed in this context worldwide.

1.5 Thesis Outline

As previously mentioned, a kinetic description will be employed for microturbulence investigations throughout this work since most of the present day tokamak plasmas operate in the long mean free path regime where wave-particle interactions become important.

First, this so-called gyrokinetic theory will be discussed in Chapter 2 in more detail. During the derivation of the basic equations, special attention will be paid to retain the full radial dependencies, thus extending previous treatments where locality, i.e. the consideration of just a small radial domain, has been assumed.

In Chapter 3, information will be provided on how the gyrokinetic Vlasov-Maxwell system of equations is numerically solved by means of the nonlinear, gyrokinetic Vlasov code GENE. Besides a presentation of the well-established local code version, special focus will be put on the recent implementation of radial variations allowing for the investigation of nonlocal effects. In particular, new boundary conditions and numerical schemes will be discussed since spectral methods which could be employed in the local code had to be replaced. Furthermore, source and sink terms will be introduced and the observables used in subsequent chapter will be defined.

Afterwards, results of several microturbulence investigations will be presented. In Chapter 4, the role of small-scale turbulence occurring on scales of the order of the electron gyroradius within much larger turbulence on ion gyroradius scales will be addressed. By studying several prototypical parameter sets describing experimentally relevant scenarios, a first evaluation of the significance of small-scale driven transport will be given. Further implications on experimentally accessible observables, as for instance, density spectra, will be discussed as well.

Another length scale comes into play if full radial temperature and density profiles are considered as is done in the newly developed global GENE version. Before first results regarding the influence of nonlocal effects are discussed, extensive benchmarking and testing efforts will be presented in Chapter 5 in order to verify the implementation. Hereafter, simulations including a recently added heat source model will be shown and discussed.

Chapter 6 finally contains the conclusions and an outlook on subsequent projects.

Chapter 2

An introduction to and an application of gyrokinetic theory

The aim of this chapter is to derive and describe the equations underlying the nonlinear gyrokinetic Vlasov code GENE which has been used to produce most of the results presented in the following chapters. Thus, an introduction to gyrokinetic theory is the first step to be taken.

The dedicated subsequent sections follow in parts the fundamental works by Brizard and Hahm, in particular their review [13]. Furthermore, the second part of this chapter presenting the derivation of the GENE specific equations is partially based on Ref. [14]. However, the latter is here substantially extended by considering additional radial variations of temperature, density and geometry which have formerly been treated only in a very narrow radial domain. With these modifications it will be possible to investigate nonlocal effects with the GENE code for the first time.

2.1 Basic ideas of gyrokinetic theory

As mentioned earlier, a kinetic description involving a 6-dimensional distribution function $f(\mathbf{x}, \mathbf{v}, t)$ per species using a Vlasov operator coupled to the Maxwell equations is the most fundamental way of modeling plasma dynamics. However, the resulting system of nonlinear integro-differential equations can in general not be solved analytically, so that a numerical approach has to be taken. Here, the variety of different space and time scales present in a typical fusion plasma demands for grid and time step resolutions which can exceed even the computing power of present-day supercomputers. Therefore, extensive analytical effort has been spent to optimize the underlying equations using simplifications or sophisticated perturbation theories [15]. One of the most popular results of the efforts, modern gyrokinetic theory [16, 17, 18, 19], will be discussed in this section.

2.1.1 The gyrokinetic ordering

Before a description of gyrokinetic theory can be given, some important experimental observations of magnetically confined high-temperature plasmas shall be reviewed briefly. In general, they are characterized as strongly turbulent systems with the following features [13]:

(i) The *relative fluctuation levels* of the turbulent quantities, e.g. the density $\delta n/n \sim \epsilon_\delta \ll 1$, are typically *very small*. Only at the plasma edge they might reach values of up to several ten percent.

(ii) The fluctuations are highly anisotropic. Due to the Lorentz force, typical correlation lengths or wavelengths perpendicular to the magnetic field are on the order of $10 - 100$ gyroradii, while up to several meters can be reached in the parallel direction. In terms of wave numbers, these findings can be written as $k_\parallel/k_\perp \sim \epsilon_\parallel \ll 1$. The equilibrium or background part of e.g. the density hardly varies on the gyroradius scale.

(iii) The spectrum of frequencies ω is typically broadband with a characteristic mean frequency on the order of the diamagnetic drift frequency $\omega_D = \mathbf{k} \cdot \mathbf{v}_D$ for a given wave vector $\mathbf{k}$ and drift velocity $\mathbf{v}_D = cT/(eB)\hat{\mathbf{b}} \times \nabla \ln p$. Here, $\hat{\mathbf{b}} = \mathbf{B}/B$ denotes the unit vector along the magnetic field line with amplitude $B = |\mathbf{B}|$, and p is the thermal plasma pressure. For typical plasma parameters, the *diamagnetic frequency* is *much smaller than the gyrofrequency* Ω. Furthermore, another typical frequency, the bounce frequency ω_b which is determined by the magnetic moment μ and the topology of the field line, can be considered small compared to Ω. Hence, $\omega/\Omega \sim \epsilon_\omega \ll 1$. Again, the background quantities, typically evolving on the confinement time scale, can be assumed to be constant.

The third property provides the basis for a simplification of the full kinetic description by reducing the description of the fast gyromotion of the charged particle to the dynamics of a charged ring as illustrated in Fig. 2.1. However, features (i) and (ii) will be employed as well.

2.1.2 Elimination of the gyroangle dependence

Approximating the full gyromotion by the dynamics of charged rings basically implies the elimination of information on the exact gyroorbit position which can be parametrized by a gyroangle. However, if certain conservation laws and adiabatic invariants shall be conserved, a very sophisticated approach has to be chosen. To facilitate the orientation along the corresponding line of arguments, an overview illustrating the most important steps of the derivation of the gyrokinetic Vlasov equation is shown in Fig. 2.2.

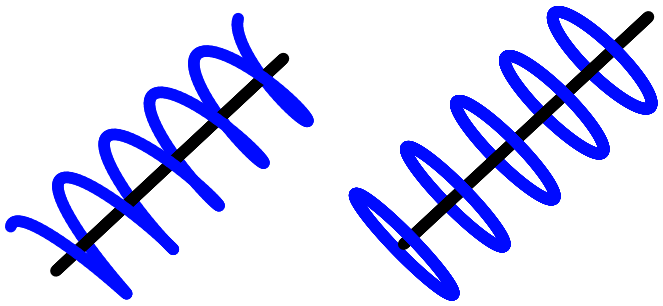

Figure 2.1: In gyrokinetic theory, the full description of the gyromotion, shown on the left side, is approximated by the dynamics of charged rings which are schematically drawn on the right side.

Based on the Hamiltonian of particles in electromagnetic fields, a corresponding one-form formulation is established to simplify a subsequent transformation to guiding-center coordinates where the gyroangle enters explicitly. The latter is then removed as desired by employing a perturbative approach. While the elimination is simply an averaging procedure for unperturbed equilibrium quantities, it turns out to be much more delicate for the perturbed part where a Lie transformation has to be utilized. The resulting gyrocenter one-form is afterwards used to establish the new Lagrangian which yields to the equations of motion when being substituted in the Euler-Lagrange equations. The thus obtained time derivatives of the gyrocenter coordinates are finally employed to determine the gyrokinetic Vlasov equation.

Particle Hamiltonian dynamics

The starting point is to determine the Hamiltonian particle dynamics. For a non-relativistic particle with mass m, charge q, and velocity $\mathbf{v}$ at position $\mathbf{x}$ in a magnetic potential $\mathbf{A}(\mathbf{x})$ and an electrostatic potential $\phi(\mathbf{x})$, it is given by the Hamiltonian

$$H(\mathbf{x},\mathbf{v}) = \frac{1}{2}mv^2 + q\phi(\mathbf{x}), \tag{2.1}$$

or the Lagrangian

$$L(\mathbf{x},\mathbf{v}) = \mathbf{p}(\mathbf{v})\cdot\dot{\mathbf{x}} - H(\mathbf{x},\mathbf{v}) \tag{2.2}$$

$$= \left(m\mathbf{v} + \frac{q}{c}\mathbf{A}(\mathbf{x})\right)\cdot\dot{\mathbf{x}} - \left(\frac{1}{2}mv^2 + q\phi(\mathbf{x})\right), \tag{2.3}$$

respectively.

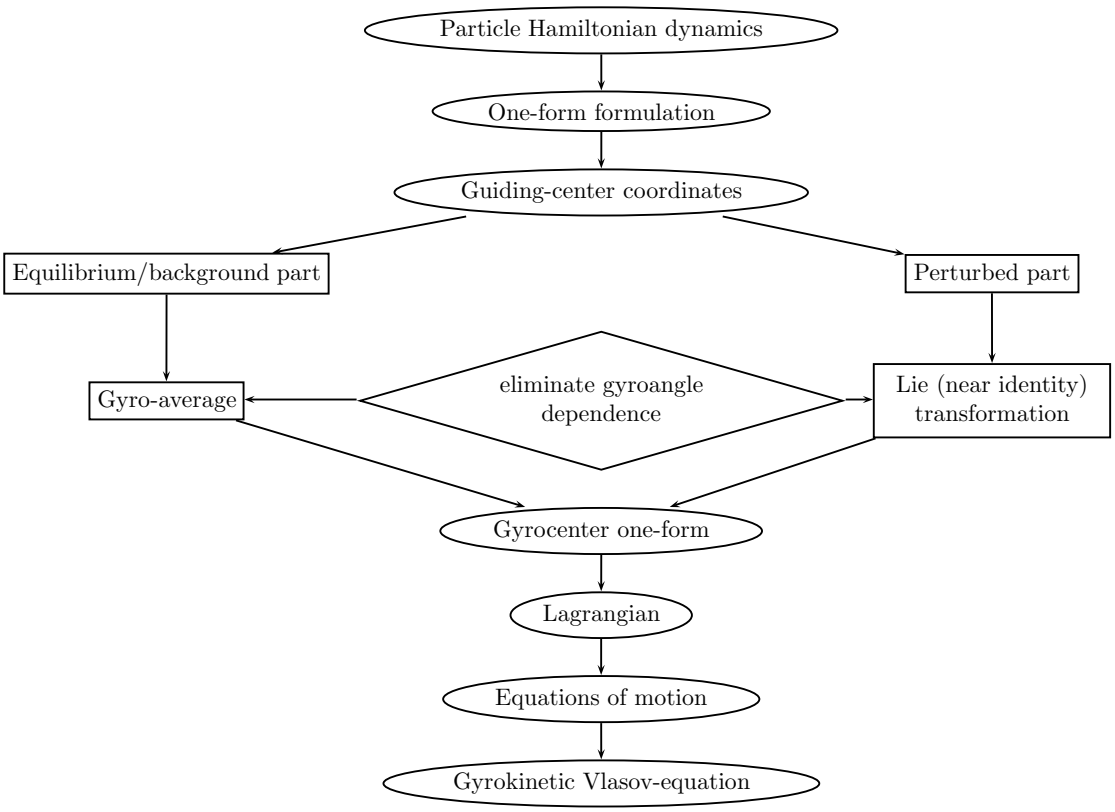

Figure 2.2: Overview of the most important steps of the derivation of the gyrokinetic Vlasov equation as used in the following.

One-form formulation

Now, in order to facilitate approximations based on the mentioned orderings, it proves advantageous to change to a different set of coordinates. For this purpose, it is favorable to continue with a one-form $\gamma(\mathbf{x}, \mathbf{v})$, implicitly defined by

$$\int L(\mathbf{x}, \mathbf{v}) \mathrm{d}t = \int \gamma(\mathbf{x}, \mathbf{v}) \tag{2.4}$$

instead of using the Lagrangian itself. A coordinate transformation can then simply be expressed by

$$\Gamma_\mu = \gamma_\nu \frac{\mathrm{d}z^\nu}{\mathrm{d}Z^\mu}. \tag{2.5}$$

where Γ and γ are the one-forms in terms of the coordinates $\mathbf{Z}$ and $\mathbf{z}$ and ν and μ are indices running through all entries therein. In the present case, the particle coordinates shall be replaced by a set of coordinates which utilizes the properties of the magnetic field. As mentioned before the latter is usually dominated by an equilibrium part $\mathbf{B}_0(\mathbf{x})$

which is almost constant along a thermal gyroradius ρ_{th} therefore fulfilling

$$\frac{\rho_{th}}{L_B} \sim \epsilon_B \ll 1. \tag{2.6}$$

Here, L_B denotes the typical scale length of the magnetic equilibrium field. These premises allow for approximating the perpendicular motion to be purely circular.

Transformation to guiding-center coordinates

Hence it is possible to introduce so-called guiding-center coordinates $Z = (\mathbf{X}, v_\parallel, \mu, \theta, t)$ which include the center of the gyration $\mathbf{X}$, the velocity along the magnetic field line $v_\parallel = \mathbf{v}\cdot\hat{\mathbf{b}}$, the gyroangle θ and the magnetic moment $\mu = mv_\perp^2/(2B)$ with $v_\perp = |\mathbf{v} - v_\parallel\hat{\mathbf{b}}|$. They are linked to the particle coordinates by the following transformation equations

$$\mathbf{x} = \mathbf{X} + \mathbf{r}(\mathbf{X}, \mu, \theta), \tag{2.7}$$

$$\mathbf{v} = v_\parallel\hat{\mathbf{b}}_0(\mathbf{X}) + v_\perp(\mathbf{X}, \mu)\mathbf{c}(\theta), \tag{2.8}$$

where $\mathbf{r}(\mathbf{X}, \mu, \theta) = \rho(\mathbf{X}, \mu)\mathbf{a}(\theta)$ denotes the gyroradius vector with the norm $\rho(\mathbf{X}, \mu) = v_\perp(\mathbf{X})/\Omega(\mathbf{X})$, and

$$\mathbf{a}(\theta) = \cos\theta\,\hat{\mathbf{e}}_1 + \sin\theta\,\hat{\mathbf{e}}_2 \qquad \text{and} \qquad \mathbf{c}(\theta) = \frac{\partial\mathbf{a}(\theta)}{\partial\theta} = -\sin\theta\,\hat{\mathbf{e}}_1 + \cos\theta\,\hat{\mathbf{e}}_2 \tag{2.9}$$

are the unit vectors in radial and in tangential direction of a circle in the local Cartesian coordinate system spanned by $(\hat{\mathbf{e}}_1, \hat{\mathbf{e}}_2, \hat{\mathbf{b}}_0)$. The direction of rotation which depends on the particle charge defines the range of the gyroangle being either $[0, 2\pi)$ or $(-2\pi, 0]$. However, as it will become more obvious in the following, it does not enter the equation which perfectly agrees with the intention of replacing the gyromotion by a gyroring description.

Perturbed guiding-center one-form

Based on the gyrokinetic ordering introduced before, in particular constraint (i), it is advantageous to split the potentials in an equilibrium and a small perturbation part as well before transforming the one-form. Neglecting electrostatic equilibrium potentials since they will not appear in the physical situations under consideration yields

$$\phi(\mathbf{x}) = \phi_1(\mathbf{x}) \qquad \text{and} \qquad \mathbf{A}(\mathbf{x}) = \mathbf{A}_0(\mathbf{x}) + \mathbf{A}_1(\mathbf{x}) \tag{2.10}$$

and thus $\gamma = \gamma_0 + \gamma_1$ with

$$\gamma_0 = \left(m\mathbf{v} + \frac{q}{c}\mathbf{A}_0(\mathbf{x})\right)\cdot\mathrm{d}\mathbf{x} - \frac{1}{2}mv^2\mathrm{d}t, \tag{2.11}$$

$$\gamma_1 = \frac{q}{c}\mathbf{A}_1(\mathbf{x})\cdot\mathrm{d}\mathbf{x} - q\phi_1(\mathbf{x})\mathrm{d}t. \tag{2.12}$$

The unperturbed part can be transformed in a straightforward way using the one-form transformation instruction of Eq. (2.5). Taking furthermore advantage of the slow spatial variation of the unperturbed quantities (see condition (ii)) allows for replacing the particle position $\mathbf{x}$ approximately by the gyrocenter position $\mathbf{X}$. Finally, remaining gyroangle dependencies, for instance in terms $\mathbf{A}_0(\mathbf{X}) \cdot \mathbf{a}(\theta)$, are removed by gyroaveraging the intermediate result with a gyroaverage operator $\mathcal{G} = \frac{1}{2\pi}\int \mathrm{d}\theta$. In summary, the unperturbed, gyroaveraged gyrocenter one-form then reads

$$\bar{\Gamma}_0 = \left(mv_\parallel \hat{\mathbf{b}}_0(\mathbf{X}) + \frac{q}{c}\mathbf{A}_0(\mathbf{X})\right) \cdot \mathrm{d}\mathbf{X} + \frac{\mu mc}{q}\mathrm{d}\theta - \left(\frac{1}{2}mv_\parallel^2 + \mu B_0(\mathbf{X})\right)\mathrm{d}t \tag{2.13}$$

The perturbed part can be evaluated in a similar way up to the intermediate result

$$\begin{aligned}\Gamma_1 =& \frac{q}{c}\mathbf{A}_1(\mathbf{X}+\mathbf{r}) \cdot \mathrm{d}\mathbf{X} + \frac{\mathbf{A}_1(\mathbf{X}+\mathbf{r}) \cdot \mathbf{a}(\theta)}{v_\perp(\mathbf{X})}\mathrm{d}\mu \\ &+ \frac{mv_\perp(\mathbf{X})}{B_0(\mathbf{X})}\mathbf{A}_1(\mathbf{X}+\mathbf{r}) \cdot \mathbf{c}(\theta)\mathrm{d}\theta - q\phi_1(\mathbf{X}+\mathbf{r})\mathrm{d}t.\end{aligned} \tag{2.14}$$

However, the strongly spatio-temporally varying fluctuating field parts prevent the formerly used simplification of replacing the particle by the gyrocenter position and hence no simple gyroaveraging procedure is applicable. Instead, another coordinate transformation is required in order to erase the gyrophase dependence.

Lie perturbation theory

A very convenient mathematical tool fitting to this kind of purpose is the Lie transform [15, 20], a particular type of near-identity coordinate transformations in extended phase space.

Here, the new set of coordinates $\bar{Z}$, being a function of a continuous smallness parameter ϵ and the old coordinates Z, is implicitly defined by the differential equation

$$\frac{\partial \bar{Z}^\nu(Z,\epsilon)}{\partial \epsilon} = G^\nu(\bar{Z}(Z,\epsilon)) \tag{2.15}$$

with the generating functions $G(\bar{Z}(Z,\epsilon))$ and the index ν running over all coordinates within $\bar{Z}$ and Z. Considering the initial condition $\bar{Z}^\nu(Z,0) = Z^\nu$, Eq. (2.15) can be rewritten as

$$\bar{Z}^\nu(Z,\epsilon) = T(\epsilon)Z^\nu, \tag{2.16}$$

where an operator $T(\epsilon) = \exp(\epsilon G^\nu)$ has been introduced. To lowest order in ϵ, it becomes $\bar{Z}^\nu(Z,\epsilon) = Z^\nu + \mathcal{O}(\epsilon)$ which is the basic property of a near-identity transformation.

Now, going from coordinates to the previously discussed one-forms, the transformation reads [15]

$$\bar{\Gamma} = T^{*-1}\Gamma + dS, \tag{2.17}$$

where S denotes a gauge function which shall later be chosen such that the resulting equations become as simple as possible. The operator T^{*-1} consists of as many individual Lie transforms using the Lie derivative for one-forms,

$$\left[L_G\Gamma\right](Z) = G^\lambda(Z)\left(\frac{\partial\Gamma_\nu(Z)}{\partial Z^\lambda} - \frac{\partial\Gamma_\lambda(Z)}{\partial Z^\nu}\right), \tag{2.18}$$

as orders in ϵ are desired. For instance, up to second order T^{*-1} becomes

$$T^{*-1} = \exp\left(-\epsilon L_1\right)\exp\left(-\epsilon^2 L_2\right) = 1 - \epsilon L_1 + \epsilon^2\left(\frac{1}{2}L_1^2 - L_2\right) + \mathcal{O}(\epsilon^3) \tag{2.19}$$

Similar expansions in ϵ of the one-forms $\bar{\Gamma}$ and Γ as well as the gauge function S facilitate setting up the following equations

$$\bar{\Gamma}_0 = \Gamma_0 + dS_0 \tag{2.20}$$

$$\bar{\Gamma}_1 = \Gamma_1 - L_1\Gamma_0 + dS_1 \tag{2.21}$$

$$\bar{\Gamma}_2 = \Gamma_2 - L_1\Gamma_1 + \left(\frac{1}{2}L_1^2 - L_2\right)\Gamma_0 + dS_2 \tag{2.22}$$

Application to the guiding-center one-form

The zeroth order equation has already been solved before, so that solely Eq. (2.21) has to be considered in the following if just terms up to the order of ϵ are kept. As discussed in more detail, e.g., in Ref. [14], the generating functions are chosen such that

$$\begin{aligned}
G_1^{\mathbf{X}} =& -\left(\frac{\hat{\mathbf{b}}_0}{B_{0\parallel}^*}\times\tilde{\mathbf{A}}_1 + \frac{\mathbf{B}_0^*}{B_{0\parallel}^*}\frac{1}{m}\frac{\partial S_1}{\partial v_\parallel} + \frac{c}{q}\frac{\hat{\mathbf{b}}_0}{B_{0\parallel}^*}\times\nabla S_1\right)\\
G_1^{\mu} =& \frac{q}{c}\frac{v_\perp}{B_0}\mathbf{A}_1\cdot\mathbf{c} + \frac{q}{mc}\frac{\partial S_1}{\partial\theta}\\
G_1^{v_\parallel} =& \frac{\Omega}{B_0}\frac{\mathbf{B}_0^*}{B_{0\parallel}^*}\cdot\left(\tilde{\mathbf{A}}_1 + \frac{c}{q}\nabla S_1\right)\\
G_1^{\theta} =& -\frac{\Omega}{B_0}\left(\frac{1}{v_\perp}\mathbf{A}_1\cdot\mathbf{a} + \frac{\partial S_1}{\partial\mu}\right).
\end{aligned} \tag{2.23}$$

If, in addition, the gauge function S_1 is set to

$$\begin{aligned}
S_1 = S_1(\theta) =& \frac{1}{\Omega}\int^\theta\left(q\tilde{\phi}_1(\mathbf{X}+\mathbf{r}(\theta')) + \frac{1}{B_{0\parallel}^*}(\hat{\mathbf{b}}_0\times\tilde{\mathbf{A}}_1(\mathbf{X}+\mathbf{r}(\theta'))\cdot\mu\nabla B_0\right.\\
&- \frac{q}{c}v_\parallel\frac{\mathbf{B}_0^*}{B_{0\parallel}^*}\cdot\tilde{\mathbf{A}}_1(\mathbf{X}+\mathbf{r}(\theta')) - \frac{q}{c}v_\perp\mathbf{A}_1(\mathbf{X}+\mathbf{r}(\theta'))\cdot\mathbf{c}(\theta')\\
&\left.+ \frac{q}{c}v_\perp\langle\mathbf{A}_1(\mathbf{X}+\mathbf{r}(\theta'))\cdot\mathbf{c}(\theta')\rangle\right)\mathrm{d}\theta',
\end{aligned} \tag{2.24}$$

all gyroangle dependencies in the one-form in first perturbation order can be removed. Here, a tilde indicates gyroangle dependent parts whereas overbars or the following brackets $\langle \ldots \rangle$ denote gyroaveraged quantities so that, e.g., the vector potential $\mathbf{A}_1$ can be divided into $\mathbf{A}_1 = \tilde{\mathbf{A}}_1 + \langle \mathbf{A}_1 \rangle$. Furthermore, the abbreviation $\mathbf{B}_0^* = \nabla \times \mathbf{A}_0^* = \nabla \times (\mathbf{A}_0 + \mathbf{B}_0 v_\parallel / \Omega)$ has been used.

Summarizing, the gyrocenter one-form up to first order in perturbation theory becomes

$$\begin{aligned}\bar{\Gamma} =& \bar{\Gamma}_0 + \bar{\Gamma}_1 \\ =& \left(m v_\parallel \hat{\mathbf{b}}_0 + \frac{q}{c}\mathbf{A}_0 + \frac{q}{c}\bar{A}_{1\parallel}\hat{\mathbf{b}}_0 \right) \cdot \mathrm{d}\mathbf{X} + \frac{\mu m c}{q}\mathrm{d}\theta - \left(\frac{1}{2} m v_\parallel^2 + q\bar{\phi}_1 + \mu \left(B_0 + \bar{B}_{1\parallel} \right) \right) \mathrm{d}t \end{aligned} \tag{2.25}$$

where as before equilibrium quantities have to be evaluated at gyrocenter $\mathbf{X}$ and perturbed potentials or fields at particle position $\mathbf{x} = \mathbf{X} + \mathbf{r}$. Furthermore, $\frac{q}{c} v_\perp \langle \mathbf{A}_1 \cdot \mathbf{c} \rangle$ has been identified as $-\mu \bar{B}_{1\parallel}$.

Finally, the pull-back operator to first order in the perturbative expansion acting on a scalar function s shall be mentioned, too, since it will become of interest e.g. in the gyrokinetic field equations. Using the Lie derivative acting on scalars

$$[L_G s](Z) = G^\nu \frac{\partial s}{\partial Z^\nu} \tag{2.26}$$

it turns out to be

$$\begin{aligned} T^* s =& \exp(\epsilon L_G) s + \mathcal{O}(\epsilon^2) \\ \approx& 1 + \epsilon \sum_\nu G^\nu \frac{\partial s}{\partial Z^\nu}. \end{aligned} \tag{2.27}$$

or, if the scalar function can be split into an equilibrium and a perturbed part, $s = s_0 + s_1$,

$$\begin{aligned} T^* s_0 =& s_0, \\ T^* s_1 =& s_1 + \frac{1}{B_0} \left[\Omega \frac{\mathbf{B}_0^*}{B_{0\parallel}^*} \cdot \tilde{\mathbf{A}}_1 \frac{\partial s_0}{\partial v_\parallel} + \left(q\tilde{\phi}_1 - \frac{q}{c} v_\parallel \frac{\mathbf{B}_0^*}{B_{0\parallel}^*} \cdot \tilde{\mathbf{A}}_1 - \mu \bar{B}_{1\parallel} \right) \frac{\partial s_0}{\partial \mu} \right]. \end{aligned} \tag{2.28}$$

2.2 The gyrokinetic Vlasov equation

Having realized the basic idea of gyrokinetics, i.e. replacing the full gyromotion by a gyroring description using elaborate perturbation methods, it is now possible to perform the next steps on the way to the gyrokinetic Vlasov equation. The first one is to construct the corresponding Lagrangian from the one-form as indicated in Eq. (2.4). Afterwards, the Euler-Lagrange equations

$$\frac{\mathrm{d}}{\mathrm{d}t} \left(\frac{\partial L}{\partial \dot{Z}^\nu} \right) - \frac{\partial L}{\partial Z^\nu} = 0 \tag{2.29}$$

are used to solve for the equations of motion for each gyrocenter coordinate. With these results and the approximation $\nabla \times (\hat{\mathbf{b}}_0 \bar{A}_{1\parallel}) = (\nabla \bar{A}_{1\parallel}) \times \hat{\mathbf{b}}_0 + \mathcal{O}(\epsilon_B) \approx (\nabla \bar{A}_{1\parallel}) \times \hat{\mathbf{b}}_0$ it is possible to transform the so-called full-F Vlasov equation for the σth species

$$\frac{\partial F_\sigma}{\partial t} + \dot{\mathbf{X}} \cdot \nabla F_\sigma + \dot{\mu} \frac{\partial F_\sigma}{\partial \mu} + \dot{v}_\parallel \frac{\partial F_\sigma}{\partial v_\parallel} = 0 \tag{2.30}$$

into

$$\begin{aligned} \frac{\partial F_\sigma}{\partial t} + \left[v_\parallel \hat{\mathbf{b}}_0 + \frac{B_0}{B_{0\parallel}^*} \left(\mathbf{v}_{\bar{\xi}} + \mathbf{v}_{\nabla B} + \mathbf{v}_c \right) \right] \cdot \\ \left\{ \nabla F_\sigma - \left(q_\sigma \nabla \bar{\phi}_1 + \frac{q_\sigma}{c} \hat{\mathbf{b}}_0 \dot{\bar{A}}_{1\parallel} + \mu \nabla \left(B_0 + \bar{B}_{1\parallel} \right) \right) \frac{1}{m_\sigma v_\parallel} \frac{\partial F_\sigma}{\partial v_\parallel} \right\} = 0 \end{aligned} \tag{2.31}$$

with the gyroaveraged modified potential

$$\bar{\xi}_1 = \bar{\phi}_1 - \frac{v_\parallel}{c} \bar{A}_{1\parallel} + \frac{\mu}{q_\sigma} \bar{B}_{1\parallel}, \tag{2.32}$$

the generalized $\mathbf{E} \times \mathbf{B}$ velocity

$$\mathbf{v}_{\bar{\xi}} = \frac{c}{B_0^2} \mathbf{B}_0 \times \nabla \bar{\xi}_1, \tag{2.33}$$

the gradient-B velocity

$$\mathbf{v}_{\nabla B_0} = \frac{\mu c}{q_\sigma B_0^2} \mathbf{B}_0 \times \nabla B_0 \tag{2.34}$$

and the curvature drift velocity

$$\mathbf{v}_c = \frac{v_\parallel^2}{\Omega_\sigma} \left(\nabla \times \hat{\mathbf{b}}_0 \right)_\perp . \tag{2.35}$$

The latter can be further evaluated with the help of Ampère's law and the equilibrium condition in magnetohydrodynamics $\nabla p_0 = \frac{1}{c} \mathbf{j}_0 \times \mathbf{B}_0$ which has already been introduced in Sec. 1.3. The final result is

$$\mathbf{v}_c = \frac{v_\parallel^2}{\Omega_\sigma} \left(\hat{\mathbf{b}}_0 \times \left[\frac{\nabla B_0}{B_0} + \frac{\beta_p}{2} \frac{\nabla p_0}{p_0} \right] \right) \tag{2.36}$$

where $\beta_p \equiv 8\pi p_0 / B_0^2$, the well known thermal to magnetic pressure ratio [21], has been used.

Basically, the only task left in terms of gyrokinetic theory is to derive the field equations. However, before approaching this point, some further simplifications will be introduced to the gyrokinetic Vlasov equation. For instance, it makes sense to utilize the flute like character of plasma microturbulence and employ some corresponding approximations. For this purpose, a coordinate system has to be established which is aligned with respect to the magnetic field. Furthermore, splitting the distribution function in an equilibrium and a fluctuating part proves advantageous in terms of computational effort. Finally, a proper normalization has to be found in order to establish dimensionless equations which are required for a numerical treatment.

2.2.1 The field aligned coordinate system

The strong anisotropy of plasma turbulence with respect to the directions along and perpendicular to the magnetic field, see constraint (ii), motivates a choice of accordingly defined space coordinates. Therefore, transformation metrics have to be constructed and and e.g. included in the gradients in Eq. (2.31). This can either be done analytically by solving the Grad-Shafranov [22, 23] equation for idealized cases (see for instance [24, 25]) or numerically by e.g. tracing magnetic field lines calculated by MHD equilibrium codes (e.g. [26, 27]). However, a detailed description is postponed to Chapter 3. Here, only properties of a field aligned coordinate system with coordinates $u^{(1,2,3)} = (x, y, z)$, namely the representation of the magnetic field

$$\mathbf{B}_0 = \mathcal{C}\, \nabla x \times \nabla y \tag{2.37}$$

and the definition of the Jacobian

$$J^{-1} = (\nabla x \times \nabla y) \cdot \nabla z = \frac{\mathbf{B_0} \cdot \nabla z}{\mathcal{C}}, \tag{2.38}$$

as well as a general metric tensor

$$g = (g^{ij}) = (\nabla u^i \cdot \nabla u^j) = \begin{pmatrix} g^{xx} & g^{xy} & g^{xz} \\ g^{xy} & g^{yy} & g^{yz} \\ g^{xz} & g^{yz} & g^{zz} \end{pmatrix} \tag{2.39}$$

are used to study the modifications which arise in the Vlasov equation, Eq. (2.31). Here, z denotes the coordinate along the field line, while x and y point along perpendicularly oriented directions as indicated by Eq. (2.37). Furthermore, from now on, x shall be the radial coordinate whereas the y axis is aligned on the flux surface spanned by $\mathbf{B}_0$. Now, with Eqs. (2.37) and (2.39) one can easily derive

$$\begin{aligned} B_0^2 &= \mathbf{B}_0 \cdot \mathbf{B}_0 \\ &= \mathcal{C}^{\,2} \left(g^{xx} g^{yy} - (g^{xy})^2 \right) \equiv \mathcal{C}^{\,2} \gamma_1 \end{aligned} \tag{2.40}$$

where the abbreviation

$$\gamma_1 = g^{11} g^{22} - g^{21} g^{12} \tag{2.41}$$

has been implicitly introduced. As it will become clear later on, γ_1 is often accompanied by the closely related terms

$$\gamma_2 = g^{11} g^{23} - g^{21} g^{13} \qquad \text{and} \qquad \gamma_3 = g^{12} g^{23} - g^{22} g^{13} \tag{2.42}$$

so that they already shall be defined at this point for the sake of completeness.

The relation above derived for B_0^2, Eq. (2.40), allows for the evaluation of the outer vector product in the drift velocities in the following way

$$\begin{aligned}\frac{1}{B_0^2}\left(\mathbf{B}_0\times\nabla\zeta\right)\cdot\nabla &= \frac{\mathcal{C}}{B_0^2}\left(\left[\nabla x\times\nabla y\right]\times\partial_i\zeta\nabla u^i\right)\cdot\nabla u^j\partial_j \\ &= \frac{1}{\mathcal{C}}\frac{g^{1i}g^{2j}-g^{2i}g^{1j}}{\gamma_1}\partial_i\zeta\partial_j \end{aligned} \tag{2.43}$$

where ζ denotes a placeholder for any scalar function or field component and $\partial_i \equiv \frac{\partial}{\partial u^i}$. On the other hand, Eqs. (2.37) and (2.38) can be used to find an expression for the parallel derivatives

$$\begin{aligned}\mathbf{B}_0\cdot\nabla &= \mathcal{C}\,\left[\nabla x\times\nabla y\right]\cdot\nabla u^i\partial_i \\ &= \frac{\mathcal{C}}{J}\partial_z \end{aligned} \tag{2.44}$$

so that the gyrokinetic Vlasov equation, Eq. (2.31), can be transformed to

$$\begin{aligned}&\frac{\partial F_\sigma}{\partial t}-\frac{q_\sigma}{m_\sigma c}\dot{\bar{A}}_{1\parallel}\frac{\partial F_\sigma}{\partial v_\parallel}+\frac{\mathcal{C}}{JB_0}\left\{v_\parallel\partial_z F_\sigma-\left(q_\sigma\partial_z\bar{\phi}_1+\mu\partial_z\left(B_0+\bar{B}_{1\parallel}\right)\right)\frac{1}{m_\sigma}\frac{\partial F_\sigma}{\partial v_\parallel}\right\} \\ &\quad+\frac{B_0}{B_{0\parallel}^*}\frac{c}{\mathcal{C}}\frac{g^{1i}g^{2j}-g^{2i}g^{1j}}{\gamma_1}\left(\partial_i\bar{\xi}_1+\frac{\mu}{q_\sigma}\partial_i B_0+\frac{m_\sigma v_\parallel^2}{q_\sigma}\left[\frac{\partial_i B_0}{B_0}+\frac{\beta_p}{2}\frac{\partial_i p_0}{p_0}\right]\right)\cdot \\ &\quad\left\{\partial_j F_\sigma-\left(q_\sigma\partial_j\bar{\phi}_1+\mu\partial_j\left(B_0+\bar{B}_{1\parallel}\right)\right)\frac{1}{m_\sigma v_\parallel}\frac{\partial F_\sigma}{\partial v_\parallel}\right\}=0. \end{aligned} \tag{2.45}$$

2.2.2 Splitting of the distribution function

In order to simplify the gyrokinetic Vlasov equation for computational purposes, it is a well established technique to split the distribution function into two parts, $F_\sigma = F_{0\sigma}+F_{1\sigma}$. The first one, $F_{0\sigma}$, is usually chosen to be close to the expected equilibrium or background distribution function and hence the second, $F_{1\sigma}$, contains the fluctuating part. Often, this kind of separation is accompanied by a corresponding ordering. Like for background and perturbed fractions of measurable moments of the distribution function, e.g. densities and temperatures, it is then assumed that $F_{1\sigma}/F_{0\sigma}\sim\epsilon_\delta\ll 1$.

In this thesis, the background distribution function is considered to be a so-called local, i.e. $\mathbf{x}$-dependent, Maxwellian in velocity space so that

$$\begin{aligned}F_\sigma(\mathbf{x},v_\parallel,\mu) &= F_{0\sigma}(\mathbf{x},v_\parallel,\mu)+F_{1\sigma}(\mathbf{x},v_\parallel,\mu) \\ &= \frac{n_{0\sigma}(\mathbf{x})}{\pi^{3/2}v_{T\sigma}^3(\mathbf{x})}\,\mathrm{e}^{-\frac{m_\sigma v_\parallel^2/2+\mu B_0(\mathbf{x})}{T_{0\sigma}(\mathbf{x})}}+F_{1\sigma}(\mathbf{x},v_\parallel,\mu). \end{aligned} \tag{2.46}$$

The derivatives are thus given by

$$\frac{\partial F_{0\sigma}}{\partial t}=0,\qquad \frac{\partial F_{0\sigma}}{\partial v_\parallel}=-\frac{m_\sigma v_\parallel}{T_{0\sigma}}F_{0\sigma},\qquad \frac{\partial F_{0\sigma}}{\partial\mu}=-\frac{B_0}{T_{0\sigma}}F_{0\sigma}, \tag{2.47}$$

and

$$\nabla F_{0\sigma} = \left[\frac{\nabla n_{0\sigma}}{n_{0\sigma}} + \frac{\nabla T_{0\sigma}}{T_{0\sigma}} \left(\frac{m_\sigma v_\parallel^2/2 + \mu B_0}{T_{0\sigma}} - \frac{3}{2} \right) - \frac{\nabla B_0}{B_0} \frac{\mu B_0}{T_{0\sigma}} \right] F_{0\sigma}. \tag{2.48}$$

The last equation can be further evaluated since background pressure and hence background temperature and density are constant on flux surfaces so that they depend solely on the radial coordinate x, which yields

$$\begin{aligned} \partial_x F_{0\sigma} &= \left[\frac{\partial_x n_{0\sigma}}{n_{0\sigma}} + \frac{\partial_x T_{0\sigma}}{T_{0\sigma}} \left(\frac{m_\sigma v_\parallel^2/2 + \mu B_0}{T_{0\sigma}} - \frac{3}{2} \right) - \frac{\partial_x B_0}{B_0} \frac{\mu B_0}{T_{0\sigma}} \right] F_{0\sigma}, \\ \partial_\nu F_{0\sigma} &= -\frac{\partial_\nu B_0}{B_0} \frac{\mu B_0}{T_{0\sigma}} F_{0\sigma} \end{aligned} \tag{2.49}$$

with the index $\nu = (y, z)$. According to Eqs. (2.31) and (2.47) one is left with two partial derivatives in time, namely in front of $F_{1\sigma}$ and $\bar{A}_{1\parallel}$. For a further treatment of the Vlasov equation, it proves therefore advantageous to combine both in a new variable

$$g_{1\sigma} = F_{1\sigma} - \frac{q_\sigma}{m_\sigma c} \bar{A}_{1\parallel} \frac{\partial F_{0\sigma}}{\partial v_\parallel} = F_{1\sigma} + \frac{q_\sigma}{c} \bar{A}_{1\parallel} \frac{v_\parallel}{T_{0\sigma}} F_{0\sigma}. \tag{2.50}$$

Using furthermore the abbreviation $\Gamma_{\sigma,\nu} = \partial_\nu F_{1\sigma} + \frac{F_{0\sigma}}{T_{0\sigma}} \partial_\nu \left(q_\sigma \bar{\phi}_1 + \mu \bar{B}_{1\parallel} \right)$ where here ν is a placeholder for the spatial coordinates (x, y, z), the full-F gyrokinetic Vlasov equation turns into

$$\begin{aligned} \frac{\partial g_{1\sigma}}{\partial t} =& \frac{c}{\mathcal{C}} \frac{B_0}{B_{0\parallel}^*} \left[\frac{\partial_x n_{0\sigma}}{n_{0\sigma}} + \frac{\partial_x T_{0\sigma}}{T_{0\sigma}} \left(\frac{m_\sigma v_\parallel^2/2 + \mu B_0}{T_{0\sigma}} - \frac{3}{2} \right) \right] F_{0\sigma}\, \partial_y \bar{\xi}_1 \\ &+ \frac{c}{\mathcal{C}} \frac{B_0}{B_{0\parallel}^*} \frac{\mu B_0 + m_\sigma v_\parallel^2}{q_\sigma B_0} \left(\partial_y B_0 + \frac{\gamma_2}{\gamma_1} \partial_z B_0 \right) \Gamma_{\sigma,x} \\ &- \frac{c}{\mathcal{C}} \frac{B_0}{B_{0\parallel}^*} \left[\frac{\mu B_0 + m_\sigma v_\parallel^2}{q_\sigma B_0} \left(\partial_x B_0 - \frac{\gamma_3}{\gamma_1} \partial_z B_0 \right) + \frac{m_\sigma}{q_\sigma} v_\parallel^2 \frac{\beta_p}{2} \frac{\partial_x p_0}{p_0} \right] \Gamma_{\sigma,y} \\ &- \frac{c}{\mathcal{C}} \frac{B_0}{B_{0\parallel}^*} \left(\partial_x \bar{\xi}_1 \Gamma_{\sigma,y} - \partial_y \bar{\xi}_1 \Gamma_{\sigma,x} \right) \\ &- \frac{\mathcal{C}}{J B_0} v_\parallel \Gamma_{\sigma,z} + \frac{\mathcal{C}}{J B_0} \frac{\mu}{m_\sigma} \partial_z B_0 \frac{\partial F_{1\sigma}}{\partial v_\parallel} \\ &+ \frac{c}{\mathcal{C}} \frac{B_0}{B_{0\parallel}^*} \frac{\mu B_0 + m_\sigma v_\parallel^2}{q_\sigma B_0} \left(\partial_y B_0 + \frac{\gamma_2}{\gamma_1} \partial_z B_0 \right) \cdot \\ &\left[\frac{\partial_x n_{0\sigma}}{n_{0\sigma}} + \frac{\partial_x T_{0\sigma}}{T_{0\sigma}} \left(\frac{m_\sigma v_\parallel^2/2 + \mu B_0}{T_{0\sigma}} - \frac{3}{2} \right) \right] F_{0\sigma} \end{aligned} \tag{2.51}$$

Here, all parallel derivatives of perturbed quantities which could directly be compared with perpendicular counterparts are neglected due to the flute like character of plasma

microturbulence, see constraint (ii). For instance, $\partial_x \bar{\xi}_1 - \frac{\gamma_3}{\gamma_1}\partial_z \bar{\xi}_1 \sim \epsilon_\delta(1+\epsilon_\parallel) \approx \partial_x \bar{\xi}_1$ where factors like γ_2/γ_1 or γ_3/γ_1 are considered to be always comparable or smaller than one. Furthermore, the only nonlinearity kept in Eq. (2.51) is stemming from the $\nabla\xi \times \mathbf{B}_0$ term. Another one, the so-called $v_\parallel$ *nonlinearity* or *parallel nonlinearity*, given here to all orders by

$$-\Bigg\{ v_\parallel \hat{\mathbf{b}}_0 \cdot \left(q_\sigma \nabla \bar{\phi}_1 + \frac{q_\sigma}{c} \dot{\bar{A}}_{1\parallel} \hat{\mathbf{b}}_0 + \mu \nabla \bar{B}_{1\parallel} \right) \\ + \frac{B_0}{B_{0\parallel}^*} \left(\mathbf{v}_{\bar{\xi}} + \mathbf{v}_{\nabla B} + \mathbf{v}_c \right) \cdot \left(q_\sigma \nabla \bar{\phi}_1 + \mu \nabla \left(B_0 + \bar{B}_{1\parallel} \right) \right) \Bigg\} \frac{1}{m_\sigma v_\parallel} \frac{\partial F_{1\sigma}}{\partial v_\parallel} \tag{2.52}$$

is neglected throughout this work since it is smaller by one order in the gyrokinetic ordering. Although arguments for keeping this term in order to formally derive and monitor an energy conservation law do exist in literature [28, 29, 30], it has been shown in [31, 32, 33] that no significant contribution is expected if the ion gyroradius to system size ratio (here: the minor tokamak radius) $\rho^* = \rho_s/a < 0.012$. This condition is usually fulfilled in core turbulence investigations in large present-day and future devices as they are considered in this work.

2.2.3 Normalization

Analytical solutions of the full gyrokinetic Vlasov-Maxwell system of equations can only be given for highly idealized cases. Hence, numerical schemes are usually applied instead where the latter naturally work with dimensionless quantities. In the following, an appropriate normalization will therefore be introduced where all physical quantities will be split into a dimensionful reference part usually identifiable by an index 'ref' and the remaining dimensionless value, earmarked with a hat. In contrast to former publications which were restricted to a very narrow radial domain, special attention is paid to include full radial profiles.

The basic reference values are the elementary charge e, a reference mass m_{ref}, a reference temperature T_{ref}, a (macroscopic) reference length L_{ref} and a reference magnetic field B_{ref}, so that e.g. the charge of the σth species can be written as $q_\sigma = e\hat{q}_\sigma$. Moreover, some composed quantities are used, which are the reference velocity $c_{\mathrm{ref}} = \sqrt{T_{\mathrm{ref}}/m_{\mathrm{ref}}}$, the reference gyrofrequency $\Omega_{\mathrm{ref}} = eB_{\mathrm{ref}}/(m_{\mathrm{ref}}c)$, the reference gyroradius $\rho_{\mathrm{ref}} = c_{\mathrm{ref}}/\Omega_{\mathrm{ref}}$ and the reference thermal to magnetic pressure ratio $\beta_{\mathrm{ref}} = 8\pi n_{\mathrm{ref}} T_{\mathrm{ref}}/B_{\mathrm{ref}}^2$.

Based on these definitions, the space and time coordinates can be expressed like

$$x = \rho_{\mathrm{ref}}\hat{x}, \qquad y = \rho_{\mathrm{ref}}\hat{y}, \qquad z = \hat{z}, \qquad t = \frac{L_{\mathrm{ref}}}{c_{\mathrm{ref}}}\hat{t} \tag{2.53}$$

where the parallel coordinate is already dimensionless since it is directly parametrized by means of the poloidal or straight field line angle in the following. This choice affects

geometry related quantities as well, so that

$$\gamma_1 = \hat{\gamma}_1, \qquad \gamma_2 = \frac{1}{L_{\text{ref}}}\hat{\gamma}_2, \qquad \gamma_3 = \frac{1}{L_{\text{ref}}}\hat{\gamma}_3, \tag{2.54}$$

$$J = L_{\text{ref}}\hat{J} \qquad \text{and} \qquad \mathcal{C} = B_{\text{ref}}\hat{\mathcal{C}}\,. \tag{2.55}$$

The velocity space coordinates are normalized as

$$v_\parallel = \hat{v}_{T\sigma}(x_0)\, c_{\text{ref}}\, \hat{v}_\parallel, \qquad \mu = \hat{T}_{0\sigma}(x_0)\, \frac{T_{\text{ref}}}{B_{\text{ref}}}\, \hat{\mu}, \tag{2.56}$$

where $v_{T\sigma}(x) = \sqrt{2T_{0\sigma}(x)/m_\sigma} = c_{\text{ref}}\, \hat{v}_{T\sigma}(x)$ denotes the thermal velocity of the σth species at radial position x. While on the one hand, a separation of scales due to different masses has been taken into account, it is not desirable to normalize the velocity space coordinates to in general radially dependent temperature profiles since such an approach would require additional interpolation schemes in corresponding derivatives or integrations. Thus, temperatures in velocity space normalization factors are just taken at a reference position x_0 which may for instance correspond to the center of the simulation domain or the position at which the profiles reach half of their maximum. However, their species dependence is still taken into account which allows for a velocity space adaption to highly separated temperature profiles which might for instance happen during strong electron heating.

The potentials and fields are chosen to be expressed as

$$\phi_1 = \frac{T_{\text{ref}}}{e}\frac{\rho_{\text{ref}}}{L_{\text{ref}}}\,\hat{\phi}_1, \qquad A_{1\parallel} = \rho_{\text{ref}} B_{\text{ref}} \frac{\rho_{\text{ref}}}{L_{\text{ref}}}\,\hat{A}_{1\parallel}, \qquad B_{1\parallel} = B_{\text{ref}}\frac{\rho_{\text{ref}}}{L_{\text{ref}}}\hat{B}_{1\parallel}, \tag{2.57}$$

and distribution functions are normalized according to

$$F_{0\sigma} = \frac{n_{\text{ref}}}{c_{\text{ref}}^3}\frac{\hat{n}_{0\sigma}(x_0)}{\hat{v}_{T\sigma}^3(x_0)}\hat{F}_{0\sigma} \qquad \text{and} \qquad F_{1\sigma} = \frac{n_{\text{ref}}}{c_{\text{ref}}^3}\frac{\rho_{\text{ref}}}{L_{\text{ref}}}\frac{\hat{n}_{0\sigma}(x_0)}{\hat{v}_{T\sigma}^3(x_0)}\hat{F}_{1\sigma}, \tag{2.58}$$

where again radial dependencies are only present in the normalized distribution functions itself. For further clarification, the normalized equilibrium part shall be given explicitly considering the previously introduced local Maxwellian

$$\hat{F}_{0\sigma}(\mathbf{x}) = \frac{\hat{n}_{p\sigma}(x)}{[\pi\hat{T}_{p\sigma}(x)]^{3/2}}\, \mathrm{e}^{-\frac{\hat{v}_\parallel^2 + \hat{\mu}\hat{B}_0(\mathbf{x})}{\hat{T}_{p\sigma}(x)}}, \tag{2.59}$$

where additional abbreviations have been introduced for density and temperature profiles which are normalized to their value at the reference position x_0, $\hat{n}_{p\sigma} = n_{0\sigma}(x)/n_{0\sigma}(x_0)$ and $\hat{T}_{p\sigma} = T_{0\sigma}(x)/T_{0\sigma}(x_0)$.

With these definitions, a first normalized version of the gyrokinetic Vlasov-equation, Eq. (2.51), can be derived

$$\begin{aligned}
\frac{\partial \hat{g}_{1\sigma}}{\partial \hat{t}} =& -\frac{1}{\hat{\mathcal{C}}}\frac{\hat{B}_0}{\hat{B}^*_{0\parallel}}\left[\hat{\omega}_{n\sigma}+\hat{\omega}_{T\sigma}\left(\frac{\hat{v}_\parallel^2+\hat{\mu}\hat{B}_0}{\hat{T}_{p\sigma}}-\frac{3}{2}\right)\right]\hat{F}_{0\sigma}\,\partial_{\hat{y}}\hat{\bar{\xi}}_1 \\
&-\frac{\hat{B}_0}{\hat{B}^*_{0\parallel}}\frac{\hat{T}_{0\sigma}(x_0)}{\hat{q}_\sigma}\frac{\hat{\mu}\hat{B}_0+2\hat{v}_\parallel^2}{\hat{B}_0}\hat{K}_x\hat{\Gamma}_{\sigma,x} \\
&-\frac{\hat{B}_0}{\hat{B}^*_{0\parallel}}\left[\frac{\hat{T}_{0\sigma}(x_0)}{\hat{q}_\sigma}\frac{\hat{\mu}\hat{B}_0+2\hat{v}_\parallel^2}{\hat{B}_0}\hat{K}_y-\frac{\hat{T}_{0\sigma}(x_0)}{\hat{q}_\sigma\hat{B}_0}\frac{\hat{v}_\parallel^2}{\hat{\mathcal{C}}}\beta_{\mathrm{ref}}\frac{\hat{p}_0}{\hat{B}_0}\hat{\omega}_{p\sigma}\right]\hat{\Gamma}_{\sigma,y} \\
&-\frac{\hat{B}_0}{\hat{B}^*_{0\parallel}}\frac{1}{\hat{\mathcal{C}}}\left(\partial_{\hat{x}}\hat{\bar{\xi}}_1\hat{\Gamma}_{\sigma,y}-\partial_{\hat{y}}\hat{\bar{\xi}}_1\hat{\Gamma}_{\sigma,x}\right) \\
&-\hat{v}_{T\sigma}(x_0)\frac{\hat{\mathcal{C}}}{\hat{J}\hat{B}_0}\hat{v}_\parallel\hat{\Gamma}_{\sigma,z}+\frac{\hat{v}_{T\sigma}(x_0)}{2}\frac{\hat{\mathcal{C}}}{\hat{J}\hat{B}_0}\hat{\mu}\partial_{\hat{z}}\hat{B}_0\frac{\partial\hat{F}_{1\sigma}}{\partial\hat{v}_\parallel} \\
&+\frac{\hat{B}_0}{\hat{B}^*_{0\parallel}}\frac{\hat{T}_{0\sigma}(x_0)}{\hat{q}_\sigma}\frac{\hat{\mu}\hat{B}_0+2\hat{v}_\parallel^2}{\hat{B}_0}\hat{K}_x\left[\hat{\omega}_{n\sigma}+\hat{\omega}_{T\sigma}\left(\frac{\hat{v}_\parallel^2+\hat{\mu}\hat{B}_0}{\hat{T}_{p\sigma}}-\frac{3}{2}\right)\right]\hat{F}_{0\sigma}
\end{aligned} \tag{2.60}$$

where the following abbreviations

$$\hat{\omega}_{n\sigma}=-\frac{L_{\mathrm{ref}}}{n_{0\sigma}(x)}\frac{\partial n_{0\sigma}(x)}{\partial x},\qquad \hat{\omega}_{T\sigma}=-\frac{L_{\mathrm{ref}}}{T_{0\sigma}(x)}\frac{\partial T_{0\sigma}(x)}{\partial x},\qquad \hat{\omega}_{p}=-\frac{L_{\mathrm{ref}}}{p_0(x)}\frac{\partial p_0(x)}{\partial x}, \tag{2.61}$$

have been used for radial density, temperature and pressure background gradients and

$$\hat{K}_x=-\frac{1}{\hat{\mathcal{C}}}\frac{L_{\mathrm{ref}}}{B_{\mathrm{ref}}}\left(\frac{\partial B_0}{\partial y}+\frac{\gamma_2}{\gamma_1}\frac{\partial B_0}{\partial z}\right)\qquad\text{and}\qquad \hat{K}_y=\frac{1}{\hat{\mathcal{C}}}\frac{L_{\mathrm{ref}}}{B_{\mathrm{ref}}}\left(\frac{\partial B_0}{\partial x}-\frac{\gamma_3}{\gamma_1}\frac{\partial B_0}{\partial z}\right)$$

for gradients of the equilibrium magnetic field. Moreover, the dimensionless form of the magnetic field prefactor is

$$\frac{\hat{B}_0}{\hat{B}^*_{0\parallel}}=\left[1+\beta_{\mathrm{ref}}\sqrt{\frac{\hat{m}_\sigma\hat{T}_{0\sigma}(x_0)}{2}}\frac{\hat{j}_{0\parallel}}{\hat{q}_\sigma\hat{B}_0^2}\hat{v}_\parallel\right]^{-1}. \tag{2.62}$$

For a numerical evaluation it is desirable to have as few memory consuming variables as possible. Therefore, the abbreviation Γ_σ is again replaced by the modified distribution function and potential in the present implementation used for this work. Further details can be found in the Appendix A.

2.3 Velocity space moments of the particle distribution function

Maxwell's equations which are later employed to determine the perturbed fields self-consistently and further quantities of interest, e.g. particle and heat fluxes, are usually formulated in particle coordinates and repeatedly involve velocity space moments of different orders. Hence, it proves useful to first investigate these terms. Starting with the definition of the ath scalar moment in $v_\parallel$ and bth in $v_\perp$,

$$M_{ab,\sigma}(\mathbf{x}) = \int f_\sigma(\mathbf{x},\mathbf{v}) v_\parallel^a v_\perp^b \mathrm{d}^3 v, \tag{2.63}$$

one arrives at the guiding-center formulation by applying the previously introduced transformation

$$M_{ab,\sigma}(\mathbf{x}) = \int \delta(\mathbf{X}+\mathbf{r}-\mathbf{x}) F_{\sigma,\mathrm{gc}}(\mathbf{X}, v_\parallel, \mu, \theta) v_\parallel^a v_\perp^b \mathcal{J} \mathrm{d}^3 X \mathrm{d}v_\parallel \mathrm{d}\mu \mathrm{d}\theta. \tag{2.64}$$

The therein used phase space Jacobian can be derived by considering the following transformation from $(\mathbf{x},\mathbf{v})$ to canonical $(\mathbf{x}, \mathbf{p} = m\mathbf{v} + \frac{q}{c}\mathbf{A}_0)$ coordinates

$$\mathrm{d}^3x \mathrm{d}^3v = \frac{1}{m^3} \mathrm{d}^3x \mathrm{d}^3p \tag{2.65}$$

and the square root of the determinant of the Lagrange tensor

$$\omega_{\lambda\nu} = \frac{\partial \bar{\Gamma}_{0,\nu}}{\partial Z^\lambda} - \frac{\partial \bar{\Gamma}_{0,\lambda}}{\partial Z^\nu} \tag{2.66}$$

which gives the Jacobian associated with the canonical to guiding center coordinates $Z = (\mathbf{X}, \mu, v_\parallel, \theta)$ transform, see e.g. Ref. [34]. Here, $\bar{\Gamma}_0$ is already known from Eq. (2.13) and $\nu, \lambda = 1,2,3,4,5,6$. Concatenating Eq. (2.65) and Eq. (2.66) yields the final result

$$\mathrm{d}^3x\, \mathrm{d}^3v = \frac{1}{m^3} \mathrm{d}^3x\, \mathrm{d}^3p = \frac{1}{m^3} \sqrt{|(\omega_{\lambda\nu})|}\, \mathrm{d}^3X \mathrm{d}v_\parallel \mathrm{d}\mu \mathrm{d}\theta = \frac{m^2 B_{0\parallel}^*}{m^3}\, \mathrm{d}^3X \mathrm{d}v_\parallel \mathrm{d}\mu \mathrm{d}\theta. \tag{2.67}$$

By substituting the Jacobian in Eq. (2.64) and employing the pull-back operator in order to use the gyrocenter instead of the guiding-center distribution function $F_{\sigma,\mathrm{gc}}$, the moments become

$$M_{ab,\sigma}(\mathbf{x}) = \int \delta(\mathbf{X}+\mathbf{r}-\mathbf{x}) T^* F_1 \frac{B_{0\parallel}^*(\mathbf{X}, v_\parallel)}{m} v_\parallel^a v_\perp^b \mathrm{d}^3X \mathrm{d}v_\parallel \mathrm{d}\mu \mathrm{d}\theta. \tag{2.68}$$

Here, only the first perturbation order is considered because it is solely required for the gyrokinetic field equations.

The pull-back operator T^* defined in Eq. (2.28) has been presented for the full distribution function so far. Hence, the F splitting has to be performed. Assuming the ordering $F_1/F_0 \sim \epsilon_\delta \ll 1$ and keeping only terms to first order, $T^*F_{1\sigma}$ becomes

$$T^*F_{1\sigma} = F_{1\sigma} + \frac{1}{B_0}\left[\frac{\mathbf{B}_0^*}{B_{0\parallel}^*}\left(\Omega_\sigma \frac{\partial F_{0\sigma}}{\partial v_\parallel} - \frac{q_\sigma}{c} v_\parallel \frac{\partial F_{0\sigma}}{\partial \mu}\right)\cdot \tilde{\mathbf{A}}_1 + \left(q_\sigma \tilde{\phi}_1 - \mu \bar{B}_{1\parallel}\right)\frac{\partial F_{0\sigma}}{\partial \mu}\right] \tag{2.69}$$

By replacing quantities marked by tilde by the gyroaveraged and the full potentials and fields, the moments can then be rewritten as

$$\begin{aligned}
M_{ab,\sigma}(\mathbf{x}) =& \frac{1}{m_\sigma}\int \delta(\mathbf{X}+\mathbf{r}-\mathbf{x}) B_{0\parallel}^*(\mathbf{X}, v_\parallel)\left\{F_{1\sigma}(\mathbf{X}) + \frac{1}{B_0(\mathbf{X})}\right. \\
&\cdot\left[\frac{\mathbf{B}_0^*(\mathbf{X}, v_\parallel)}{B_{0\parallel}^*(\mathbf{X}, v_\parallel)}\left(\Omega_\sigma(\mathbf{X})\frac{\partial F_{0\sigma}(\mathbf{X})}{\partial v_\parallel} - \frac{q_\sigma}{c} v_\parallel \frac{\partial F_{0\sigma}(\mathbf{X})}{\partial \mu}\right)\cdot\left(\mathbf{A}_{1\parallel}(\mathbf{X}+\mathbf{r}) - \bar{\mathbf{A}}_{1\parallel}(\mathbf{X})\right)\right. \\
&\left.\left. + \left(q_\sigma(\phi_1(\mathbf{X}+\mathbf{r}) - \bar{\phi}_1(\mathbf{X})) - \mu \bar{B}_{1\parallel}(\mathbf{X})\right)\frac{\partial F_{0\sigma}(\mathbf{X})}{\partial \mu}\right]\right\} v_\parallel^a v_\perp^b \mathrm{d}^3X \mathrm{d}v_\parallel \mathrm{d}\mu \mathrm{d}\theta \\
=& \frac{2\pi}{m_\sigma}\int B_{0\parallel}^*(\mathbf{x}, v_\parallel)\left\{\langle F_{1\sigma}(\mathbf{x}-\mathbf{r})\rangle + \frac{1}{B_0(\mathbf{x})}\right. \\
&\cdot\left[\frac{\mathbf{B}_0^*(\mathbf{x}, v_\parallel)}{B_{0\parallel}^*(\mathbf{x}, v_\parallel)}\left(\Omega_\sigma(\mathbf{x})\frac{\partial F_{0\sigma}(\mathbf{x})}{\partial v_\parallel} - \frac{q_\sigma}{c} v_\parallel \frac{\partial F_{0\sigma}(\mathbf{x})}{\partial \mu}\right)\cdot\left(\mathbf{A}_{1\parallel}(\mathbf{x}) - \langle \bar{\mathbf{A}}_{1\parallel}(\mathbf{x}-\mathbf{r})\rangle\right)\right. \\
&\left.\left. + \left(q_\sigma(\phi_1(\mathbf{x}) - \langle\bar{\phi}_1(\mathbf{x}-\mathbf{r})\rangle) - \mu\langle \bar{B}_{1\parallel}(\mathbf{x}-\mathbf{r})\rangle\right)\frac{\partial F_{0\sigma}(\mathbf{x})}{\partial \mu}\right]\right\} v_\parallel^a v_\perp^b \mathrm{d}v_\parallel \mathrm{d}\mu
\end{aligned} \tag{2.70}$$

where again the freedom of evaluating equilibrium quantities either at particle or gyrocenter position has been utilized and the θ integration has been performed. In the following, the particle position ($\mathbf{x}$) dependence of fields, distribution functions, gyrofrequencies and temperatures will be skipped for reasons of readability.

If F_0 is consistently chosen to be a local Maxwellian as before, the integral containing $A_{1\parallel}$ vanishes. Furthermore, the $v_\parallel$-integration can be performed analytically because the fields do not depend on that coordinate. In summary, Eq. (2.70) becomes

$$\begin{aligned}
M_{ab,\sigma}(\mathbf{x}) =& \pi\left(\frac{2B_0}{m_\sigma}\right)^{b/2+1}\iint \frac{B_{0\parallel}^*}{B_0}\langle F_{1\sigma}(\mathbf{x}-\mathbf{r})\rangle v_\parallel^a \mu^{b/2}\mathrm{d}v_\parallel \mathrm{d}\mu - \frac{n_{0\sigma}B_0}{T_{0\sigma}^2} v_{T_\sigma}^a \left(\frac{2B_0}{m_\sigma}\right)^{b/2} \\
&\cdot\left[\Upsilon(a) + \frac{8\pi T_{0\sigma}}{B_0^2}\frac{j_{0\parallel}}{q_\sigma v_{T\sigma}}\Upsilon(a+1)\right]\left\{\left(\frac{T_{0\sigma}}{B_0}\right)^{b/2+1}(b/2)!\, q_\sigma\phi_1(\mathbf{x})\right. \\
&\left. - \int\left(q_\sigma\langle\bar{\phi}_1(\mathbf{x}-\mathbf{r})\rangle + \mu\langle\bar{B}_{1\parallel}(\mathbf{x}-\mathbf{r})\rangle\right)\mathrm{e}^{-\frac{\mu B_0}{T_{0\sigma}}}\mu^{b/2}\mathrm{d}\mu\right\}
\end{aligned} \tag{2.71}$$

with the abbreviation

$$\Upsilon(a) = \frac{1}{\sqrt{\pi}} \int_{-\infty}^{\infty} x^a \mathrm{e}^{-x^2} dx = \begin{cases} 0, & a \text{ odd} \\ 1, & a = 0 \\ \frac{1 \cdot 3 \cdots (a-1)}{\sqrt{2}^a} & a \text{ even} \end{cases} \tag{2.72}$$

for the $v_\parallel$ integral. The normalized version is

$$\begin{aligned} M_{ab,\sigma}(\mathbf{x}) =& n_{\mathrm{ref}} \hat{n}_{0\sigma}(x_0) c_{\mathrm{ref}}^{a+b} \hat{v}_{T\sigma}^{a+b}(x_0) \frac{\rho_{\mathrm{ref}}}{L_{\mathrm{ref}}} \Bigg\{ \pi \hat{B}_0^{b/2} \iint \hat{B}_{0\parallel}^* \langle \hat{F}_{1\sigma}(\mathbf{x} - \mathbf{r}) \rangle \hat{v}_\parallel^a \hat{\mu}^{b/2} \mathrm{d}\hat{v}_\parallel \mathrm{d}\hat{\mu} \\ & - \frac{\hat{n}_{p\sigma}}{\hat{T}_{0\sigma}} \hat{T}_{p\sigma}^{(a+b)/2} \left[\Upsilon(a) + \beta_{\mathrm{ref}} \frac{\hat{T}_{0\sigma}}{\hat{B}_0^2} \frac{\hat{j}_{0\parallel}}{\hat{q}_\sigma \hat{v}_{T\sigma}} \Upsilon(a+1) \right] \Bigg((b/2)! \, \hat{q}_\sigma \hat{\phi}_1(\mathbf{x}) \\ & - \left(\frac{\hat{B}_0}{\hat{T}_{p\sigma}} \right)^{\frac{b}{2}+1} \int \left(\hat{q}_\sigma \langle \hat{\tilde{\phi}}_1(\mathbf{x} - \mathbf{r}) \rangle + \hat{T}_{0\sigma}(x_0) \hat{\mu} \langle \hat{\tilde{B}}_{1\parallel}(\mathbf{x} - \mathbf{r}) \rangle \right) \mathrm{e}^{-\frac{\hat{\mu}\hat{B}_0}{\hat{T}_{p\sigma}}} \hat{\mu}^{b/2} \mathrm{d}\hat{\mu} \Bigg) \Bigg\}. \end{aligned} \tag{2.73}$$

2.4 The gyrokinetic field equations

As pointed out earlier, the fluctuating fractions of the potentials and fields ϕ_1, $A_{1\parallel}$, and $B_{\parallel 1}$ appearing in the Vlasov equation are calculated self-consistently using the corresponding Maxwell equations.

2.4.1 The Poisson equation

The perturbed electrostatic potential is linked to the perturbed charge density by means of the Poisson equation

$$-\nabla^2 \phi_1(\mathbf{x}) = 4\pi \sum_\sigma n_{1\sigma}(\mathbf{x}) q_\sigma \tag{2.74}$$

where σ is running over all species and $n_{1\sigma}$ denotes the density perturbation of the σth species which is the $(0,0)$-velocity space moment of the distribution function $f_{1\sigma}(\mathbf{x}, \mathbf{v})$ in particle coordinates

$$n_{1\sigma}(\mathbf{x}) = \int f_{1\sigma}(\mathbf{x}, \mathbf{v}) \mathrm{d}^3 v \tag{2.75}$$

$$= M_{00,\sigma}(\mathbf{x}). \tag{2.76}$$

Using the expression for $M_{00}(\mathbf{x})$ which has been derived in Eq. (2.71) and neglecting parallel derivatives of the potential $\nabla^2 \approx \nabla_\perp^2 = g^{xx} \frac{\partial^2}{\partial x^2} + 2g^{xy} \frac{\partial}{\partial x} \frac{\partial}{\partial y} + g^{yy} \frac{\partial^2}{\partial y^2}$ as given by

the gyrokinetic ordering yields

$$-\nabla_\perp^2\phi_1(\mathbf{x}) = 4\pi\sum_\sigma\left(q_\sigma\bar{n}_{1\sigma} + n_{0\sigma}\frac{q_\sigma^2}{T_{0\sigma}}\left[\frac{B_0}{T_{0\sigma}}\int\langle\bar{\phi}_1(\mathbf{x}-\mathbf{r})\rangle\,\mathrm{e}^{-\frac{\mu B_0}{T_{0\sigma}}}\,\mathrm{d}\mu - \phi_1(\mathbf{x})\right]\right.$$
$$\left. + \frac{n_{0\sigma}q_\sigma B_0}{T_{0\sigma}^2}\int\mu\langle\bar{B}_{1\parallel}(\mathbf{x}-\mathbf{r})\rangle\,\mathrm{e}^{-\frac{\mu B_0}{T_{0\sigma}}}\,\mathrm{d}\mu\right) \tag{2.77}$$

where the gyrocenter density,

$$\bar{n}_{1\sigma} = \frac{2\pi}{m}\iint B_{0\parallel}^*\langle F_{1\sigma}(\mathbf{x}-\mathbf{r})\rangle\mathrm{d}v_\parallel\mathrm{d}\mu, \tag{2.78}$$

has been introduced. Moving furthermore all ϕ_1 dependent terms to the left side results in

$$-\frac{1}{4\pi}\nabla_\perp^2\phi_1(\mathbf{x}) - \sum_\sigma n_{0\sigma}\frac{q_\sigma^2}{T_{0\sigma}}\left[\frac{B_0}{T_{0\sigma}}\int\langle\bar{\phi}_1(\mathbf{x}-\mathbf{r})\rangle\,\mathrm{e}^{-\frac{\mu B_0}{T_{0\sigma}}}\,\mathrm{d}\mu - \phi_1(\mathbf{x})\right] =$$
$$\sum_\sigma\left(q_\sigma\bar{n}_{1\sigma} + \frac{n_{0\sigma}q_\sigma B_0}{T_{0\sigma}^2}\int\mu\langle\bar{B}_{1\parallel}(\mathbf{x}-\mathbf{r})\rangle\,\mathrm{e}^{-\frac{\mu B_0}{T_{0\sigma}}}\,\mathrm{d}\mu\right). \tag{2.79}$$

Now, based on the left hand side of Eq. (2.79), a Poisson-Operator can be defined

$$\mathcal{P}[\phi_1] = \left\{-\frac{1}{4\pi}\nabla_\perp^2\phi_1 + \sum_\sigma n_{0\sigma}\frac{q_\sigma^2}{T_{0\sigma}}\left[\phi_1(\mathbf{x}) - \frac{B_0}{T_{0\sigma}}\int\mathcal{G}\left[\mathcal{G}\left[\phi_1(\mathbf{x}-\mathbf{r})\right]\right]\mathrm{e}^{-\frac{\mu B_0}{T_{0\sigma}}}\,\mathrm{d}\mu\right]\right\} \tag{2.80}$$

which has to be formally inverted in order to solve Poisson's equation for the electrostatic potential. Here, $\mathcal{G}$ denotes the previously introduced gyroaveraging operator.

Normalized Poisson equation

As for the gyrokinetic Vlasov equation, a dimensionless form can be derived for Poisson's equation using the normalization introduced in Sec. 2.2.3

$$\left\{-\hat{\nabla}_\perp^2\hat{\lambda}_D^2\hat{\phi}_1(\mathbf{x}) + \sum_\sigma\hat{n}_{0\sigma}\frac{\hat{q}_\sigma^2}{\hat{T}_{0\sigma}}\left[\hat{\phi}_1(\mathbf{x}) - \frac{\hat{B}_0}{\hat{T}_{p\sigma}}\int\mathcal{G}\left[\mathcal{G}\left[\hat{\phi}_1(\mathbf{x}-\mathbf{r})\right]\right]\mathrm{e}^{-\frac{\hat{\mu}\hat{B}_0}{\hat{T}_{p\sigma}}}\,\mathrm{d}\hat{\mu}\right]\right\}$$
$$= \sum_\sigma\hat{n}_{0\sigma}(x_0)\hat{B}_0\hat{q}_\sigma\left(\pi\iint\frac{\hat{B}_{0\parallel}^*}{\hat{B}_0}\langle\hat{F}_{1\sigma}(\mathbf{x}-\mathbf{r})\rangle\mathrm{d}\hat{v}_\parallel\mathrm{d}\hat{\mu} + \frac{\hat{n}_{p\sigma}}{\hat{T}_{p\sigma}^2}\int\hat{\mu}\langle\hat{\bar{B}}_{1\parallel}(\mathbf{x}-\mathbf{r})\rangle\,\mathrm{e}^{-\frac{\hat{\mu}\hat{B}_0}{\hat{T}_{p\sigma}}}\,\mathrm{d}\hat{\mu}\right) \tag{2.81}$$

where remaining reference quantities in the $\hat{\nabla}_\perp^2$ prefactor have been combined to

$$\hat{\lambda}_D = \lambda_D/\rho_{\mathrm{ref}} = \sqrt{\frac{T_{\mathrm{ref}}}{4\pi\rho_{\mathrm{ref}}^2 n_{\mathrm{ref}}e^2}} = \sqrt{\frac{B_{\mathrm{ref}}^2}{4\pi n_{\mathrm{ref}}m_{\mathrm{ref}}c^2}} \tag{2.82}$$

which can be identified as the normalized Debye length.

Adiabatic electrons

In the limit of weightless electrons, $m_e/m_i \to 0$, the thermal velocity of the electrons is much larger than the ion counterpart, $v_{Te}/v_{Ti} \propto \sqrt{m_i/m_e} \to \infty$, so that fluctuations of the electrostatic potential along the magnetic field lines are almost instantaneously balanced by the electrons. This implies the short-circuiting of a whole flux surface if the latter can be spanned by a single field line. Thus, a modified adiabaticity relation

$$\frac{n_{1e}}{n_{0e}} = \frac{e}{T_{0e}}(\phi_1 - \langle\phi_1\rangle_{\mathrm{FS}}) \tag{2.83}$$

is established to link the perturbed electron density and the electrostatic potential. Here, $\langle\cdots\rangle_{\mathrm{FS}}$ denotes flux surface averaging [35] which must not be confused with a simple surface average but is defined for an arbitrary function $f(\mathbf{x})$ as

$$\begin{aligned}\langle f\rangle_{\mathrm{FS}}(x) =& \frac{\partial}{\partial V}\int_V f(\mathbf{x})\mathrm{d}V' \\ =& \iint f(\mathbf{x})J(\mathbf{x})\mathrm{d}y\mathrm{d}z \Big/ \iint J(\mathbf{x})\mathrm{d}y\mathrm{d}z.\end{aligned} \tag{2.84}$$

Furthermore, advantage is taken of the approximately vanishing electron gyroradius, $\rho_e/\rho_i \propto \sqrt{m_e/m_i} \to 0$ to replace corresponding gyroaverages by the gyrocenter values and therefore identifying the perturbed electron density with the $(0,0)$ velocity space moment of F_{1e}

$$n_{1e} = \bar{n}_{1e} = \frac{2\pi}{m_e}\iint B^*_{0\parallel}F_{1e}(\mathbf{x})\mathrm{d}v_\parallel\mathrm{d}\mu = \frac{n_{0e}e}{T_{0e}}(\phi_1 - \langle\phi_1\rangle_{\mathrm{FS}}). \tag{2.85}$$

This relation motivates to not explicitly advance the electron distribution function thus saving a significant amount of computational effort and is moreover used to simplify the Poisson equation, Eq. (2.77), to

$$\begin{aligned}0 =& \sum_{\sigma\neq e}\left(q_\sigma\bar{n}_{1\sigma} + n_{0\sigma}\frac{q_\sigma^2}{T_{0\sigma}}\left[\frac{B_0}{T_{0\sigma}}\int\langle\bar{\phi}_1(\mathbf{x}-\mathbf{r})\rangle\,\mathrm{e}^{-\frac{\mu B_0}{T_{0\sigma}}}\,\mathrm{d}\mu - \phi_1(\mathbf{x})\right]\right) \\ &+ \frac{n_{0e}e^2}{T_{0e}}\left(\langle\phi_1\rangle_{\mathrm{FS}} - \phi_1(\mathbf{x})\right).\end{aligned} \tag{2.86}$$

Here, the left hand side has been neglected in agreement with the long wavelength approximation which has been introduced by assuming a negligible electron gyroradius. In addition, magnetic fields have not been considered. Switching to an operator notation, the Poisson equation in case of adiabatic electrons becomes

$$\hat{\mathcal{P}}_{ae}[\hat{\phi}_1] = \pi\sum_{\sigma\neq e}\hat{n}_{0\sigma}(x_0)\hat{q}_\sigma\iint\hat{B}^*_{0\parallel}\langle\hat{F}_{1\sigma}(\mathbf{x}-\mathbf{r})\rangle\mathrm{d}\hat{v}_\parallel\mathrm{d}\hat{\mu} + \frac{\hat{n}_{0e}}{\hat{T}_{0e}}\langle\hat{\phi}_1\rangle_{\mathrm{FS}}$$

with the normalized Poisson-operator for adiabatic electrons

$$\hat{\mathcal{P}}_{ae}[\hat{\phi}_1] \equiv \left\{ \frac{\hat{n}_{0e}}{\hat{T}_{0e}} \hat{\phi}_1(\mathbf{x}) + \sum_{\sigma \neq e} \hat{n}_{0\sigma} \frac{\hat{q}_\sigma^2}{\hat{T}_{0\sigma}} \left[\hat{\phi}_1(\mathbf{x}) - \frac{\hat{B}_0}{\hat{T}_{p\sigma}} \int \mathcal{G} \left[\mathcal{G} \left[\hat{\phi}_1(\mathbf{x}-\mathbf{r}) \right] \right] \mathrm{e}^{-\frac{\hat{\mu}\hat{B}_0}{\hat{T}_{p\sigma}}} \, \mathrm{d}\hat{\mu} \right] \right\} \tag{2.87}$$

The flux surface averaged potential is obtained by flux surface averaging the whole quasi-neutrality equation, Eq. (2.86), thus erasing the electron contribution. In addition, a separate and independent treatment of operators and potentials is assumed. The final result is

$$\langle \hat{\phi}_1 \rangle_{\mathrm{FS}} = \pi \sum_{\sigma \neq e} \hat{n}_{0\sigma} \hat{q}_\sigma \langle \hat{\mathcal{P}}_{ae} \rangle_{\mathrm{FS}}^{-1} \left\langle \iint \hat{B}_{0\parallel}^* \langle \hat{F}_{1\sigma}(\mathbf{x}-\mathbf{r}) \rangle \mathrm{d}\hat{v}_\parallel \mathrm{d}\hat{\mu} \right\rangle_{\mathrm{FS}} \tag{2.88}$$

with

$$\langle \hat{\mathcal{P}}_{ae} \rangle_{\mathrm{FS}} = \sum_{\sigma \neq e} \hat{n}_{0\sigma} \frac{\hat{q}_\sigma^2}{\hat{T}_{0\sigma}} \left[\mathbb{1} - \frac{\hat{B}_0}{\hat{T}_{p\sigma}} \left\langle \int \mathcal{G}\mathcal{G} \, \mathrm{e}^{-\frac{\hat{\mu}\hat{B}_0}{\hat{T}_{p\sigma}}} \, \mathrm{d}\hat{\mu} \right\rangle_{\mathrm{FS}} \right] \tag{2.89}$$

Adiabatic ions

If on the other hand a short-wavelength approximation is applied, all terms containing averages over the ion gyromotion vanish so that Eq. (2.76) becomes

$$\frac{n_{1i}}{n_{0i}} = -\frac{q_i}{T_{0i}} \phi_1 \tag{2.90}$$

for ions and consequently the following normalized Poisson equation

$$\begin{aligned} \left\{ -\hat{\nabla}_\perp^2 \hat{\lambda}_D^2 \hat{\phi}_1(\mathbf{x}) + \hat{n}_{0i} \frac{\hat{q}_\sigma^2}{\hat{T}_{0i}} \hat{\phi}_1(\mathbf{x}) + \frac{\hat{n}_{0e}}{\hat{T}_{0e}} \left[\hat{\phi}_1(\mathbf{x}) - \frac{\hat{B}_0}{\hat{T}_{pe}} \int \mathcal{G} \left[\mathcal{G} \left[\hat{\phi}_1(\mathbf{x}-\mathbf{r}) \right] \right] \mathrm{e}^{-\frac{\hat{\mu}\hat{B}_0}{\hat{T}_{pe}}} \, \mathrm{d}\hat{\mu} \right] \right\} \\ = -\pi \hat{n}_{0e}(x_0) e \iint \hat{B}_{0\parallel}^* \langle \hat{F}_{1e}(\mathbf{x}-\mathbf{r}) \rangle \mathrm{d}\hat{v}_\parallel \mathrm{d}\hat{\mu} \end{aligned} \tag{2.91}$$

can be set up for the present limiting case.

2.4.2 Ampère's law

Using the Coulomb gauge $\nabla \cdot \mathbf{A} = 0$, Ampère's law can be expressed by terms of the magnetic potential as

$$\nabla \times \mathbf{B} = \nabla \times (\nabla \times \mathbf{A}) = -\nabla^2 \mathbf{A} = \frac{4\pi}{c} \mathbf{j} + \frac{1}{c} \frac{\partial \mathbf{E}}{\partial t}. \tag{2.92}$$

In the absence of equilibrium electric fields it turns into

$$-\nabla_\perp^2 A_{1\parallel} = \frac{4\pi}{c} j_{1\parallel}. \tag{2.93}$$

for the perturbed parallel component using the same approximations provided by the gyrokinetic ordering as, for instance, in the derivation of Poisson's equation. The emerging perturbed parallel current density can be expressed by the $(1,0)$ velocity space moment of the distribution function. With the help of Eq. (2.73) one arrives at

$$\begin{aligned}
-\nabla_\perp^2 A_{1\parallel} =& \frac{4\pi}{c} \sum_\sigma q_\sigma M_{10,\sigma}(\mathbf{x}) \\
=& \frac{4\pi}{c} \sum_\sigma q_\sigma n_{\mathrm{ref}} \hat{n}_{0\sigma}(x_0) c_{\mathrm{ref}} \hat{v}_{T\sigma}(x_0) \frac{\rho_{\mathrm{ref}}}{L_{\mathrm{ref}}} \left\{ \pi \iint \hat{B}_{0\parallel}^* \langle \hat{F}_{1\sigma}(\mathbf{x}-\mathbf{r}) \rangle \hat{v}_\parallel \mathrm{d}\hat{v}_\parallel \mathrm{d}\hat{\mu} \right. \\
& - \frac{\beta_{\mathrm{ref}}}{2} \frac{\hat{n}_{p\sigma} \hat{j}_{0\parallel}}{\hat{q}_\sigma \hat{B}_0^2 \hat{v}_{T\sigma}(x_0)} \left[\hat{q}_\sigma \hat{\phi}_1(\mathbf{x}) - \frac{\hat{B}_0}{\hat{T}_{p\sigma}} \int \left(\hat{q}_\sigma \langle \hat{\bar{\phi}}_1(\mathbf{x}-\mathbf{r}) \rangle \right. \right. \\
& \left. \left. \left. + \hat{T}_{0\sigma}(x_0) \hat{\mu} \langle \hat{\bar{B}}_{1\parallel}(\mathbf{x}-\mathbf{r}) \rangle \right) \mathrm{e}^{-\frac{\hat{\mu}\hat{B}_0}{\hat{T}_{p\sigma}}} \mathrm{d}\hat{\mu} \right] \right\}
\end{aligned} \tag{2.94}$$

which turns into

$$\begin{aligned}
-\hat{\nabla}_\perp^2 \hat{A}_{1\parallel} =& \sum_\sigma \left\{ \frac{\beta_{\mathrm{ref}}}{2} \hat{q}_\sigma \hat{n}_{0\sigma}(x_0) \hat{v}_{T\sigma}(x_0) \pi \iint \hat{B}_{0\parallel}^* \langle \hat{F}_{1\sigma}(\mathbf{x}-\mathbf{r}) \rangle \hat{v}_\parallel \mathrm{d}\hat{v}_\parallel \mathrm{d}\hat{\mu} \right. \\
& - \frac{\beta_{\mathrm{ref}}^2}{4} \frac{\hat{n}_{0\sigma} \hat{j}_{0\parallel}}{\hat{B}_0^2} \left[\hat{q}_\sigma \hat{\phi}_1(\mathbf{x}) - \frac{\hat{B}_0}{\hat{T}_{p\sigma}} \int \left(\hat{q}_\sigma \langle \hat{\bar{\phi}}_1(\mathbf{x}-\mathbf{r}) \rangle \right. \right. \\
& \left. \left. \left. + \hat{T}_{0\sigma}(x_0) \hat{\mu} \langle \hat{\bar{B}}_{1\parallel}(\mathbf{x}-\mathbf{r}) \rangle \right) \mathrm{e}^{-\frac{\hat{\mu}\hat{B}_0}{\hat{T}_{p\sigma}}} \mathrm{d}\hat{\mu} \right] \right\}
\end{aligned} \tag{2.95}$$

when normalizing the remaining terms.

If $F_{1\sigma}$ is furthermore replaced by the dimensionless version of Eq. (2.50)

$$\hat{F}_{1\sigma} = \hat{g}_{1\sigma} + \frac{\hat{q}_\sigma}{\sqrt{2\hat{m}_\sigma \hat{T}_{0\sigma}(x_0)}} \frac{\partial \hat{F}_{0\sigma}}{\partial \hat{v}_\parallel} \hat{\bar{A}}_{1\parallel} \tag{2.96}$$

one arrives at the following normalized equation

$$\begin{aligned}
& \left\{ -\hat{\nabla}_\perp^2 \hat{A}_{1\parallel} + \frac{\beta_{\mathrm{ref}}}{2} \sum_\sigma \frac{\hat{n}_{0\sigma} \hat{q}_\sigma^2}{\hat{m}_\sigma \hat{T}_{p\sigma}} \hat{B}_0 \int \langle \hat{\bar{A}}_{1\parallel}(\mathbf{x}-\mathbf{r}) \rangle \, \mathrm{e}^{-\frac{\hat{\mu}\hat{B}_0}{\hat{T}_{p\sigma}}} \mathrm{d}\hat{\mu} \right\} \\
& = \sum_\sigma \left\{ \frac{\beta_{\mathrm{ref}}}{2} \hat{q}_\sigma \hat{n}_{0\sigma}(x_0) \hat{v}_{T\sigma}(x_0) \pi \iint \hat{B}_{0\parallel}^* \langle \hat{g}_{1\sigma}(\mathbf{x}-\mathbf{r}) \rangle \hat{v}_\parallel \mathrm{d}\hat{v}_\parallel \mathrm{d}\hat{\mu} \right. \\
& \quad - \frac{\beta_{\mathrm{ref}}^2}{4} \frac{\hat{n}_{0\sigma} \hat{j}_{0\parallel}}{\hat{B}_0^2} \left[\hat{q}_\sigma \hat{\phi}_1(\mathbf{x}) - \frac{\hat{B}_0}{\hat{T}_{p\sigma}} \int \left(\hat{q}_\sigma \langle \hat{\bar{\phi}}_1(\mathbf{x}-\mathbf{r}) \rangle \right. \right. \\
& \quad \left. \left. \left. + \hat{T}_{0\sigma}(x_0) \hat{\mu} \langle \hat{\bar{B}}_{1\parallel}(\mathbf{x}-\mathbf{r}) \rangle \right) \mathrm{e}^{-\frac{\hat{\mu}\hat{B}_0}{\hat{T}_{p\sigma}}} \mathrm{d}\hat{\mu} \right] \right\}.
\end{aligned} \tag{2.97}$$

However, depending on the chosen numerical scheme, solving Eq. (2.97) for $\hat{A}_{1\parallel}$ in the presented form might be affected by the so-called *Ampère cancellation problem* which stems from different treatments of the $v_\parallel$ integration. While an analytical integration in this direction can and has been performed on the left hand side, one is forced to evaluate the right hand side numerically. Therefore, it has been proven advantageous to even use a numerical $v_\parallel$ integration in the computation of $\hat{M}_{10}$ in order to avoid numerical inconsistencies.

Finally, the gyrokinetic field equations shall now be completed by considering the perpendicular component of Ampère's law,

$$(\nabla \times \mathbf{B}_1)_\perp = \frac{4\pi}{c}\mathbf{j}_{1\perp}, \tag{2.98}$$

in order to obtain an equation for the parallel magnetic field $B_{1\parallel}$. Neglecting once again the parallel derivatives and replacing $\mathbf{j}_{1\perp}$ by the corresponding vector moment yields

$$\partial_{\bar{y}} B_{1\parallel}\hat{\mathbf{e}}_1 - \partial_{\bar{x}} B_{1\parallel}\hat{\mathbf{e}}_2 = \frac{4\pi}{c}\sum_\sigma q_\sigma \int \delta(\mathbf{X}+\mathbf{r}-\mathbf{x}) v_\perp \mathbf{c}(\theta) T^* F_{1\sigma} \mathrm{d}^3X \mathrm{d}^3v \tag{2.99}$$

in the local Cartesian coordinate system $(\hat{\mathbf{e}}_1, \hat{\mathbf{e}}_2, \hat{\mathbf{b}}_0)$ with the coordinates $(\bar{x}, \bar{y}, \bar{z})$. By considering $\mathbf{c}(\theta) = (-\sin\theta\hat{\mathbf{e}}_1 + \cos\theta\hat{\mathbf{e}}_2)$, one obtains

$$\begin{aligned}\begin{pmatrix} \partial_{\bar{y}} B_{1\parallel} \\ -\partial_{\bar{x}} B_{1\parallel} \end{pmatrix} =& \frac{4\pi^2}{c}\sum_\sigma q_\sigma \left(\frac{2B_0}{m_\sigma}\right)^{\frac{3}{2}} \Bigg\{ \int \frac{B^*_{0\parallel}}{B_0} \langle (-\sin\theta\hat{\mathbf{e}}_1 + \cos\theta\hat{\mathbf{e}}_2) F_{1\sigma}(\mathbf{x}-\mathbf{r})\rangle \sqrt{\mu}\mathrm{d}v_\parallel \mathrm{d}\mu \\ &+ \frac{q_\sigma}{T_{0\sigma}} \int \langle (-\sin\theta\hat{\mathbf{e}}_1 + \cos\theta\hat{\mathbf{e}}_2)\, \bar{\phi}_1(\mathbf{x}-\mathbf{r})\rangle F_{0\sigma}\sqrt{\mu}\mathrm{d}v_\parallel \mathrm{d}\mu \\ &+ \frac{1}{T_{0\sigma}} \int \langle (-\sin\theta\hat{\mathbf{e}}_1 + \cos\theta\hat{\mathbf{e}}_2)\, \bar{B}_{1\parallel}(\mathbf{x}-\mathbf{r})\rangle F_{0\sigma}\mu^{3/2}\mathrm{d}v_\parallel \mathrm{d}\mu \Bigg\}. \end{aligned} \tag{2.100}$$

Obviously, the field equation for $B_{1\parallel}$ involves some more complicated operations compared to the Poisson equation and the parallel component of Ampère's law. Two vector components appear in Eq. (2.100), and all θ integrations include additional $\sin\theta$ or $\cos\theta$ terms so that they cannot be expressed by $\mathcal{G}$. In order to avoid the corresponding definition of several new operators at this point, a further discussion is postponed to the next chapter.

2.5 Collisions

Up to now, the basic features of fusion plasmas, in particular their high temperatures but low densities, have been used to establish a kinetic description by means of the Vlasov equation which evolves a distribution function considering just indirect particle

interactions through collectively generated fields. For the application to some plasma discharges, however, direct particle interactions, to lowest order binary collisions, may constitute a weak but still important ingredient. In these cases, an additional collision operator, here $C(F_\sigma, F_{\sigma'})$, is constructed and attached to the right hand side of the Vlasov equation,

$$\frac{\partial F_\sigma}{\partial t} + \dot{\mathbf{X}} \cdot \nabla F_\sigma + \dot{\mu} \frac{\partial F_\sigma}{\partial \mu} + \dot{v}_\parallel \frac{\partial F_\sigma}{\partial v_\parallel} = \sum_{\sigma'} C(F_\sigma, F_{\sigma'}). \tag{2.101}$$

However, in this work, collisions are rarely addressed and are not yet considered in the extensive code modification which will be discussed in the next chapter. Hence, the reader is invited to consult a recent publication [36] where one possible model, namely a Landau-Boltzmann collision operator,

$$C(F_\sigma, F_{\sigma'}) = \frac{\partial}{\partial \mathbf{v}} \cdot \left(\overleftrightarrow{D} \cdot \frac{\partial}{\partial \mathbf{v}} - \mathbf{R} \right) F_\sigma \tag{2.102}$$

is linearized and treated in a consistent way with the approximations used above. Here, $\overleftrightarrow{D}$ denotes a diffusion tensor

$$\overleftrightarrow{D} = \frac{2\pi q_\sigma^2 \, q_{\sigma'}^2}{m_\sigma^2} \ln \Lambda_c \frac{\partial^2}{\partial \mathbf{v} \partial \mathbf{v}} \int F_{\sigma'} \left| \mathbf{v} - \mathbf{v}' \right| \mathrm{d}^3 v' \tag{2.103}$$

with the Coulomb logarithm $\ln \Lambda_c$, see e.g. Ref. [21], and

$$\mathbf{R} = \frac{4\pi q_\sigma^2 \, q_{\sigma'}^2}{m_\sigma \, m_{\sigma'}} \ln \Lambda_c \frac{\partial}{\partial \mathbf{v}} \int \frac{F_{\sigma'}}{|\mathbf{v} - \mathbf{v}'|} \mathrm{d}^3 v' \tag{2.104}$$

is the dynamical friction.

2.6 Chapter summary

In this chapter, the reader has been introduced to the gyrokinetic theory which forms the underlying theoretical framework for the remainder of this thesis. While the first part has been a review of the general derivation, specific assumptions which are employed for the implementation of the plasma microturbulence code GENE have been presented in the second. In contrast to previous works describing earlier versions of this code, special attention has been paid on keeping the possibility of radially varying temperature and density profiles. Furthermore, a slightly enhanced phase space Jacobian has been considered. In the next chapter, a detailed description of the implementation of these equations into the GENE code will be given.

Chapter 3

Upgrading GENE to a nonlocal code

On the basis of the gyrokinetic equations derived in the previous chapter, the reader will now be introduced to the main tool used in this work - the GENE (*Gyrokinetic Electromagnetic Numerical Experiment*) code. Initially developed by F. Jenko [37], the program has been maintained and extended at the Max-Planck-Institut für Plasmaphysik and the Garching Computing Centre for about a decade. Some of the most important mile stones along this way are reported in [38, 14, 39, 40, 36, 41]. Since 2007, regular public releases have been distributed [42], and since 2008, several cooperations with other institutes have been launched for future software development and application. The full software suite comes along with a powerful post-processing tool which has been substantially extended in the course of this work.

This chapter is organized as follows. First, two different concepts, i.e. the *local* and *global* approaches, are discussed. While the former has been employed within GENE from the very beginning, the implementation of the latter constitutes an essential part of this thesis. Due to its profound and complex nature, this task been performed in a joint effort with collaborators from CRPP, Lausanne. Contributions being implemented without any involvement of the author of this thesis will be indicated.

The second section details the employed geometries. On the basis of the thereby defined transformation to curvilinear coordinates, an introduction to the basic concept of a flux tube and the associated boundary conditions can be given in local and global fashion. In a next step, a discussion of the implementation of operators mentioned in the previous chapter, e.g. the gyroaverage operator, follows. Before concluding with the definitions of observables and sources and sinks terms employed in subsequent chapters, further numerical schemes relevant for GENE are presented.

Naturally, the sections of this chapter dealing with the local code version are partially based on previous publications, e.g. on Refs. [14, 36, 41]. However, GENE modifications to include global effects are published within this work for the first time.

3.1 Local vs. global simulations

Traditionally, two alternative concepts are used when implementing the gyrokinetic equations with appropriate boundary conditions.

If the perpendicular turbulence scale (on the order of the ion gyroradius) is much smaller than the characteristical system sizes, as can be approximately assumed for the larger present day devices JET, DIII-D, ASDEX-Upgrade, etc. and definitely for future devices like ITER, a so-called *local* approach can be taken. Here, all profiles are evaluated just at a single position so that e.g. temperatures and densities are constant throughout the whole simulation domain. However, as can be justified in a multiscale approach, first order derivatives explicitly appearing in Eq. (2.60) are kept as well in order to establish e.g. the linear gradient driving terms. Furthermore, periodic boundary conditions are then used for both perpendicular directions, x and y. This approach is justified if the corresponding simulation box lengths are chosen to be larger than the correlation lengths and thus a negligible artificial influence originating from the boundary conditions on the turbulent system can be safely assumed. In addition, periodic boundary conditions automatically keep the (average) background gradients fixed and facilitate the application of spectral techniques in the x and y directions. The latter, in turn, allow for a simple and very accurate computation of corresponding derivatives and operators in the gyrokinetic Vlasov-Maxwell system of equations as will be shown later.

The alternative *nonlocal* or *global* approach has to be chosen if equilibrium quantities significantly vary within the simulation domain. Naturally, periodic boundary conditions cannot be applied - at least in the radial direction. The y direction is not affected since temperature and density, for instance, are constant on flux surfaces. Hence, a spectral method can still be taken for the latter but the former has to be discretized on a real space grid.

Concluding, the *global* approach is physically more comprehensive but numerically more demanding and potentially less accurate when treating e.g. radial derivatives. Hence, the *local* one is often the first choice for investigations of turbulent systems with $\rho_{\mathrm{ref}}/L_{\mathrm{ref}} \ll 1$ where the normalization length L_{ref} is of the order of R, a, L_T, or L_n.

3.2 Geometry

Before a more detailed description e.g. of the boundary conditions can be given for both approaches, some light shall be shed on which geometries and coordinates are actually considered. As mentioned in Chapter 2, a field aligned coordinate system should be employed in order to reduce the computational effort. Furthermore, the magnetic field has been represented as $\mathbf{B}_0 = \mathcal{C}\,\nabla x \times \nabla y$. In the following, examples will be given how the coordinates x and y are constructed based on an equilibrium magnetic field $\mathbf{B}_0$ either

given by analytical solutions of the Grad-Shafranov equation or by numerical results of MHD codes.

3.2.1 Axisymmetric systems

For magnetic tokamak core equilibria where ripples arising from non-ideal coil geometries are negligible, an axisymmetric geometry can be considered. Here, the magnetic field can be written in terms of a "flux surface label" ϱ, defined by $\mathbf{B}_0 \cdot \nabla \varrho = 0$ and two angle-like coordinates ϑ and φ as illustrated in Fig. 3.1. Hence, the helical winding of a magnetic

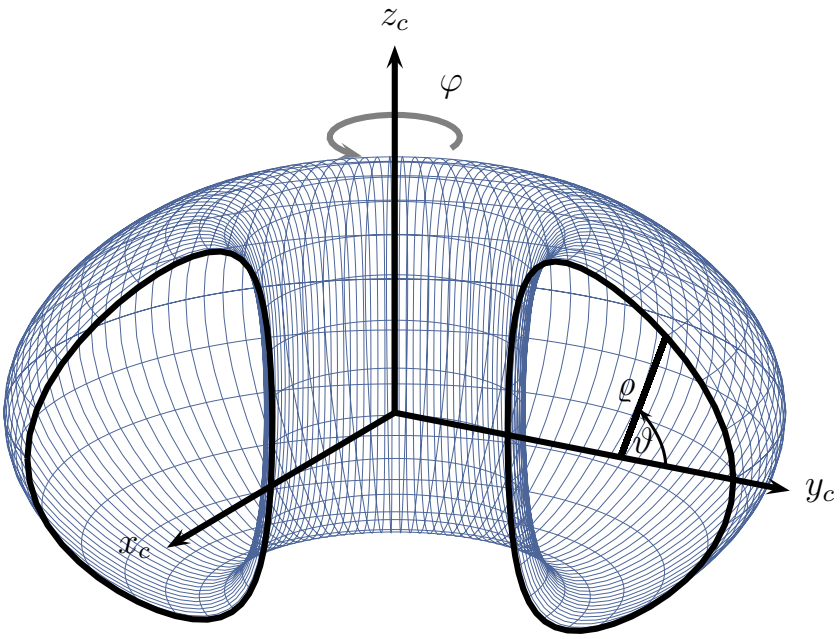

Figure 3.1: Definition of the flux surface label ϱ and the two angles ϑ and φ in general toroidal geometry. The grid lines do not represent field lines, but lines of constant ϑ and φ.

field on a flux surface around a torus can be expressed by $\mathbf{B}_0 = B_0^{\vartheta}\hat{\mathbf{e}}_{\vartheta} + B_0^{\varphi}\hat{\mathbf{e}}_{\varphi}$. However, a more suitable set of coordinates is chosen such that the magnetic field lines are straight. As shown in [35] a transformation of one of the angle coordinates is sufficient to achieve this property. In tokamaks, it is often the symmetry angle φ (measuring rotation about the major axis) which is retained and hence ϑ is replaced by a new angle ζ. The latter is then required to fulfill the relation

$$\frac{\mathrm{d}\varphi}{\mathrm{d}\zeta} = \frac{B_0^{\varphi}}{B_0^{\zeta}} = \frac{\mathbf{B}_0 \cdot \nabla\varphi}{\mathbf{B}_0 \cdot \nabla\zeta} = q(\varrho) \tag{3.1}$$

where q denotes the safety factor defined by

$$\begin{aligned} q =& \frac{\mathrm{d}\Psi_t}{\mathrm{d}\Psi_p} = \frac{\Psi_t'}{\Psi_p'} \\ \sim& \frac{\textit{number of toroidal magnetic field line turns}}{\textit{poloidal turn}} \end{aligned} \tag{3.2}$$

with the toroidal and poloidal magnetic fluxes, $\Psi_t = 1/(2\pi)\iiint_V \mathbf{B}_0 \cdot \nabla\varphi \,\mathrm{d}V$ and $\Psi_p = 1/(2\pi)\iiint_V \mathbf{B}_0 \cdot \nabla\vartheta \,\mathrm{d}V$, and their derivatives Ψ_t' and Ψ_p' with respect to the flux surface label ϱ. Employing a field line label

$$\nu(\varrho, \zeta, \varphi) = \frac{\Psi_p'}{2\pi}\left(q(\varrho)\zeta - \varphi\right) \equiv \frac{\Psi_p'}{2\pi}\,\hat{\nu} \tag{3.3}$$

allows to represent the magnetic field as

$$\mathbf{B}_0 = \nabla\varrho \times \nabla\nu \tag{3.4}$$

which can be further transformed into

$$\begin{aligned} \mathbf{B}_0 =& \nabla\varrho \times \left(\frac{1}{2\pi}\left[\Psi_p''\hat{\nu}\nabla\varrho + \Psi_p'\nabla\hat{\nu}\right]\right) \\ =& \frac{\Psi_p'}{2\pi}\nabla\varrho \times \nabla\hat{\nu} \end{aligned} \tag{3.5}$$

if $\hat{\nu}$ is used instead of ν, or into

$$\mathbf{B}_0 = \nabla\Psi \times \nabla\hat{\nu} \tag{3.6}$$

if $\varrho = \Psi_p/2\pi \equiv \Psi$ is chosen as is often done for tokamaks.

Finally, a mapping to flux tube coordinates (x, y, z) has to be considered. Since both perpendicular directions, x and y, shall be given in units of lengths to be consistent with Chapter 2 whereas the parallel direction z is kept dimensionless, a general transformation appears to be

$$x = C_x(\varrho) \qquad y = C_y(\varrho)\,\hat{\nu} \qquad z = \zeta \tag{3.7}$$

with the flux function $C_x(\varrho)$ converting the flux surface label ϱ to the radial flux tube coordinate x and similarly $C_y(\varrho)$ for the $\hat{\nu}$ to y transformation. Hence, the corresponding gradients are

$$\nabla x = C_x'\nabla\varrho, \tag{3.8}$$

$$\nabla y = C_y'\,\hat{\nu}\nabla\varrho + C_y\nabla\hat{\nu}, \tag{3.9}$$

$$\nabla z = \nabla\zeta, \tag{3.10}$$

and thus Eq. (3.5) can be rewritten as

$$\begin{aligned}\mathbf{B}_0 =& \frac{\Psi_p'}{2\pi}\nabla\varrho\times\left(\frac{1}{C_y}\left[\nabla y - C_y'\hat{\nu}\nabla\varrho\right]\right)\\ =& \frac{\Psi_p'}{2\pi C_x' C_y}\nabla x\times\nabla y\end{aligned} \tag{3.11}$$

By comparing with Eq. (2.37) it becomes evident that

$$\mathcal{C} \equiv \frac{\Psi_p'}{2\pi C_x' C_y}. \tag{3.12}$$

Circular and $\hat{s}-\alpha$ model

Besides a very simple slab geometry, two models, namely an ad-hoc circular, concentric model and a shifted circle ($\hat{s}-\alpha$) model, are available within GENE and used in most of the simulations shown later. Triggered by several benchmarking efforts [43, 44], the latter has become a standard scheme being employed in many local codes although being slightly inconsistent. The former, on the other hand, is self-consistently derived but does not consider Shafranov shifts in its current version. It has recently been implemented by X. Lapillonne et al. [27] and is of special relevance for the global code since it allows for the desired consideration of radial dependencies.

Thus, the main steps of the derivation shall briefly be mentioned. Assuming a known safety factor profile $q(r)$ and a magnetic field

$$\mathbf{B}_0 = B_{\mathrm{ref}}\left[\frac{R_0}{R}\hat{\mathbf{e}}_\varphi + \frac{r}{R}\frac{1}{q(r)\sqrt{1-\varepsilon^2}}\hat{\mathbf{e}}_\vartheta\right] \tag{3.13}$$

with circular, concentric flux surfaces so that the flux label ϱ can be identified with their radii r, the straight field line angle becomes

$$\zeta = \zeta(r,\vartheta) = 2\arctan\left[\sqrt{\frac{1-\varepsilon}{1+\varepsilon}}\tan\left(\frac{\vartheta}{2}\right)\right]. \tag{3.14}$$

As illustrated in Fig. 3.2, R_0 denotes the major radius (radius of magnetic axis), r the radius of a flux surface, $\varepsilon = r/R_0$ the corresponding inverse aspect ratio and $R = R_0 + r\cos\vartheta$.

The flux coordinates are $u^1 = x = r$, $u^3 = z = \zeta$, and $u^2 = y = r_0/q_0(q\zeta - \varphi)$ where r_0 is the radius of a reference flux surface and $q_0 = q(r_0)$. With these choices, the desired metric coefficients can be constructed by means of

$$g^{ij} = \frac{\partial u^i}{\partial v^k} g^{kl}_{\mathrm{Torus}} \frac{\partial u^j}{\partial v^l} \tag{3.15}$$

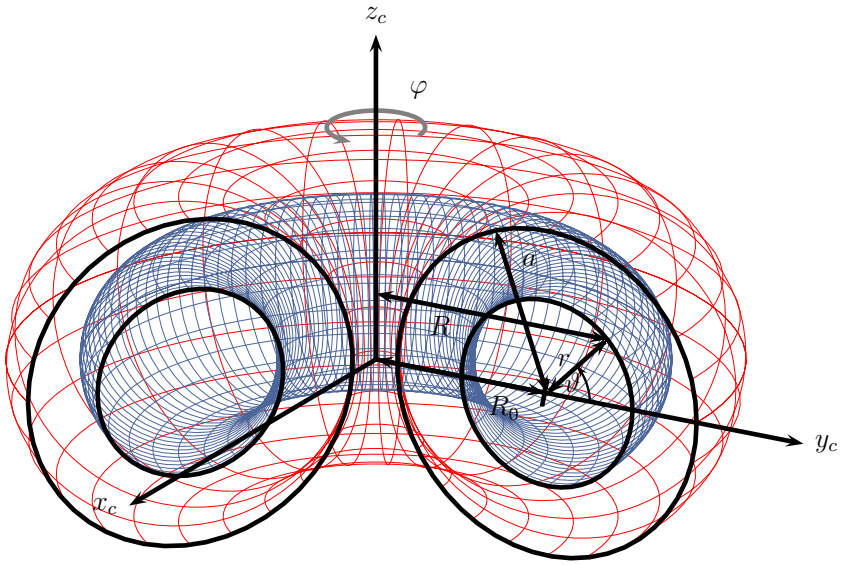

Figure 3.2: Illustration of a circular, concentric toroidal geometry. Here, R_0 denotes the major radius (radius of magnetic axis), r the radius of a flux surface (blue), $R = R_0 + r\cos\vartheta$, and a the radius of the last closed flux surface (red).

where

$$\left(g^{ij}_{\text{Torus}}\right) = \begin{pmatrix} 1 & 0 & 0 \\ 0 & r^{-2} & 0 \\ 0 & 0 & R^{-2} \end{pmatrix} \tag{3.16}$$

is the metric transforming a Cartesian coordinate system (x_c, y_c, z_c) to torus coordinates $v^{(1,2,3)} = (r, \vartheta, \varphi)$. The final result is

$$g = \begin{pmatrix} 1 & \frac{r_0}{q_0}\frac{\partial(q\zeta)}{\partial r} & \frac{\partial\zeta}{\partial r} \\ \frac{r_0}{q_0}\zeta\frac{\partial(q\zeta)}{\partial r} & \frac{r_0^2}{q_0^2}\left[\left(\frac{\partial(q\zeta)}{\partial r}\right)^2 + \frac{1}{R^2} + q^2\left(\frac{1}{r}\frac{\partial\zeta}{\partial\vartheta}\right)^2\right] & \frac{r_0}{q_0}\left[\frac{\partial(q\zeta)}{\partial r}\frac{\partial\zeta}{\partial r} + q\left(\frac{1}{r}\frac{\partial\zeta}{\partial\vartheta}\right)^2\right] \\ \frac{\partial\zeta}{\partial r} & \frac{r_0}{q_0}\left[\frac{\partial(q\zeta)}{\partial r}\frac{\partial\zeta}{\partial r} + q\left(\frac{1}{r}\frac{\partial\zeta}{\partial\vartheta}\right)^2\right] & \left(\frac{\partial\zeta}{\partial r}\right)^2 + \left(\frac{1}{r}\frac{\partial\zeta}{\partial\vartheta}\right)^2 \end{pmatrix} \tag{3.17}$$

with

$$\frac{\partial\zeta}{\partial\vartheta} = \sqrt{1-\varepsilon^2}\frac{R_0}{R} = \frac{\bar{q}}{q}\frac{R_0}{R}, \tag{3.18}$$

$$\frac{\partial(q\zeta)}{\partial r} = \zeta\frac{\partial q}{\partial r} + q\frac{\partial\zeta}{\partial r} = \zeta\frac{\partial q}{\partial r} - q\frac{q^2}{\bar{q}^2}\frac{\sin\zeta}{R_0}, \tag{3.19}$$

and the abbreviation $\bar{q} = q\sqrt{1-\varepsilon^2}$. In case of large aspect ratios, $a/R \ll 1$, an approximation to first order in $\varepsilon = r/R \leq a/R$, as derived in Ref. [27], can be employed.

Slightly generalizing the expressions presented in this reference by retaining the full radial dependence yields

$$\begin{aligned}
g^{xx} =& 1, \\
g^{xy} =& g^{yx} = \hat{s}z - \frac{q}{q_0}\varepsilon_0 \sin z, \\
g^{xz} =& g^{zx} = -\varepsilon\frac{\sin z}{r}, \\
g^{yy} =& (\hat{s}z)^2 - 2\frac{q}{q_0}\varepsilon_0\hat{s}z\sin z + \frac{q^2}{q_0^2}\frac{r_0^2}{r^2}\left(1 - 2\varepsilon\cos\vartheta\right), \\
g^{yz} =& g^{zy} = \frac{1}{r_0}\left[-\hat{s}z\varepsilon_0\sin z + \frac{q}{q_0}\frac{r_0^2}{r^2}\left(1 - 2\varepsilon\cos\vartheta\right)\right], \\
g^{zz} =& \frac{1}{r^2}\left(1 - 2\varepsilon\cos\vartheta\right),
\end{aligned} \tag{3.20}$$

where $\varepsilon_0 = r_0/R_0$ denotes the inverse aspect ratio of the reference flux surface and $\cos\vartheta = (\cos z - \epsilon)/(1 - \epsilon\cos z)$. Employing furthermore the limit $\epsilon \to 0$, and hence $\epsilon_0 \to 0$, finally gives the $\hat{s} - \alpha$ model without Shafranov shift. Including the latter yields in local approximation and normalized fashion

$$\hat{g}_{\hat{s}-\alpha} = \begin{pmatrix} 1 & \hat{s}\hat{z} - \alpha\sin\hat{z} & 0 \\ \hat{s}\hat{z} - \alpha\sin\hat{z} & 1 + (\hat{s}\hat{z} - \alpha\sin\hat{z})^2 & L_{\mathrm{ref}}/r_0 \\ 0 & L_{\mathrm{ref}}/r_0 & L_{\mathrm{ref}}^2/r_0^2 \end{pmatrix} \tag{3.21}$$

with $\alpha = \frac{q_0^2 R_0}{L_{\mathrm{ref}}}\beta_{\mathrm{ref}}\sum_\sigma \hat{n}_{0\sigma}\hat{T}_{0\sigma}\left(\hat{\omega}_{T\sigma} + \hat{\omega}_{n\sigma}\right)$. Although Eq. (3.21) represents one of the simplest descriptions of a toroidal geometry and is thus quite often used, it suffers from a severe defect. In order to take into account trapped electron effects, ϵ_0 terms have to be kept in the representation of the magnetic field, $\hat{B}_0 = 1/(1 + \epsilon_0\cos\hat{z})$. Hence, the normalized Jacobian $\hat{J} = 1/\hat{B}_0$ becomes inconsistent with the determinant $|g_{\hat{s}-\alpha}|$ which is equal to zero.

3.2.2 Arbitrary geometries

Apart from simple (semi-)analytic model geometries, arbitrarily shaped MHD equilibria can be considered by employing either the CHEASE [45, 27] or the TRACER [26] interfaces. The latter, for instance, uses a field line tracing algorithm applied to numerically determined magnetic configurations to compute the desired coordinate system. An example which has been dealing successfully with the complicated geometry of the future stellarator experiment W7-X, and where the author of this thesis has been involved, is shown in Ref. [46].

3.3 Flux tube approach and boundary conditions

The flute like character of plasma microturbulence, already considered in the gyrokinetic ordering, furthermore allows for an optimization of the simulation volume with respect to computational costs and coverage of the main physical effects. In particular, it is quite common to choose a simulation box which covers only a fraction of the flux surface in the y direction rather than the whole flux surface. In addition, only an integer number of poloidal turns is taken into account in order to capture variations on a flux surface. For example, in tokamaks with negligible toroidal ripples, it is sufficient to consider just one poloidal turn due to the axisymmetry. The boundary conditions which are directly connected with this kind of concept, known as flux tube approach [47, 48, 49, 50], will be discussed in the following.

3.3.1 Radial boundary condition

As mentioned earlier, periodic boundary conditions,

$$F(x,y,z) = F(x+L_x,y,z), \tag{3.22}$$

are employed in the local code which allow for using the Fourier back and forth transformations

$$F(k_x,y,z) = \frac{1}{L_x}\int_0^{L_x} \mathrm{d}x\, \mathrm{e}^{-\mathrm{i}k_x x}\, F(x,y,z) \quad \text{and} \quad F(x,y,z) = \sum_{k_x} \mathrm{e}^{\mathrm{i}k_x x}\, F(k_x,y,z) \tag{3.23}$$

with the discrete Fourier mode numbers $k_x = i \cdot 2\pi/L_x$, i being an integer. This choice, however, is only justifiable if the simulation domain can be restricted in the radial direction without influencing the turbulent system as well. The resulting simulation box is then a very thin but long tube which gets distorted and tilted when following the center field line.

Of course, such assumptions are not applicable in global computations since radial and in general non-periodic variations of equilibrium quantities shall be kept. Here, it is, e.g., reasonable to implement Dirichlet or von-Neumann boundary conditions if turbulent fluctuations are expected to decrease towards the radial boundaries. In this thesis, the first option has been used in gyroaveraging procedures and in radial derivatives.

3.3.2 Boundary condition in y direction

In the y direction, often called binormal (referring to the orthogonal vectors $(\hat{\mathbf{e}}^x, \hat{\mathbf{e}}^y, \hat{\mathbf{e}}_z)$ at outboard midplane) or toroidal (with respect to the alignment of the corresponding covariant basis vector $\hat{\mathbf{e}}_y$) direction, periodic boundary conditions are taken in the local

as well as the global code. However, a full flux surface, i.e. $\hat{\nu} = [0, 2\pi)$, is only covered in special cases. Instead, an integer fraction

$$\Delta\hat{\nu} = \frac{2\pi}{n_0} \tag{3.24}$$

is chosen as suggested by the flux tube concept. As pointed out in Ref. [51], such an approach leads to a thinning out of mode numbers in y direction as becomes obvious if a Fourier transformation

$$F(x, k_y, z) = \frac{1}{L_y} \int_0^{L_y} \mathrm{d}y \, \mathrm{e}^{-\mathrm{i}k_y y} \, F(x, y, z) \tag{3.25}$$

is applied. Here, $L_y = C_y \Delta\hat{\nu}$ and hence the discrete mode number spectrum is given by $k_y = k_y^{\min} \cdot j$ with $k_y^{\min} = 2\pi/L_y = n_0/C_y$ and j being integer-valued. Thus, increasing the toroidal mode number n_0 similarly increases $k_y^{\min}$ or - if $k_y^{\min}$ shall be kept constant - the possible j values are restricted to $j = n_0 \cdot l$ with $l = 0, 1, 2, \ldots$.

3.3.3 Parallel boundary condition

The parallel (z) boundary condition is the most delicate one. Following a magnetic field line in an axisymmetric equilibrium for an integer number of poloidal turns yields similar physical situations at both ends. However, for irrational q they do not match due to the interplay of straight field line angle $\zeta \approx \vartheta$ and field line label ν. For radially varying safety factors the situation becomes even worse due to a tilting of the simulation box.

Hence, the ν variation has to be included to compensate for these effects. In angle-like coordinates in the relevant directions the parallel boundary condition then reads

$$F(x, \hat{\nu}, \zeta + 2\pi) = F(x, \hat{\nu} - 2\pi q, \zeta) \tag{3.26}$$

Now, transforming to flux tube coordinates yields

$$F(x, y, z + L_z) = F(x, y - 2\pi q C_y, z) \tag{3.27}$$

or, alternatively using a Fourier representation in y,

$$F(x, k_y, z + L_z) = F(x, k_y, z) \exp\left(-2\pi\mathrm{i} q k_y C_y\right). \tag{3.28}$$

Further replacing k_y as before by $k_y = j \cdot k_y^{\min} = j \cdot n_0/C_y$ eliminates the C_y function so that the parallel boundary condition becomes

$$F(x, k_y, z + L_z) = F(x, k_y, z) \exp\left(-2\pi\mathrm{i} n_0 q(x) j\right). \tag{3.29}$$

The local limit

In the local code, $q(x)$ is Taylor-expanded up to first order in x about the central flux surface here denoted by r_0

$$q(x) \approx q_0 + \left.\frac{\mathrm{d}q}{\mathrm{d}x}\right|_{r_0} (x - r_0).$$

If furthermore a dimensionless magnetic shear parameter

$$\hat{s} = \frac{r_0}{q_0} \left.\frac{\mathrm{d}q}{\mathrm{d}x}\right|_{r_0} \tag{3.30}$$

is introduced, one arrives at

$$q(x) \approx q_0 \left(1 + \hat{s}\frac{x - r_0}{r_0}\right). \tag{3.31}$$

Hence, the parallel boundary condition as derived in Eq. (3.29) becomes

$$F(x, k_y, z + L_z) = F(x, k_y, z) \exp\left[-2\pi \mathrm{i} n_0 q_0 j\right] \exp\left[-2\pi \mathrm{i} k_y C_y q_0 \hat{s}(x - r_0)/r_0\right], \tag{3.32}$$

where n_0 has again been replaced by $k_y C_y$ in the last factor. Usually, advantage is now taken of the freedom of choice for ρ_{ref}/a in the local code (arbitrarily small flux tube in perpendicular direction) to assume $n_0 q_0$ to be integer-valued and $C_y = r_0/q_0$. Hence, the first exponential function in Eq. (3.32) evaluates to one. Finally, a Fourier representation in x reads as follows

$$F(k_x, k_y, z + L_z) = F(k_x', k_y, z) \exp\left[2\pi \mathrm{i} k_y \hat{s} r_0\right]. \tag{3.33}$$

with $k_x' = k_x + 2\pi\hat{s}k_y$ so that k_x and k_y become coupled. This interference impresses a constraint on the box sizes since the discreteness of wave numbers demands

$$k_x' = k_x^{\min} \cdot l = k_x^{\min} \cdot i + 2\pi\hat{s}k_y^{\min} \cdot j, \qquad l, i, j \in \mathbb{Z} \tag{3.34}$$

which can only be fulfilled if

$$\mathcal{N} = \frac{2\pi\hat{s}k_y^{\min}}{k_x^{\min}} = \hat{s}k_y^{\min} L_x, \qquad \mathcal{N} \in \mathbb{Z}. \tag{3.35}$$

Eq. (3.33) may hence be written as

$$\begin{aligned} F(k_x, k_y, z + L_z) &= F(k_x', k_y, z) \exp\left[2\pi \mathrm{i} j \mathcal{N}(L_x/2)/L_x\right] \\ &= F(k_x', k_y, z)(-1)^{\mathcal{N}j} \end{aligned} \tag{3.36}$$

with $k_x' = k_x^{\min} \cdot (i + \mathcal{N}j)$ and $r_0 = L_x/2$.

3.4 The gyroaverage operator

Several basic equations contain gyroaveraged quantities, e.g.

$$\langle F_1(\mathbf{x}-\mathbf{r})\rangle = \mathcal{G}\left[F_1(\mathbf{x}-\mathbf{r})\right] \tag{3.37}$$

where $\mathbf{r} = \mathbf{r}(\theta)$ is the radial vector orthogonally aligned to the magnetic field and $\mathcal{G} = \frac{1}{2\pi}\int_0^{2\pi} \mathrm{d}\theta$ denotes the previously defined gyroaverage operator. In this section, the global as well as local representation shall be derived.

3.4.1 Global representation

The following derivation of the gyroaverage operator and a first implementation trace back to T. Dannert. However, significant extensions as, for instance, the crucial implementation of radially varying metrics have been done in the course of this work.

As mentioned in Sec. 3.3.2, both local as well as global representations use periodic boundary conditions in the y direction which allows for switching to a Fourier representation. Hence, Eq. (3.37) can be written as

$$\langle F_1(\mathbf{x}-\mathbf{r})\rangle = \frac{1}{2\pi}\sum_{k_y}\int_0^{2\pi} F_1(x-r^1, k_y, z)\,\mathrm{e}^{\mathrm{i}k_y(y-r^2)}\,\mathrm{d}\theta. \tag{3.38}$$

Although x and y are coordinates perpendicular to the magnetic field, they are in general non-orthogonal which has to be considered when describing the circular gyro motion. Hence, the obvious choice of $\mathbf{r}(\theta) = \rho\left(\cos\theta\,\hat{\mathbf{e}}^{\bar{x}} + \sin\theta\,\hat{\mathbf{e}}^{\bar{y}}\right)$ in a local, Cartesian coordinate system $(\bar{x}, \bar{y}, \bar{z})$ with $\hat{\mathbf{e}}^{\bar{z}} = \hat{\mathbf{b}}$ has to be transformed to flux tube coordinates. Choosing without loss of generality the local radial axis to point along the radial flux coordinate $\hat{\mathbf{e}}^{\bar{x}} = \nabla x/\left|\nabla x\right| = \nabla x/\sqrt{g^{11}}$ and thus

$$\begin{aligned}
\hat{\mathbf{e}}^{\bar{y}} =& \hat{\mathbf{e}}^{\bar{z}} \times \hat{\mathbf{e}}^{\bar{x}} = \hat{\mathbf{b}} \times \frac{\nabla x}{\sqrt{g^{11}}} \\
=& \frac{\nabla x \times \nabla y}{\sqrt{\gamma_1}} \times \frac{\nabla x}{\sqrt{g^{11}}} \\
=& \frac{1}{\sqrt{\gamma_1}}\left(\nabla y\sqrt{g^{11}} - \nabla x\frac{g^{12}}{\sqrt{g^{11}}}\right)
\end{aligned} \tag{3.39}$$

yields as flux tube components

$$r^1 = \mathbf{r}\cdot\nabla x = \sqrt{g^{11}(x,z)}\rho_\sigma(x,z,\mu)\cos\theta \tag{3.40}$$

and

$$r^2 = \mathbf{r}\cdot\nabla y = \left(g^{12}(x,z)\rho_\sigma(x,z,\mu)\cos\theta + \sqrt{\gamma_1(x,z)}\rho_\sigma(x,z,\mu)\sin\theta\right)/\sqrt{g^{11}(x,z)}. \tag{3.41}$$

Here, all equilibrium quantities, in particular metric coefficients but also the magnetic field hidden in $\rho_\sigma(x,z,\mu) = \sqrt{2\mu B_0/m_\sigma}/\Omega_\sigma = \sqrt{2\hat{\mu}\hat{m}_\sigma\hat{T}_{0\sigma}(x_0)/(\hat{q}_\sigma^2\hat{B}_0(x,z))}\rho_{\mathrm{ref}}$ are expanded to zeroth order, i.e. evaluated just at the center position x since variations on the gyroradius scale are assumed to be negligible. However, this approximation might be problematic close to the magnetic axis or edge where geometry related quantities strongly vary. An alternative gyroaveraging scheme avoiding any approximation in the metric is therefore currently under investigation and will be implemented soon [52].

Besides this issue, another problem arises due to the numerical representation of the radial direction which will be addressed now. Since a continuous representation is naturally not available, a discretization on a grid, e.g. $x_{(i)}$ with the index $i = 0, .., N_x - 1$ is used instead. Here, the index should not be confused with a covariant vector element, and N_x represents the number of radial grid points. Depending on the actual size of the gyroradius and the number of grid points along a gyrocircle, a resolution being much higher than the one required to capture the physical effects under investigation would be necessary just for this operation. A possible remedy is to perform an interpolation before the calculation of gyroaverages. Here, finite elements have been proven to be a reasonable choice [53]. Thus, the function to be gyroaveraged is now rewritten in terms of finite-element base functions $\Lambda_n(x)$

$$F_1(x) = \sum_n \Lambda_n(x) F_1(x_{(n)}) \tag{3.42}$$

where $F_1(x_{(n)})$, the value of F_1 on the coarse-grained grid at position $x_{(n)}$, is used as the weight of the nth base function. Alternatively, the vectors $\mathbf{\Lambda} = (\Lambda_0, \ldots, \Lambda_{N_x-1})^T$ and $\mathbf{F}_1 = (F_1(x_{(0)}), \ldots, F_1(x_{(N_x-1)}))^T$ can be defined to transform Eq. (3.42) into

$$F_1(x) = \mathbf{F}_1 \cdot \mathbf{\Lambda}(x). \tag{3.43}$$

Applying this modification to Eq. (3.38) yields

$$\langle F_1(\mathbf{x}_{(i)} - \mathbf{r})\rangle = \frac{1}{2\pi}\sum_{k_y,n} F_1(x_{(n)}, k_y, z)\, \mathrm{e}^{\mathrm{i}k_y y} \int_0^{2\pi} \Lambda_n(x_{(i)} - r^1)\, \mathrm{e}^{-\mathrm{i}k_y r^2}\, \mathrm{d}\theta \tag{3.44}$$

or, in terms of a matrix-vector multiplication,

$$\langle \mathbf{F}_1(\mathbf{x} - \mathbf{r})\rangle = \sum_{k_y} \mathrm{e}^{\mathrm{i}k_y y}\, \mathcal{G}(x, k_y, z, \mu) \cdot \mathbf{F}_1(x, k_y, z). \tag{3.45}$$

where the gyroaverage operator is understood as a matrix with elements

$$\begin{aligned}\mathcal{G}_{in}(x, k_y, z, \mu) &= \frac{1}{2\pi}\int_0^{2\pi} \Lambda_n(x_{(i)} - r^1)\, \mathrm{e}^{-\mathrm{i}k_y r^2}\, \mathrm{d}\theta \\ &= \frac{1}{\pi}\int_0^{\pi} \Lambda_n(x_{(i)} - \sqrt{g^{11}}\rho\cos\theta)\, \mathrm{e}^{-\mathrm{i}\frac{g^{21}}{\sqrt{g^{11}}}k_y\rho\cos\theta} \cdot \\ &\qquad \cos\left(\sqrt{\frac{\gamma_1}{g^{11}}}k_y\rho\sin\theta\right)\, \mathrm{d}\theta.\end{aligned} \tag{3.46}$$

Here, the metric terms are of course still functions of x and z and the gyroradius is $\rho = \rho_\sigma(x, z, \mu)$. However, those additional dependencies have been dropped here for reasons of readability.

As will be shown in the course of the next paragraph, gyroaverages of quantities evaluated at $\mathbf{x} = \mathbf{X} + \mathbf{r}$, for instance

$$\langle \phi_1(\mathbf{X} + \mathbf{r}) \rangle = \sum_{k_y} \mathrm{e}^{\mathrm{i}k_y Y} \, \mathcal{G}(X, k_y, z, \mu) \cdot \phi_1(X, k_y, z), \tag{3.47}$$

can be expressed similarly employing an identical gyroaveraging matrix. Here, ϕ_1 is analogously meant to be a vector containing the values on the coarse grid.

Consecutive gyroaverages

The gyrokinetic field equations, Eqs. (2.81) and (2.97) contain terms with consecutive gyroaverages which shall be investigated separately here:

$$\begin{aligned} \langle \bar{\phi}_1(\mathbf{x} - \mathbf{r}) \rangle =& \mathcal{G}\left[\mathcal{G}\left[\phi_1(\mathbf{x} - \mathbf{r})\right]\right] \\ =& \frac{1}{4\pi^2} \int_0^{2\pi} \mathrm{d}\theta \int \mathrm{d}^3 X \delta(\mathbf{X} + \mathbf{r}(\theta) - \mathbf{x}) \int_0^{2\pi} \mathrm{d}\theta' \phi_1(\mathbf{X} + \mathbf{r}(\theta')). \end{aligned} \tag{3.48}$$

The consideration of the discretization in the radial direction and of a Fourier representation in the y direction together with the evaluation of the δ function yields

$$\langle \bar{\phi}_1(\mathbf{x} - \mathbf{r}) \rangle = \sum_{k_y} \frac{1}{4\pi^2} \int_0^{2\pi} \mathrm{d}\theta \int_0^{2\pi} \mathrm{d}\theta' \phi_1(x_{(i)} - r^1(\theta) + r^1(\theta'), k_y) \, \mathrm{e}^{\mathrm{i}k_y (y - r^2(\theta) + r^2(\theta'))} \, . \tag{3.49}$$

Now, the previously mentioned interpolation using the base functions $\Lambda(x)$ is applied to $\phi(x)$ in order to allow for high accuracy (θ,θ') integrations

$$\langle \bar{\phi}_1(\mathbf{x} - \mathbf{r}) \rangle = \sum_{k_y, n} \frac{\mathrm{e}^{\mathrm{i}k_y y}}{4\pi^2} \int_0^{2\pi} \mathrm{d}\theta \, \mathrm{e}^{-\mathrm{i}k_y r^2(\theta)} \int_0^{2\pi} \mathrm{d}\theta' \, \mathrm{e}^{\mathrm{i}k_y r^2(\theta')} \, \Lambda_n(x_{(i)} - r^1(\theta) + r^1(\theta')) \phi_1(x_{(n)}, k_y). \tag{3.50}$$

By inserting $r_1(\theta')$ and $r_2(\theta')$ from Eqs. (3.40) and (3.41) and treating the θ' integration as in Eq. (3.46) one arrives at

$$\begin{aligned} \langle \bar{\phi}_1(\mathbf{x} - \mathbf{r}) \rangle = & \sum_{k_y, n} \frac{\mathrm{e}^{\mathrm{i}k_y y}}{2\pi^2} \int_0^{2\pi} \mathrm{d}\theta \, \mathrm{e}^{-\mathrm{i}k_y r^2(\theta)} \int_0^{\pi} \mathrm{d}\theta' \, \mathrm{e}^{\mathrm{i}\frac{g^{21}}{\sqrt{g^{11}}} k_y \rho \cos\theta'} \cos\left(\sqrt{\frac{\gamma_1}{g^{11}}} k_y \rho \sin\theta' \right) \\ & \Lambda_n(x_{(i)} - r^1(\theta) + \sqrt{g^{11}} \rho \cos\theta') \, \phi_1(x_{(n)}, k_y). \end{aligned} \tag{3.51}$$

Substituting θ' by $-\theta'' + \pi$ yields

$$\langle \bar{\phi}_1(\mathbf{x}-\mathbf{r})\rangle = \sum_{k_y,n} \frac{\mathrm{e}^{\mathrm{i}k_y y}}{2\pi^2} \int_0^{2\pi} \mathrm{d}\theta\, \mathrm{e}^{-\mathrm{i}k_y r^2(\theta)} \int_0^{\pi} \mathrm{d}\theta''\, \mathrm{e}^{-\mathrm{i}\frac{g^{21}}{\sqrt{g^{11}}}k_y\rho\cos\theta''} \cos\left(\sqrt{\frac{\gamma_1}{g^{11}}}k_y\rho\sin\theta''\right) \Lambda_n(x_{(i)} - r^1(\theta) - \sqrt{g^{11}}\rho\cos\theta'')\,\phi_1(x_{(n)},k_y) \tag{3.52}$$

where θ'' dependent parts can be replaced by the gyromatrix, Eq. (3.46), so that

$$\langle \bar{\phi}_1(\mathbf{x}-\mathbf{r})\rangle = \sum_{k_y,n} \frac{\mathrm{e}^{\mathrm{i}k_y y}}{2\pi} \int_0^{2\pi} \mathrm{d}\theta\, \mathrm{e}^{-\mathrm{i}k_y r^2(\theta)}\, \mathcal{G}_{in}(x_{(i)} - r^1(\theta))\phi_1(x_{(n)},k_y) \tag{3.53}$$

which confirms Eq. (3.47) in retrospect. Identifying $\mathcal{G}_{in}(x_{(i)} - r^1(\theta))$ as a function which is again interpolated, it is straightforward to show

$$\langle \bar{\phi}_1(\mathbf{x}-\mathbf{r})\rangle = \sum_{k_y} \mathrm{e}^{\mathrm{i}k_y y} \sum_{m,n} \mathcal{G}_{im}\mathcal{G}_{mn}\phi_1(x_{(n)},k_y) \tag{3.54}$$

which can be cast into a matrix multiplication

$$\langle \bar{\phi}_1(\mathbf{x}-\mathbf{r})\rangle = \sum_{k_y} \mathrm{e}^{\mathrm{i}k_y y}\, \mathcal{G}^2\phi_1(x,k_y) \tag{3.55}$$

if $\phi_1(x,k_y)$ is again understood as a vector containing the function values on the radial coarse grid.

Choice of the base functions

In order to avoid further computational effort, the base functions $\Lambda_n(x)$ are chosen such that the coarse grid values can easily be extracted again, which happens if the interpolated function coincides with the original values. Furthermore, $\Lambda_n(x)$ is considered to be finite just in the vicinity of the coarse grid points $x_{(n)}$, thus becoming zero when approaching the next neighboring grid point. Possible alternatives taking into account several grid points, for instance splines, would require a solution of a linear system of equations.

The simplest choice in this context are polynomials. Here, additional constraints, in particular derivative values on the coarse grid, are required if boundary conditions are only provided for two coarse grid points. Thus, a function $f(x)$ may be described by polynomials $P_{n,m}$ of odd degree p,

$$f(x) = \sum_{n=0}^{N_x} \sum_{m=0}^{(p-1)/2} \frac{\partial^m}{\partial x^m} f(x)\bigg|_{x=x_{(n)}} P_{n,m}(x), \tag{3.56}$$

e.g. using the constraints

$$\frac{\partial^u}{\partial x^u} P_{n,m}(x)\bigg|_{x=x_{(j)}} = \delta_{jn}\delta_{um} \tag{3.57}$$

with the indices $j = n, (n+1)$ and $u = 0, \ldots, (p-1)/2$. Changing again to a matrix-vector notation where $\mathbf{f}$ contains all function values on the coarse grid, derivatives of mth order can be formally represented by the mth power of a matrix $\mathcal{D}$. The construction of the latter then depends on the finite difference scheme actually chosen for the numerical evaluation of derivatives. In summary, Eq. (3.56) becomes

$$f(x) = \sum_{m=0}^{p} \mathbf{P}_m(x)\mathcal{D}^m\mathbf{f} \tag{3.58}$$

where $\mathbf{P}_m = (P_{0,m}, \ldots, P_{N_x-1,m})^T$. By comparison with Fig. 3.43 it is finally possible to determine the full finite element base function to

$$\mathbf{\Lambda}(x) = \sum_{m=0}^{p} \mathbf{P}_m(x)\mathcal{D}^m. \tag{3.59}$$

The first three solutions to lowest degree, $p = 1, 3, 5$, are plotted in Fig. 3.3 together with a test function. For most applications, polynomials of degree $p = 5$ seem to be sufficient in terms of accuracy and computational effort.

Application to the field equations

Having derived a gyroaverage calculation instruction for a discrete and not necessarily periodic representation of the radial direction in Sec. 3.4, one can now apply those findings to the field equations. The matrix representation of the gyroaverage operator allows for casting the left hand sides of the field equations into matrices, as well. In order to solve for the desired field they are afterwards inverted. For instance, the Poisson equation, Eq. (2.81), becomes

$$\hat{\phi}_1(\mathbf{x}) = \hat{\mathcal{P}}^{-1} \cdot \pi \sum_\sigma \hat{n}_{0\sigma}(x_0)\hat{q}_\sigma \iint \hat{B}^*_{0\|}\mathcal{G}\hat{F}_{1\sigma}\mathrm{d}\hat{v}_\|\mathrm{d}\hat{\mu} \tag{3.60}$$

where the Poisson-matrix is given by

$$\hat{\mathcal{P}} = \left\{ -\hat{\nabla}^2_\perp \hat{\lambda}^2_D + \sum_\sigma \hat{n}_{0\sigma}\frac{\hat{q}^2_\sigma}{\hat{T}_{0\sigma}}\left[\mathbb{1} - \frac{\hat{B}_0}{\hat{T}_{p\sigma}}\int \mathcal{G}^2\, \mathrm{e}^{-\frac{\hat{\mu}\hat{B}_0}{\hat{T}_{p\sigma}}}\,\mathrm{d}\hat{\mu}\right]\right\} \tag{3.61}$$

with

$$\hat{\nabla}^2_\perp = \hat{g}^{xx}\hat{\mathcal{D}}^2 + 2\mathrm{i}\hat{g}^{xy}\hat{\mathcal{D}}\,\hat{k}_y - \hat{g}^{yy}\mathbb{1}\hat{k}^2_y. \tag{3.62}$$

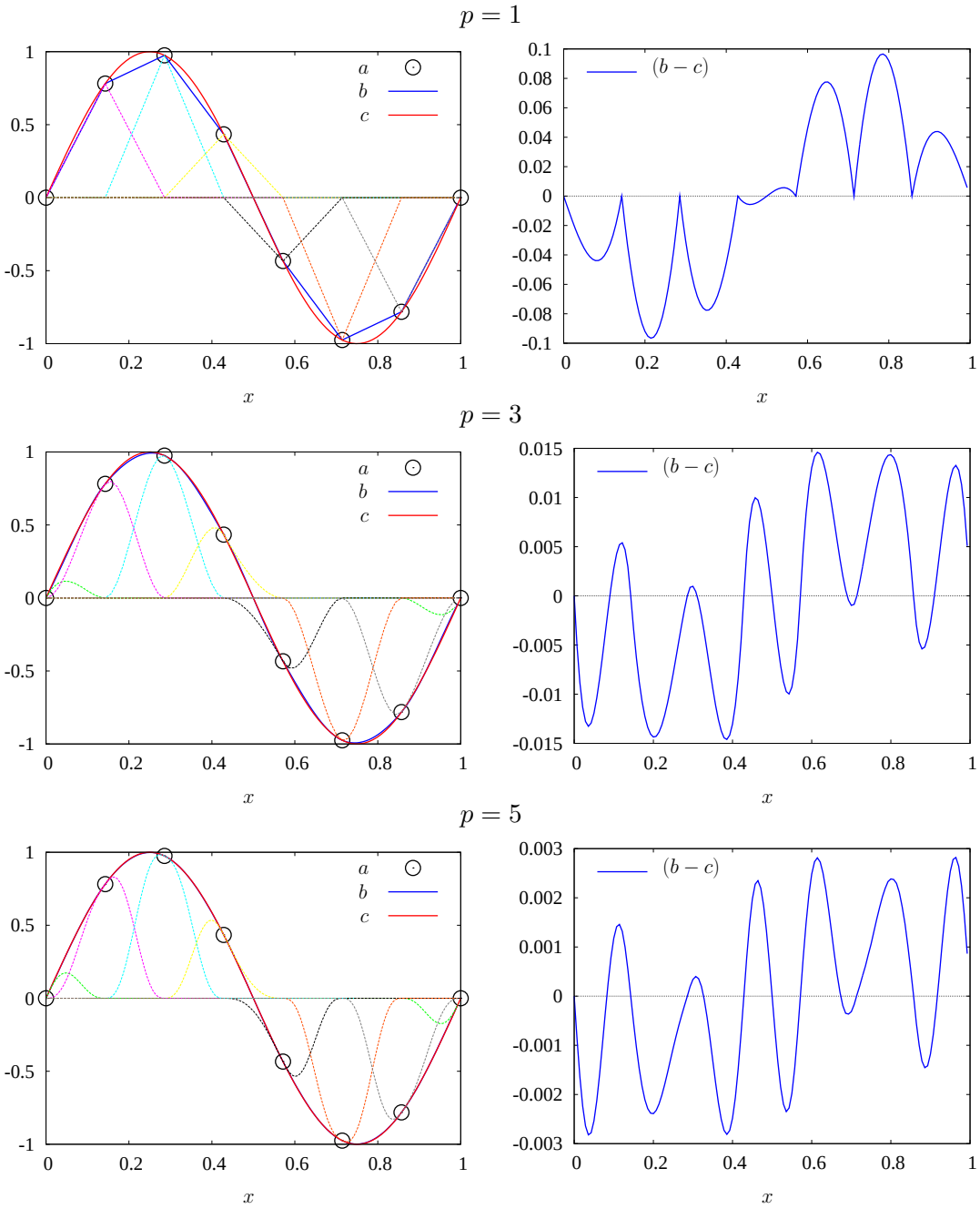

Figure 3.3: Illustration and comparison of the finite element interpolation implemented in GENE for different polynomial degrees p. On the left side, black dots (a) represent the values of a test function $\sin(2\pi x)$ (c) on a coarse grid whereas the blue line (b) indicates interpolation results using the base functions drawn as dotted lines. Since differences between (b) and (c) are hardly visible, they are explicitly shown on the right side.

Here, $\hat{\mathcal{D}}$ denotes a matrix containing the finite difference stencil for radial derivatives. The $\hat{\nabla}_\perp^2$ matrix is also used in Ampère's law which can now be written as

$$\begin{aligned}\hat{A}_{1\parallel} =& \left\{ -\hat{\nabla}_\perp^2 + \frac{\beta_{\mathrm{ref}}}{2} \sum_\sigma \frac{\hat{n}_{0\sigma}\hat{q}_\sigma^2}{\hat{m}_\sigma \hat{T}_{p\sigma}} \hat{B}_0 \int \mathcal{G}^2 \, \mathrm{e}^{-\frac{\hat{\mu}\hat{B}_0}{\hat{T}_{p\sigma}}} \, \mathrm{d}\hat{\mu} \right\}^{-1} \\ & \cdot \sum_\sigma \frac{\beta_{\mathrm{ref}}}{2} \hat{q}_\sigma \hat{n}_{0\sigma}(x_0) \hat{v}_{T\sigma}(x_0) \pi \iint \hat{B}_{0\parallel}^* \mathcal{G} \hat{g}_{1\sigma} \hat{v}_\parallel \mathrm{d}\hat{v}_\parallel \mathrm{d}\hat{\mu}. \end{aligned} \tag{3.63}$$

Note that $B_{1\parallel}$ fluctuations are not considered here. This approximation is employed in most global codes due to the significant additional effort and well justified in the low β limit, see Ref. [14, 36]. Consistently, all contributions attributed to the second term of $\hat{B}_{0\parallel}^*$, see Eq. (2.62), can be neglected, as well. In fact, most present-day tokamaks can be treated in this limit. Only spherical tokamaks and some stellarators exhibit β values where an extended electromagnetic description is required.

3.4.2 The local limit

Using periodic boundary conditions in both perpendicular directions allows for representing gyroaverages in the following way

$$\begin{aligned}\langle F_1(\mathbf{x}-\mathbf{r})\rangle =& \frac{1}{2\pi} \sum_{\mathbf{k}_\perp} \int_0^{2\pi} F_1(\mathbf{k}_\perp, z) \, \mathrm{e}^{\mathrm{i}\mathbf{k}_\perp(\mathbf{x}-\mathbf{r})} \, \mathrm{d}\theta \\ =& \sum_{\mathbf{k}_\perp} F_1(\mathbf{k}_\perp, z) \, \mathrm{e}^{\mathrm{i}\mathbf{k}_\perp \mathbf{x}} \frac{1}{2\pi} \int_0^{2\pi} \mathrm{e}^{-\mathrm{i}\mathbf{k}_\perp \mathbf{r}} \, \mathrm{d}\theta. \end{aligned} \tag{3.64}$$

With $|\mathbf{r}| = \rho$ and an appropriately chosen coordinate system, the θ-integration

$$\begin{aligned}\frac{1}{2\pi} \int_0^{2\pi} \mathrm{e}^{-\mathrm{i}\mathbf{k}_\perp \mathbf{r}} \, \mathrm{d}\theta =& \frac{1}{2\pi} \int_0^{\pi} \mathrm{e}^{-\mathrm{i}k_\perp \rho \cos(\theta)} \, \mathrm{d}\theta + \frac{1}{2\pi} \int_\pi^{2\pi} \mathrm{e}^{-\mathrm{i}k_\perp \rho \cos(\theta)} \, \mathrm{d}\theta \\ =& \frac{1}{2\pi} \int_0^{\pi} \mathrm{e}^{-\mathrm{i}k_\perp \rho \cos(\theta)} \, \mathrm{d}\theta + \frac{1}{2\pi} \int_0^{\pi} \mathrm{e}^{\mathrm{i}k_\perp \rho \cos(\theta')} \, \mathrm{d}\theta' \\ =& \frac{1}{2} J_0(-k_\perp \rho) + \frac{1}{2} J_0(k_\perp \rho) = J_0(k_\perp \rho) \end{aligned} \tag{3.65}$$

can be expressed by the Bessel function $J_n(x) = \frac{\mathrm{i}^{-n}}{\pi} \int_0^\pi \mathrm{e}^{\mathrm{i}x\cos\theta} \cos(n\theta) \mathrm{d}\theta$ in zeroth order. Hence, the gyroaverage operator is given by the scalar function

$$\mathcal{G} = J_0(k_\perp \rho) \tag{3.66}$$

in the local limit. Here, $k_\perp = \left(g^{xx}k_x^2 + 2g^{xy}k_x k_y + g^{yy}k_y^2\right)^{1/2}$ in non-orthogonal coordinates, and $\rho = \rho_\sigma(\mu, z)$.

Application to the field equations

Again, the results derived above shall be applied to the field equations. Since the gyroaverage operator can be written in the local limit as a scalar function, consecutive averages turn out to be corresponding powers. Hence, the normalized Poisson equation simply becomes

$$\hat{\phi}_1(\mathbf{x}) = \frac{\sum_\sigma \hat{n}_{0\sigma}\hat{q}_\sigma \left(\pi \iint \hat{B}^*_{0\parallel} J_0(k_\perp\rho_\sigma)\hat{F}_{1\sigma}\mathrm{d}\hat{v}_\parallel\mathrm{d}\hat{\mu} + \hat{B}_0 \int J_0(k_\perp\rho_\sigma)\hat{\mu}\hat{\tilde{B}}_{1\parallel}\,\mathrm{e}^{-\hat{\mu}\hat{B}_0}\,\mathrm{d}\hat{\mu}\right)}{\hat{k}_\perp^2\hat{\lambda}_D^2 + \sum_\sigma \hat{n}_{0\sigma}\frac{\hat{q}_\sigma^2}{\hat{T}_{0\sigma}}\left[1 - \hat{B}_0\int J_0^2(k_\perp\rho_\sigma)\,\mathrm{e}^{-\hat{\mu}\hat{B}_0}\,\mathrm{d}\hat{\mu}\right]}. \tag{3.67}$$

Here, all temperature and density profiles have been evaluated at just one reference position x_0 as suggested by the local approximation. Hence, $\hat{T}_{0\sigma} = \hat{T}_{0\sigma}(x_0)$, $\hat{n}_{0\sigma} = \hat{n}_{0\sigma}(x_0)$, and $\hat{T}_{p\sigma} = 1$, $\hat{n}_{p\sigma} = 1$. In a last step, the modified Bessel functions can be used to define $\Gamma_n = \mathrm{e}^{-x}\hat{I}_n(x)$ whose zeroth order, for instance, can be identified as $\Gamma_0(b_\sigma) = \hat{B}_0\int_0^\infty J_0^2(k_\perp\rho_\sigma)\,\mathrm{e}^{-\hat{\mu}\hat{B}_0}\,\mathrm{d}\hat{\mu}$ with $b_\sigma = k_\perp^2 v_{T\sigma}^2/(2\Omega_\sigma^2)$. By further replacing the gyroaveraged magnetic field component $\hat{\tilde{B}}_{1\parallel} = I_1(k_\perp\rho_\sigma)\hat{B}_{1\parallel}$ [14, 36], one obtains

$$\hat{\phi}_1(\mathbf{x}) = \frac{\sum_\sigma \hat{n}_{0\sigma}\hat{q}_\sigma \left(\pi \iint \hat{B}^*_{0\parallel} J_0(k_\perp\rho_\sigma)\hat{F}_{1\sigma}\mathrm{d}\hat{v}_\parallel\mathrm{d}\hat{\mu} + \left(\Gamma_0(b_\sigma) - \Gamma_1(b_\sigma)\right)\hat{B}_{1\parallel}/\hat{B}_0\right)}{\hat{k}_\perp^2\hat{\lambda}_D^2 + \sum_\sigma \hat{n}_{0\sigma}\frac{\hat{q}_\sigma^2}{\hat{T}_{0\sigma}}\left[1 - \Gamma_0(b_\sigma)\right]}. \tag{3.68}$$

Similarly, the parallel component of Ampère's law, Eq. (2.97), can be rewritten as

$$\begin{aligned}\hat{A}_{1\parallel} =& \frac{\beta_{\mathrm{ref}}}{2}\sum_\sigma \left\{\hat{q}_\sigma\hat{n}_{0\sigma}\hat{v}_{T\sigma}\pi\iint \hat{B}^*_{0\parallel}J_0(k_\perp\rho_\sigma)\hat{g}_{1\sigma}\hat{v}_\parallel\mathrm{d}\hat{v}_\parallel\mathrm{d}\hat{\mu}\right.\\ &\left. - \frac{\beta_{\mathrm{ref}}}{2}\frac{\hat{n}_{0\sigma}\hat{j}_{0\parallel}}{\hat{B}_0^2}\left[\left(1-\Gamma_0(b_\sigma)\right)\hat{q}_\sigma\hat{\phi}_1 - \hat{T}_{0\sigma}\left(\Gamma_0(b_\sigma) - \Gamma_1(b_\sigma)\right)\hat{B}_{1\parallel}\right]\right\}\\ &\cdot\left(\hat{k}_\perp^2 + \beta_{\mathrm{ref}}\sum_\sigma\frac{\hat{n}_{0\sigma}\hat{q}_\sigma^2}{\hat{m}_\sigma}\pi\hat{B}_0\iint\hat{v}_\parallel^2 J_0^2(k_\perp\rho_\sigma)\hat{F}_{0\sigma}\mathrm{d}\hat{v}_\parallel\mathrm{d}\hat{\mu}\right)^{-1}.\end{aligned} \tag{3.69}$$

The perpendicular component, see Eq. (2.100), allows for establishing the following equation

$$\begin{aligned}\hat{B}_{1\parallel} =& \frac{\beta_{\mathrm{ref}}}{2}\sum_\sigma\left\{\pi\hat{B}_0^{3/2}\frac{\hat{n}_{0\sigma}\hat{q}_\sigma\hat{v}_{T\sigma}}{\hat{k}_\perp}\int\frac{\hat{B}^*_{0\parallel}}{\hat{B}_0}\sqrt{\hat{\mu}}J_1(k_\perp\rho_\sigma)\hat{F}_{1\sigma}\mathrm{d}\hat{v}_\parallel\mathrm{d}\hat{\mu}\right.\\ &\left. + \frac{\hat{n}_{0\sigma}\hat{q}_\sigma}{\hat{B}_0}\left(\Gamma_0(b_\sigma) - \Gamma_1(b_\sigma)\right)\hat{\phi}_1\right\}\cdot\left(1 - \beta_{\mathrm{ref}}\sum_\sigma\frac{\hat{n}_{0\sigma}\hat{T}_{0\sigma}}{\hat{B}_0^2}\left(\Gamma_0(b_\sigma) - \Gamma_1(b_\sigma)\right)\right)^{-1}.\end{aligned} \tag{3.70}$$

Here, intermediate steps have been skipped since all simulations presented in this thesis have been performed in the low β limit. A full derivation can be found, e.g., in Ref. [36].

3.5 Further numerical schemes

The gyrokinetic Vlasov-Maxwell system consists of integro-differential equations. Thus, numerical methods have been implemented to address the discretization of derivatives and integrations which shall briefly be described in the following.

3.5.1 Time stepping scheme

For the simulation of problems dealing just with the linear part of the Vlasov equation, Eq. (2.60), two different approaches, namely implicit and explicit time stepping schemes, can be used to determine the time evolution,

$$\frac{\partial g}{\partial t} = \mathcal{V}(t, g(t)). \tag{3.71}$$

While implicit schemes do not impose any stability limit on the time step Δt, they are usually quite expensive in terms of computational effort due to obligatory matrix inversions. Explicit schemes, on the other hand, are only stable for a certain range of possible time steps. Therefore, an iterative sparse matrix solver based on the PETSc [54, 55, 56] and SLEPc [57, 58] packages has been included into Gene [40, 59, 36, 60] to allow amongst others for the determination of the most critical eigenvalue and thus the largest possible linear time step. Details on the implementation as well as discussions of the different approaches can be found in [36].

For nonlinear simulations three different implementations of the Runge-Kutta (RK) scheme are available, in particular RK of third and fourth order and a modified version of the latter. In this thesis, most of the simulations were performed using the fourth order RK scheme which can be written as

$$g_{n+1} = g_n + \frac{\Delta t}{6}\left(k_1 + 2k_2 + 2k_3 + k_4\right) \tag{3.72}$$

with $t_{n+1} = t_n + \Delta t$, $g_n = g(t_n)$ and

$$\begin{aligned} k_1 =& \mathcal{V}(t_n, g_n), \\ k_2 =& \mathcal{V}(t_n + \Delta t/2, g_n + k_1 \Delta t/2), \\ k_3 =& \mathcal{V}(t_n + \Delta t/2, g_n + k_2 \Delta t/2), \\ k_4 =& \mathcal{V}(t_n + \Delta t, g_n + k_3 \Delta t). \end{aligned}$$

Taking into account the nonlinearity, namely the $\nabla\xi \times \mathbf{B}$ advection term, might eventually further restrict the time step below the linear limit. This dynamical process is treated by means of an automatic time step adaption using an approximation of the Courant-Friedrichs limit [14]. In case of marginal adjustments due to the advection terms, a modified RK of fourth order using six stencils proves more efficient. However, in most of the simulations presented in this thesis, the time step is strongly decreased below the linear limit which is why the usual RK 4th order is chosen.

3.5.2 Spatial and velocity space derivatives

Provided that a Fourier representation can be chosen, as e.g. always in the y direction, all derivatives can be replaced by

$$\frac{\partial f}{\partial x} \to \mathrm{i}k_x f(k_x) \tag{3.73}$$

without any loss of accuracy. Else, several finite difference schemes are at hand. However, the fourth order centered scheme has been proven to guarantee sufficient accuracy at a reasonable computational effort. Hence,

$$\frac{\partial f}{\partial x} \to \frac{f(x_{(i-2)}) - 8f(x_{(i-1)}) + 8f(x_{(i+1)}) - f(x_{(i+2)})}{12\Delta x}. \tag{3.74}$$

A drawback linked to centered schemes is a possible decoupling of neighboring grid points if boundary conditions turn out to have finite influence throughout the simulation domain. In order to compensate for such effects, additional numerical or *hyper* diffusion terms $\mathcal{H}$ acting on the distribution function $F_{1\sigma}$ have been added to the Vlasov equation. Typically, fourth order derivatives with stencils of second order,

$$\mathcal{H}(F_{1\sigma}) = \eta \frac{-F_{1\sigma}(x_{(i-2)}) + 4F_{1\sigma}(x_{(i-1)}) - 6F_{1\sigma}(x_{(i)}) + 4F_{1\sigma}(x_{(i+1)}) - F_{1\sigma}(x_{(i+2)})}{16}, \tag{3.75}$$

are employed where the input parameter η has been constructed to be independent of resolution. Further details on the implementation and the influence of numerical diffusion terms can be found in [41].

3.5.3 Numerical integration

While spatial integration operations are performed by simply replacing the integrals by sums,

$$\int_{-L_x/2}^{L_x/2} f(x)\,\mathrm{d}x \to \sum_i f(x_{(i)})\Delta x, \tag{3.76}$$

more sophisticated methods are applied to numerically compute the velocity space integrals, e.g. required in Eq. (2.73). In the μ direction, a Gaussian quadrature scheme is used so that Gauß-Legendre knots are used instead of equidistant grid points, and in the $v_\parallel$ direction, a modified trapezoidal scheme is implemented.

3.5.4 The nonlinearity

Nonlinear terms in the Vlasov equation, for instance, $N(x,y) \sim \partial_y \bar{\xi}_1 \partial_x g_{1\sigma}$, would be represented as convolutions in a one- or two-dimensional Fourier space, e.g. in the global

code as

$$\begin{aligned} N(x,k_y) =& \frac{1}{L_y}\int_0^{L_y} \mathrm{d}y\, \mathrm{e}^{-\mathrm{i}k_y y}\, N(x,y) \\ =& \sum_{k_y'} \partial_x \bar{\xi}_1(x, k_y - k_y')\mathrm{i}k_y' g_{1\sigma}(x,k_y'). \end{aligned} \tag{3.77}$$

However, the complexity of the nonlinearity computation is then estimated as $\mathcal{O}(n^2)$, n being the number of operations. A back transform to real space, on the other hand, requires just $\mathcal{O}(n \log n)$, so that the nonlinearity is the only part of the code where a full real space representation is chosen as originally described in Ch. 2. The fast Fourier transformations (FFT) are computed using one of the state-of-the-art numerical libraries, FFTW [61], ESSL [62], or MKL [63].

Anti-aliasing techniques

As can be seen in Eq. (3.77) and Eq. (3.36), various mechanisms exist which couple modes having different wave numbers. Hence, aliasing may occur in discretized schemes if at some point smaller scales than covered by the necessarily finite resolution are reached. In order to avoid the manifestation of aliasing, namely artificial generation of larger scale structures, different techniques have been implemented. In Fourier space, a so-called 3/2 rule can be applied which introduces, for instance, in the radial direction, $N_x/2$ additional modes with vanishing amplitude before back-transforming to real space in order to solve the nonlinearity. Afterwards, they are disbanded again. In real space, aliasing can be avoided either by hyper diffusion or by a real space emulation of the Fourier space anti-aliasing based on interpolation schemes, e.g. Lagrange interpolation [64].

3.6 Observables

GENE comes along with several flavors of output data. The reasons are, on the one hand, the difference in quantities of interest, and, on the other hand, the storage requirements. For instance, the full distribution function is only written out a few times per simulation since it might take up to several 10 GB per entry. The most commonly used diagnostics are thus computing velocity space and/or space moments of the distribution function and hence write out just three-dimensional or one-dimensional data.

A single entry of the NRG output file for example includes for each species the following volume averaged values of the normalized velocity space moments $|\hat{n}_\sigma|^2$, $|\hat{u}_{\parallel,\sigma}|^2$, $|\hat{T}_{\parallel,\sigma}|^2$, $|\hat{T}_{\perp,\sigma}|^2$, $\hat{\Gamma}_{\mathrm{es},\sigma}$, $\hat{\Gamma}_{\mathrm{em},\sigma}$, $\hat{Q}_{\mathrm{es},\sigma}$, and $\hat{Q}_{\mathrm{em},\sigma}$. In more detail, the perturbed density is as before,

cf. Eq. (2.76), given by

$$\hat{n}_\sigma = \frac{n_\sigma}{n_{0\sigma}(x_0)\rho_{\mathrm{ref}}/L_{\mathrm{ref}}} = \hat{M}_{00}, \tag{3.78}$$

and the mean parallel velocity by

$$\hat{u}_{\parallel,\sigma} = \frac{u_{\parallel,\sigma}}{v_{T\sigma}(x_0)\rho_{\mathrm{ref}}/L_{\mathrm{ref}}} = \frac{\hat{M}_{10}}{\hat{n}_{p\sigma}}. \tag{3.79}$$

The perturbed parallel temperature is defined through

$$n_{0,\sigma}T_{\parallel 1,\sigma} = p_{\parallel 1,\sigma} - T_{\parallel 0,\sigma}n_{1,\sigma} = m_\sigma \iiint \left(v_\parallel - u_{1\parallel,\sigma}\right)^2 F_{1\sigma}\mathrm{d}^3v - T_{\parallel 0,\sigma}n_{1,\sigma}, \tag{3.80}$$

see for instance [65]. Keeping only linear terms of perturbed quantities then yields

$$\hat{T}_{\parallel 1,\sigma} = \frac{T_{\parallel 1,\sigma}}{T_{0\sigma}\rho_{\mathrm{ref}}/L_{\mathrm{ref}}} = \frac{2\hat{M}_{20} - \hat{T}_{p\sigma}\hat{M}_{00}}{\hat{n}_{p\sigma}} \tag{3.81}$$

and similarly (with $p_{\perp 1,\sigma} = \frac{m_\sigma}{2}\iiint v_\perp^2 F_{1\sigma}\mathrm{d}^3v$)

$$\hat{T}_{\perp 1,\sigma} = \frac{T_{\perp 1,\sigma}}{T_{0\sigma}\rho_{\mathrm{ref}}/L_{\mathrm{ref}}} = \frac{\hat{M}_{02} - \hat{T}_{p\sigma}\hat{M}_{00}}{\hat{n}_{p\sigma}}. \tag{3.82}$$

The remaining entries are the electrostatic (es) and electromagnetic (em) fractions of the radial particle and heat fluxes. Both are, in principle, given by correlations with the contravariant radial component of the drift velocity

$$\mathbf{v}_D = \mathbf{v}_\xi + \mathbf{v}_{\nabla B_0} + \mathbf{v}_c,$$

compare with Sec. 2.2 except for the additional gyroaverage therein. However, in case of up-down symmetric devices or geometries which possess only weak asymmetries as are presented in this thesis, the $\nabla\xi \times \mathbf{B}$ velocity turns out to be strongly dominant so that additional magnetic field configuration terms can be safely neglected. The radial particle flux Γ is then calculated by

$$\Gamma_\sigma(\mathbf{x}) = \iiint v_\xi^x(\mathbf{x}) F_{1\sigma}(\mathbf{x},\mathbf{v})\,\mathrm{d}^3v \tag{3.83}$$

and the heat flux Q by

$$Q_\sigma(\mathbf{x}) = \iiint \frac{1}{2} m_\sigma v^2 v_\xi^x(\mathbf{x}) F_{1\sigma}(\mathbf{x},\mathbf{v})\,\mathrm{d}^3v \tag{3.84}$$

where

$$v_\xi^x(\mathbf{x}) = \mathbf{v}_\xi(\mathbf{x}) \cdot \nabla x = -\frac{c}{\mathcal{C}}\partial_y \xi_1(\mathbf{x}) \tag{3.85}$$

denotes the contravariant component of the $\nabla\xi \times \mathbf{B}$ velocity. The corresponding normalized versions are then

$$\hat{\Gamma}_\sigma(\mathbf{x}) = \frac{\Gamma_\sigma(\mathbf{x})}{\Gamma_{\mathrm{gB}}} = -\frac{\hat{n}_{0\sigma}(x_0)}{\hat{\mathcal{C}}}\left[\frac{\partial\hat{\phi}_1(\mathbf{x})}{\partial\hat{y}}\hat{M}_{00}(\mathbf{x}) - \hat{v}_{T\sigma}(x_0)\frac{\partial\hat{A}_{1\parallel}(\mathbf{x})}{\partial\hat{y}}\hat{M}_{10}(\mathbf{x}) + \frac{\hat{T}_{0\sigma}(x_0)}{\hat{q}_\sigma\hat{B}_0}\frac{\partial\hat{B}_{1\parallel}(\mathbf{x})}{\partial\hat{y}}\hat{M}_{02}(\mathbf{x})\right] \tag{3.86}$$

and

$$\begin{aligned}\hat{Q}_\sigma(\mathbf{x}) =& \frac{Q_\sigma(\mathbf{x})}{Q_{\mathrm{gB}}} \\ =& -\frac{\hat{n}_{0\sigma}(x_0)\hat{T}_{0\sigma}(x_0)}{\hat{\mathcal{C}}}\left[\frac{\partial\hat{\phi}_1(\mathbf{x})}{\partial\hat{y}}\left(\hat{M}_{20}(\mathbf{x}) + \hat{M}_{02}(\mathbf{x})\right)\right. \\ & \left. -\hat{v}_{T\sigma}(x_0)\frac{\partial\hat{A}_{1\parallel}(\mathbf{x})}{\partial\hat{y}}\left(\hat{M}_{30}(\mathbf{x}) + \hat{M}_{12}(\mathbf{x})\right) + \frac{\hat{T}_{0\sigma}(x_0)}{\hat{q}_\sigma\hat{B}_0}\frac{\partial\hat{B}_{1\parallel}(\mathbf{x})}{\partial\hat{y}}\left(\hat{M}_{22}(\mathbf{x}) + \hat{M}_{04}(\mathbf{x})\right)\right]\end{aligned} \tag{3.87}$$

with $\Gamma_{\mathrm{gB}} = n_{\mathrm{ref}}c_{\mathrm{ref}}\rho_{\mathrm{ref}}^2/L_{\mathrm{ref}}^2$ and $Q_{\mathrm{gB}} = p_{\mathrm{ref}}c_{\mathrm{ref}}\rho_{\mathrm{ref}}^2/L_{\mathrm{ref}}^2$. For some investigations it is helpful to separate the electrostatic and electromagnetic contributions to the total fluxes. Hence, Γ and Q are in this context computed using just the ϕ_1 dependent part of ξ_1 for the former and the remaining part of ξ_1 for the latter.

An often found alternative transport description which shall be briefly mentioned here uses the corresponding diffusivities D_σ and χ_σ which are linked to the fluxes by Fick's first law,

$$\Gamma_\sigma = -D_\sigma\frac{\partial n_{0\sigma}}{\partial x} \qquad \text{and} \qquad Q_\sigma = -n_{0\sigma}\chi_\sigma\frac{\partial T_{0\sigma}}{\partial x}. \tag{3.88}$$

Inverting and normalizing yields

$$\hat{D}_\sigma = \frac{D_\sigma}{D_{\mathrm{gB}}} = \frac{\hat{\Gamma}_\sigma}{\hat{n}_{0\sigma}\hat{\omega}_{n\sigma}} \qquad \text{and} \qquad \hat{\chi}_\sigma = \frac{\chi_\sigma}{\chi_{\mathrm{gB}}} = \frac{\hat{Q}_\sigma}{\hat{n}_{0\sigma}\hat{T}_{0\sigma}\hat{\omega}_{T\sigma}}.$$

with $D_{\mathrm{gB}}, \chi_{\mathrm{gB}} = c_{\mathrm{ref}}\rho_{\mathrm{ref}}^2/L_{\mathrm{ref}}$. However, these definitions are only applicable to circular and concentric geometries. The diffusivities in general geometries are discussed in Appendix B.2.

3.6.1 Global code specific observables

This section is dedicated to a description of observables which are restricted to global codes and which will be employed in a later chapter.

Given a fully developed nonlinear simulation, it is quite common that the fluctuations exhibit fractions being constant on flux surfaces through mode couplings. Therefore,

new temperature and density profiles can be constructed by adding those amplitudes to the background profiles. Although only very small modifications being on the order of $\rho_{\mathrm{ref}}/L_{\mathrm{ref}}$ are implied by the gyrokinetic ordering, it is a worthwhile effort since temperature and density gradients might nevertheless be substantially affected. However, only global codes allow for a consistent investigation since $\rho_{\mathrm{ref}}/L_{\mathrm{ref}}$ is not specified in the local approximation. The according calculation using normalized quantities is given by

$$\hat{T}_\sigma(x) = \hat{T}_{0\sigma}(x) + \langle \hat{T}_{1\sigma}(\mathbf{x}) \rangle_{\mathrm{FS}} \frac{\rho_{\mathrm{ref}}}{L_{\mathrm{ref}}} \qquad \text{and} \qquad \hat{\omega}_{T\sigma}(x) = \frac{L_{\mathrm{ref}}}{L_{T\sigma}} = -L_{\mathrm{ref}} \frac{\partial}{\partial x} \ln \hat{T}_\sigma(x), \tag{3.89}$$

and similarly for the density. For some applications where the modified linear driving terms, $\hat{\omega}_T(x)$ and $\hat{\omega}_n(x)$, are compared with the measured fluxes, additional radial averages are employed which will be discussed on a case by cases basis.

3.7 Sources and sinks

Without any additional source or sink term, an upper limit for the turbulent fluctuations is given by the flattening of the initial temperature and density profiles as described in the previous section. If the corresponding gradients become comparable to the threshold values, the turbulence drive itself is thus strongly reduced so that eventually a state close to marginality is reached. As already mentioned above, local codes circumvent these issues by employing periodic boundary conditions which keep the (average) gradients fixed. Global codes, on the other hand, have to use Dirichlet or floating, von Neumann boundary conditions. In this thesis, only the former is applied in GENE. With this choice, temperature and density fluctuations are forced to vanish at the radial boundaries thus fixing the profiles at these points. A full relaxation which would flatten the whole profile is therefore impossible. However, this is not necessarily a disadvantage since such strong relaxations would violate the gyrokinetic ordering anyway. On the other hand, small profile variations close to the boundaries might generate large gradients and therefore significant fluctuation levels being incompatible with the Dirichlet condition. In order to avoid according numerical instabilities, an artificial damping can be activated. This so-called Krook term is simply added to the right hand side of the normalized Vlasov equation, $\hat{\mathcal{V}}(t, g(t))$, as follows,

$$\frac{\partial \hat{g}_{1\sigma}}{\partial t} = \hat{\mathcal{V}}(t, g(t)) - \hat{\nu}_{\mathrm{Krook}}(x) \hat{g}_{1\sigma}. \tag{3.90}$$

Here, $\hat{\nu}_{\mathrm{Krook}}(x)$ denotes a function being comparable to the maximum linear growth rate at the boundaries but vanishing towards the center of the simulation domain. In this work, a fourth order polynomial decaying to zero within less than 10% of the simulation box width is typically chosen at each boundary.

For some investigations, it is interesting to artificially keep the profile variations on a very low level and study the resulting transport features. An according operator, for instance a Krook operator acting over the whole radial domain but just affecting the zonal components, is currently in development.

However, a physically more relevant application of global codes is to perform flux driven simulations. Here, localized heat or particle sources are employed to model a plasma discharge and predict the temperature and density profiles. This scenario is thus antipodal to the gradient driven simulations where the fluxes are the final products. Given the typically large uncertainties in the experimentally measured gradients which constrain comparisons between simulations and experiments, flux driven simulations provide an interesting alternative. The first steps along those lines have already been taken in GENE. For instance, a rate ν_{src} measured in $c_{\mathrm{ref}}/\rho_{\mathrm{ref}}$, at which heat is coupled into the plasma or removed, is implemented as

$$\frac{\partial \hat{g}_{1\sigma}}{\partial \hat{t}} = \hat{\mathcal{V}}(t, g(t)) + \hat{\nu}_{\mathrm{src}}(x) \left(\frac{\hat{v}_{\parallel}^2 + \hat{\mu}\hat{B}_0}{\hat{T}_{p\sigma}} - \frac{3}{2} \right) \hat{F}_{0\sigma} \tag{3.91}$$

where $\hat{\nu}_{\mathrm{src}}(x)$ is a profile function which is used to localize the heat source, e.g. by means of a Gaussian. The particle number conservation is ensured by the property

$$\hat{\nu}_{\mathrm{src}}(x) \int \left(\frac{\hat{v}_{\parallel}^2 + \hat{\mu}\hat{B}_0}{\hat{T}_{p\sigma}} - \frac{3}{2} \right) \hat{F}_{0\sigma} \mathrm{d}\hat{v}_{\parallel} \mathrm{d}\hat{\mu} = 0 \tag{3.92}$$

which can easily be confirmed analytically.

3.8 Chapter summary

The aim of the present chapter was to familiarize the reader with the implementation and concepts of the two main branches used for gyrokinetic simulations. While the *local* approach, where just a very narrow radial region about a central magnetic field line is considered, has originally been the only option in GENE, it is now substantially supplemented by a global approach keeping full radial profile information. Due to the enormous conceptual and structural changes, a joint effort including several people at CRPP, Lausanne, and IPP, Garching, has been made to implement these nonlocal effects. In the course of this work several main modifications, amongst others the implementation of the density, temperature and metric profile terms throughout the whole code, the transformation of the linear part of the Vlasov equation into direct (x) space as well as the global version of the parallel boundary condition, have been contributed.

Tests and benchmarks demonstrating the full operability of the newly developed global code will be shown separately in Chapter 5.

Chapter 4

Multiscale simulations

4.1 Introduction

A large variety of modes involving a wide range of space and time scales may potentially contribute to the heat and particle transport in magnetically confined fusion plasmas. However, simulations covering all scales involved turn out to be beyond the scope of today's supercomputing resources. As a remedy, turbulence modes on different scales are often assumed to be decoupled so that investigations of modes e.g. on the ion gyroradius scale become feasible. In this chapter, though, one of the first efforts of self-consistently simulating spatio-temporally separated turbulence modes, in part published in Refs. [66, 67], is presented. Core turbulence is investigated employing parameters at which trapped electron modes (TEM) as well as ion and electron temperature gradient (ITG/ETG) modes – the latter being separated in space and time by the square root of the ion-to-electron mass ratio – are excited. Besides insights into the cross-scale couplings and interactions, these simulations support former predictions about the significance of electron temperature gradient driven modes even in the presence of turbulent, long wavelength fluctuations.

This chapter is organized as follows. At the beginning, previous findings concerning the role of electron scale microturbulence are reviewed. Afterwards, detailed descriptions of the parameter sets employed in the multiscale simulations are given. First physical insights and optimizations of the numerical parameters are discussed on the basis of linear simulations and secondary instability analyses. Nonlinear results, in particular heat and particle fluxes as well as density and frequency spectra, are presented hereafter. Finally, possible extensions of these findings to other physical situations are discussed.

4.1.1 Historical context

Usually, turbulent transport in magnetic fusion devices is thought to be carried mainly by long-wavelength modes, $k_\perp \rho_s < 1$, where the main agents driving turbulent fluctuations in the core region at moderate plasma β are considered to be the ion temperature gradient

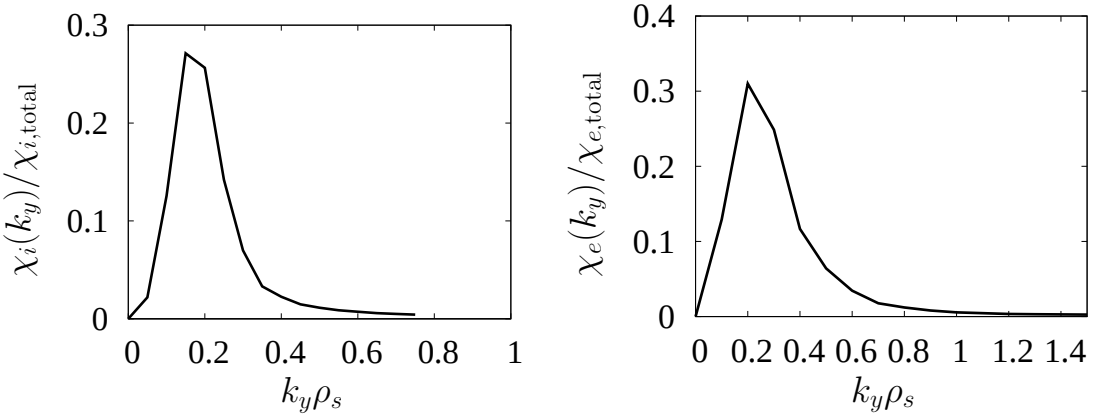

Figure 4.1: Binormal thermal diffusivity spectra for ITG modes with adiabatic electrons (left) and TEM turbulence with kinetic ions. Here, both spectra are normalized to the corresponding total values.

and the trapped electron mode, while in the edge region, other microinstabilities like electron drift waves or resistive ballooning modes may also contribute [68, 69].

Typically, the involved mode numbers peak around $k_\perp \rho_s \approx 0.2$, as is exemplarily illustrated in Fig. 4.1. Larger wave numbers, in particular $k_y\rho_s \gg 1$, have in the past mostly been considered to be negligible. Besides experimental and numerical problems which hampered the investigation and therefore any detailed judgment on the role of such sub-ion scales, it was due to estimates like the mixing length argument which kept this assumption alive. In the following, a brief introduction of the latter will be given.

Mixing length estimate

An intuitive but rather simplifying way of estimating the thermal transport produced by plasma micro-turbulence is based on the mixing length argument. Here, the formation of turbulent eddies with radial extent w_x in collisionless plasmas is considered. Assuming magnetic fluctuations to be negligible, particles are predominantly convected by the (electrostatic) $\mathbf{E} \times \mathbf{B}$ velocity, thus following more or less the contour lines of the eddy structures. Hence, their maximum radial excursion is limited by the radial eddy width. However, propagating in time, the eddies start to dissolve again, e.g., by breaking up into smaller eddies. An upper limit for the diffusivities can therefore be estimated if the associated time scale is of the order of the plasma particle drift time taken from the inward eddy side to the outboard side so that a radial distance w_x is crossed during a time τ. Applying a random walk argument to the homogeneous and isotropic limit of the heat equation then yields $\chi \sim w_x^2/\tau$. If furthermore τ is assumed to be of the order of the inverse drift frequency $\omega_{D\sigma}$, and $w_x \sim \rho_\sigma$ where σ denotes the species index as

before, the heat diffusivity is given by $\chi_\sigma \sim \omega_{D\sigma}\rho_\sigma^2$ or

$$\begin{aligned}\chi_\sigma \sim& \frac{v_{th,\sigma}^2}{\Omega_\sigma}\frac{k_\perp}{L_\perp}\rho_\sigma^2 \\ \sim& \frac{\rho_\sigma}{L_\perp} v_{th,\sigma}(k_\perp\rho_\sigma)\rho_\sigma \\ \sim& \frac{\rho_\sigma^2 v_{th,\sigma}}{L_\perp}\end{aligned} \tag{4.1}$$

if $k_\perp\rho_\sigma \sim \mathcal{O}(1)$, $v_{th,\sigma} = \sqrt{T_{0\sigma}/m_\sigma}$, and the drift frequency can be replaced by the modulus of the diamagnetic drift frequency which can be derived using fluid models, see for instance Refs. [49, 14]. The latter includes the perpendicular gradient lengths which are for the present consideration assumed to be of the same order ($L_\perp \sim L_{T\sigma} \sim L_n \sim R_0$).

The final result $\chi_{\mathrm{gB}}^{(\sigma)} = \rho_\sigma^2 v_{th,\sigma}/L_\perp$ is often referred to as gyro-Bohm diffusivity, see e.g. Ref. [48], since it differs from the result derived by D. Bohm, E.H.S. Burhop, and H. Massey in 1946 (according to Ref. [11]) by an additional gyroradius-to-macroscopic-length ratio, $\rho_\sigma/L_\perp$. A direct comparison of independent ion and electron scale turbulence by means of the gyro-Bohm diffusivity yields

$$\begin{aligned}\chi_i/\chi_e \sim& \chi_{\mathrm{gB}}^{(i)}/\chi_{\mathrm{gB}}^{(e)} \\ =& \frac{1}{Z_i^2}\sqrt{\left(\frac{T_{0i}}{T_{0e}}\right)^3 \frac{m_i}{m_e}}\end{aligned} \tag{4.2}$$

which would imply $\chi_i \gg \chi_e$ for typical plasma parameter regimes where the square root of the cubic temperature ratio and the squared ion charge number Z_i seldom compensate the square root of the mass ratio. For example, the latter evaluates at least to $\sqrt{m_i/m_e} \gtrsim \sqrt{m_p/m_e} \approx 42.85$ whereas $Z_i \sim 1$ and $T_{0i} \sim T_{0e}$ for plasma core parameters.

The mixing length argument is supported by the gyrokinetic theory in the primitive case where only linear and electrostatic terms and either adiabatic electrons (ae) or adiabatic ions (ai) are considered. In that limit, both field equations, Eq. (2.91) and Eq. (2.87) in Sec. 2.4.1, become invariant under exchanges of the species index since the additional flux surface average ($k_y = 0, k_\parallel = 0$) in the adiabatic electron Poisson equation is linearly irrelevant. A similar argument holds for the Vlasov equation which differs just by the species index. Hence, a linear description of electrostatic ITG-ae and ETG-ai mode driven turbulence is identical except for the reference species which can be seen as a justification of Eq. (4.2).

However, there is strong experimental evidence, e.g. in Refs. [70, 71, 72, 73], that the standard paradigm of insignificant transport drive at small (electron gyroradius) scales cannot capture the behavior of heat transport in the electron channel in a number of important situations. These include, in particular, plasmas with internal or edge transport barriers. Here, the question arises which mechanism sets the residual anomalous

electron thermal transport level inside a barrier, assuming that the turbulence at long wavelengths is suppressed by equilibrium $\mathbf{E}\times\mathbf{B}$ shear flows and that the ions are basically neoclassical [74, 75, 76]. Moreover, discharges with strong electron heating may also exhibit a decoupling of ion and electron heat transport which is best explained in terms of scale separation. For instance, it was found in recent DIII-D experiments that by adding electron cyclotron resonance heating, the long-wavelength dynamics (density fluctuation level) and the ion heat flux remain more or less unchanged while the short-wavelength dynamics at $k_\perp \rho_s \sim 4 - 10$ is strongly enhanced, accompanied by a substantial increase in the electron thermal diffusivity [72]. Furthermore, a detailed investigation of electron space and time scales has been carried out in NSTX which can be considered as first experimental proof of ETG modes driving turbulent transport [77].

In view of future fusion reactors where the α particles will mainly heat the electrons, theory and simulation are thus confronted with assessing the role of the spectral region $k_\perp \rho_s \gg 0.2$, in particular for electron thermal transport.

Early gyrokinetic simulations of electron temperature gradient driven turbulence [37, 78, 79] – mostly (although not exclusively) employing the adiabatic ion approximation and neglecting magnetic trapping – indicated that despite their small spatio-temporal scales, ETG modes can induce electron thermal diffusivities which clearly exceed the previously mentioned, naïve expectations, $\chi_e \gg \rho_e^2 v_{te}/L_{Te}$.

The reason for this is, as mentioned before, the symmetry breaking term in the Poisson equation, or, more specifically, the flux surface averaged potential. This subtle difference greatly influences the turbulent structure formation as can be seen in Fig. 4.2. While ITG and ETG mode structures agree qualitatively in the initial simulation phase where nonlinear terms are subdominant, they become quite distinguishable as soon as those terms gain importance. In particular, the ITG mode is strongly influenced by zonal flows, i.e. shear flows with $k_y = 0$ and $k_\parallel = 0$. ETG modes, on the other hand, still form radially elongated structures, so-called streamers, which allow for higher transport levels in the corresponding directions.

Thus, ETG turbulence has become a serious candidate for explaining experimental findings like the ones described above. In follow-up gyrokinetic work [80, 81, 44, 82, 83] that included magnetic trapping, this basic scenario was confirmed, but it also became clear that it can be hard to achieve saturation in adiabatic ion models. Moreover, one is even lead to question the validity of the resulting framework since in the long-wavelength limit, ETG modes often transition smoothly into TEMs which, in turn, extend down to the ion scales. However, these modes are not treated correctly in the adiabatic ion approximation – and ITG modes are excluded altogether. Consequently, what is really called for are nonlinear gyrokinetic simulations in which both electron and ion spatio-temporal scales are covered self-consistently. Pioneering work along these lines was reported in Ref. [84], where it was found that by employing edge-like parameters,

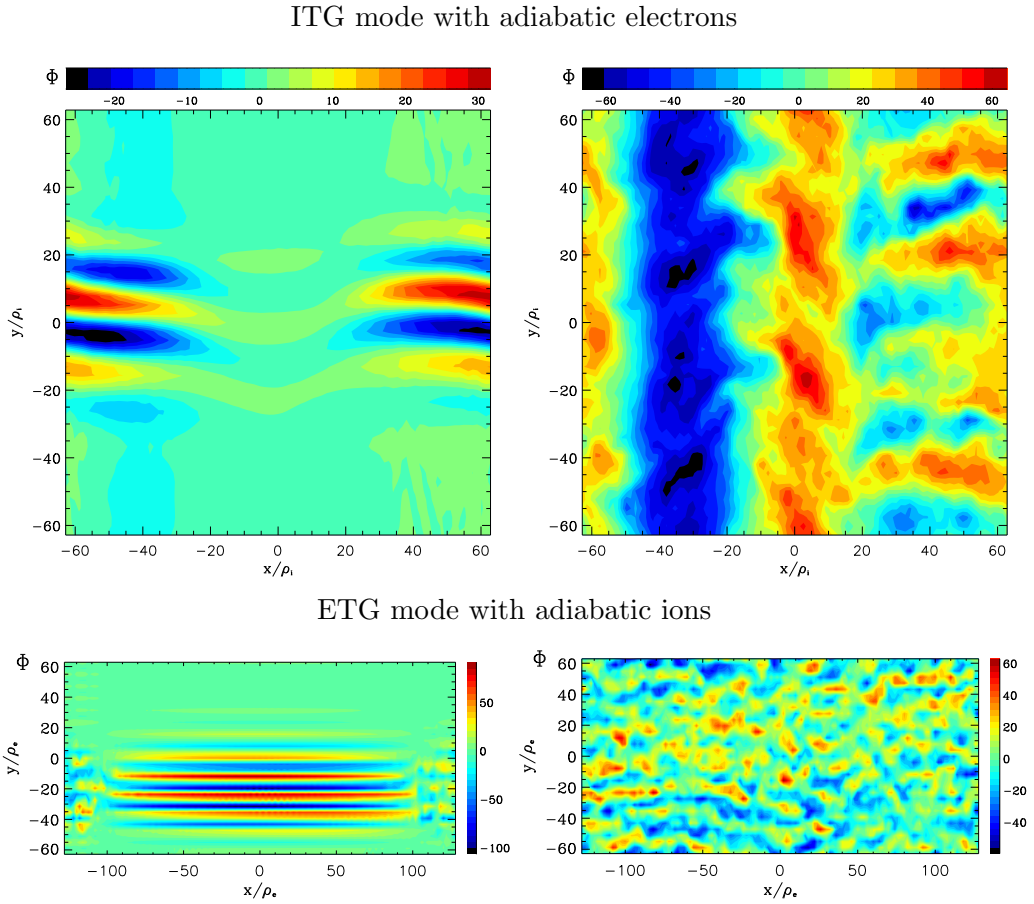

Figure 4.2: Contour plots of the electrostatic potential at the outboard midplane for ITG-ae (upper half, with axes normalized to ρ_i) and ETG-ai (lower half, with axes normalized to ρ_e), each at two different times. The first snapshots (left) are taken during the linear phase at the beginning of the simulation, the second ones (right) in the quasi-stationary state where nonlinear terms are involved, as well.

ETG-induced electron thermal transport is capable of setting a base level in the H-mode pedestal region. On the other hand, there have been similar studies for core parameters recently, exhibiting only small relative high-k contributions [85]. As shall be demonstrated below, the low-k drive in these simulations has been unrealistically strong, however. In contrast to that, the results presented in this thesis will show that for realistic ion heat (and particle) flux levels and in the presence of unstable ETG modes, there tends to be a scale separation between electron and ion thermal transport, i.e., the former may exhibit substantial or even dominant high-k contributions.

4.2 Simulation details

The physical and numerical parameters chosen in these investigations are detailed in the present section. In order to avoid too many effects which have an impact on the turbulent systems under investigation that would needlessly complicate a subsequent interpretation and cause significantly more computational effort, magnetic field fluctuations and collisions are neglected in the following study even though GENE is able to include them. Furthermore, all simulations are performed in $\hat{s}$-α geometry with $\alpha = 0$, consistent with the electrostatic limit $\beta \ll 1$ which allows for employing a relatively moderate number of grid points in the parallel direction. Most physical parameters correspond to the so-called Cyclone Base Case (CBC) [43], i.e., $q_0 = 1.4$, $\hat{s} = 0.8$, $\epsilon = r/R_0 = 0.18$, $n_{0i} = n_{0e} \equiv n_0$, and $T_{0i} = T_{0e} \equiv T_0$ are employed. The density and temperature gradients are varied, however, with the basic settings being

(A) $R_0/L_{Te} = 6.9$, $R_0/L_{Ti} = 6.9$, $R_0/L_n = 2.2$,

(B) $R_0/L_{Te} = 6.9$, $R_0/L_{Ti} = 5.5$, $R_0/L_n = 0$,

(C) $R_0/L_{Te} = 6.9$, $R_0/L_{Ti} = 0$, $R_0/L_n = 0$.

The first choice (A) represents an expansion of the CBC parameter set to two species. It serves as a starting point and – as it turned out during this work – as an extended benchmark case since Waltz et al. [85] picked the same case.

Choosing the numerical parameters is a much more delicate task than setting the physical ones, since the former strongly depend on the latter. As will be shown later, it is virtually impossible to perform numerical convergence tests – i.e., checking the resolution by increasing the number of grid points – with today's computer resources for the multiscale simulations at hand. Therefore, careful investigations of the presumably required grid sizes and resolutions are called for in advance.

For this purpose, two approaches prove to be helpful. On one hand, linear simulations give first insights regarding the minimum settings and the physics to be expected for the physical parameters. On the other hand, experience with single-scale simulations may be utilized.

4.2.1 Linear results

Typically, linear investigations focus on the linear growth rate and real frequency of the dominant eigenmode at each binormal mode number k_y. For the smallest realistic ion to electron mass ratio $m_i/m_e = m_p/m_e \approx 1836$ these results are shown in Fig. 4.3.

Here, two (local) growth rate maxima can clearly be distinguished in case (A) where equally steep electron and ion gradients are specified. The first one is close to $k_y\rho_s = 0.35$ and is linked to a positive frequency, whereas the second is larger by a factor of ≈ 23,

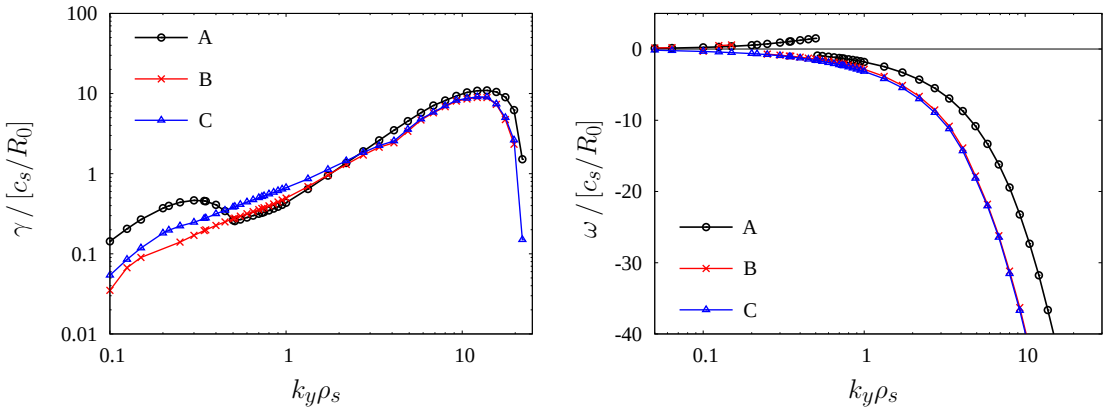

Figure 4.3: Linear growth rates (left) and real frequencies (right) vs. binormal wave number using a proton-electron mass ratio and (A) $R_0/L_{Ti} = R_0/L_{Te} = 6.9$, $R_0/L_n = 2.2$, (B) $R_0/L_{Ti} = 5.5$, $R_0/L_{Te} = 6.9$, $R_0/L_n = 0$, and (C) $R_0/L_{Ti} = 0$, $R_0/L_{Te} = 6.9$, $R_0/L_n = 0$.

has a negative real frequency, and is found at $k_y\rho_s \approx 14$ which translates to $k_y\rho_e \approx 0.325$ on electron scales. Although all these findings strongly support an identification of the respective modes as ITG and ETG modes, they do not reflect a perfect isomorphy as has been previously predicted. However, the simulations presented in this section do consider kinetic electrons throughout the whole wave number range. Thus, e.g. the presence of trapped electrons will affect the ITG modes and also lead to trapped electron modes. The existence of the latter can be confirmed either by running the eigenvalue solver within GENE which will be done at a later point or simply by observing the jump in frequency at $k_y\rho_s \approx 0.5$. Since pure ETG modes are not driven at $k_y\rho_e \sim 0.01$, the most likely explanation of a mode propagating in electron diamagnetic drift direction is a TEM becoming dominant. However, following the real frequency to higher wave numbers into the ETG mode domain, no additional significant jump or change of slope can be observed. On the other hand, it is evident that TEMs cannot drive the very high-k turbulence since frequencies beyond the bounce frequency $\omega_b \sim v_{th,e}\sqrt{\epsilon}/(qR_0)$ are virtually impossible for these modes. Evaluating the intersection with linear fits of the actually measured real frequency in Fig. 4.3 thus yields an upper wave number limit of $k_y\rho_s \approx 6.5$. Therefore, a TEM/ETG mode transition must take place for physical reasons but seems to be unverifiable in terms of eigenvalues for the chosen parameters. Such scenarios of smoothly transitioning and thus indistinguishable modes have recently been found for several plasma microinstabilities [40] if the physical parameters are chosen close to exceptional points on the eigenvalue surface. The latter do exist due to the non-Hermiticity of the linear gyrokinetic operator [36].

Lowering the ion temperature gradient to 5.5 as done in parameter set (B) mainly affects the ITG modes. Although still being dominant or marginally subdominant at

large scales, the transition to TEM takes place earlier, and a corresponding maximum in growth rate is barely visible. The modified behaviors of growth rate and frequency at intermediate to high wave numbers is caused by the assumption of flat density profiles which has been introduced for simplicity.

Setting (C) $R_0/L_{Ti} = 0$ in a last step completely removes any ITG mode so that the TEM-ETG hybrid mode governs ion as well as electron scales.

4.2.2 Numerical parameters for nonlinear multiscale runs using a realistic mass ratio

Based on these results, some requirements for nonlinear box and grid parameters can be derived. A rough estimate for one of the most important quantities, the heat transport Q, can e.g. be given using a simple quasi-linear transport model [38] where $Q \propto Q^{(ql)} = \gamma/\langle k_\perp^2 \rangle$. Considering just $k_x = 0$, which is typically the dominant radial wave number, and furthermore the s-α metric derived in Eq. (3.21), allows for replacing $\langle k_\perp^2 \rangle$ by $\langle k_\perp^2 \rangle \approx (1 + \hat{s}^2 \langle z^2 \rangle) k_y^2$. Here, $\langle \ldots \rangle$ denotes an average defined by $\langle z^2 \rangle = \int z^2 \phi(k_y, z) \mathrm{d}z / \int \phi(k_y, z) \mathrm{d}z$, which takes into account the parallel mode structure [38, 14, 36]. The resulting heat flux estimates are presented in Fig. 4.4. Since a

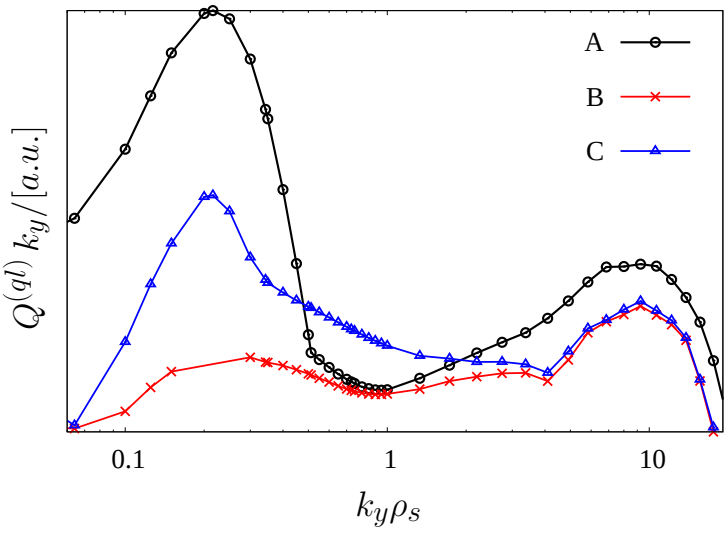

Figure 4.4: Estimated heat transport contributions obtained with a simple quasi-linear model for the parameter sets (A) $R_0/L_{Ti} = R_0/L_{Te} = 6.9$, $R_0/L_n = 2.2$, (B) $R_0/L_{Ti} = 5.5$, $R_0/L_{Te} = 6.9$, $R_0/L_n = 0$, and (C) $R_0/L_{Ti} = 0$, $R_0/L_{Te} = 6.9$, $R_0/L_n = 0$.

logarithmic abscissa is used to facilitate a better overview of ion and electron scale contributions, a somewhat unconventional but helpful way to display the data is introduced. While the usual log-log plots can be misleading since the area underneath a curve has no direct physical meaning, plotting $k_y Q^{(ql)}(k_y)$ vs. k_y on a log-lin scale circumvents

this problem. In more detail, contributions of certain mode ranges, usually given by $Q \sim \sum_{k_y} Q(k_y)\Delta k_y$, can also be expressed in terms of $Q \sim \sum_{k_y} Q(k_y) k_y \Delta(\log k_y)$, if a logarithmic scaling is used.

The results shown in Fig. 4.4 would imply that the binormal box size and resolution should be chosen at least such that $k_y^{\min}\rho_s \approx 0.05$ and $k_y^{\max}\rho_s \approx 20$. However, nonlinear single-scale ETG simulations performed in the context of this work, see Fig. 4.5, and

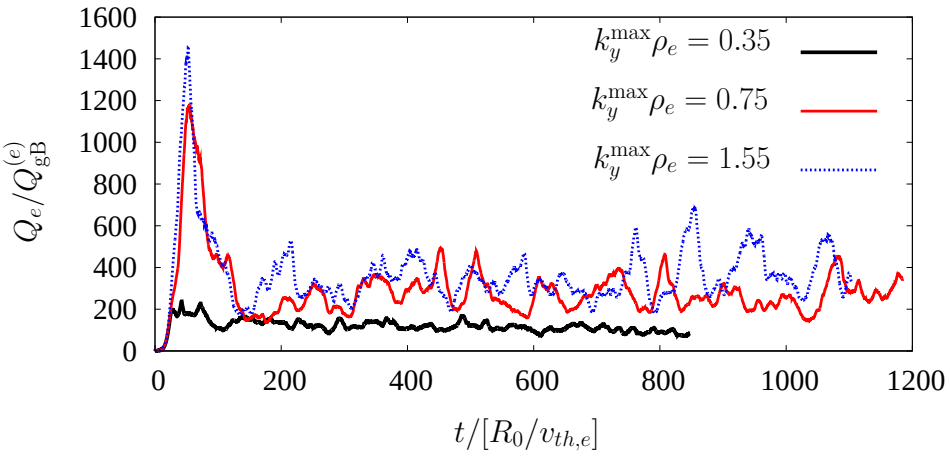

Figure 4.5: Electron heat flux resulting from single-scale simulations restricted to $0.05 \leq k_y\rho_e \leq k_y^{\max}\rho_e$ using parameter set (A) and a reduced mass ratio of $m_i/m_e = 400$. Clearly, a resolution of $k_y^{\max}\rho_e = 0.35$ underestimates the ETG driven electron heat transport.

an ETG benchmarking effort [44] both revealed a significant underestimation of ETG driven transport in that case. Instead, an appropriate binormal resolution is given by $k_y^{\max}\rho_e \sim 1$ which translates to $k_y^{\max}\rho_s \sim 42$ for the proton-to-electron mass ratio.

The required radial resolution can be determined by looking at the ballooning representation of the linear modes which takes into account the connections of radial wave numbers as described by Eq. (3.36). Only if the modes are sufficiently small when reaching the highest wave numbers, they can be considered to be physical. While linear GENE simulations can be performed using $\mathcal{N} = 1$ – i.e., connecting each k_x mode for each k_y independently – a nonlinear simulation will unavoidably have a fixed box size and thus $\mathcal{N}(k_y) = \mathcal{N}(k_y^{\min}) \cdot k_y/k_y^{\min}$, cf. Sec. 3.3.3. Hence, if ballooning structures would keep their shape over wide binormal mode ranges, an enormous radial resolution would be necessary. However, toroidal ITG and ETG modes evolve mainly at the tokamak outboard mid-plane where curvature and gradients point in the same direction, which is typically accompanied by narrow ballooning. Trapped particle modes, however, usually develop wider structures and/or several peaks since motion along the field line is strongly hampered. In summary, one would expect broad ballooning at low-k where TEM is dominantly or sub-dominantly present and narrow structures at high-k where

ETG modes are exclusively driving the turbulence. These predictions are supported by Fig. 4.6 where the linear mode structures of the parameter sets under investigation are plotted. Here, the most demanding modes require up to 16 connections and are located at $k_y\rho_s \approx 0.8$, a region where TEMs are typically excited. At high-k, two or less connections seem to be sufficient, being in line with TEMs vanishing at $k_y\rho_s \gtrsim 6.5$ as has been shown earlier.

Ion temperature gradient driven turbulence is known to exhibit strong zonal flow components which might completely dominate the turbulent structure formation if electrons are assumed to be adiabatic, cf. Fig. 4.2. In the presence of kinetic electrons, zonal flows might still break up linear streamers but may also develop more isotropic vortices. Hence, a quadratic box size of $(L_x, L_y) = (128\rho_s, 128\rho_s)$ may be considered a standard choice. However, taking $(L_x, L_y) = (64\rho_s, 64\rho_s)$ is still a reasonable choice if deviations of about 10 percent in the low-k transport channels are acceptable.

Based on the arguments presented above, the following numerical parameters should be chosen: $k_y^{\min} = 0.1, k_y^{\max} = 42$, L_x should be close to $64\rho_s$ but also has to fulfill the quantization constraint $L_x = \mathcal{N}/(\hat{s}k_y^{\min})$, Eq. (3.36). Hence, with $\mathcal{N} = 5$, L_x becomes $62.5\rho_s$. In order to allow for 16 parallel connections at $k_y\rho_s = 1$, at least $n_{k_x} = \mathcal{N}{\cdot}16{\cdot}10 = 800$ radial mode numbers are necessary. If one was to request at least one connection at $k_y^{\max}$, $n_{k_x} = \mathcal{N} \cdot 2 \cdot 420 = 4200$ modes would be required which is far more demanding. A more careful analysis of the growth rates close to the ETG peak on the other hand reveals modifications of just 10% if no connections are considered, thus justifying the above choices.

Adding the remaining dimensions as used in the aforementioned linear simulations yields a minimum grid of $(x, y, z, v_\parallel, \mu) \approx (800, 400, 16, 32 - 64, 8 - 16)$ for each species. Considering in addition the fast (parallel) electron dynamics which strongly reduce the time step and on the other hand the relatively slow ion dynamic which has to be resolved as well, a computational resource requirement of $3,000,000$ standardized CPUh can be estimated per simulation which clearly exceeds present-day project budgets. Thus, alternative and cheaper numerical parameters have to be found which leave the main physical effects untouched.

4.2.3 Reduced ion/electron mass ratio

A very important parameter which would immediately allow to significantly reduce the computational effort is the ion-to-electron mass ratio which governs the separation of ion and electron scales. Considering the temporal and the perpendicular spatial dimensions whose resolutions scale with the square root of the mass ratio, a total scaling of the computational time $T \sim (m_i/m_e)^{3/2}$ can be estimated.

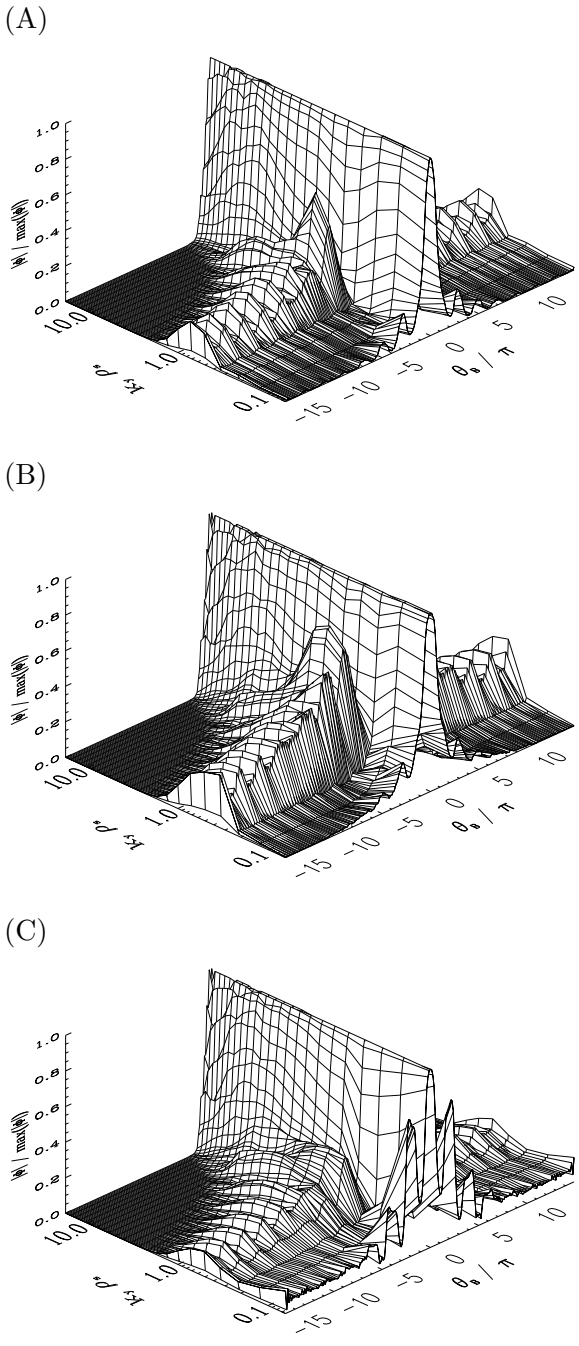

Figure 4.6: Ballooning mode structures gained from linear simulations using the parameter sets (A),(B), and (C). Here, the radial box size has been adapted in order to establish $\mathcal{N} = 1$ in Eq. (3.36) for each k_y mode. Obviously, the mode structure tends to be very narrow at high wave numbers so that less connections are required in this regime.

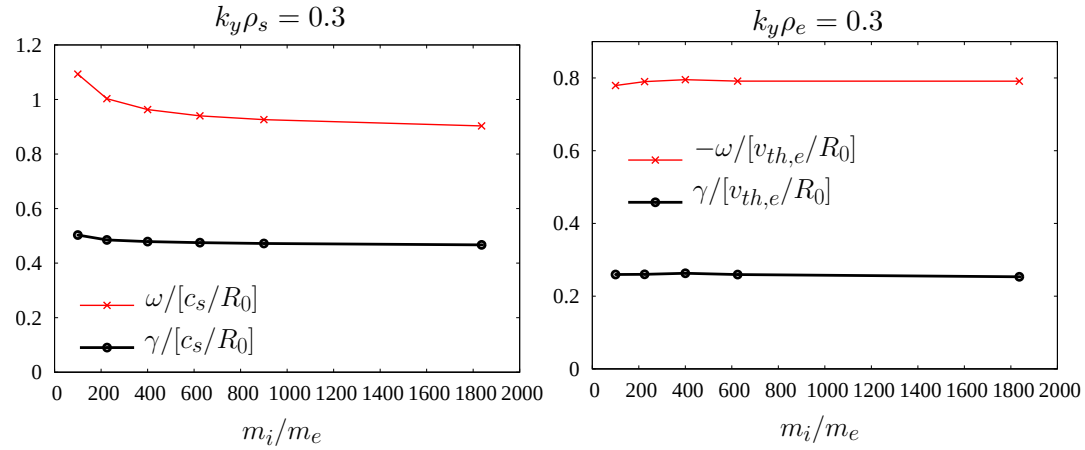

Figure 4.7: Mass ratio dependence of linear growth rates (black) and real frequencies (red) at $k_y\rho_s = 0.3$ (left) and $k_y\rho_e = 0.3$ (right) for parameter set (A).

Mass ratio effects on linear behavior

Again, linear simulation results shall serve as an indication for the determination of a still reasonable mass ratio. The intermediate wave number region between ion and electron scales is certainly affected since time and perpendicular scales are squeezed together with decreasing mass ratio. Therefore, TEM, for instance, become stable at $k_y\rho_s \gtrsim 2.5$ already. However, it is of special interest whether the fully developed ETG and TEM/ITG modes, e.g. the growth rate maxima for parameter set (A), itself are affected. A corresponding plot is therefore presented in Fig. 4.7 which proves ITG/TE modes on ion scales and ETG modes on electron scales to be quite robust against scale compressions. Only at mass ratios smaller than 400, differences of more than 10% can be observed.

Nonlinear saturation mechanisms

Investigating the influence of mass ratio changes on the linear behavior is only a first step. A more detailed prediction can be given if nonlinear saturation mechanisms are taken into account.

In various publications, e.g. in [78, 37, 86] and references therein, the nonlinear saturation of ITG and ETG modes is discussed in the framework of secondary instability theory. The main idea, originally proposed by Cowley et al. [48], is described below.

Driven by radial density and temperature gradients, a linear mode grows exponentially, developing radially elongated structures, cf. Fig. 4.2. Now, if a sufficiently large amplitude is reached, those streamers may in turn generate steep gradients in the binormal (y) direction, thus being a source of free energy for new instabilities. Another way to understand possible actions of the nonlinear terms is to liken them to Kelvin-Helmholtz

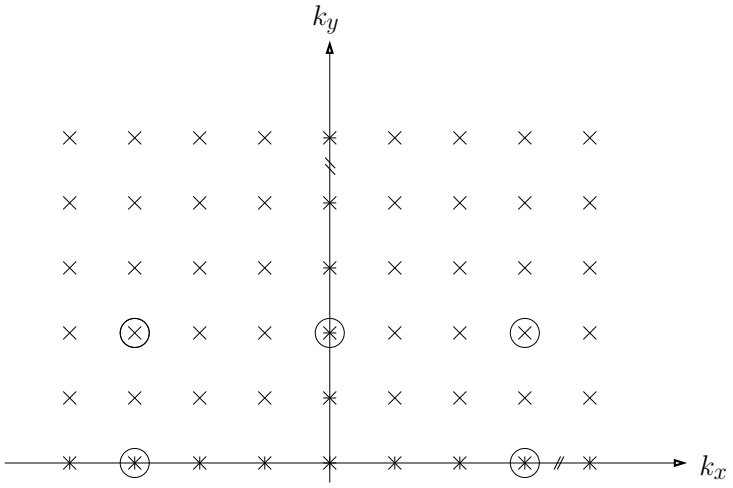

Figure 4.8: Illustration of selected modes (encircled) for secondary instability analysis. Effectively, only four modes are considered since real valued physical quantities fulfill $\phi(\mathbf{k}) = \phi^*(-\mathbf{k})$ in Fourier space.

[87, 88] instabilities. Advected by the $\mathbf{E} \times \mathbf{B}$ velocity, particles drift around streamers of the electrostatic potential and thus form oppositely directed flows above and below an eddy. As it is well known from fluid turbulence or atmospheric physics, such neighboring flow layers with different velocities turn out to be susceptible to small perturbations and are therefore eventually weakened.

In general, saturation is thought to be achieved if the growth rates of primary and secondary instabilities are balanced quasi-stationarily. However, the nonlinear dynamics are far from being fully understood. For example, it may even be possible that secondary instabilities are subject to tertiary instabilities [89]. Nevertheless, several simple models have been proposed to capture the most important effects and thus estimate the transport levels for specific parameter sets [79].

One of these reduced descriptions is derived in the framework of a simple Hasegawa-Mima type fluid model [90, 91, 92]. Here, it has indeed been shown that the saturation amplitude is determined by a balance between the streamer's linear growth rate γ_l and the secondary mode's nonlinear growth rate γ_{nl}. For this purpose, only few modes need to be considered: a streamer mode ϕ_b with $(k_x, k_y) = (0, b)$, two sidebands $\phi_\pm$ with $(a, \pm b)$, and a zonal flow ϕ_0 with $(k_x, k_y) = (a, 0)$, as plotted in Fig. 4.8. As shown in Ref. [86], adding more side bands to the fluid model description does not alter the basic findings.

In order to apply the Hasegawa-Mima type model to nonlinear gyrokinetics, the following steps have been performed. As in Ref. [46], where as spin-off of this work a gyrokinetic secondary instability analysis was applied to stellarators for the first time,

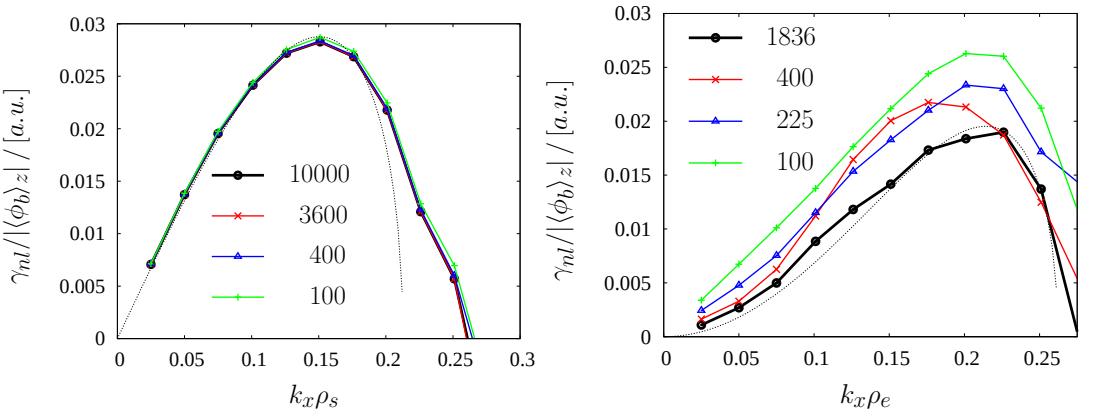

Figure 4.9: Nonlinear (secondary) growth rate γ_{nl} averaged and weighed by amplitude in the parallel direction and divided by the streamer amplitude $|\phi_b| = |\langle\phi_1(k_y\rho_{s,e} = 0.3)\rangle_{x,z}|$. Here, the same parameters as in multiscale simulation (A) have been employed — except for the magnetic shear which has been set to zero. The left plot displays the result on ion scales where $b = k_y\rho_s = 0.3$ has been used. On the opposite site $b = k_y\rho_e = 0.3$ thus showing the response on electron scales. The numbers in the legend indicate the ion to electron mass ratio and the dotted lines are fits as further explained in the text.

the initial condition is chosen to be the result of a preceding linear simulation where only the streamer mode was (strongly) excited. To avoid a mixing of linear and nonlinear effects, the former are suppressed in the nonlinear continuation. Furthermore, nonlinear back couplings to the streamer mode are switched off so that this mode stays constant in time to emulate the large amplitude behavior throughout the whole simulation. The normalized binormal mode number b is chosen close to the fastest growing linear modes, in particular $b = k_y\rho_s = 0.3$ for an ion scale investigation and $b = k_y\rho_e = 0.3$ for a corresponding electron scale simulation. The resulting nonlinear growth rates at $k_y = 0$ are shown in Fig. 4.9 as functions of the radial wave number k_x. Here, the same parameters as for multiscale simulation (A) have been employed —except for the magnetic shear which has been set to zero and the mass ratio which is varied. The former choice is due to a greater flexibility for k_x values and in order to facilitate comparisons with two-dimensional fluid model predictions. For instance, F. Jenko [92] proposes a nonlinear growth rate of

$$\gamma^2_{nl,\mathrm{ITG}} = \frac{2a^2b^2(1+b^2-a^2)}{1+a^2+b^2}|\phi_b|^2 - \Delta\Omega^2 \tag{4.3}$$

for ITG modes and

$$\gamma^2_{nl,\mathrm{ETG}} = \frac{2a^4b^2(b^2-a^2)}{(1+a^2)(1+a^2+b^2)}|\phi_b|^2 - \Delta\Omega^2 \tag{4.4}$$

for ETG modes where $\Delta\Omega$ is a frequency mismatch that is small compared to $|\phi_b|^2$. Fits to $\gamma^2_{nl,\mathrm{ITG}}(a) \sim c_1a^2 + c_2a^4$ and $\gamma^2_{nl,\mathrm{ETG}}(a) \sim d_1a^4 + d_2a^6$, assuming $p^2, q^2 \ll 1$ and

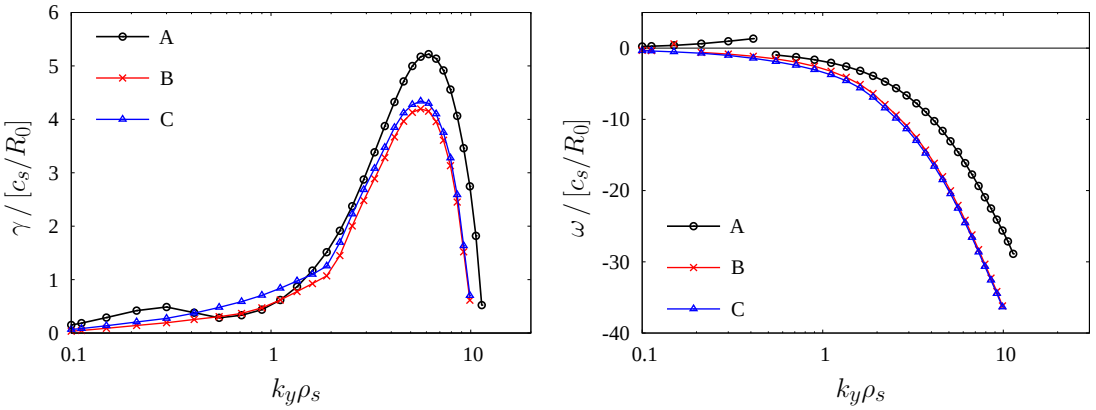

Figure 4.10: Converged linear growth rates (left) and real frequencies (right) vs. binormal wave number using a mass ratio of $m_i/m_e = 400$ and (A) $R_0/L_{Ti} = R_0/L_{Te} = 6.9$, $R_0/L_n = 2.2$, (B) $R_0/L_{Ti} = 5.5$, $R_0/L_{Te} = 6.9$, $R_0/L_n = 0$, and (C) $R_0/L_{Ti} = 0$, $R_0/L_{Te} = 6.9$, $R_0/L_n = 0$.

$c_1, c_2, d_1, d_2 \in \mathbb{R}$, are included as thin, dotted lines for one specific mass ratio in Fig. 4.9 and show good agreement.

Summarizing, the mass ratio seems to have no major influence on secondary instabilities on ion scales. This finding slightly changes on electron scales. If the maximum nonlinear growth rate is supposed not to deviate than $\sim 10\%$ from the proton-to-electron mass ratio value, $m_i/m_e \sim 400$ defines an approximate lower limit. Considering a finite magnetic shear of $\hat{s} = 0.8$ does not alter these findings significantly. In fact, the mass ratio dependence on electron scales becomes even a little weaker.

Finally, it shall be noted that mass ratio effects on TEM which might exhibit a different saturation mechanism [14, 36] seem to have only minor influence —at least if ETG modes are linearly stable. According to nonlinear simulation results presented in Ref. [14], there is no qualitative change in the underlying physics if $m_i/me = 400$ is taken instead of $m_i/m_e = 1836$.

4.2.4 Final parameter choice

As shown above, a reduced mass ratio of $m_i/m_e = 400$ seems to be a reasonable choice to explore the main physics in an ion-electron-scale simulation. Linear simulation results with up to 64×16 velocity space $(\mu, v_\parallel)$ grid points are shown in Fig. 4.10. Indeed, growth rates and real frequencies seem to agree qualitatively with those gained with realistic mass ratio, see Fig. 4.3. However, in order to further decrease the computational effort, several tests have been undertaken to relax some of the resolution and box constraints. Finally, the perpendicular box size is chosen to be $(L_x, L_y) = (64\rho_s, 64\rho_s)$, and $768 \times 384 \times 16$ real space grid points are used in the radial, binormal, and par-

allel direction, respectively, as well as 32×8 grid points in $(v_\parallel, \mu)$ space. Again, the resulting growth rates and frequencies are presented, see Fig. 4.11. Although some modifications at intermediate wave numbers are observed, they are not expected to change the general behavior of the physical system. Hence, all following multiscale simulations are performed using the reduced parameter set; nonetheless, each simulation requires of $\sim 100,000$ CPUh.

A last remark is dedicated to hyperdiffusion. As explained in more detail in Ref. [93], the parallel hyperdiffusion coefficient should roughly be set with respect to the linear growth rates. In single-scale simulations it is thus typically taken to be comparable to the highest linear growth rate. Although slowly growing modes then have a much higher hyperdiffusion amplitude, it is usually a reasonable choice since the effect of the hyperdiffusivity is more or less constant above a critical value for a wide range of amplitudes. In multiscale simulations, however, it might happen that an upper limit being comparable to the Courant limit in the time stepping schemes is exceeded which drives the simulations instable. Therefore, a hyperdiffusion coefficient roughly following the linear growth rate is mimicked by using a parabolic function at low and intermediate k_y and being constant at $k_y \rho_e > 0.2$.

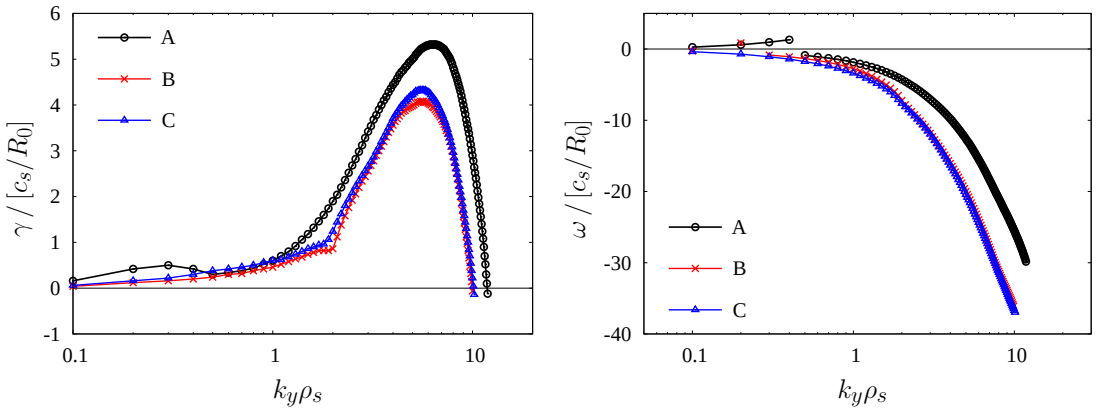

Figure 4.11: Linear growth rates (left) and real frequencies (right) vs. binormal wave number using a mass ratio of $m_i/m_e = 400$, a total of 76 connections at $k_y = k_y^{\min}$, 16 grid points in the parallel direction, 32×8 in the parallel and perpendicular velocity space direction and (A) $R_0/L_{Ti} = R_0/L_{Te} = 6.9$, $R_0/L_n = 2.2$, (B) $R_0/L_{Ti} = 5.5$, $R_0/L_{Te} = 6.9$, $R_0/L_n = 0$, and (C) $R_0/L_{Ti} = 0$, $R_0/L_{Te} = 6.9$, $R_0/L_n = 0$.

4.3 Nonlinear simulation results

4.3.1 Heat and particle transport

The main aim of gyrokinetic simulations is to understand and predict the radial anomalous heat and particle transport levels which determine plasma confinement. Therefore, corresponding fluxes and diffusivities are presented first. Throughout this chapter, they are normalized to $\Gamma_{\mathrm{gB}} = n_0\chi_{\mathrm{gB}}/R_0$, $Q_{\mathrm{gB}} = p_0\chi_{\mathrm{gB}}/R_0$, and $\chi_{\mathrm{gB}} = c_s\rho_s^2/R_0$ if $m_{\mathrm{ref}} = m_i$ or, if electron scales are considered, to $\Gamma^{(e)}_{\mathrm{gB}} = n_0\chi^{(e)}_{\mathrm{gB}}/R_0$, $Q^{(e)}_{\mathrm{gB}} = p_0\chi^{(e)}_{\mathrm{gB}}/R_0$, and $\chi^{(e)}_{\mathrm{gB}} = v_{th,e}\rho_e^2/R_0$.

A first impression of the nonlinear results using parameter set (A) can be obtained by regarding Fig. 4.12, where the time traces of the volume averaged fluxes are plotted in (the simulation's natural) electron scale normalization. Here, a clear sign for multiscale features being present in the simulation can already be found in the transition from the linear to the nonlinear phase. The latter is typically characterized by some *overshoot* or peak where the nonlinear terms just become comparable to the linear ones and eventually reduce the transport again until a quasi-stationary state is reached. While the ion heat

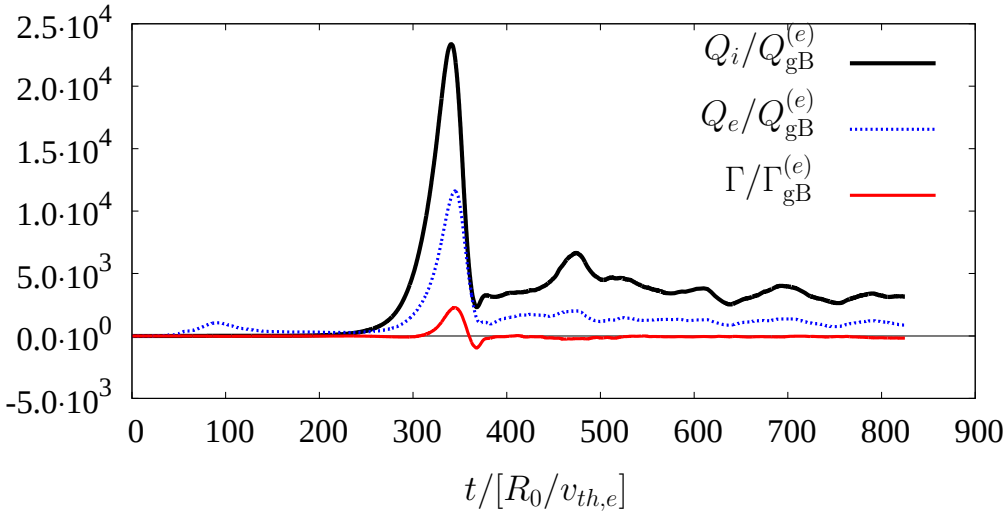

Figure 4.12: Time trace of the volume averaged heat and particle fluxes for (A) $R_0/L_{Ti} = R_0/L_{Te} = 6.92$, $R_0/L_n = 2.2$.

channel only exhibits a single pronounced overshoot at $t \approx 340R_0/v_{th,e}$, the electron heat channel possesses two, one at $t \approx 90R_0/v_{th,e}$ and one coinciding with the ion heat channel peak. This second peak in the electron heat flux, however, is most likely just an electron response to the large ion heat channel overshoot caused by the ITG mode driven turbulence. The first peak, on the other hand, appears on a much shorter time scale which is quite plausible when comparing with the linear findings, cf. Fig. 4.11.

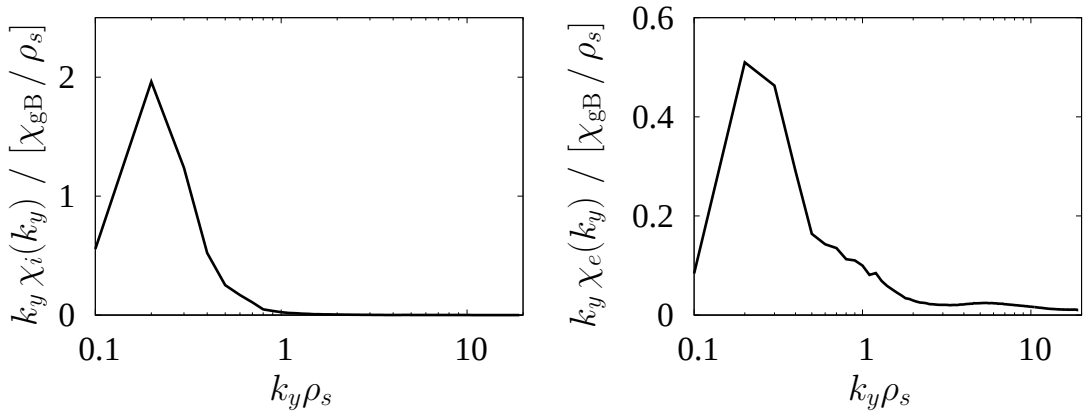

Figure 4.13: Time-averaged ion (left) and electron (right) thermal heat diffusivities multiplied by the binormal wave number vs. binormal wave number for (A) $R_0/L_{Ti} = R_0/L_{Te} = 6.92$, $R_0/L_n = 2.2$.

Here, growth rates assigned to electron temperature gradient driven turbulence have been separated in time by about one order of magnitude, thus giving evidence that ETG modes are responsible for the first peak. Furthermore, the overshoot amplitude is separated by one order of magnitude as well. This is in line with previously described mixing length estimates which hold true as long as the linearly stable $k_y = 0$ mode is not excited. As soon as the nonlinear mode couplings become important, those estimates potentially fail to predict the correct transport levels.

Apart from these first insights obtained from the linear physics and the initial overshoots, it is usually more important to consider the quasi-stationary state where the turbulence is fully established. For this purpose, time averages covering at least several eddy turn-over times up to the whole quasi-stationary state domain should be performed in order to allow for sufficient statistics. The corresponding results are given by $Q_i \approx 164\,Q_{\mathrm{gB}}$, $Q_e \approx 56\,Q_{\mathrm{gB}}$, and $\Gamma \approx -4\,\Gamma_{\mathrm{gB}}$ in ion scale normalization which is more convenient for comparison with other publications. Thus, the ion heat transport is almost three times as large as the electron counterpart, and a relatively small particle pinch is observed.

However, the most interesting question in the context of this work is the transport fraction that is driven by different scales, which now motivates to turn towards spectral representations of the fluxes. Binormal spectra are of particular importance since background density and temperature profiles vary only radially, and thus, even small-scale ($k_\perp\rho_s > 1$) turbulence can exhibit large mode amplitudes near $k_x = 0$, cf. Fig. 4.2.

In Fig. 4.13 the time-averaged binormal (k_y) spectra of the thermal diffusivities multiplied by k_y are presented. In contrast to pure ITG or TEM simulations (with ETG modes linearly stable), where both thermal diffusivity spectra tend to peak at $k_y\rho_s \sim 0.2$

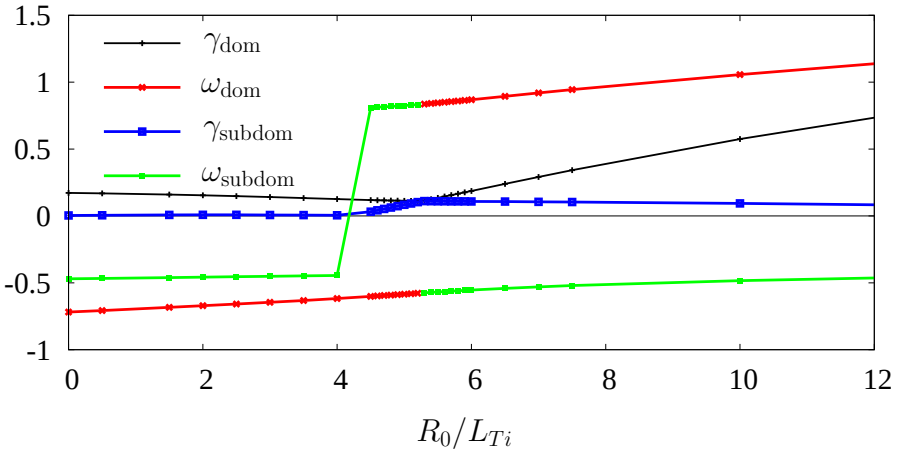

Figure 4.14: Growth rates and real frequencies of the dominant and first subdominant modes in units of c_s/R_0 at $k_y\rho_s = 0.2$ as functions of the ion temperature gradient R_0/L_{Ti}. The remaining gradients, $R_0/L_{Te} = 6.9$ and $R_0/L_n = 0$, are kept constant. Clearly, a mode transition can be identified around $R_0/L_{Ti} = 5.3$ where the dominant mode exhibits a change of sign in real frequency changes. Furthermore, modes with positive real frequency become stable below $R_0/L_{Ti} \sim 4.5$

and fall off quickly with k_y, a relatively small but finite fraction of 10.5% of the total χ_e [$\approx 8\,\chi_{\mathrm{gB}}$] originates from wave numbers $k_y\rho_s > 1$. This is in good agreement with simulation results presented in [83] where a high-k contribution of 13.8% has been found using the same physical parameters.

In order to interpret the found fluxes correctly, it is necessary to compare them with the experimental ones, using the plasma parameters underlying the CBC values employed here. This way, one finds that the ion thermal diffusivity obtained from the simulation, $\chi_i^{\mathrm{sim}} \approx 23.7\,\chi_{\mathrm{gB}}$, exceeds the experimentally determined value of $\chi_i^{\mathrm{exp}} \approx 0.36\,\chi_{\mathrm{gB}}$ [43] by almost two orders of magnitude. A likely key reason for this dramatic difference is that the normalized ion temperature gradient R_0/L_{Ti} – on which ITG turbulence depends very strongly but whose extraction from experimental temperature profile data is usually difficult – has been chosen somewhat too large.

In fact, these findings gave motivation to define parameter set (B). The idea was to lower the ion temperature gradient to a value where TEMs become comparable and eventually the main agent driving the transport. For this purpose, a linear scan over several R_0/L_{Ti} values was performed at the position of the nonlinear transport peak, $k_y\rho_s \sim 0.2$. Originally, this was done using the better resolved parameter set, and a simple fluid model was then employed to estimate the linear threshold of the ITG mode. With the recent implementation of the eigenvalue solver it became possible to revise the results. Furthermore using the reduced parameters, the resulting ITG-TEM threshold is now slightly corrected to $R_0/L_{Ti} = 5.3$ instead of 5.5 where a clear change of sign

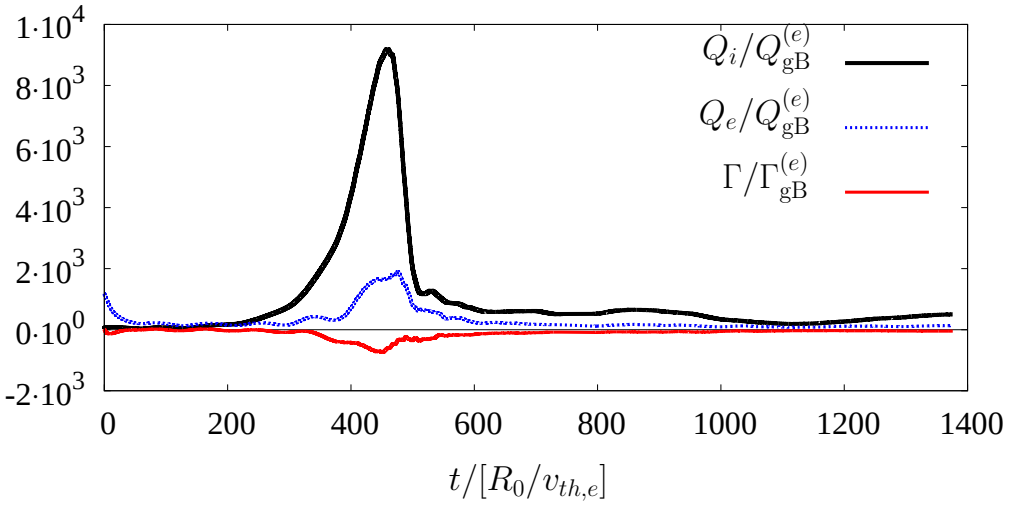

Figure 4.15: Time trace of heat and particle fluxes for (B) $R_0/L_{Ti} = 5.5, R_0/L_{Te} = 6.92$, $R_0/L_n = 0$.

takes place in real frequency, cf. Fig. 4.14. In addition, ITG modes become stable below $R_0/L_{Ti} \approx 4.5$ which is about 10% lower than estimated with a fluid model.

As previously seen in the linear results presented in Sec. 4.2.4, a combined TE and ETG mode now dominates over (almost) the entire k_y range, but the ITG mode coexists in the low-k_y region (up to $k_y\rho_s \sim 0.5$), exhibiting a growth rate which is roughly comparable to that of the TEM.

This is partially reflected in the corresponding nonlinear simulation, presented in Fig. 4.15, where the ion and electron fluxes are now less clearly separated. However, the former is still almost three times larger than the latter, $Q_i \approx 16\, Q_{\mathrm{gB}}$ and $Q_e \approx 5.3\, Q_{\mathrm{gB}}$, and the electron heat flux decreases with reduced ion temperature gradient which is surprising at first sight. But the apparent contradiction to the linear results can be resolved in parts by the following argument. The electron heat transport in parameter set (A) has large low-k contributions originating from ITG modes which may appear due to the different saturation mechanisms and possible nonlinear interaction, e.g. between TEM and ITG mode driven turbulence. A decreased ITG drive may therefore well be responsible for a reduction of the electron heat flux level. The particle flux is again small, $\Gamma \approx -2\,\Gamma_{\mathrm{gB}}$, and directed inward.

Compared to the previous time trace of parameter set (A), the very beginning of the simulation looks somewhat atypical which can easily be explained. Due to the nonlinear time step adaption which essentially decreases the time step when reaching higher amplitudes, overshoots become very costly in terms of computational time. Theoretically, the latter can be reduced if the initial condition is chosen close to the expected saturated state which actually motivated the implementation of an initial state using prescribed

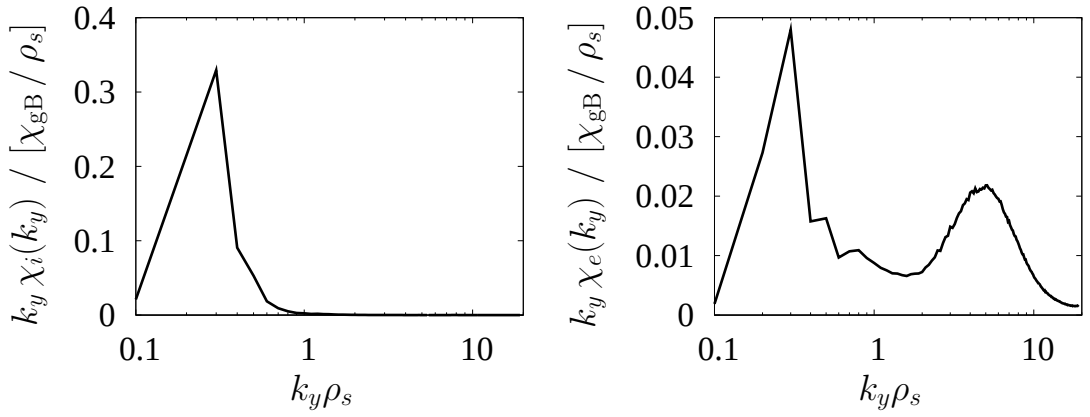

Figure 4.16: Binormal (k_y) spectra of the time-averaged ion (left) and electron (right) thermal fluxes for case (B) with $R_0/L_n = 0$, $R_0/L_{Ti} = 5.5$, and $R_0/L_{Te} = 6.9$. For these parameters, a scale separation between both channels is observed.

power laws in the perpendicular and a ballooning like structure in the parallel direction in GENE. Although being successful for some single-scale simulations, see for instance Ref. [41], guessing a useful initial state for multiscale purposes turned out to be practically impossible. Another idea was to use the saturated state of a preceding simulation with reduced resolution instead. Unfortunately, even such a preparation which has been used in Fig. 4.15 did not show the desired result.

Coming back to the simulation results, a closer look at the heat transport spectra is now due. While the ion heat channel strongly resembles the previously observed spectra with just a slight shift of the transport peak to the next higher mode number, a completely different behavior is observed for the thermal electron diffusivity, cf. Fig. 4.16. Besides the usual peak at low-k, another significant contribution arises from the very small wavelengths being of the order of the electron gyroradius. In absolute numbers, 42% of the electron heat transport is now driven by high-k_y ($k_y\rho_s > 1.0$) modes. As previously discussed, ETG modes are most likely the only turbulence types active in that range. At larger wavelengths, however, it is unclear whether it is an ITG mode or a TEM that is nonlinearly dominant so that further analysis is required. According investigations, e.g. of nonlinear frequency spectra, will be presented later in this chapter.

Since the simulation results obviously depend very strongly on R_0/L_{Ti}, a simulation in which just TEMs and ETG modes are driving the turbulence is considered, as well. This may happen, e.g., in plasmas with dominant electron heating, relatively high β values, substantial equilibrium $\mathbf{E}\times\mathbf{B}$ shear, or internal transport barriers. As previously stated, the profile gradients for this simulation are chosen to be (C) $R_0/L_{Te} = 6.9$ and $R_0/L_{Ti} = R_0/L_n = 0$. In this context, it might be useful to note that the choice of R_0/L_{Ti} should not matter too much as long as ITG modes are clearly subdominant

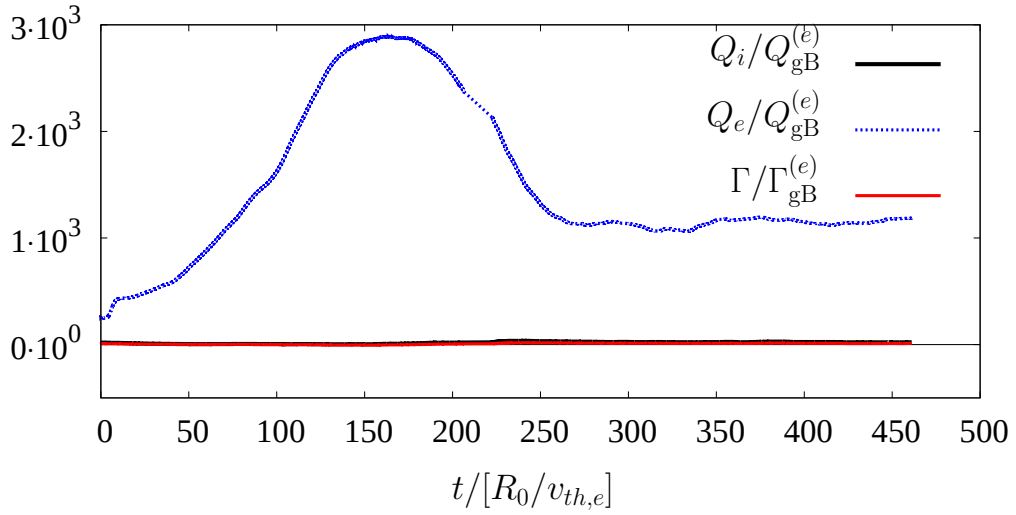

Figure 4.17: Time trace of heat and particle fluxes for (C) $R_0/L_{Ti} = 0, R_0/L_{Te} = 6.92$, $R_0/L_n = 0$.

(both, linearly and nonlinearly). In addition, R_0/L_n should be chosen small enough, such that the TEM is ∇T_e-driven and not ∇n-driven (in the latter case, one would obtain large outward particle fluxes which are usually hard to reconcile with experimental conditions).

The time trace shown in Fig. 4.17 reveals a completely different behavior compared to the ones presented previously. As expected by the absence of ITG modes, only a very small time averaged ion heat flux of $Q_i \approx 1\, Q_{\mathrm{gB}}$ can be observed. Additionally, a very small outward particle flux of $\Gamma \approx 0.6\, \Gamma_{\mathrm{gB}}$ is measured. The time averaged electron heat flux $Q_e \approx 60\, Q_{\mathrm{gB}}$, however, is now almost one order of magnitude higher compared to parameter set (B), although no additional driving has been applied. Before discussing this issue in more detail, another comment shall be made concerning this time trace. While electron time scales are well-resolved at $t \sim 450\, R_0/v_{th,e}$, one might wonder whether large-scale turbulence is already well-described at that point. Hence, another simulation has been performed for parameter set (C) which has been restricted to the ion scales by choosing a different cut-off in the binormal direction, $(k_y \rho_s)^{\max} = 1.5$, and a radial resolution of $\Delta x \sim 0.5\, \rho_s$. The corresponding time trace, see Fig. 4.18, indeed shows a burst at $t \approx 1000\, R_0/v_{th,e}$. However, the transport levels before and after are very similar. In addition, the corresponding spectra have been evaluated and presented in Fig. 4.19. Again, no major modifications are observed, which supports stopping the multiscale simulation (C) at the time chosen in Fig. 4.17.

Comparing the single-scale spectra with the full multiscale simulation result displayed in Fig. 4.20 reveals two surprising effects. Firstly, an unphysical pile-up at high wave numbers is observed if linearly driven smaller scales are cut away. Thus, only in the

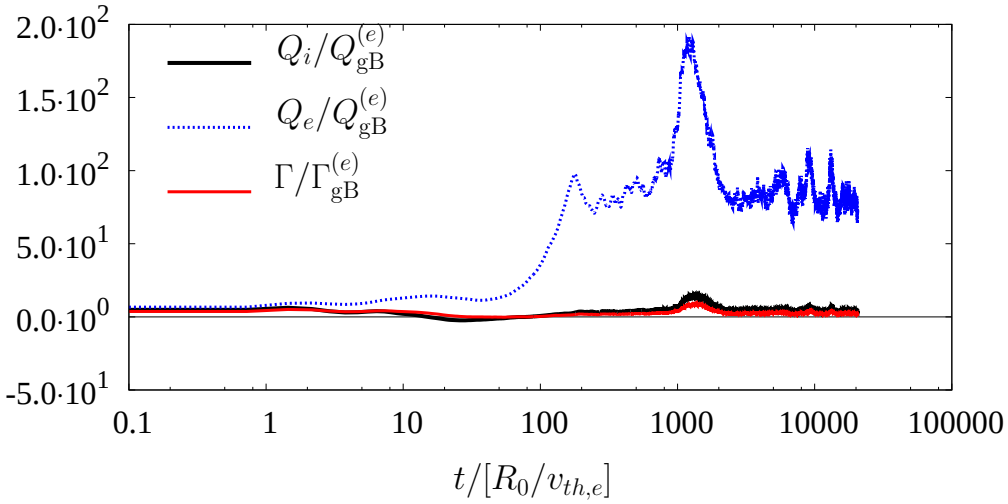

Figure 4.18: Logarithmic time trace of heat and particle fluxes for a single-scale simulation using an identical gradient setting as in parameter set (C), $R_0/L_{Ti} = 0, R_0/L_{Te} = 6.92$, $R_0/L_n = 0$.

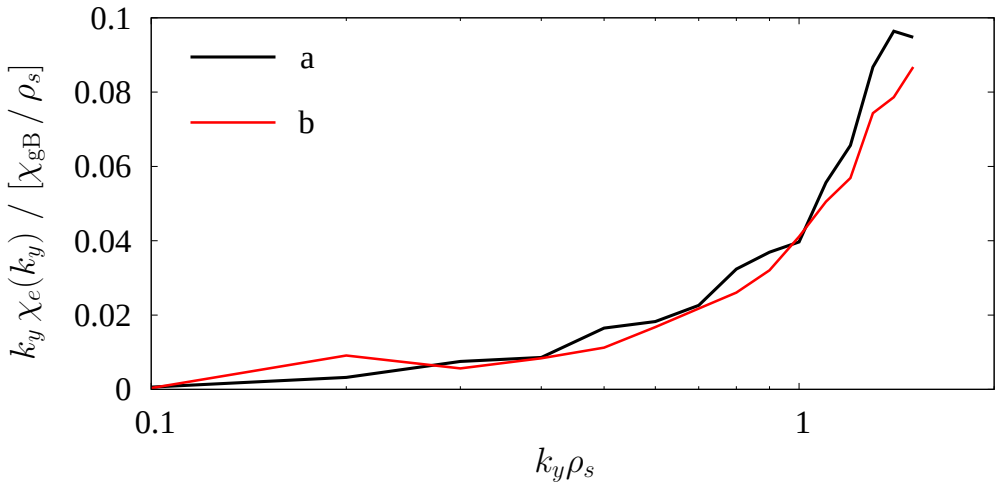

Figure 4.19: Binormal (k_y) spectra of electron thermal diffusivities of the single-scale simulation multiplied by the binormal wave number and averaged over (a) $t = 200 - 500\,R_0/v_{th,e}$ and (b) $t = 20000 - 20560\,R_0/v_{th,e}$.

absence of high-k excitations it is possible to perform simulations covering, e.g., just the ion scales, cf. Fig. 4.20, where in the right plot ETG modes have been stabilized by employing a different temperature ratio.

Secondly, the additional high-k modes seem not only to increase the overall transport but also the transport at large scales. However, since the single-scale simulation is clearly unphysical and only presented to check for convergence with respect to time, it is difficult if not impossible to judge whether cross-scale coupling like noise excitation is actually

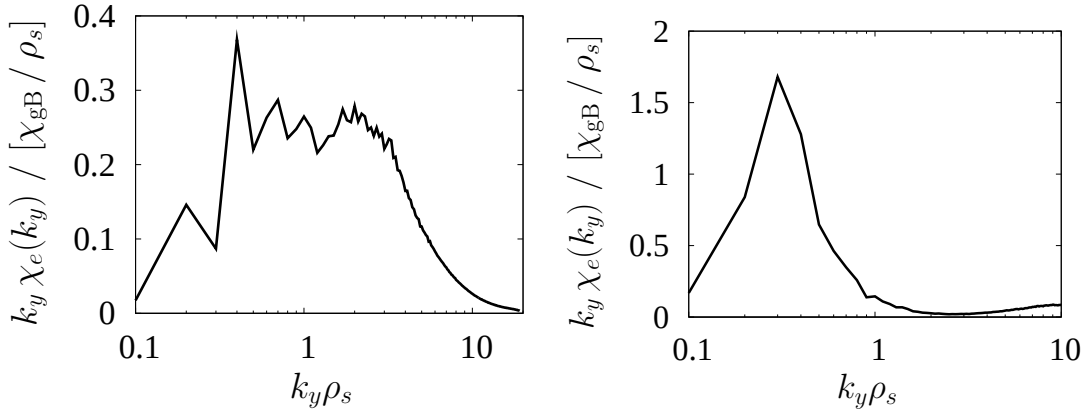

Figure 4.20: Binormal (k_y) spectra of the electron thermal diffusivity for the TEM-ETG multiscale turbulence simulation (C) (left) and, for comparison, a pure TEM turbulence simulation where ETG modes are linearly stable (right).

responsible for this increase.

Inspecting Fig. 4.20 in more detail, one finds that here – in contrast to pure TEM or ETG turbulence simulations where the transport spectra are usually localized in fairly narrow regions of k_y space (see, e.g., right plot of Fig. 4.20 and Ref. [79]) – a wide range of modes contributes significantly to the overall thermal diffusivity of $\chi \approx 8.8\,\chi_{\mathrm{gB}}$. About 30% of the transport is driven in the "classical" TEM range, $k_y\rho_s \lesssim 0.5$. The remaining high-k contribution can be divided into a TEM-ETG turbulence region up to $k_y\rho_s \lesssim 2$ (at this point, the trapped electron bounce frequency matches approximately the mode frequency for parameter set (C)) and an ETG region at $k_y\rho_s \gtrsim 2$. The thermal transport fraction produced in the latter region is almost equal to that of the low-k region, namely about 30%. However, the electron thermal diffusivity of the present TEM-ETG turbulence simulation is higher than the heat diffusivity obtained with $R_0/L_{Ti} = 5.5$, thus again diverging from experimental values [44].

In order to complete the presentation of transport features gained from the multiscale simulations, the analysis is now extended to the particle transport spectra and by decomposing the wave number contributions according to both k_x and k_y. For this purpose, contour plots using logarithmically distributed colors are shown in Figs. 4.21 and 4.22. As previously observed in the binormal spectra, which have been averaged over time and the remaining dimensions, it becomes again obvious that the ion heat flux spectra are always found to be dominated by binormal wavelengths of the order of many ($\gtrsim 10$) ion gyroradii, in good qualitative agreement with pure large-scale turbulence simulations (see, e.g., Ref. [94]). On the other hand, the electron heat flux behaves differently, showing increasing high-k contributions with decreasing low-k (R_0/L_{Ti}-caused) drive. However, this tendency is not found to be isotropic in (k_x, k_y)-space. As men-

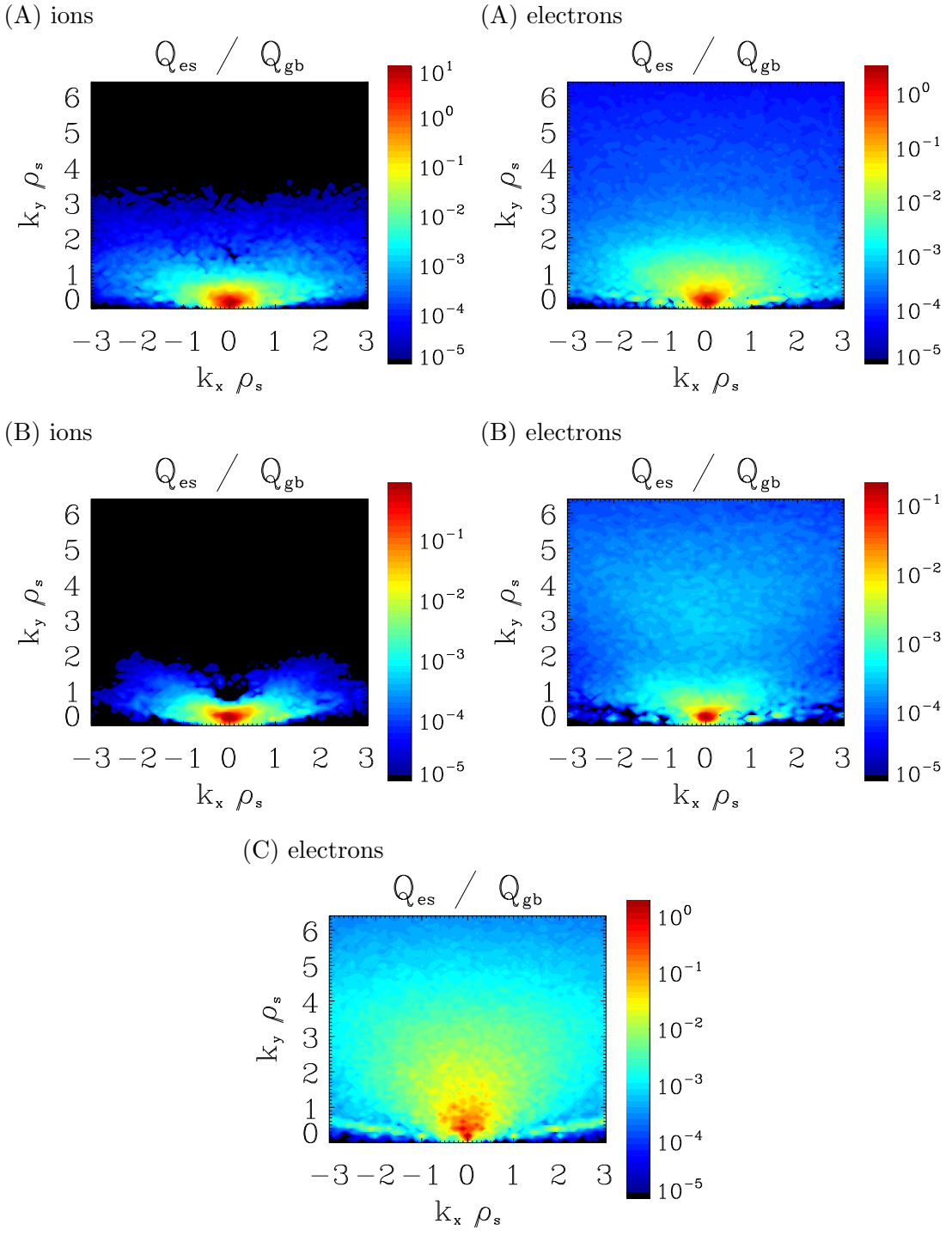

Figure 4.21: Time-averaged heat fluxes (normalized to Q_{gB}) vs. radial and binormal wave numbers for the multiscale simulations (A) to (C). In case (C), the ion heat flux is negligible and therefore not shown.

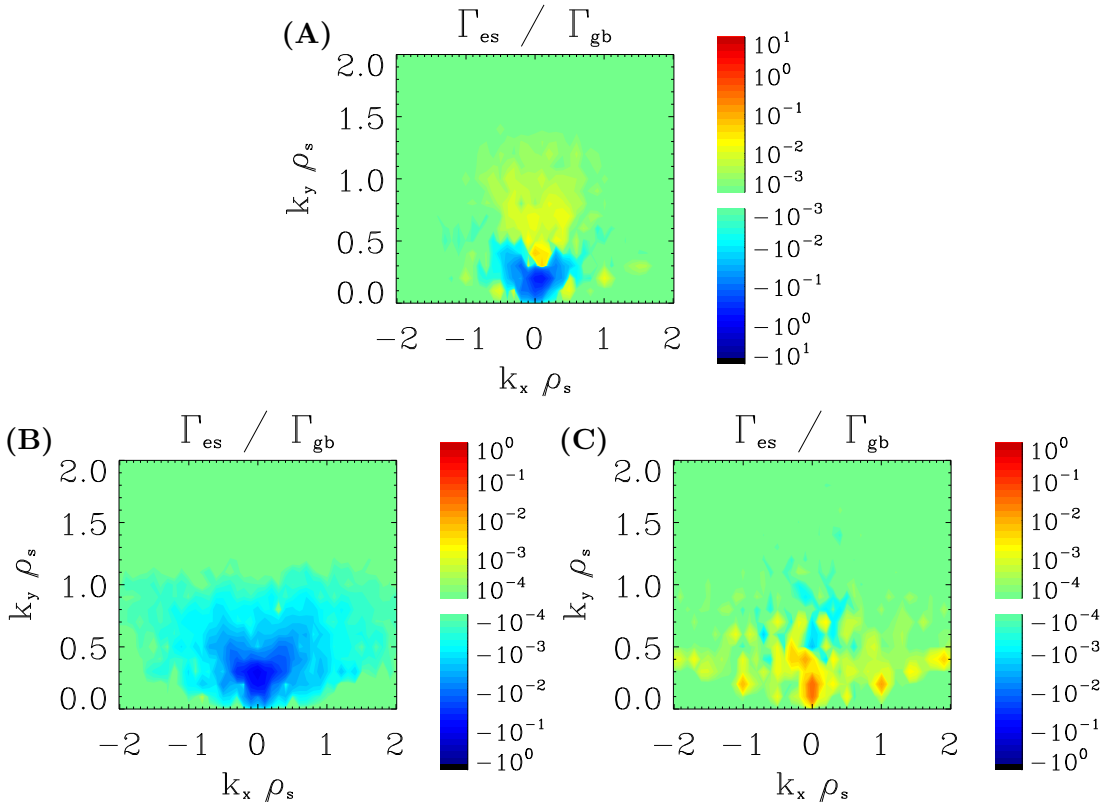

Figure 4.22: Particle fluxes (normalized to Γ_{gB}) averaged over time and parallel direction vs. radial and binormal wave numbers for the multiscale simulations (A) to (C).

tioned before, the high-k_y ($k_y\rho_s > 1.0$) fraction of the electron heat transport rises from $\sim$ 10% in case (A) to $\sim$ 40% in case (B) and finally reaches more than 50% in case (C). In the radial direction, the $k_x\rho_s > 1.0$ fraction in case (A) is about 11% which is almost identical to the respective k_y fraction. However, in cases (B) and (C), the high-k_x contributions amount to values around 30%, therefore implying an anisotropic heat flux spectrum. The physical origin of these high-k anisotropies is most likely the existence of small-scale streamers [37, 78, 66], as will be discussed in more detail in the next section.

The particle fluxes, presented in Fig. 4.22, are directed inwards (describing a particle pinch) in cases (A) and (B), but change sign in case (C) where ITG modes are not excited anymore. These findings are consistent with ITG/TEM simulation results as reported in Ref. [14] where dominant particle pinches have only been observed for $R_0/L_{Ti} > 0$.

For all three parameter sets, there are no significant high-k ($k\rho_s > 1$) contributions to the particle transport. This is in line with general expectations based on the fact that the ions become adiabatic at these scales.

Discussion

The heat fluxes presented above are summarized in Fig. 4.23, together with two additional simulation results which shall help to resolve the domain where ITG modes become subdominant. Here, the values at $R_0/L_{Ti} = 5.5$ seem to slightly differ from the general trend. One possible reason is the bursty behavior of the heat fluxes at $R_0/L_{Ti} = 5.2$ which complicates the determination of a sufficiently converged value and thus increases the uncertainty for this data point. But although restricting the window for time averaging to a region between two consecutive bursts, the data points at $R_0/L_{Ti} = 5.2$ and $R_0/L_{Ti} = 5.5$ seem not to fit perfectly. Hence, the slight misalignment might be a physical effect or an artifact linked to space-time resolution issues, which could be investigated in more detail once more computational resources are available.

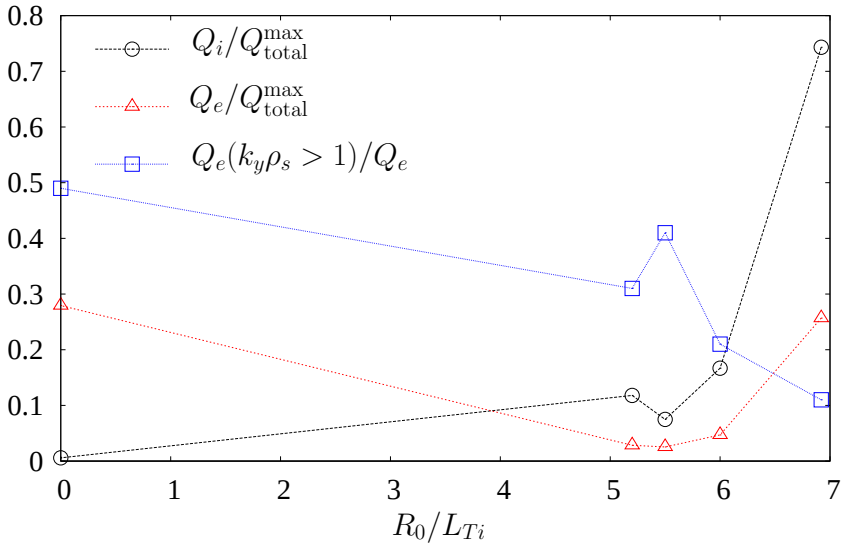

Figure 4.23: Ion and electron heat flux as functions of the ion temperature gradient normalized to the maximum total heat transport which is reached for parameter set (A). In addition, the high-k fraction of the electron heat flux is displayed. Note that parameter set (A) includes a different density gradient of $R_0/L_n = 2.2$. Furthermore, the simulation performed at $R_0/L_{Ti} = 5.2$ exhibits bursts which are not included in the presented time averaged value by choosing the time window accordingly.

Nevertheless, the general trend is expected to be already well-reflected in Fig. 4.23, and it is now time to address the following problems:

(I) Why is the high-k fraction so small in the dominant ITG and quite large in the TEM-ETG case?

(II) Why is the electron heat flux reduced when the ion temperature gradient is decreased to a value where ITG modes become subdominant?

(III) Do linear features survive within the nonlinear simulations?

The first question is in part motivated by the linear simulation results. When comparing the growth rates in Fig. 4.11 with the actually measured heat fluxes, it might be astonishing that high-k mode numbers do not contribute a larger fraction for parameter set (A). With ITG and ETG modes being driven by similar gradient settings and a weaker saturation mechanism of ETG modes, much higher transport levels should be observed in that range. But such a notion would neglect any TEM influence and cross-coupling effect. However, the TEMs turn out to be subdominant even in the nonlinear simulation as will be shown later. The cross-coupling effects, on the other hand, are then thought to be the most likely reason for a partial transport suppression. This statement is supported by snapshots of the electrostatic potential, see Fig. 4.24, taken at outboard mid-plane where due to the ballooning character most turbulent transport is driven. A first glimpse at Fig. 4.24 suggests that the large-scale ITG dynamics dominate,

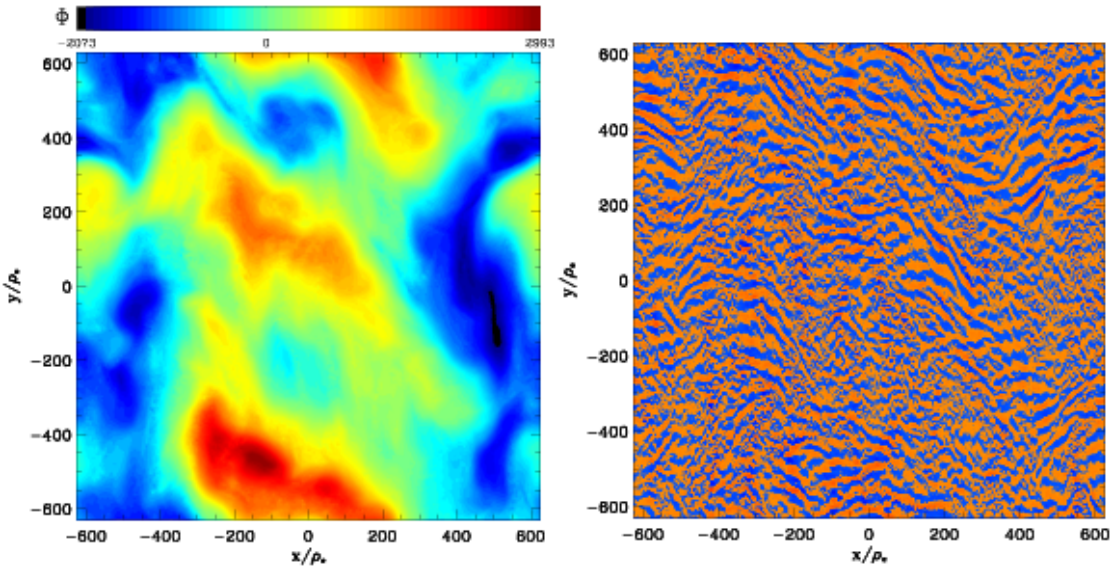

Figure 4.24: Snapshot of the electrostatic potential at the outboard mid-plane for case (A) with $R_0/L_{Ti} = R_0/L_{Te} = 6.9$, and $R_0/L_n = 2.2$, showing a dominance of large-scale, ITG vortices, and the same data with all $k_y\rho_s < 2$ modes filtered out, demonstrating the existence of small-scale ETG streamers which are subject to vortex stretching.

since structures elongated in the y direction strongly resemble the shape of weak zonal flows. Applying a high-pass filter reveals the co-existence of short-wavelength structures within or between the large-scale vortices. However, these very thin ETG streamers seem to be strongly distorted, which may reduce the corresponding transport. Another conceivable effect of large vortices on small eddies is a local modification of the temperature and density gradients, which would alter the linear physics and possibly cause

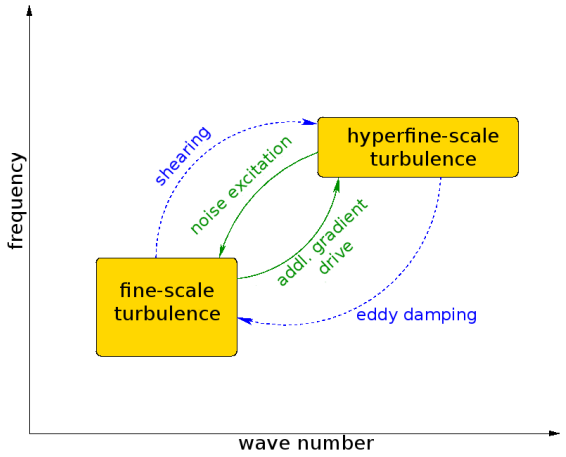

Figure 4.25: Illustration of possible cross-scale couplings adapted from Ref. [95]

streamers to appear in binormal direction, the latter only contributing marginally to the radial transport. Unfortunately, a local code provides only limited possibilities for an according investigation because turbulent temperature and density fluctuations should be seen in relation to the corresponding equilibrium quantities. As already mentioned in Sec. 3.6.1, it is thus hard to calculate consistent gradients in the $\rho^* \to 0$ limit. Further potential cross-scale coupling effects which are discussed in detail by Itoh and coworkers [95, 96, 97] are illustrated in Fig. 4.25. Besides the already mentioned effects of large scale turbulence on the small scale one, they additionally consider noise excitation and eddy damping which may act in the inverse direction. However, at this point, the reader shall be reminded that direct investigations of such effects are not feasible. For example, they would require comparisons with singe-scale simulations in order to identify cross-couplings. However, simply cutting away parts of the spectrum may exhibit artificial structures as seen, e.g., in Fig. 4.19. A possible alternative would be to investigate ITG/TEM turbulence by stabilizing ETG modes – for instance via choosing a temperature ratio of $T_e/T_i = 3$ – and pure ETG modes by reducing the influence of trapped particles by assuming a very small inverse aspect ratio. Of course, both approaches are questionable since they change the underlying physics.

Therefore, one has to rely, e.g., on the contour plots which are not affected by the above mentioned complications. In the following, an examination on how a reduction in R_0/L_{Ti} influences the short wavelength turbulence shall be based on them.

Switching off the density gradient and setting $R_0/L_{Ti} = 5.5$ obviously causes no dramatic changes in the corresponding contour plots which are presented in Fig. 4.26. However, the large scale structures are now less zonal flow-like, and small scales are now even visible in the unfiltered plot. By compiling several subsequent snapshots to a movie, it is furthermore possible to observe the opposite drift directions of large and small scale

vortices. This is a surprising result since linearly, ITG modes are the dominant large-scale turbulence type only at $k_y\rho_s \lesssim 0.2$ —all remaining low-k modes are dominated by TEMs which would drift in the same direction as the small-scale ETG modes.

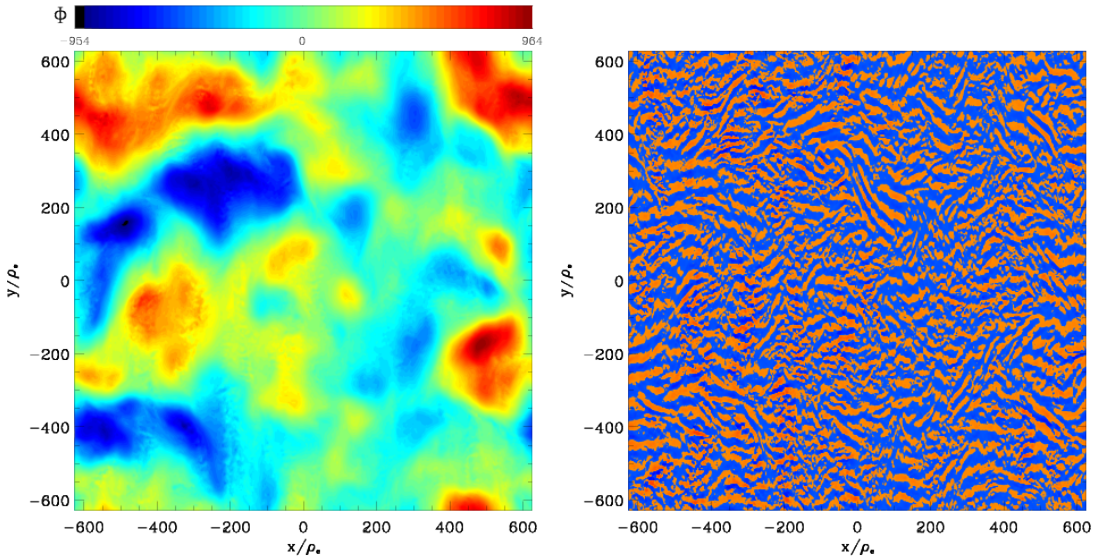

Figure 4.26: Snapshot of the electrostatic potential at the outboard mid-plane for case (B) with $R_0/L_{Ti} = 5.5$, $R_0/L_{Te} = 6.9$, and $R_0/L_n = 0$, showing a dominance of large-scale, isotropic ITG vortices, and the same data with all $k_y\rho_s < 2$ modes filtered out, demonstrating the existence of small-scale ETG streamers which are again subject to vortex stretching.

The flat ion temperature profile simulation reveals a completely different behavior compared to that with low-k ITG turbulence. Instead of isotropic vortices, the contour plots of the electrostatic potential exhibit radially elongated structures with a multitude of different length scales, as can be seen in Fig. 4.27. This streamer-like behavior is in line with previous (pure) ETG and TEM simulations [37, 38]. A comparison of the filtered images in Figs. 4.24 and 4.26 on the one hand and Fig. 4.27 on the other suggests that the medium-k and high-k fluctuations are now less affected by the large-scale fluctuations than in the ITG cases. This statement is supported by the good agreement of the electron thermal diffusivities in simulations restricted to $k_\perp\rho_s > 1$ [79] and in the current multiscale simulation, evaluated at $k_y\rho_s > 1$. In other words, it is much easier for the small ETG streamers to evolve within the also radially elongated TEM vortices than in the isotropic or zonal flow-like structures. The high-k transport is thus boosted.

Having developed a first understanding of how small-scale modes interact with long-wavelength turbulence in magnetically confined fusion plasmas, one can now move on to

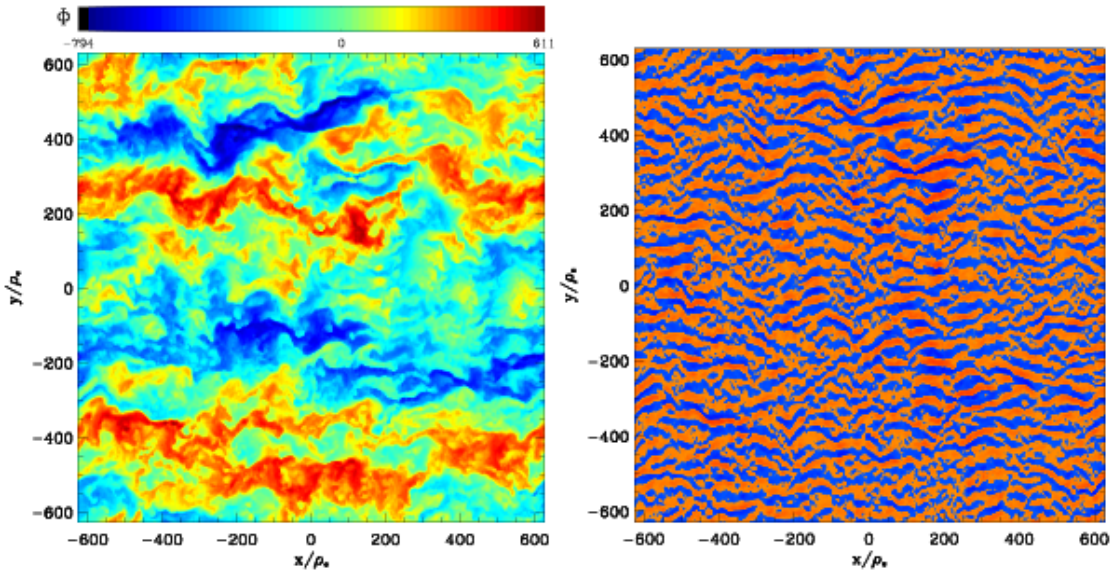

Figure 4.27: Electrostatic potential contour at the low-field side for case (C) with $R_0/L_{Ti} = 0$ and $R_0/L_{Te} = 6.9$, and the same contour neglecting all modes $k_y\rho_s < 2$.

the second question (II) on page 85 regarding possible reasons for a decreasing electron heat flux when approaching the linear ITG/TEM transition. The most obvious one is that large fractions of the electron heat channel are here driven by ITG modes and not by the electron turbulence types TEM and ETG. For example, a simulation without density and electron temperature gradients but otherwise using similar parameters as in (A) yields up to $Q_e/Q_i = 10\%$ which would indeed constitute a significant fraction in simulation (A). Furthermore, such transport minima seem to occur quite often close to linear mode transitions as has recently been reported by F. Merz for single-scale, multi-mode turbulence simulations [36]. Finally, transport levels can also be analyzed by means of cross phases between fluctuating quantities like ϕ_1, n_1, $T_{\parallel 1}$, or $T_{\perp,1}$. The underlying motivation is given by the flux average calculation itself, cf. Sec. 3.6, which can alternatively be written as

$$\Gamma = \frac{1}{V\,\Delta t}\int_0^{\Delta t} \mathrm{d}t \int_V \mathrm{d}^3x\, n_{1\sigma}(\mathbf{x},t) v_\xi^x(\mathbf{x},t), \tag{4.5}$$

see e.g. Ref. [98], and

$$Q_\sigma = \frac{1}{V\,\Delta t}\int_0^{\Delta t} \mathrm{d}t \int_V \mathrm{d}^3x \left(\frac{3}{2}T_{0\sigma}n_{1\sigma}(\mathbf{x},t) + \frac{1}{2}n_{0\sigma}T_{\parallel 1}(\mathbf{x},t) + n_{0\sigma}T_{\perp 1}(\mathbf{x},t)\right) v_\xi^x(\mathbf{x},t) \tag{4.6}$$

thus representing a correlation of two signals. Considering that here, $v_\xi^x(\mathbf{x},t) \propto \mathrm{i}k_y\phi_1$, the fluxes will reach a maximum if the relative phases between ϕ_1 and $(n_1, T_{\parallel 1}, T_{\perp 1})$

are close to odd multiples of $\pi/2$. If the cross phases are, on the other hand, close to multiples of π, no transport is observed. Results of a corresponding analysis are presented in Fig. 4.28. Here, the cross phases between two fluctuating quantities are evaluated for each k_y mode by sampling all values obtained for each x and z grid point in a histogram, which is then weighed by the corresponding amplitudes. In addition, linear simulation results, in particular the maxima of the cross phases, are included as dashed lines for comparison. Clearly, cross phases between ϕ_1 and n_{1e} (displayed in the first column of Fig. 4.28) are linearly and nonlinearly unfavorable for the transport fluxes since they exhibit values close to 0 and $\pm\pi$, respectively. This finding is in line with the relatively small particle fluxes found in all presented multiscale simulations. In the large ITG case (A), both remaining cross phases, $\phi_1 \times T_{\parallel 1}$ and $\phi_1 \times T_{\perp 1}$, exhibit almost identical distances to their respective nearest unfavorable phase angle at small wave numbers. The corresponding heat transport fractions are indeed similar if the factor of 1/2 appearing in Eq. (4.6) is not considered. At larger wave numbers, however, they show different behavior. Linearly and nonlinearly, the phase between ϕ_1 and $T_{\parallel 1}$ becomes less distinctive so that a maximum can hardly be identified. The dashed line in Fig. 4.28 indicating the maximum cross phase is therefore to be handled with care, and the deviations between both simulation types are not of major concern. The cross phase $\alpha(\phi_1, T_{\perp 1})$, on the other hand, first stays within a certain range which is close to $5\pi/6$ before slowly transitioning to $\alpha \approx 0$ for $k_y\rho_s \gtrsim 1$. This finding is different than what might be expected from linear simulations. Here, a jump in phase angle to values about $\pi/2 - 4\pi/3$ is observed at $k_y\rho_s \approx 0.5$ where ITG modes become linearly stable. Therefore, it seems that nonlinear ITG features dominate up to $k_y\rho_s \sim 1$, thus wiping out the intermediate-scale TEM dynamics and also reducing the ETG fluctuations. In case (B), the low-k cross phases imply strong $T_\parallel$ contributions. However, the $T_{\perp 1}$ fraction is still larger due to higher amplitudes of the perpendicular temperature. A significant high-k mode range, in particular $2 \lesssim k_y\rho_s \lesssim 5$, possesses cross phases close to $\pi/2$ in both cases, thus more or less compensating the amplitude reduction at these scales and therefore causing the previously mentioned scale separation. While comparisons with linear results are again difficult for $\phi_1 \times T_{\parallel 1}$ due to a broad linear cross phase distribution, they reveal a similar behavior for the $\phi_1 \times T_{\perp 1}$ cross phases as in case (A). Thus, ITG features seem to nonlinearly extend up to $k_y\rho_s \approx 1$ which is much higher than in the linear simulation where a jump in phase angle is observed at $k_y\rho_s \approx 0.4$. However, it is also surprising that ITG mode features manifest themselves at all. Except for $k_y\rho_s \approx 0.2$, TEM turbulence should be dominant as has been shown in Fig. 4.11. Hence, the good low-k agreement of the $\phi_1 \times T_{\perp 1}$ phase angles with those of the strong ITG case rather than the TEM-ETG case suggests strong subdominant ITG modes being present below the dominant TEM. Finally, in case (C) where ITG modes are stable, the $\phi_1 \times T_{\parallel 1}$ cross phase remains close to 0 while a value of about $\pi/2$ is found over a wide range of wave

numbers for the $\phi_1 \times T_{\perp 1}$ cross phase. The electron heat transport is thus almost solely driven through this channel. Linear and nonlinear cross phases are found to bear strong resemblance.

Although question (III) on differences or similarities between linear and nonlinear features has now been answered partially, it will be addressed again in the next section where experimentally accessible quantities are considered.

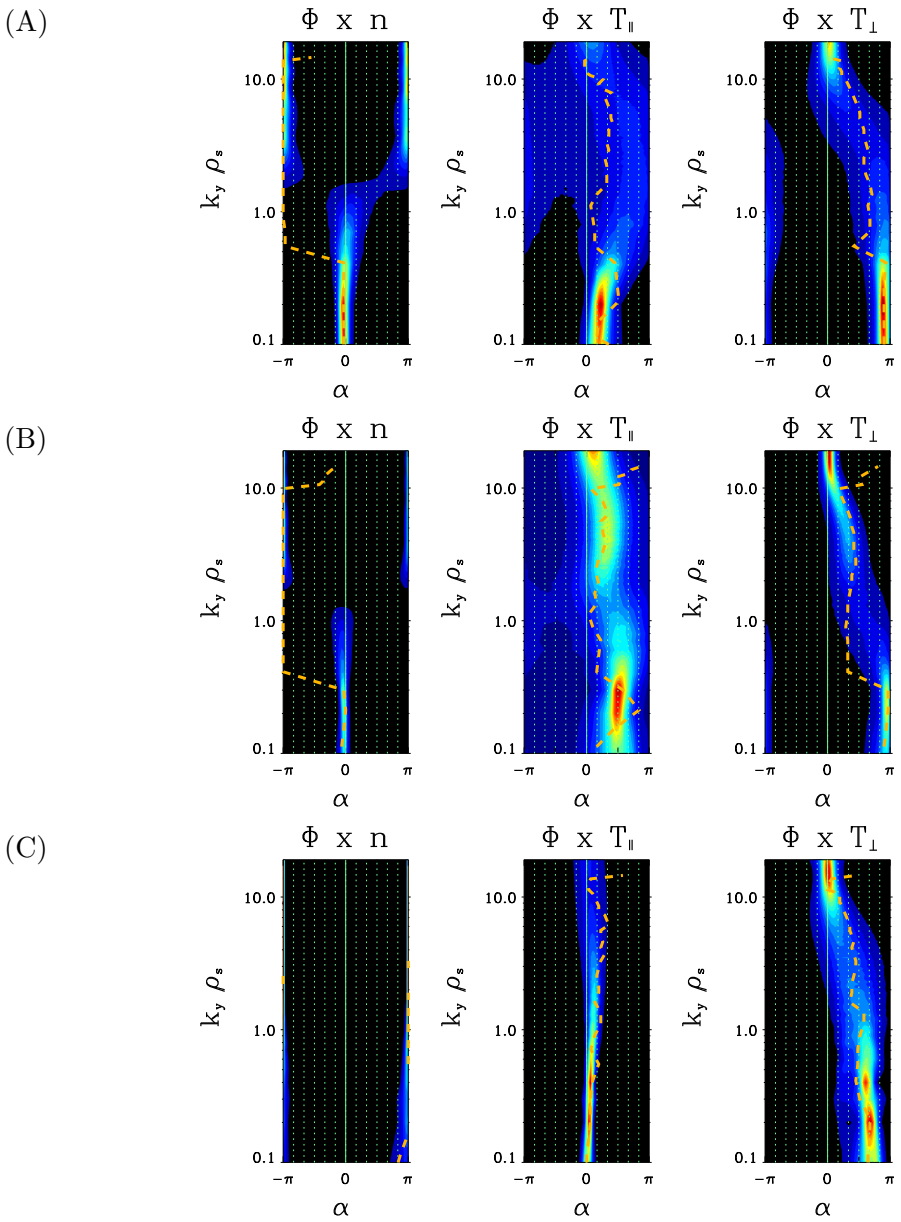

Figure 4.28: Cross phases (weighed by amplitude per k_y mode) between electrostatic potential and electron density and temperatures, plotted against phase angle α and binormal wave number k_y for the multiscale simulations (A) to (C). The dashed lines represent the respective maxima of the linear cross phases.

4.4 Density spectra

The collection of significant evidence in experiment and numerical simulation that high-k modes, namely ETG modes, may exhibit substantial or even dominant contributions to the electron heat transport under certain conditions – e.g., in plasmas with dominant electron heating, relatively high β values, substantial equilibrium $\mathbf{E} \times \mathbf{B}$ shear, and (internal or edge) transport barriers – triggered a serious effort in the fusion community to extend existing experimental diagnostics into the high wave number regime (see, e.g., Refs. [99, 100, 101, 102]). Unfortunately, the list of observables does not include electron temperature and electrostatic potential fluctuations (or their cross phases). Thus, it is currently not possible to determine electron heat flux spectra directly. Instead, most high-k diagnostics measure density fluctuation spectra. While the latter may serve as an indicator of the role of turbulence on sub-ion-gyroradius scales, little is known about their connection with electron heat flux spectra. Therefore, the following section is dedicated to an investigation of several experimentally accessible quantities – as, for instance, density or frequency spectra – by means of nonlinear gyrokinetic simulations covering both electron and ion spatio-temporal scales self-consistently.

Up to now, most core turbulence simulations have been performed for situations in which there was only one mode type driving the system. In these "pure" cases, the density fluctuation spectrum in the binormal direction, $S(k_y) = \langle |n_1(\mathbf{k}, \omega)|^2 \rangle_{x,z,\omega}$, with $\langle \dots \rangle$ denoting averages over quantities listed as indices, usually exhibits a maximum at $k_y \rho_s \sim 0.1 - 0.2$. The radial spectra $S(k_x) = \langle |n_1(\mathbf{k}, \omega)|^2 \rangle_{y,z,\omega}$, however, typically peak at wave numbers close to zero if concentric circular flux surfaces are considered. Therefore, a low-k anisotropy is always present. At higher wave numbers, a power law $S(k_{x,y}) \propto k_{x,y}^{-a}$ is typically seen in both perpendicular directions. Unfortunately, only a small number of publications contain numerically determined density spectra explicitly. Based on the few existing ones, a rough range for the power law exponent can be stated by $a = 3 - 5$ (see, e.g., Refs. [103, 38, 104]) which is consistent with the experimental findings $a \sim 3.5 \pm 0.5$ for intermediate wave numbers, $0.3 \lesssim k_y \rho_s \lesssim 1.0$ (see, e.g., Ref. [100] and references therein). For pure ETG turbulence, a similar behavior has been observed in numerical simulations, where ρ_s is replaced by the electron gyroradius ρ_e [79, 105].

Examples of such "pure" turbulence simulation results are presented in Fig. 4.29. In particular, they comprise highly resolved ITG modes, temperature gradient driven TEMs with linearly stable ETG modes, and additionally ETG modes employing a box size restricted to high-k wave numbers but retaining nonadiabatic ion dynamics. The underlying physical parameters are chosen close to the multiscale parameters presented in Sec. 4.2.4. The few exceptions are listed in the following. In the ITG simulation, the gradients are $R_0/L_{Ti} = 6.92$, $R_0/L_{Te} = 0$, $R_0/L_n = 0$ whereas the TEM case uses

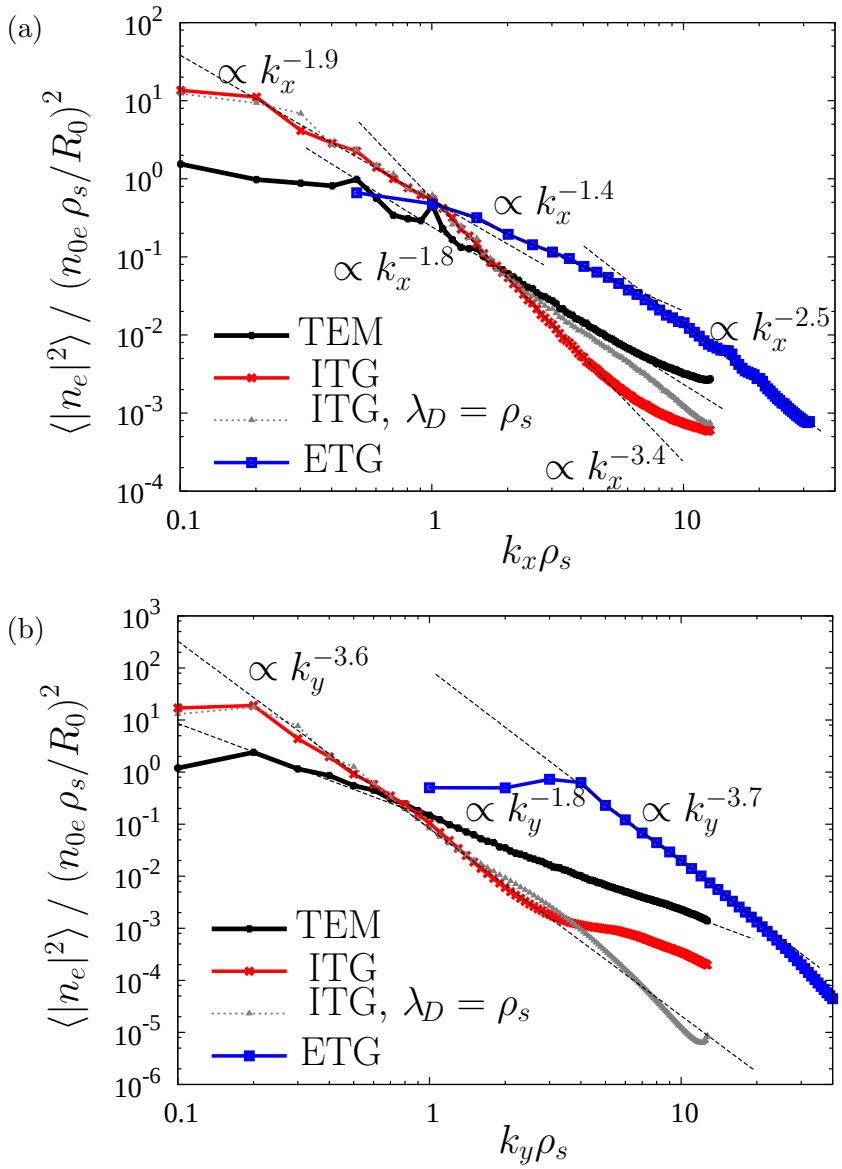

Figure 4.29: Squared electron density fluctuations for pure ITG, TEM, and ETG turbulence cases as a function of (a) radial and (b) binormal wave number, each averaged over the remaining directions and time. Since exact characteristics depend strongly on the chosen parameters, these results are only presented to demonstrate that the power law exponent is typically in the range of $2-4$, but not necessarily isotropic.

$R_0/L_{Ti} = 0$, $R_0/L_{Te} = 6.92$, $R_0/L_n = 0$ and $T_e/T_i = 3$. The settings for the ETG simulation are the CBC values extended to two species, therefore $R_0/L_{Ti} = R_0/L_{Te} = 6.92$ and $R_0/L_n = 2.22$.

In comparison to the previously stated range for power law exponents, the binormal spectra are slightly flatter – which might be due to the use of different physical parame-

ters or higher resolution. Furthermore, a bulge at high k_y in the ITG density spectrum is observed which may be caused by a nonlinearly excited ETG mode, an effect which has been reported before, see Ref. [85]. Its absence in a simulation using the same parameters except for a finite Debye length of $\lambda_D = \rho_s$ supports this physical interpretation.

While "pure" turbulence simulations have the great advantage of minimizing the degree of complexity in performing and analyzing the runs, they usually represent idealized situations which are, in general, of limited value for direct comparisons with experimental findings. Thus, a step towards more realistic simulations involves the study of mixtures of two or more different turbulence types as they occur in the multiscale simulations mentioned before. Corresponding density spectra can be found in Fig. 4.30. As the ion temperature gradient is decreased, a bulge at $k_y\rho_s \approx 2-5$ (corresponding to $k_y\rho_e \approx 0.10-0.25$) develops and becomes more and more pronounced. Since most of the ETG-induced transport is located in this wave number range and the radial spectrum does not show such a distinctive structure, it seems likely that these modifications of the binormal spectra is caused by the ETG modes, cf. Fig. 4.29. Above and below this wave number range, the observed power laws more or less match those known from pure turbulence simulations, except for case (A), where an unusually small exponent appears at the highest k_y values. This is thought to be a numerical effect, however, which is expected to disappear with increased perpendicular resolution. In any case, a pronounced bulge in the binormal density spectrum as occurring in case (C) violates the often employed assumption of isotropic density spectrum at high-k modes. This can clearly be seen in contour plots, see Fig. 4.31, where the density spectra for cases (A) and (C) are plotted in k_x-k_y space. While the former exhibits a more or less circular shape at $k_x\rho_s \sim k_y\rho_s \sim 1$, the latter displays an elongation in binormal direction at those wave numbers. The explanation for this finding can be derived from Sec. 4.3.1. Here, a similar deformation has been observed in Fig. 4.21 which can be attributed to the existence of ETG-scale streamers being hampered by the presence of strong ITG turbulence in the case (A), whereas they are well-developed in case (C). Naturally, this anisotropy is not restricted to turbulence mixtures and may also be present in pure turbulence cases, as can be seen by comparing the k_x and k_y power law exponents in Fig. 4.29.

Such anisotropies at short wavelengths should be taken into account when comparing numerical with experimental results. For example, it is quite common to average (numerically derived) squared amplitudes over the radial direction when displaying k_y spectra, while several detectors in experiments consider only a narrow region about $k_x \approx 0$, see for instance the description of the modified ALTAIR [106] coherent forward Thomson scattering diagnostic in the Tore Supra device [100]. In order to facilitate comparisons with results originating from such diagnostics, k_y spectra for $k_x = 0$ have been evaluated, as well. They are shown in Fig. 4.32, and, as expected, they significantly differ from those presented in Fig. 4.29b and Fig. 4.30b. Most obviously, the power law exponents change.

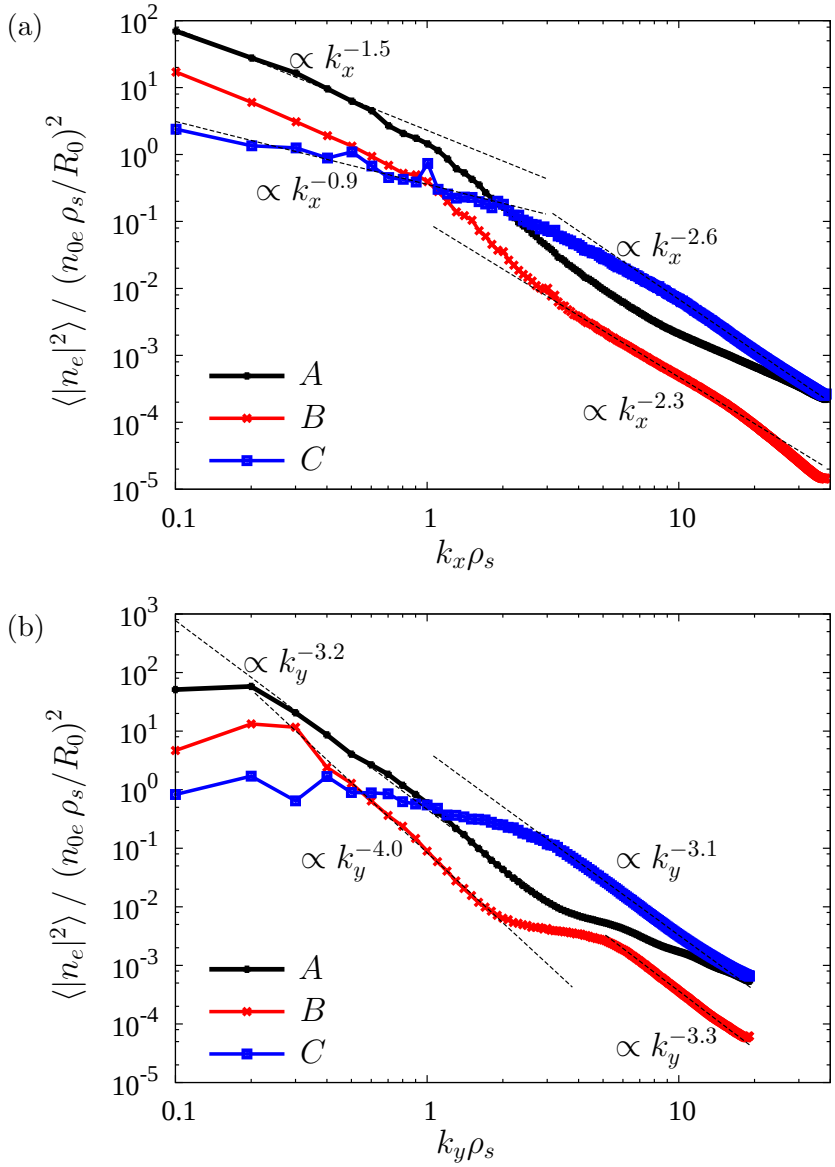

Figure 4.30: Squared electron density fluctuations for the multiscale simulations (A) to (C) as functions of (a) k_x and (b) k_y, averaged over the remaining directions and time.

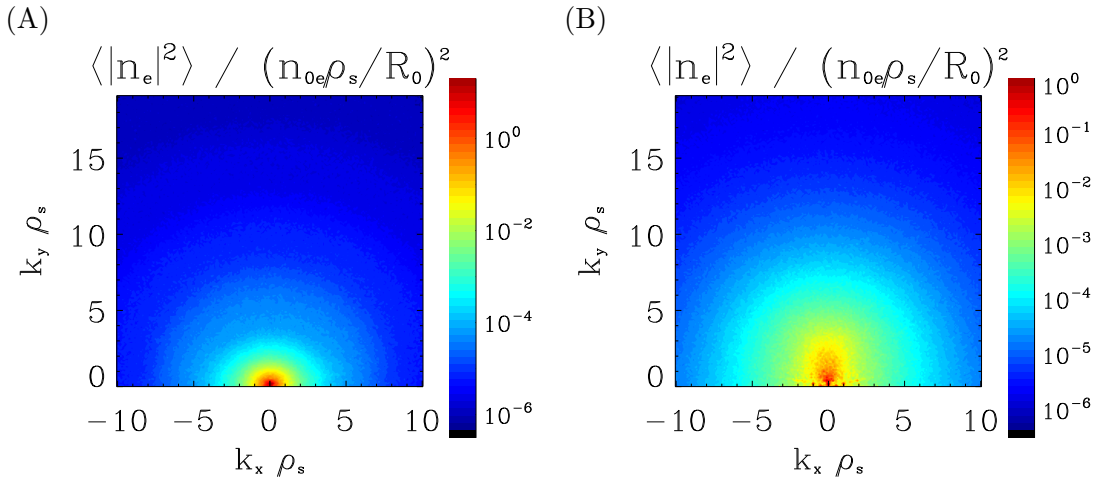

Figure 4.31: Squared electron density fluctuations as functions of k_x and k_y from the multiscale simulations (A) and (C).

One now finds exponents up to $a \approx 5$, and if a fit is applied to the range $4 \lesssim k_y\rho_s \lesssim 7$ in the pure ETG turbulence case, one even arrives at $a \approx 7.4$. These values are quite close to the experimental findings presented in [100, 107, 108] where $a \approx 3.5$ was found at low-k, and $a \approx 6.5 - 7$ in the high-k regime. Such characteristics are actually in good qualitative agreement with those of case (C), but the power law exponents do not match. One finds $a \approx 1.9$ at $0.15 < k_y\rho_s < 2$ and $a \approx 5$ at $4 < k_y\rho_s < 10$. A possible mechanism which might help reducing the difference is the Debye shielding since it may steepen the spectrum at high wave numbers (see, e.g., Ref. [105]). Naturally, a change of plasma parameters or magnetic geometry may also lead to better agreement. Similar arguments apply to the radial direction where Gurchenko and co-workers report a power law transition from $a \approx 2.5$ to $a \approx 6.2$ at $k_y\rho_s \sim 9$ [109].

Summarizing, an essence to be taken from these multiscale simulations is that a tendency to flatten density spectra in the $k_y\rho_e \gtrsim 0.1$ region may be a signature for strong ETG activity (note that for a realistic mass ratio of $m_i/m_e = 1836$ or $m_i/m_e = 3675$, this corresponds to $k_y\rho_s \gtrsim 4$ and $k_y\rho_s \gtrsim 6$, respectively). If the long-wavelength dynamics is dominated by ITG modes, the fall-off up to that point will still be substantial, however, and presumably no high-k peaks are to be expected. Nevertheless, the ETG-induced contributions to the total electron heat flux can be large since most of it is driven by the positive correlations between fluctuations of the electrostatic potential and the electron *temperature*, both of which tend to decay more slowly than the *density* fluctuations. The respective spectra of these quantities are shown in Fig. 4.33 – however, they cannot be measured in current experiments.

In a final remark, it shall be pointed out that power law investigations are an important

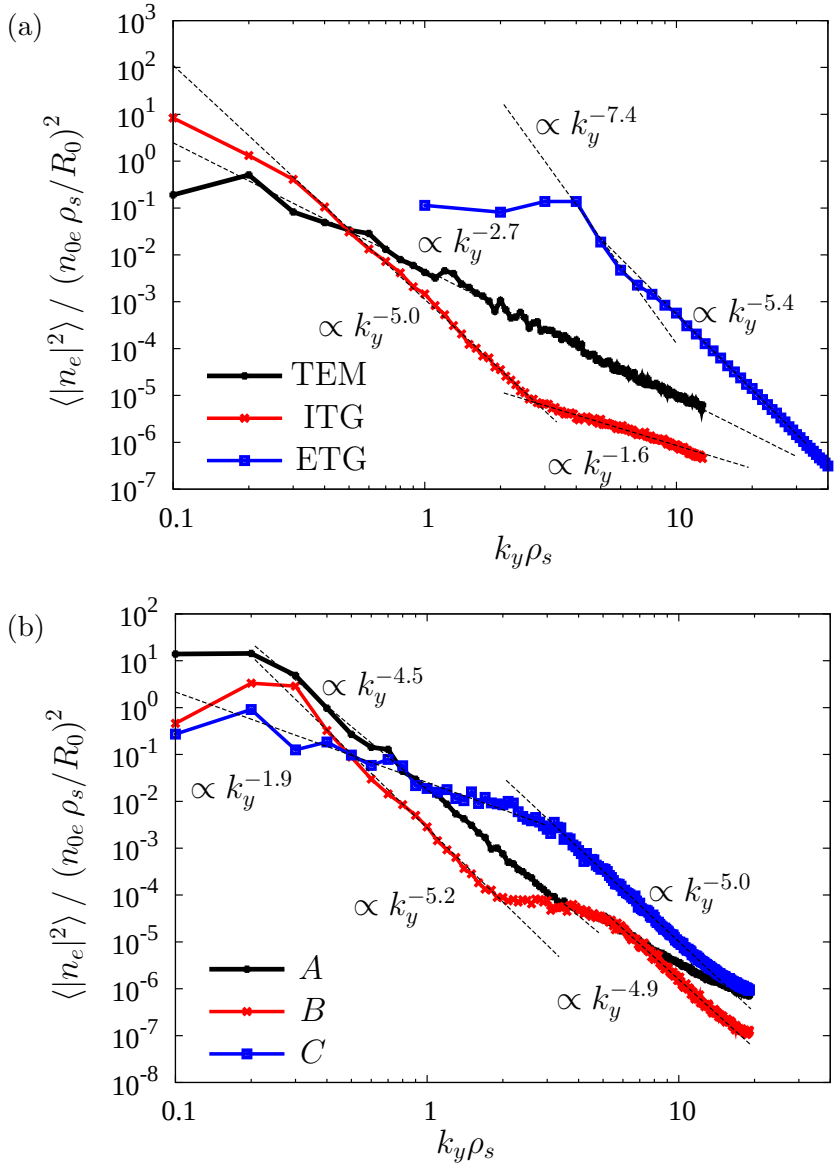

Figure 4.32: Squared electron density fluctuations evaluated at $k_x\rho_s = 0$ and averaged over the parallel direction and time for (a) pure turbulence cases, cf. Fig. 4.29b, and (b) turbulence mixtures, cf. Fig. 4.30b.

tool in gaining insights into the nature of plasma turbulence. The two most famous scaling laws in turbulence theory, Kolmogorov's five-thirds-law for three dimensional fluid turbulence and the dual cascade in two dimensional fluids developed by Kraichnan, Batchelor and Leith, for instance, assume self-similarity, locality, and isotropy (the latter only in the perpendicular directions). Clearly, almost all those requirements fail in the scenarios discussed above. Furthermore, sharply defined injection and dissipation scales

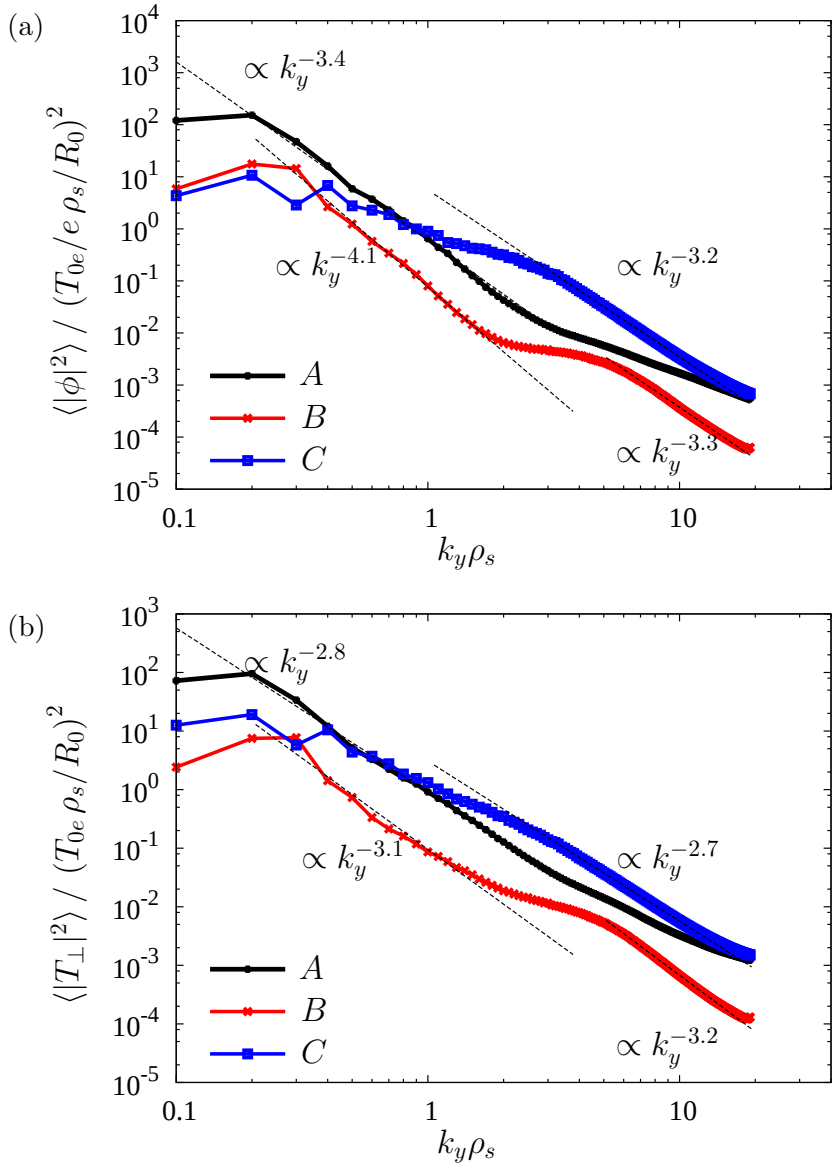

Figure 4.33: Squared (a) electrostatic potential and (b) perpendicular temperature fluctuations averaged over the radial and parallel direction and time for the multiscale simulations (A) to (C).

enclosing an inertial range do not exist since wide ranges of wave numbers are excited linearly, cf. Fig. 4.3. Hence, further numerical investigations are required to provide new bases for alternative analytical models explaining and predicting the power laws, see for instance Ref. [110].

4.5 Frequency spectra and phase velocities

Besides density spectra, spectra of (nonlinear) frequencies or phase velocities represent additional experimentally accessible turbulence characteristics. As will be seen in the following, they might help answering the third question raised in Sec. 4.3.1 on the significance of linear features in saturated plasma microturbulence. Both frequencies and phase velocities are often closely linked to the respective linear quantities, such that relevant information can already be inferred from rather inexpensive linear gyrokinetic simulations. On the other hand, nonlinear effects seem to change the dominant mode within a certain k range with respect to the linear expectations, which has to be taken into account when attempting to compare results from experiments and simulations.

Two different diagnostics have been added to the GENE post-processing tool in order to access the desired nonlinear frequencies. The first one is based on the assumption $\phi_1(t) \sim \mathrm{e}^{\mathrm{i}\omega t}$ which considers just one strong dominant mode with frequency ω governing the dynamics of fluctuating quantities. Hence, given a discrete time series of ϕ_1,

$$\omega \approx \mathrm{Im}\left[\ln\left(\frac{\phi(t)}{\phi(t-\Delta t)}\right)\right]/\Delta t, \tag{4.7}$$

can be applied to approximate the frequency. Naturally, this approach is convenient for linear runs where the mode possessing the largest growth rate eventually determines the entire dynamics. Thus, an identical algorithm is implemented in GENE itself to calculate growth rate and frequency directly and stop (linear) initial value calculations as soon as the values of all z and connected k_x grid points lie within a predefined confidence interval —assuming the frequencies follow a normal distribution.

Nonlinearly, this approximation has to be handled with care, however, especially if two or more modes are strongly excited at the same wave number. In that case, the resulting value is not necessarily identical with the dominant real frequency but closely linked to the first moment of the frequency spectrum. However, Eq. (4.7) usually yields a robust and easily accessible quantity which at least allows to determine, e.g., whether a certain wave number is influenced more by ITG or by TE-ETG modes.

The corresponding results are shown in Fig. 4.34 together with the linear frequency of the dominant mode. Clearly, nonlinear and linear frequencies agree well over a significant region in k_y space in simulation (C). On the contrary, both simulations with unstable ITG modes (A,B) show differences when the ITG mode becomes linearly subdominant at $k_y\rho_s \approx 0.4$. Instead of changing sign, the nonlinear real frequency predominantly remains positive up to $k_y\rho_s \approx 1.5$. Possible explanations for this finding are strong, linearly subdominant modes which become dominant nonlinearly due to different saturation mechanisms or, on the other hand, modes which transfer some of their features to neighboring scales.

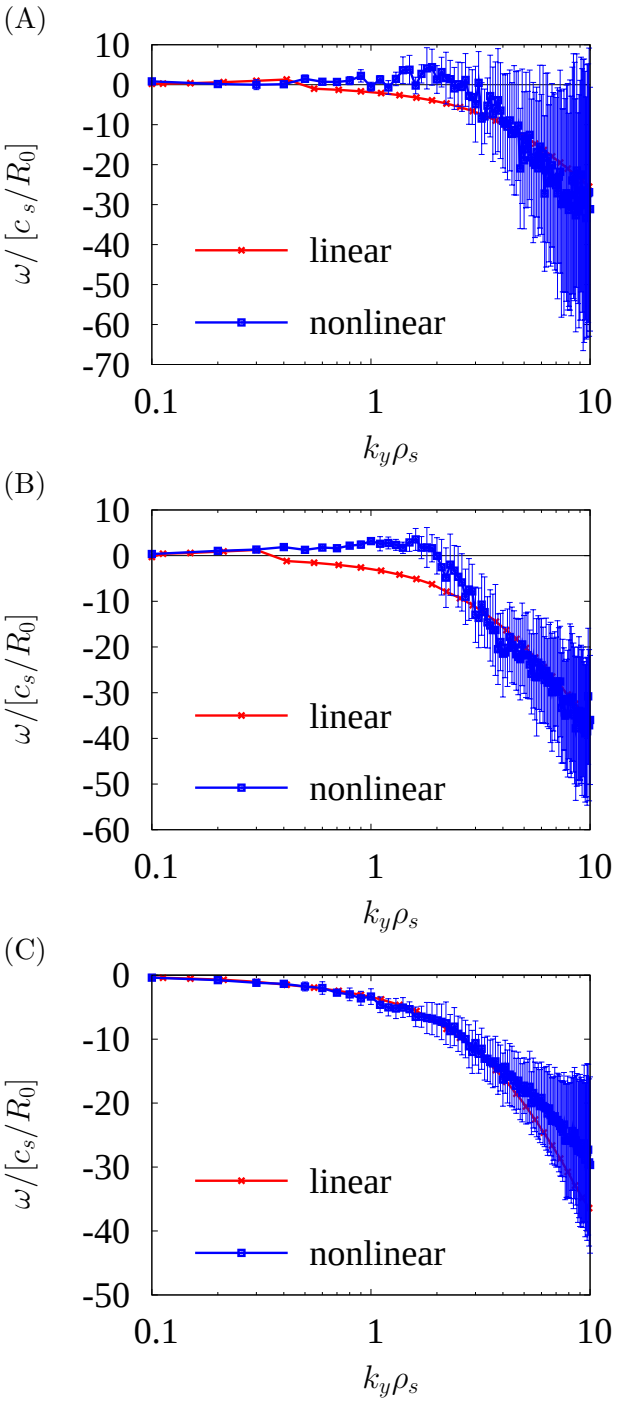

Figure 4.34: Dominant real frequency, defined as the median of Eq. (4.7) at $k_x\rho_s = 0$ for the multiscale simulations (A) to (C) with (blue) and without (red) consideration of the nonlinearity. The error bars denote the one standard deviations.

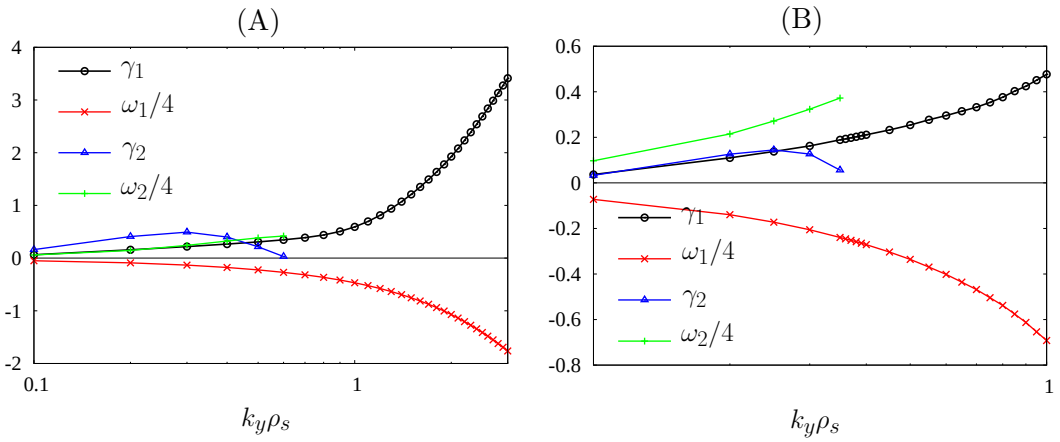

Figure 4.35: Linear growth rates and real frequencies of the dominant and the first subdominant mode at $k_x\rho_s = 0$ in c_s/R_0 in the small-to-medium k_y, range using the same parameters as in the multiscale simulations (A) and (B).

Hence, the eigenvalue solver is now employed to investigate where modes characterized by positive frequencies are subdominantly excited. As can be seen in Fig. 4.35, an upper limit can be found around $k_y\rho_s \approx 0.5$ which rules out the first explanation mentioned above, at least for $k_y\rho_s \gtrsim 0.5$. At very high wave numbers, the nonlinear behavior reflects the linear one again to good approximation. Furthermore, the one standard deviations are shown in Fig. 4.34 as error bars. With increasing wave number, they become larger; thus, it is more difficult to assign certain frequencies to small-scale fluctuations. This may, in part, be due to cross-scale interactions with large-scale turbulence [84]. Nevertheless, in all cases shown here, the existence of ETG turbulence at high wave numbers is clearly reflected in the frequency spectra.

As already mentioned in the beginning of this section, a second approach to examine nonlinear frequencies is available. Here, time traces of fluctuating quantities are analyzed by means of Fourier transforms. However, the stochastic behavior of turbulence does not provide periodicity in time, which is why windowed FFTs employing either Hamming or Hanning apodization functions being well-known from signal processing theory, see e.g. Ref. [111], are used. A disadvantage is the decreased resolution in frequency $\Delta\omega = 2\pi/\Delta t$, since the full time range is typically split into several windows. Since the results do not differ significantly from those shown in Fig. 4.34, they are only presented for one multiscale simulation (B) in Fig. 4.36.

Finally, phase velocities $v_{\mathrm{ph}} = \omega/k_y$ can be computed on the basis of the aforementioned frequencies. For the parameters under consideration, they are bound to the range $|v_{\mathrm{ph}}| \lesssim 5\, c_s\rho_s/R_0$. While case (C) exhibits almost a constant value of $-3.5\, c_s\rho_s/R_0$, the situation changes when ITG modes are present. Here, a positive phase velocity up to $5\, c_s\rho_s/R_0$ is observed at $k_y\rho_s \lesssim 1-2$, while higher wave numbers exhibit $v_{\mathrm{ph}} < 0$.

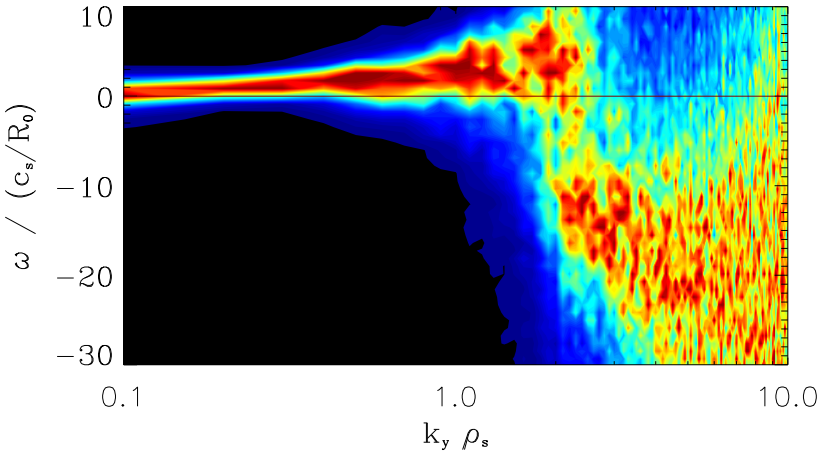

Figure 4.36: Frequency spectra of $|\phi_1(k_x = 0)|$ vs. binormal wave number k_y for multiscale simulation (B).

4.6 Beyond the prototypical parameter sets

As stated in the beginning of this chapter, several physical effects have been neglected in the foregoing multiscale investigation for the sake of simplicity. For instance, only electrostatic plasmas in a simplified geometry have been considered. While the former assumption may have only a minor influence when investigating low-β discharges, the latter might potentially result in significant quantitative as well as qualitative differences, see, for example, Ref. [27].

Therefore, simulation results using parameters and geometries from actual experimental discharges shall be discussed in the following. In particular, the ohmic DIII-D discharge #126848 at $t = 1800\,\mathrm{ms}$ and $\rho/\alpha = 0.35$ is considered, with data kindly provided by T. Rhodes. Here, $\rho = \rho_{\mathrm{tor}} = (\Psi_{\mathrm{tor}}/\pi B_{\mathrm{ref}})^{1/2}$ replaces r as the radial coordinate since noncircular flux surfaces are considered, cf. Fig. 4.37, and $\alpha = \rho|_{\mathrm{separatrix}}$ is comparable to the minor radius. The corresponding metric coefficients are extracted from the specified MHD equilibrium using the TRACER code by P. Xanthopolous [26] which also provides GENE parameters. The latter are the safety factor $q_0 = 1.34$, the magnetic shear $\hat{s} = 0.66$, the normalized electron temperature gradient $\omega_{Te} = 2.6093$, the ion temperature gradient $\omega_{Ti} = 1.9531$, the temperature ratio $T_i/T_e = 0.6717$, and $\beta_{\mathrm{ref}} = 2.015{\cdot}10^{-3}$. For now, only a single ion species (deuterium) is taken into account since impurities are not expected to contribute significantly in the plasma core and would thus only require more computational effort. Therefore, $n_e = n_i$ and $\omega_n \equiv \omega_{ne} = 0.667 \approx \omega_{ni}$ is assumed. Taking further into account the inverse aspect ratio analogon, $\varepsilon = \rho/R_0 \sim 0.16$, it becomes apparent that the full parameter set is comparable to the multiscale parameter

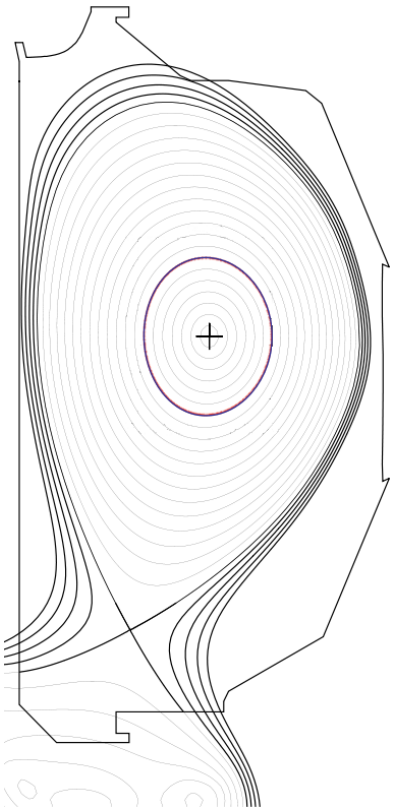

Figure 4.37: Flux surfaces at different ρ_{tor} for DIII-D discharge #126848 at $t = 1800\,\mathrm{ms}$. The flux surface used for the local simulations is highlighted. Source: [112]

set (B). Indeed, linear growth rates and real frequencies shown in Fig. 4.38 look quite similar to the results for said case. As before, two maxima can be identified. The one at low k can be attributed to ITG modes, and the one at high k to ETG modes, following the same argument as before. In between and presumably below the ITG mode, a TEM or TEM/ETG hybrid mode is linearly unstable.

Nonlinear results in terms of heat diffusivity spectra – calculated with respect to the noncircular geometry as described in Appendix B.2 – are presented in Fig. 4.39. Clearly, they resemble previous findings gained with a reduced parameter set. In particular, the ion heat channel is basically ($> 80\%$) driven by $k_y\rho_s < 0.5$ modes, whereas the electron heat diffusivity exhibits contributions of more than 40% originating from $k_y\rho_s > 0.5$ and almost one quarter at $k_y\rho_s > 1$. The numerical parameters of the underlying simulation are the following. In the parallel (z) direction, 24 grid points are used which is higher than in the $\hat{s}$-α case due to the more complicated magnetic field structure. The perpendicular box size is chosen to be $(L_x, L_y) = (64\rho_s, 64\rho_s)$ and 192×384 real space grid points are chosen along these directions. In $(v_\parallel, \mu)$ space, 32×8 grid points are used, as before. The

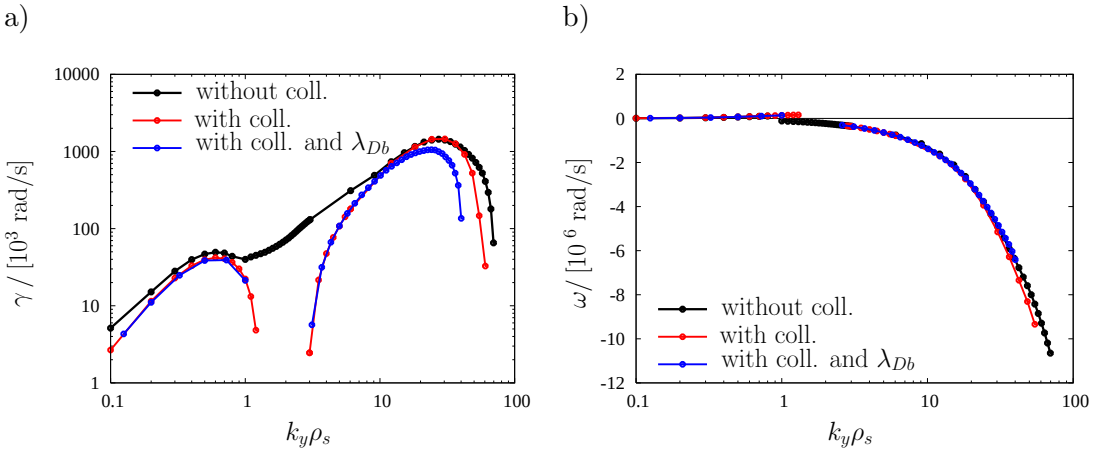

Figure 4.38: Linear growth rate (a) and frequency (b) vs. binormal wave number for discharge 126848 using a mass ratio of $m_i/m_e = 3675.12$.

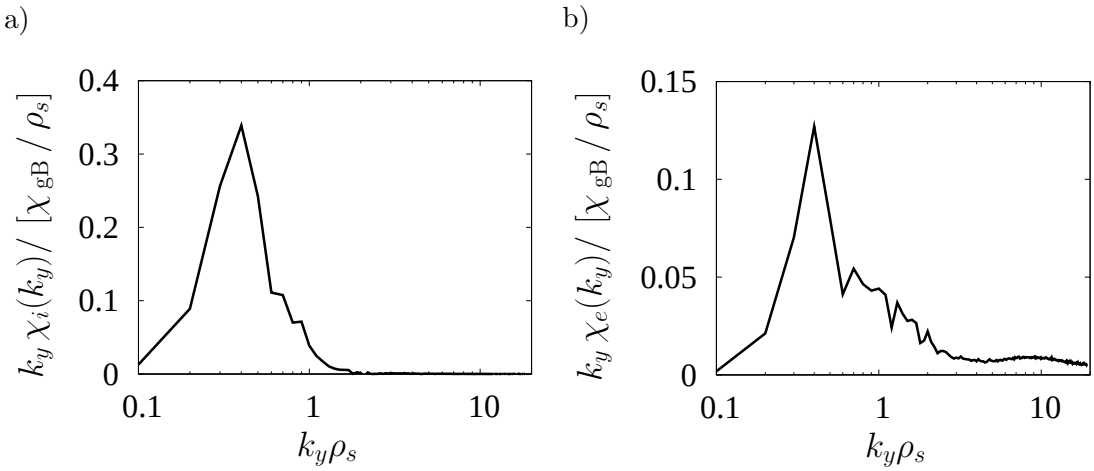

Figure 4.39: Ion (a) and electron (b) heat diffusivities for #126848, multiplied by the binormal wave number vs. binormal wave number. Here, a mass ratio of $m_i/m_e = 400$ is used, and collisions as well as a Debye length are neglected.

mass ratio is again reduced to $m_i/m_e = 400$ which complicates a direct comparison with the experimental values. Assuming a deuterium mass for the ions implies unnaturally heavy electrons with a mass being 4.6 times larger than in reality. The heat diffusivities are then evaluated $\chi_e^{\mathrm{sim}} \sim 3.1\,\mathrm{m}^2/\mathrm{s}$ for electrons and $\chi_i^{\mathrm{sim}} \sim 7.0\,\mathrm{m}^2/\mathrm{s}$ for ions. Contrary to the previously discussed CBC simulation, the difference to the measured diffusivities, $\chi_e^{\mathrm{exp}} \sim 0.6\,\mathrm{m}^2/\mathrm{s}$ and $\chi_i^{\mathrm{exp}} \sim 1.2\,\mathrm{m}^2/\mathrm{s}$ [112], is not one or two orders of magnitude but still a factor of $5-6$. Again, a strong dependence on the turbulent transport to the actual gradient settings might serve as a possible explanation. For example, lowering the ion temperature gradient $\omega_{Ti} = 1.953$ by 20% almost bisects the ion heat diffusivity χ_i^{sim} to

$3.7\,\mathrm{m}^2/\mathrm{s}$. Unfortunately, χ_e^{sim} increases to $6.8\,\mathrm{m}^2/\mathrm{s}$ in this case. Thus, if uncertainties in the gradients would be responsible for the mismatch, a two-dimensional – or, if the temperature ratio is also varied, three-dimensional – nonlinear parameter scan would be required. While such studies have been successfully accomplished when considering only low-k turbulence, full multiscale investigations of this type are not feasible at the moment.

Naturally, the actual numerical parameter choice is a possible candidate for the transport overestimation, as well. Increasing, for instance, the very low radial resolution may raise the high-k electron heat transport level since ETG modes are probably underresolved. On the other hand, this effect might be compensated partly by considering a finite Debye length. The latter is evaluated to $\lambda_D \approx 1.3\,\rho_e$ for the discharge under investigation and is therefore linearly stabilizing the highest mode numbers, as can indeed be observed in Fig. 4.38. Computing the Debye length as defined by Eq. (2.82) for

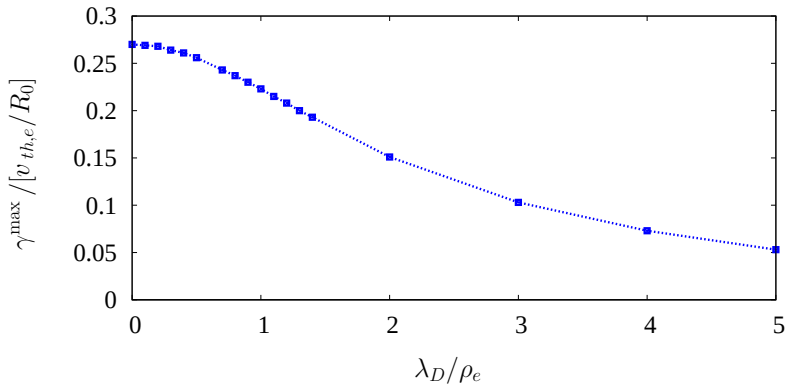

Figure 4.40: Example for the maximum linear growth rate dependence on the Debye length. Here, a pure ETG mode in $\hat{s}$-α geometry is considered.

ITER-like parameters, namely $B_{\mathrm{ref}} \approx 5\,\mathrm{T}$ and $n_e \approx 10^{20}\,\mathrm{m}^{-3}$, leads to a slightly higher value of $\lambda_D \approx 1.6\,\rho_e$. For pure ETG mode simulations in $\hat{s}$-α geometry, this would cause a reduction of about 1/3 in the *maximum* linear growth rate as is shown in Fig. 4.40. Coming back to the DIII-D results, Fig. 4.38 reveals the influence of collisions which are not considered in the nonlinear simulation due to the additionally required computational effort. Most likely, collisions will reduce the transport at low and intermediate wave numbers since TEMs are obviously most susceptible to such modifications. This finding is in agreement with simple explanations arguing that a significant fraction of trapped particles might be (more quickly) turned into passing ones as soon as binary collisions become important. Unfortunately, a detailed investigation of possible effects on turbulence covering several scales has to be left for future work. Finally, an external $\mathbf{E} \times \mathbf{B}$ shear might, in principle, reduce the low-k turbulence, as shown in Ref. [84].

The aim of this section was to demonstrate the general possibility of significant high-k

transport contributions in more experimentally adapted simulations than those used for the basic multiscale study. Assuming that a fraction of $\sim 11\%$ originating from $k_y\rho_s > 2$ will most likely not be affected even by a total omission of TEMs and that collisions and external shear flows tend to decrease the low-k transport level by a significant factor, the original purpose can be considered fulfilled.

4.7 Chapter summary and conclusions

Motivated by recent experimental and theoretical findings on the importance of high-k ETG modes, several nonlinear gyrokinetic simulations employing the GENE code have been dedicated to study the behavior of these modes in the presence of long-wavelength turbulence, in particular ITG and TE modes. For this purpose, two spatial and temporal scales connected to these turbulence types had to be covered self-consistently. The resulting numerical problem turned out to be on the verge of present day's supercomputing capabilities and has therefore rarely been addressed in the past. Using three different prototypical sets of parameters, it has been found that for realistic ion heat (and particle) flux levels and in the presence of unstable ETG modes, there tends to be a scale separation between ion and electron thermal transport. In contrast to the former, the latter may exhibit substantial or even dominant high-wave-number contributions carried by ETG modes and short-wavelength TEMs. Compared to TEM simulations with linearly stable ETG modes, it becomes clear that ETG modes may potentially influence the transport spectrum over a surprisingly wide range, down to $k_y\rho_s \approx 0.5$ in the cases studied here.

In terms of experimentally accessible spectral quantities, it was found that multiscale simulations involving unstable ETG modes tend to exhibit a flat region in the binormal wave number spectrum of density fluctuations at $k_y\rho_e \gtrsim 0.1$. At both longer and shorter wavelengths, power law decays are observed which are more or less in line with respect to earlier, single-scale simulation results. In the case of a TEM-ETG turbulence mixture (with stable ITG modes), a remarkable level of agreement with recent experimental findings, claiming that the power law exponent becomes much larger at $k_y\rho_s \gtrsim 1$, has been observed. However, the results do not match quantitatively, most probably because several potentially important physical effects (like collisions, magnetic fluctuations, realistic geometry, or a finite Debye length) were neglected here for simplicity. It shall also be noted that most experimental measurements were done close to the edge, while all multiscale simulations in this chapter employed typical core parameters and geometries. In addition, increasing the mass ratio to realistic values would lead to a further separation of ion and electron scales and would therefore likely alter the results quantitatively.

Based on the investigations on the influence of the mass ratio on the growth rate maxima presented in this chapter, qualitative findings are nevertheless expected to remain

valid, in particular the fact that high-k modes may contribute significantly to the electron heat transport, although the density spectra may exhibit a rather fast decay. This effect might be even further enhanced in situations where ITG modes are hampered and thus subdominant or (nonlinearly) stable as in plasmas, e.g., with dominant electron heating, relatively high β values, substantial equilibrium $\mathbf{E} \times \mathbf{B}$ shear, or internal transport barriers. Simulations for specific fusion devices employing more complete physics are left for future work.

On the other hand, the experimental detection of a flat region in the binormal wave number spectrum of the density fluctuations at around $k_y \rho_e \gtrsim 0.1$ would be a good indication for the existence of strong ETG activity. Currently, several diagnostics are under development or being extended to capture the small scales, so that comparisons between experiments and numerical results might become possible in the near future. Naturally, such investigations would not need to be restricted to density spectra but could also be based on measurements of frequencies or phase velocities at short wavelengths, as has been shown above.

Chapter 5

Benchmarks and first results including nonlocal effects

The present chapter is dedicated to the verification of the global GENE implementation and the presentation of first nonlocal results. The first task is performed by means of several benchmarks—either with analytical test cases or – if they already exist – with other codes solving the same or very similar sets of equations. In the following, several corresponding studies with increasing complexity will be presented.

5.1 The local limit

A first obvious test is a direct comparison of both implementations available in GENE, i.e. the approach based on spectral methods and the one employing finite differences and interpolations in radial direction instead. Naturally, this practice cannot be utilized for the verification of nonlocal contributions, but ensures that both versions produce similar results when using the same physical parameters and boundary conditions. However, examples are not shown because they constitute a sub-ensemble of the next, more elaborate test. Here, radially varying profiles are included and ρ^* is then decreased until the global code eventually reaches the local limit. As a side effect, first judgments on the validity of local simulations for specific devices can be drawn.

For this purpose, two different profile types also used in other codes, e.g. ORB5 [113, 114], will be employed in the following. The first one is defined by

$$\begin{aligned} \hat{T}_{i,e} &= \exp\left[-\kappa_T \varepsilon \Delta T \tanh\left(\frac{(x-x_0)/a}{\Delta T}\right)\right], \\ \hat{n}_{i,e} &= \exp\left[-\kappa_n \varepsilon \Delta n \tanh\left(\frac{(x-x_0)/a}{\Delta n}\right)\right] \end{aligned} \tag{5.1}$$

and will be called the *peaked* (gradient) profile. The second type is characterized by *flat*

top gradient profiles and is defined by

$$\hat{T}_{i,e} = \left[\frac{\cosh\left(\frac{(x-x_0)/a+\delta T}{\Delta T}\right)}{\cosh\left(\frac{(x-x_0)/a-\delta T}{\Delta T}\right)}\right]^{-\kappa_T\,\varepsilon\,\Delta T/2} \quad \text{and} \quad \hat{n}_{i,e} = \left[\frac{\cosh\left(\frac{(x-x_0)/a+\delta n}{\Delta n}\right)}{\cosh\left(\frac{(x-x_0)/a-\delta n}{\Delta n}\right)}\right]^{-\kappa_n\,\varepsilon\,\Delta n/2}. \tag{5.2}$$

Here, δT and ΔT (and δn, Δn, respectively) are characteristic profile widths as demonstrated in Fig. 5.1. Furthermore, $\kappa_T = \max(R_0/L_T)$ and $\kappa_n = \max(R_0/L_n)$ denote the maximum temperature and density gradient values and ε is the inverse aspect ratio between minor radius a and major radius R_0. They will be set similar to the CBC parameters used before, i.e. $\kappa_T = 6.96$, $\kappa_n = 2.23$ and $\varepsilon = 0.36$. In addition, the shape of

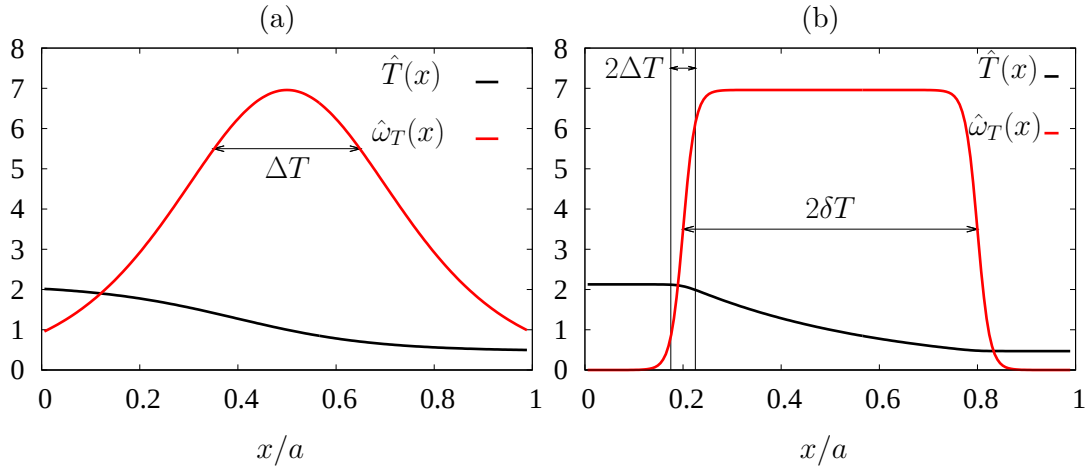

Figure 5.1: Illustration of the normalized background temperature profiles together with the normalized gradients described in Sec. 5.1. The density profiles are chosen similar but may have different widths and amplitudes.

the flux surfaces is assumed to be circular and concentric with a safety factor profile of $q(x/a) = 0.498(x/a)^4 - 0.466(x/a)^3 + 2.373(x/a)^2 + 0.854$ so that $q_0 = q(x_0 = 0.5) = 1.42$ matches the CBC value.

5.1.1 ρ^* scan with fixed box size in ion gyroradius units

In a first test, the radial simulation box length is kept fixed with respect to the gyroradius. Hence, with decreasing ρ^* parameter, it becomes smaller and smaller compared to the minor radius a so that eventually only a very narrow region about a central flux surface at $x/a = 0.5$ is taken into account. Naturally, such simulations should be close to those performed with a local code if periodic boundary conditions are assumed. The resulting growth rates using adiabatic electrons are presented in Fig. 5.2. Note that each simulation has been performed at the wave number being closest to $k_y\rho_s = 0.3$.

However, the exact value cannot be chosen in general since the quantization condition, see Sec. 3.3.3, has to be fulfilled. The resulting deviations tend to be larger with increasing ρ^* values which explains the jagged behavior in this region. All in all, a very good agreement with the local result can be observed for different profiles and widths at small ρ^*. However, at larger ρ^* values both code versions start to diverge. For instance, at a

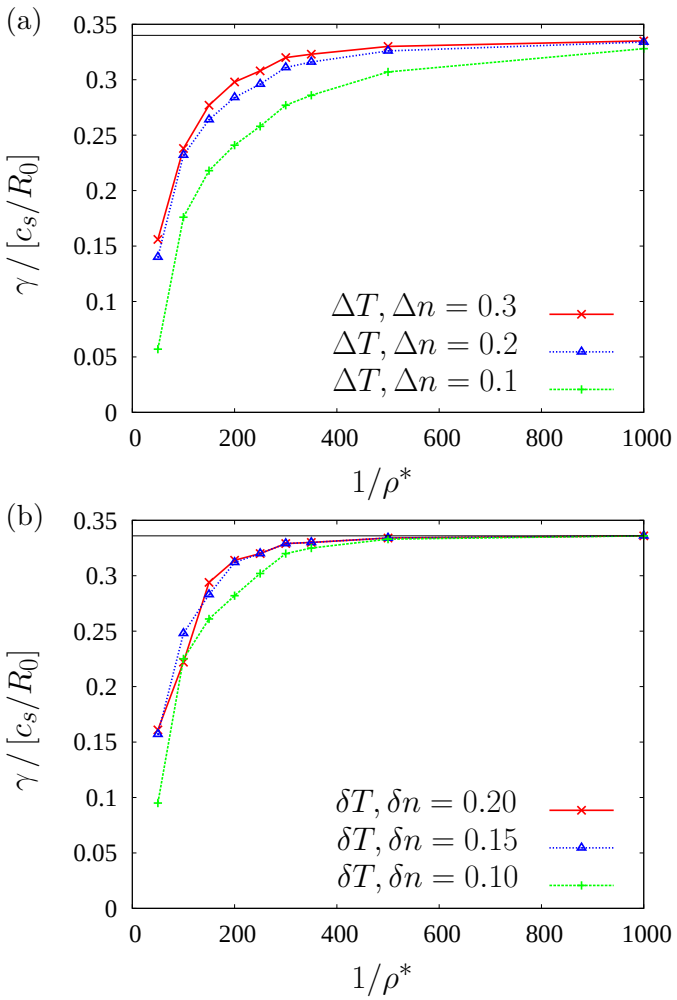

Figure 5.2: Growth rate of an ITG mode with adiabatic electrons at $k_y\rho_s \approx 0.3$ as function of the inverse ρ^* value using (a) the peaked and (b) the flat temperature and density gradient profiles. The latter are additionally employing $\Delta T, \Delta n = 0.025$ as second characteristical width. Here, the radial simulation box length is kept fixed with respect to the gyroradius and the number of grid points is set to (a) $(64 \times 16 \times 48 \times 16)$ and (b) $(64 \times 16 \times 64 \times 32)$ in the $(x, z, v_\parallel, \mu)$ directions. The local code result using the maximum gradients is shown as thin, black line.

ratio of $\rho^* = 1/200$ which can be reached in medium-sized tokamaks, the differences are about $12 - 16\%$ when using the peaked profile with $\Delta T = 0.3$ and 0.2. Going further to even narrower gradient profiles with $\Delta T = 0.1$, the deviation increases to almost

30%. However, such strongly peaked profiles are unlikely to be realized in experiments. Changing to another profile shape, as shown in Fig. 5.2(b), does not significantly alter these findings. For example, employing the peaked profile with $\Delta T = 0.2$ and the flat shape with $\delta T = 0.1$ yields growth rates which deviate by less than 5%—only at $\rho^* = 1/50$ a significant difference can be observed.

5.1.2 ρ^* scan with fixed box size with respect to the minor radius

A second approach is to fix the radial simulation box size with respect to the macroscopic length, in particular the minor radius. A change in ρ^* thus corresponds to a change of the gyroradius. This effect has to be considered when choosing the number of grid points since the resolution has to be adjusted for each ρ^* value due the strong correlation between the gyroradius and the actual turbulent length scale. The resulting growth

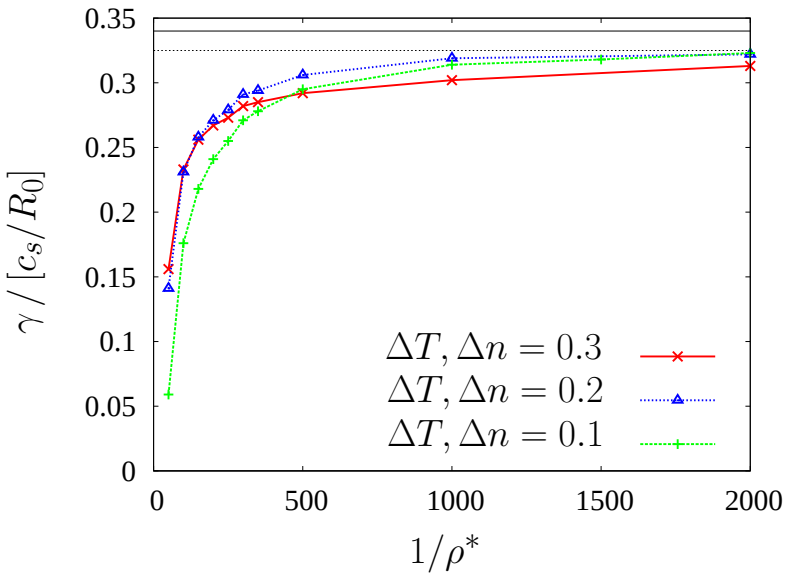

Figure 5.3: Growth rate of an ITG mode with adiabatic electrons at $k_y\rho_s = 0.3$ as function of inverse ρ^* using the peaked temperature and density profile. Here, the radial simulation box length is kept fixed with respect to the minor radius a and $(16 \times 48 \times 16)$ grid points are employed in the $(z, v_\parallel, \mu)$ directions while the number of radial grid points is adjusted to each ρ^* value. The local code result using the maximum gradients is shown as thin, solid black line for $k_x\rho_s = 0$ and as black, dashed line for $k_x\rho_s = -0.038$.

rates of ITG simulations using adiabatic electrons are shown in Fig. 5.3. Again, a fast convergence towards the local results can be observed with decreasing ρ^* values. While the difference for the narrowest gradient profile with $\Delta T, \Delta n = 0.1$ amounts, for instance, to more than 80% at $\rho^* = 1/50$, it is already decreased to 30% at $\rho^* = 1/200$. However, at smaller ρ^* only a very slow convergence compared to the first ρ^* test is

observed. On the other hand, it might seem astonishing that this kind of test converges

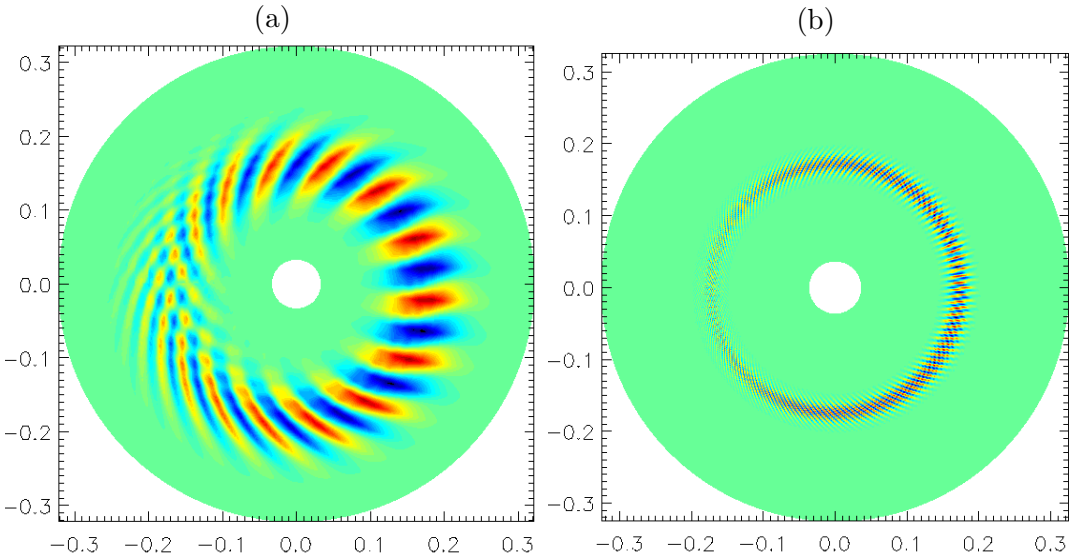

Figure 5.4: Poloidal cross-section of the electrostatic potential for (a) $\rho^* = 1/100$ and (b) $\rho^* = 1/1000$. Although temperature and density profiles are kept constant, a decreasing eddy size is observed.

towards the linear result at all, given that only a very narrow region possesses the same gradient drive as in the local simulation. A possible explanation is given by Cowley and co-workers [48] who estimate the radial extend of a turbulent eddy to scale as $\sim \sqrt{\rho_s L_T}$. Thus, with decreasing gyroradius and constant temperature gradient profile, the vortices become more and more localized about the maximum gradient as can be seen in Fig. 5.4 where poloidal cross-sections are presented for two different settings of ρ^*, namely 1/100 and 1/1000. Indeed, the ratio of the radial widths is here given by $3.1 \approx \sqrt{10}$. The mentioned localization about the maximum gradient might now help to explain the increasing growth rate since the eddies now "feel" a stronger drive. On the other hand, the square root dependence on ρ_s is a first but probably not comprehensive explanation for the slower convergence. An additional issue is, for instance, a slight tilting of the eddies which can be seen in Fig. 5.4. As explained in Ref. [49], such finite ballooning angles θ_0 are linked to finite k_x values by $k_x = -k_y \hat{s} \theta_0$. Indeed, the agreement between the local and the nonlocal code gets even better when those effects are considered. For instance, k_x can be estimated to be $k_x \rho_s \approx -0.0377$ for the narrowest profile at $\rho^* = 1/500$. The corresponding local result is included in Fig. 5.3 as thin, dashed line. Obviously, the agreement with the global growth rates at small ρ^* is improved.

5.1.3 Kinetic electrons and electromagnetic effects

Up to now, all ρ^* tests have been performed using adiabatic electrons and thus without any magnetic effect. However, the consideration of both kinetic electrons and $A_{\parallel 1}$ does does not change the general behavior as can be seen in Fig. 5.5. Here, the electron

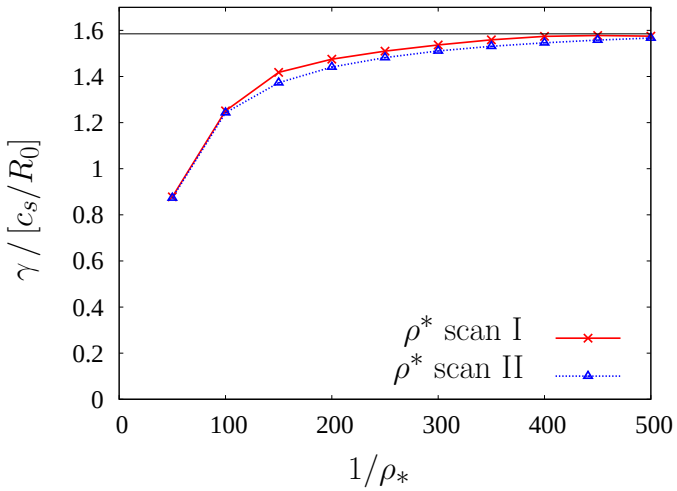

Figure 5.5: Growth rate at $k_y\rho_s \approx 0.284$ as function of the inverse ρ^* value. Here, kinetic electrons with a proton-electron mass ratio are considered as well as a finite β_{ref} of 2.5%. The temperature and density gradient profiles are peaked with $\Delta T_{i,e}, \Delta n = 0.3$. The radial simulation box is kept fixed with respect to (I) the gyroradius and (II) the minor radius. Here, the number of grid points is set to $(128 \times 16 \times 64 \times 16)$ n the $(x, z, v_\parallel, \mu)$ directions. The local code result using the maximum gradients is shown as thin, black line.

and ion temperature and density gradient profiles are chosen to be peaked, i.e. following Eq. (5.1) with $\Delta T, \Delta n = 0.3$. The mass ratio is set to $m_i/m_e = 1836$ as in hydrogen plasmas. Furthermore, $\beta_{\text{ref}} = 2.5\%$ so that kinetic ballooning modes dominate. Generally, both resolutions in the $(x, v_\parallel)$ directions need to be increased to higher values if kinetic electrons are considered. The most likely reason for this is the electron behavior at mode rational flux surfaces [115], i.e. flux surfaces with low-order rational safety factor. Here, magnetic field lines connect to themselves after few poloidal turns which allows the electrons to become non-adiabatic. In the present case, at least (128×64) grid points had to be taken in the $(x, v_\parallel)$ directions.

Based on these local limit tests, one can state that the applicability of local codes to medium or large-scale tokamaks is strongly supported in the linear regime. However, the particular convergence behavior depends on the chosen profiles.

5.2 Rosenbluth-Hinton test

A well established test for gyrokinetic codes is based on the time evolution of an initial $\mathbf{E} \times \mathbf{B}$ zonal flow impulse in a toroidal plasma with circular flux surfaces and a large aspect ratio. In the absence of collisions and any nonlinear coupling, a rapid but damped oscillation of the geodesic acoustic mode (GAM) [116] is observed which relaxes to a finite stationary value A_R so that

$$\frac{\langle \phi_1 \rangle_{\mathrm{FS}}(x,t)}{\langle \phi_1 \rangle_{\mathrm{FS}}(x,t=0)} = (1 - A_R)\, \mathrm{e}^{-\gamma_G t} \cos(\omega_G t) + A_R. \tag{5.3}$$

In the local limit and for adiabatic electrons, the residual has been analytically predicted by Rosenbluth and Hinton [117, 118] to be

$$A_R = \frac{1}{1 + 1.6\, q(x)^2 / \sqrt{x/R_0}}. \tag{5.4}$$

Since zonal flows are identified as one of the most important saturation mechanisms in several parameter regimes, for instance in ITG mode dominated turbulence, it is widely accepted that this test has to be passed by gyrokinetic codes. For the local GENE version, detailed benchmark results are available in [14] and [41] where the latter work focuses on the influence of additional hyperdiffusion terms.

In the following investigation, the same physical parameters as in Sec. 5.1.1 are employed—except for the temperature and density profiles which are taken to be constant as in the analytic calculation. The number of grid points in the $(x, z, v_\parallel, \mu)$ directions is $(63 \times 16 \times 128 \times 16)$ and the box lengths are chosen to be $(L_x, L_{v_\parallel}, L_\mu) = (48\rho_{\mathrm{ref}}, 3\, v_{Ti}(x_0), 9\, T_{0i}(x_0)/B_{\mathrm{ref}})$. The resulting residual levels at the center of the simulation domain are plotted in Fig. 5.6 for several ρ^* values. While the deviation from the Rosenbluth-Hinton prediction is significant at large ρ^*, it becomes less than 10% at $1/\rho^* \gtrsim 200$. In contrast to the former case, the latter appears to have a flatter safety factor profile throughout the simulation domain, thus being more consistent with the work by Rosenbluth and Hinton where a constant q has been assumed. However, a perfect agreement between the numerical and analytical results is never achieved in this test. Nevertheless, taking into account the approximations performed by Rosenbluth and Hinton, e.g. the large aspect ratio assumption, the benchmark can be considered to be successful.

A further example employs parameters being similar but not identical to those presented in Ref. [113]. In particular, they prescribe a linear safety factor profile $q(x/a) = 0.7 + 0.9 \cdot (x/a)$ and an inverse aspect ratio of $a/R_0 = 1/10$. With this choice, an even better agreement with the analytic prediction can be expected, although ρ^* is taken to be 1/40. The numerical parameters are the same as before, except for the radial direction where 48 grid points are taken along a box length of $L_x = 38\rho_{\mathrm{ref}}$. Contrary to local

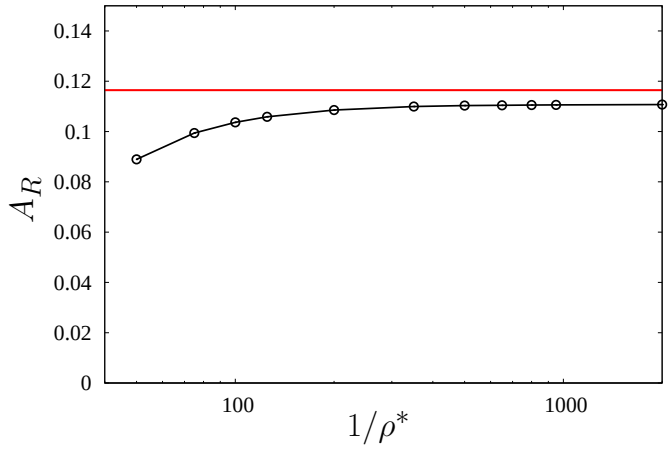

Figure 5.6: Rosenbluth-Hinton residual (black dots and line) evaluated at the radial center position of the simulation box for different settings of ρ^*. The red line indicates the Rosenbluth-Hinton prediction.

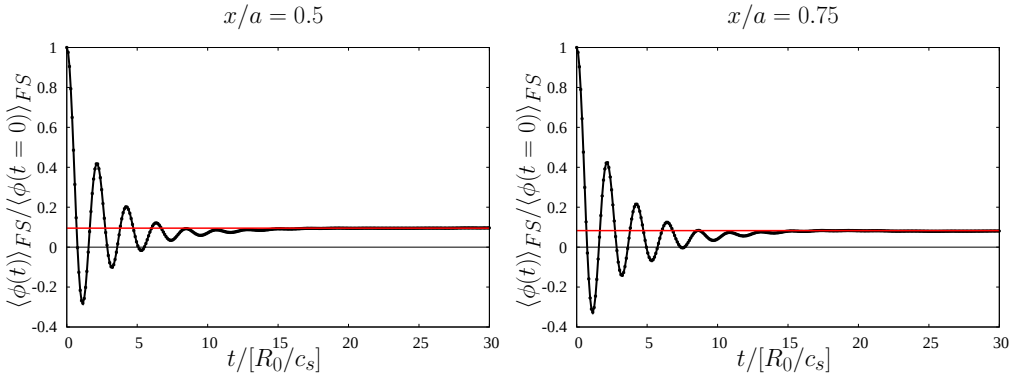

Figure 5.7: Rosenbluth-Hinton test at two different radial positions using a linear safety factor profile. The red line indicates the residual as predicted by Rosenbluth and Hinton.

codes where exactly one safety factor q and radial position x/R_0 tuple is chosen and thus just one residual can be investigated per simulation, a global code automatically provides results for a wide parameter range. Therefore, time traces taken at two different radial positions are presented in Fig. 5.7. In both cases, the damped oscillations end up in residual levels which are indeed in very good agreement with the prediction made in Eq. (5.4). Furthermore, the frequencies gained by fitting the time traces to Eq. (5.3) deviate by less than 5% from another analytical result,

$$\omega_G \frac{R_0}{c_s} = \sqrt{\frac{(7/\tau_e + 4)\mathcal{A}_G}{2}} \tag{5.5}$$

with $\tau_e = T_e/T_i$ and $\mathcal{A}_G = \left[1 + (2(23 + 16\tau_e + 4\tau_e^2))/(q(7 + 4\tau_e))^2\right]$, which can be found

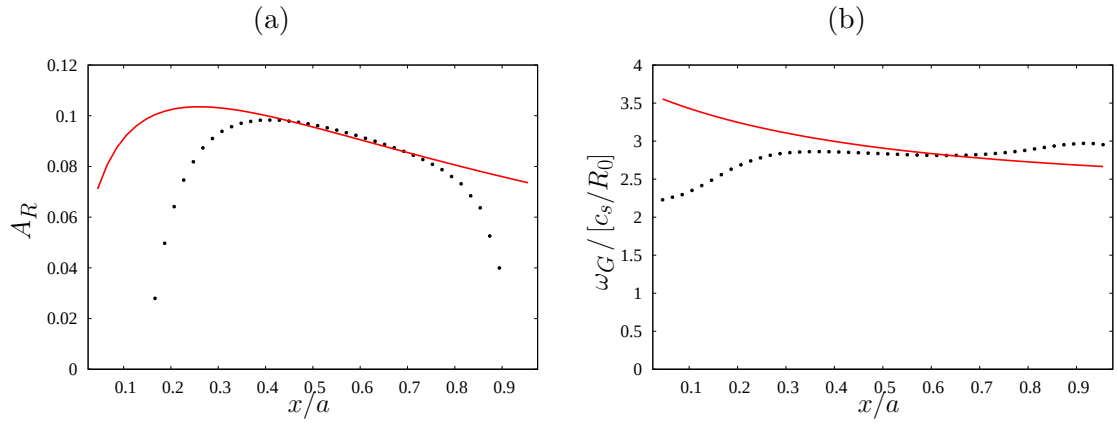

Figure 5.8: Rosenbluth-Hinton residual (a) and oscillation frequency (b) evaluated at all radial positions except for the two outermost grid points. The black dots represent numerical results whereas the red solid line illustrates the analytical prediction. Note that negative values are suppressed.

in Ref. [119]. Motivated by these results, another plot is shown in Fig. 5.8 where the residual level and the oscillation frequency are displayed for all radial positions except for the two outermost grid points. Clearly, both values agree well with the predictions within $0.3 \lesssim x/a \lesssim 0.8$. The deviations at the remaining radial positions can be attributed to the Dirichlet boundary condition. Considering the relatively large reference gyroradius $\rho_s = 0.025\,a$ employed in this simulation, it is obvious that gyroaverages at intermediate to high μ values, which might partially be calculated outside the simulation domain, may exhibit an influence even at radial positions being far away from the boundaries. Indeed, simulations at smaller ρ^* ($\rho^* = 1/100, 1/200$), possess a narrower transition region but do not show such excellent agreement. For instance, numerical and analytical residual levels deviate up to about 20% at $x/a = 0.3$. Hence, the remarkable coincidence found in the present case seems to be restricted to a very narrow parameter regime.

5.3 Linear benchmarks

Having successfully passed the Rosenbluth-Hinton and local limit tests, more complicated scenarios involving more comprehensive physical effects can be studied.

In this section, direct comparisons between GENE and the global particle-in-cell (PIC) code GYGLES [120] solving the linear gyrokinetic equations are presented. Once again, parameters similar to the CBC set are employed so that $\varepsilon = a/R_0 = 0.6043\,\mathrm{m}/1.6714\,\mathrm{m} = 0.3616$. The temperature and density profiles of the gyrokinetic ions and adiabatic electrons are assumed to follow Eq. (5.1) with gradient peak values of $\kappa_T = 6.9589$ and $\kappa_n = 2.2320$ at $x_0 = 0.5\,a$. The characteristical widths, see Fig. 5.1, are set to

$\Delta T = \Delta n = 0.3$. Extracting from the DIII-D discharge 81499 which constitutes the CBC basis, a temperature of $T_0(x_0) = 1.9693\,\mathrm{keV}$ and a reference magnetic field of $B_{\mathrm{ref}} = 1.9\,\mathrm{T}$ allows for estimating $\rho^* \approx 1/180$ in case of pure Deuterium plasmas. The geometry is chosen to be circular concentric as before with a parabolic safety factor profile of

$$q(x/a) = 0.854 + 2.4045\,(x/a)^2. \tag{5.6}$$

The resulting growth rates and frequencies gained by GYGLES [121] and GENE are presented in Fig. 5.9 and show excellent agreement except for the highest k_y modes. However, this deviation can be explained by the different treatment of gyroaverage and

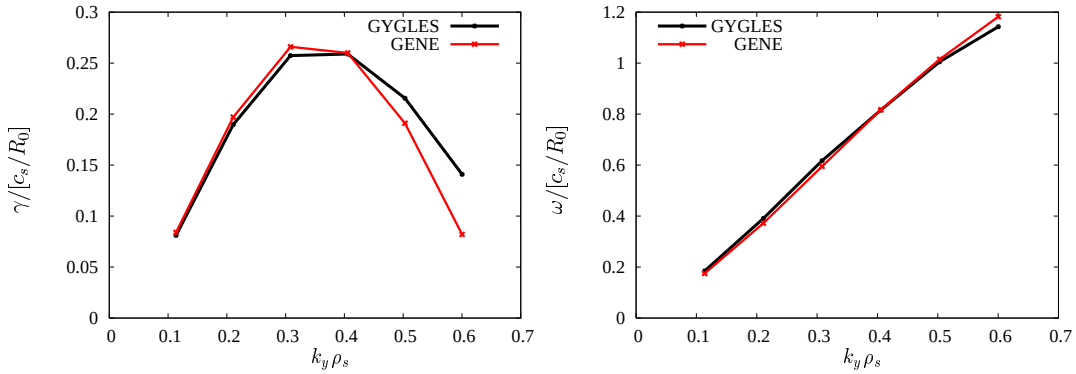

Figure 5.9: A comparison of growth rates (left) and real frequencies (right) calculated by the linear, gyrokinetic PIC code GYGLES and the global GENE version for an adiabatic electrons test case further described in the text.

field operators at these wave numbers. In the GYGLES version at hand, a long wavelength approximation, $k_\perp \rho \ll 1$, is applied so that Larmor radius effects are kept up to second order $(k_\perp \rho)^2$ while all orders are considered in GENE.

The numerical GENE parameters employed in the present linear study are the following. At each binormal wave number, the radial box size is set to $L_x = 160\rho_s$ and 16 grid points are used in the parallel direction. All remaining grid sizes and resolutions vary. For instance, at low wave numbers, i.e. $k_y\rho_s < 0.5$, $(160 \times 32 \times 16)$ grid points in the $(x, v_\parallel, \mu)$ directions and a velocity space box of $(L_{v_\parallel}, L_\mu) = (3\,v_{Ti}(x_0), 9\,T_{0i}(x_0)/B_{\mathrm{ref}})$ turn out to be sufficient while at higher wave numbers up to $(256 \times 64 \times 128)$ grid points and $(L_{v_\parallel}, L_\mu) = (5\,v_{Ti}(x_0), 18\,T_{0i}(x_0)/B_{\mathrm{ref}})$ are required.

In general, it is not surprising that the velocity space resolution and the box sizes have to be increased compared to typical local code settings since velocity space structures vary with the thermal velocity or the temperature, respectively. Taking into account the fixed normalization to a reference temperature, cf. Sec. 2.2.3, the according boxes have thus to be enlarged to cover the structures at high temperatures, and highly resolved

to consider the small structures at low temperature. However, only a fraction of the simulation domain centered around the gradient peak actually needs to be considered in this argument. Otherwise, an estimate based on the present total temperature variation by a factor of about 4 would demand for higher resolutions and larger box sizes than actually required. Indeed, local simulations confirm regions with $R_0/L_{Ti} \lesssim 3.3$ to be linearly stable so that underresolved grids at those radial positions may exhibit a negligible influence in a global investigation.

Up to now, only explanations for a general increase of grid sizes and resolutions have been given which are not considered to exhibit a k_y dependence. However, the linear benchmark revealed an additional requirement for high resolutions at higher wave numbers—especially in μ direction. This effect is most likely caused by oscillating terms appearing in the gyroaverage operator, Eq. (3.46), which contain $k_y\rho_\sigma(x, z, \mu)$. In numerical μ integrations being performed, e.g. in the field equations, those terms clearly raise the necessary number of according grid points if the oscillations become faster with higher k_y.

5.4 Nonlinear benchmark

In 2008, a test case for nonlinear gyrokinetic simulations with adiabatic electrons has been defined within the framework of the European Integrated Tokamak Modeling (ITM) benchmarking effort [122] and is now employed to check the nonlinear GENE behavior.

The underlying physical parameters are very similar to those used in the linear GYGLES-GENE comparison so that only important deviations are listed in the following. In particular, they comprise the temperature and density profiles since their gradients are not peaked but flat over a wide radial range. In fact their shapes bear strong resemblance to those shown in Fig. 5.1(b). However, they are not identical since the corresponding function is

$$\omega_{(T,n)}(r) = \kappa_{(T,n)} \left(1 - \operatorname{sech}^2\left[(r - r_i)/(a\Delta r)\right] - \operatorname{sech}^2\left[(r - r_a)/(a\Delta r)\right]\right) \tag{5.7}$$

with $r_i/a = 0.1$, $r_a/a = 0.9$ and $\Delta r = 0.04$.

The benchmark itself describes a nonlinear relaxation problem, i.e. no additional sources or sinks are applied. As mentioned in Sec. 3.7, the instability is then first expected to develop due to the linear ITG drive being prescribed by the initial gradient profiles. As soon as nonlinear couplings sufficiently excite the zonal components, a further increase is prevented by the nonlinear saturation mechanisms. In addition, the linear drive is reduced due to a flattening of the temperature profile.

The chosen observable is the volume averaged ion thermal diffusivity as a function of the average ion temperature gradient in the radial domain $0.4 < r/a < 0.6$. Sampling both values at successive time points generates a *cloud* of points as can be seen

in Fig. 5.10. The following stages can be identified: At the beginning, the thermal dif-

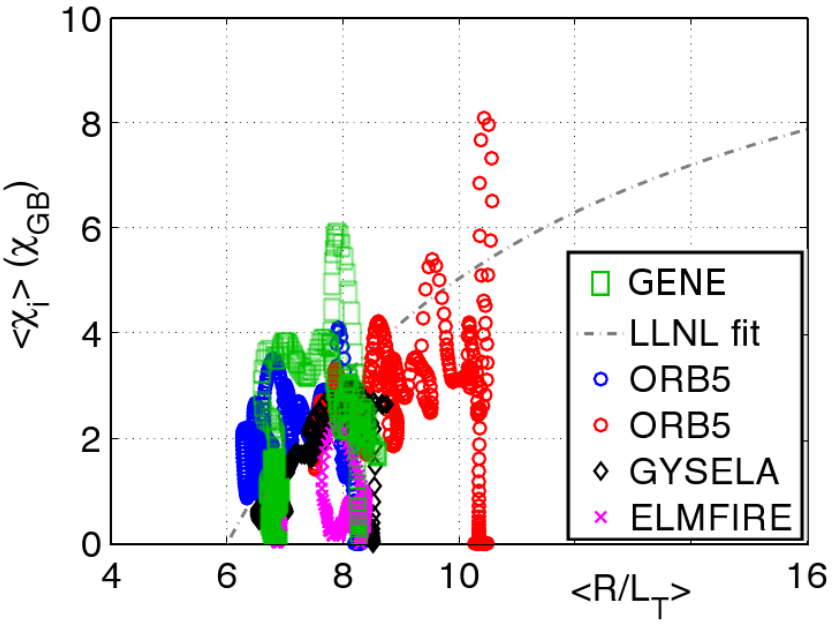

Figure 5.10: Volume averaged ion thermal diffusivity in units of $\chi_{\mathrm{GB}} = c_s \rho_s^2 / a$ vs. the normalized ion temperature gradient. The points represent both values at successive time points. Here, nonlinear GENE simulation results are merged with the results of other gyrokinetic codes published in [122] (modified and printed with permission).

fusivity grows at a fixed temperature gradient, thus clearly reflecting the linear phase. As soon as the nonlinearity becomes important, an overshoot occurs which is followed by a first saturation phase where the diffusivity and the gradient both fluctuate around a constant value for some time. Eventually, the ion temperature profile starts to relax and thus lowers the heat diffusivity.

All these features have been found within the ITM benchmarking effort by the nonlinear, gyrokinetic PIC codes ORB5, GYSELA [123, 124], and ELMFIRE [125] and can well be reproduced with GENE, see Fig. 5.10. However, the uncertainties given by the point *clouds* are quite large. Furthermore, different time windows have obviously been used, since no full relaxation is observed although, e.g., ORB5 employed a floating boundary condition at the inner boundary. GENE, on the other hand, is currently operating with Dirichlet boundary conditions which fix the temperatures at the boundaries. A corresponding plot of the total ion temperature and its normalized gradient is shown in Fig. 5.11. In this context, two particular features shall be pointed out. Firstly, the maximum relative deviation from the original background profile is here about 20%. This relaxation test is therefore at risk to violate the limits set by the gyrokinetic ordering. Secondly, a gradient reduction is only observed in the center of the simulation domain.

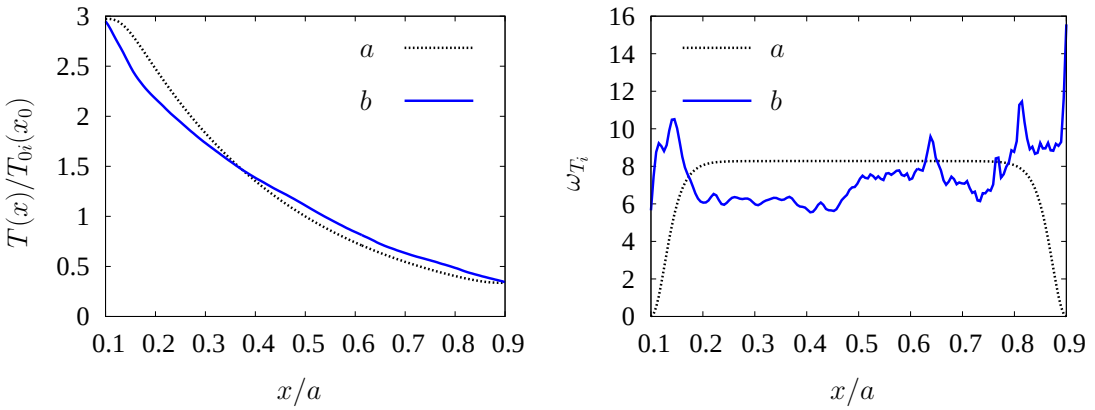

Figure 5.11: Total temperature (left) and normalized temperature gradient (right) calculated as shown in Eq. (3.89) (a) at $t = 0\,R_0/c_s$ and (b) averaged over the last 15% of the full simulation time.

At the boundaries, however, the gradients become very large since no additional damping terms are applied.

Comparison with local code results

Besides global code results, Fig. 5.10 additionally includes the LLNL fit which is based on the results of several US gyrokinetic flux-tube codes [43] and which can well be reproduced with the local GENE version [122]. With all point clouds being close to this fit line, one could be led to state a good agreement between the nonlocal and local simulations. However, the local flux-tube codes typically employ the $\hat{s}$-α model in the Cyclone benchmark case whereas all global codes in Fig. 5.10 used the circular model. A difference would therefore be expected. In Ref. [27] it is argued that the agreement is observed for CBC parameters since geometry and finite ρ^* effects cancel each other coincidentally. In order to investigate these claims, one could either perform a nonlinear ρ^* scan or simply implement a radially dependent $\hat{s}$-α model into the global code. The second alternative is chosen in the following and the results are presented in Fig. 5.12. Here, volume averages are plotted as functions of the averaged temperature gradients for two different GENE simulations. The one labeled (a) is based on the circular equilibrium whereas the $\hat{s}$-α model has been employed for curve (b). In both simulations, peaked gradient profiles with $\Delta T, \Delta n = 0.3$ have been initialized and Krook damping terms have been applied in order to reduce the fluctuations at the boundaries. Furthermore, the maximum gradient has been set to $\kappa_T = 6.96$. Although both simulations seem to coincide for a certain time period, they clearly differ in the end. While the simulation using a circular geometry relaxes to temperature gradients of about 5.4, a value exactly matching the local result is observed for the $\hat{s}$-α model. With regard to the Dimits shift,

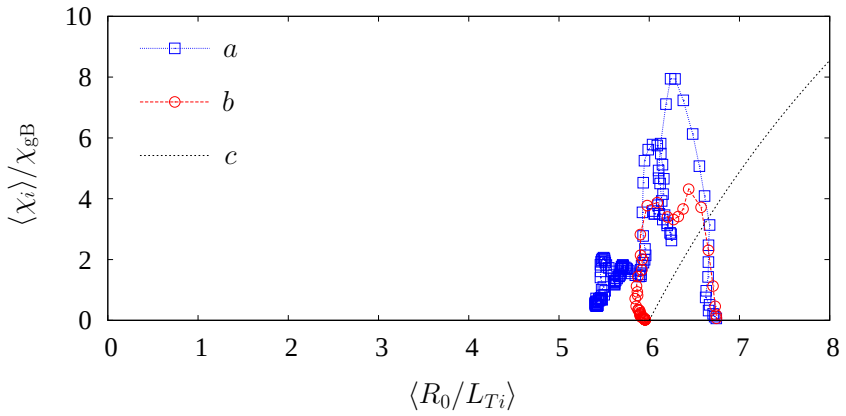

Figure 5.12: Volume averaged ion thermal diffusivity in units of χ_{gB} vs. the normalized ion temperature gradient for simulations with (a) the circular and (b) a radially dependent $\hat{s}$-α model. The LLNL fit result is included for comparison as curve (c).

these findings are in line with the linear thresholds presented for local GENE simulations in Ref. [27] since they similarly decrease from $\omega_T^{\text{crit}} \approx 4.2$ in the $\hat{s}$-α case to $\omega_T^{\text{crit}} \approx 3$. Changing from the circular geometry to a radially varying $\hat{s}$-α model thus clearly the affects global code results, which provides further evidence for the coincidental agreement between local and global codes in Fig. 5.10.

5.5 Sources and Sinks

The implementation of additional terms acting as sources and sinks has been discussed in Sec. 3.7. In this section, corresponding examples will be presented.

5.5.1 Application of the Krook damping term

The nonlinear benchmark presented above exhibited large temperature gradients close to the boundaries, see Fig. 5.11. Such strong linear drives may cause high fluctuation amplitudes which may potentially become inconsistent with the Dirichlet condition, the latter enforcing vanishing amplitudes at the boundaries. Although the benchmark case seems to be numerically stable, it shall nevertheless be used to study the effect of the Krook damping term. A corresponding plot is presented in Fig. 5.13. Here, two buffer zones are established by the $\hat{\nu}_{\text{Krook}}$ profile, labeled by (d). The maximum amplitude is set to $5\, c_s/R_0$ at both boundaries, and is thus several times larger than the maximum linear growth rate. However, only about 4% of the simulation domain are directly affected at each side since the damping term profile quickly decreases by means of a fourth order polynomial. The time-averaged temperature gradient profiles with and without Krook term demonstrate the desired behavior. While normalized gradient values of up to 16 are

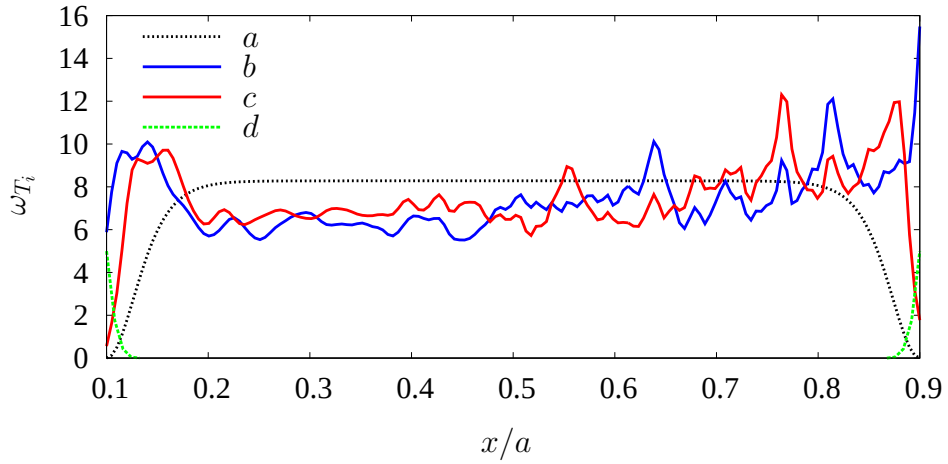

Figure 5.13: Normalized temperature gradient profile averaged over $t = 100 - 115\, R_0/c_s$ without (b) and with (c) a Krook damping term. For comparison, the initial background profile (a) and the Krook amplitude profile $\hat{\nu}_{\text{Krook}}$ (d), cf. Eq. (3.90), are presented as well.

observed at the outer boundary in the simulation without any damping, they are kept far below the linear threshold in the same radial region if the Krook term is switched on. Within the center, both profiles bear strong resemblance so that similar heat fluxes can be expected. Indeed, the heat diffusivities shown in Fig. 5.14 are quite close during

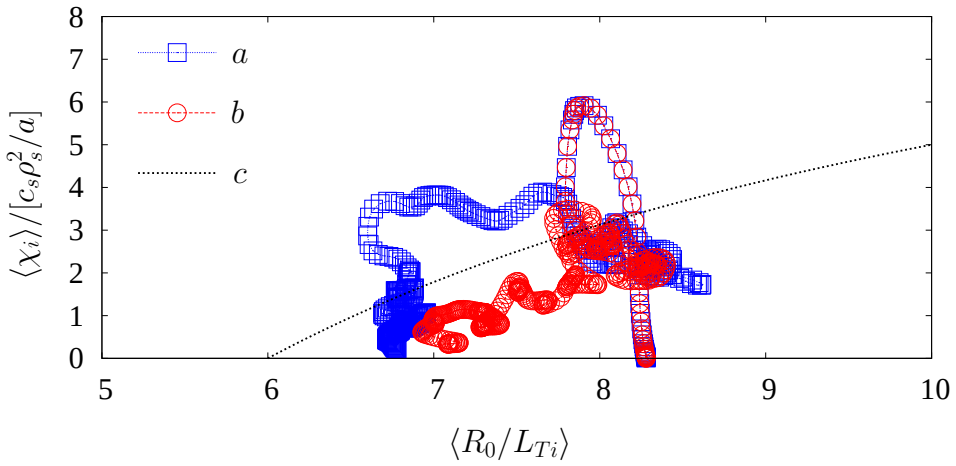

Figure 5.14: Volume averaged ($0.4 < x/a < 0.6$) ion thermal diffusivity vs. the normalized ion temperature gradient. Time trace (a) denotes the simulation without any numerical damping as shown in Fig. 5.10 while a Krook term is considered in (b). For comparison, the LLNL fit [43] is included as curve (c).

the last 10% of the simulation where the time average has been evaluated. However, during the gradient relaxation period they differ significantly which has to be considered

in future simulations. According diagnostics – measuring, for instance, the particle and energy modifications caused by the Krook term – are currently under development and will facilitate further insights soon.

5.5.2 Effects of the heat source

The basic features of the heat source which has been introduced in Sec. 3.7 will be explored in the following. Motivated by current experiments where the plasma heating is typically localized within a certain radial domain, the source profile is chosen to be Gaussian shaped and close to the magnetic axis. A corresponding plot can be found in Fig. 5.15. Here, two temperature profiles are shown, as well. The black dotted line

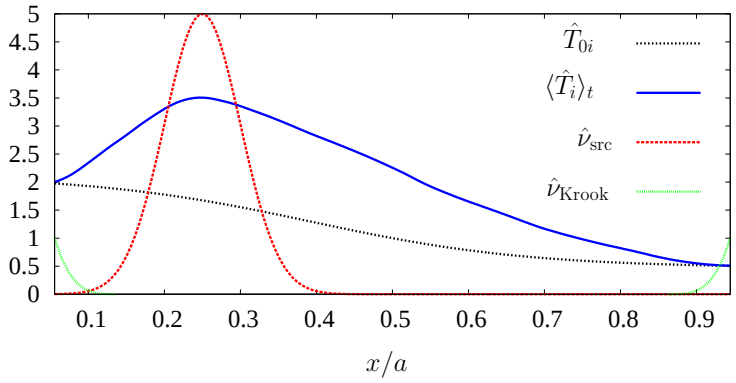

Figure 5.15: Temperature and source term profiles. Here, $\hat{T}_{0i}$ denotes the initial temperature profile, $\langle \hat{T}_i \rangle_t$ the profile including the flux surface averaged fluctuations averaged over $t = 371 - 421\, R_0/c_s$, $\hat{\nu}_{\mathrm{src}}$ the heat source profile, and $\hat{\nu}_{\mathrm{Krook}}$ the Krook term profile.

represents the initial profile while the blue solid line indicates the time averaged temperature including the flux surface averaged fluctuations. The latter is clearly increased and exhibits a maximum value at the same position as the heat source. With the density keeping a fixed value, the principle operational capability of the source term can be considered to be confirmed. However, it shall be noted that the presented simulation has not developed a quasi-stationary state. Furthermore, a large relative difference is observed between the initial equilibrium temperature and the temperature propagated in time. In order to avoid inconsistencies with the gyrokinetic ordering, one could, for instance, stop the simulation once the deviations become significant and continue with an correspondingly updated equilibrium. In addition, a more advanced set of sources and sinks and floating boundary conditions might help to avoid these inconsistencies. All these suggestions are going to be addressed in the near future.

However, although the physics might not be fully consistent, the simulation already reveals some interesting features which could be of possible relevance for future flux-driven simulations. The heat flux, for instance, exhibits outward propagating structures which

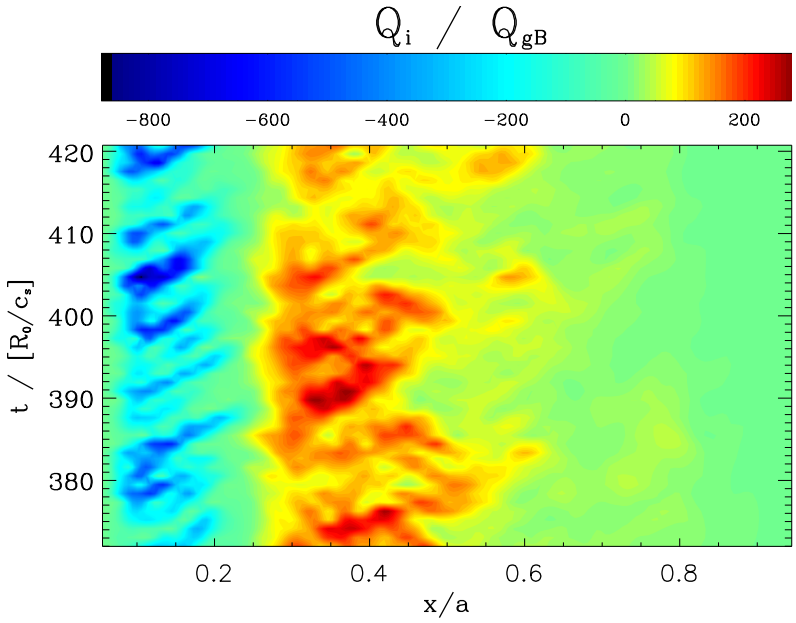

Figure 5.16: Radial heat flux Q_i in units of Q_{gB} as function of the normalized radius and time. The tilted stripes indicate an outward propagation of the heat flux amplitudes.

can be observed by means of tilted stripes in Fig. 5.16. Interestingly, they bear strong resemblance with so-called avalanches which have been reported in global simulations including an additional toroidal momentum, see Ref. [126]. The blue colored inward transport may be surprising at first sight. However, with a temperature maximum not coinciding with the inner boundary, strong negative temperature gradients appear and inward transport becomes not unlikely.

5.6 Chapter summary

The newly developed global GENE version has been extensively tested and benchmarked. In particular, they comprised ρ^* scans, Rosenbluth-Hinton tests, as well as linear and nonlinear inter-code benchmarks. Within these simulations, it has been confirmed that linear local simulations are justified for medium- to large-scale fusion devices. Furthermore, global simulations with slightly different magnetic geometries have been presented which support arguments for a coincidental agreement of local and global codes in nonlinear simulations employing the CBC parameters. Finally, the general operational functionality of the implemented numerical and physical source and sink terms has been demonstrated. Along this lines, avalanches have been observed which are first examples for nonlocal effects which might appear in future flux-driven simulations being adapted to specific experiments.

Chapter 6

Conclusions

In the course of this thesis work, the gyrokinetic plasma turbulence code GENE has been fundamentally extended by the consideration of radial temperature, density and magnetic geometry variations. These modifications which comprise changes of the underlying equations as well as the numerical schemes are essential for the future investigation of nonlocal phenomena. In addition, GENE has been utilized to study the behavior of small-scale fluctuations within large-scale plasma microturbulence, a topic which is of great interest e.g. for future fusion devices where the small-scale turbulence is expected to be strongly driven.

Below, a brief review of the most important findings is presented for each chapter. Furthermore, an outlook on possible future research topics is given.

6.1 Summary

Gyrokinetic theory

The gyrokinetic theory underlying the description of microturbulence throughout this thesis has been briefly reviewed. Hereafter, the remaining steps towards the final system of equations implemented into the plasma turbulence code GENE have been presented. In contrast to previous publications deriving similar equations for earlier GENE versions, special attention has been paid to the consideration of full radial profiles of temperature, density and geometry. Furthermore, a more general phase space volume has been included which is expected to show improved energy conserving properties in case of significant electromagnetic effects.

Upgrading GENE to a nonlocal code

Former versions of GENE were using the local approximation exclusively. One major purpose of this thesis was to relax this constraint and implement the aforementioned profiles to allow for the investigation of nonlocal effects. Since most of the numerical schemes had been highly optimized for the local version, almost all core parts of the code had to be redesigned and rewritten. For instance, new boundary conditions in the radial

and parallel directions had to be designed, and the Fourier representation in the radial direction had to be abandoned, thus requiring new interpolation schemes. Furthermore, a first model for heat sources and sinks has been implemented.

Coupled ITG/TEM and ETG driven turbulence

Given the expected strong electron heating by α particles in future fusion devices, as well as the experimental and theoretical indication of a possible relevance of electron temperature gradient driven modes, the urgent question arises whether high-k turbulence may contribute substantially to the electron heat transport in the presence of ion-gyroradius-scale turbulence. Due to the enormous computational demands of simulations covering electron and ion space and time scales self-consistently, it is currently virtually impossible to perform extensive parameter scans. Therefore, only a few prototypical parameter sets have been chosen in this thesis. In the first case – which was motivated by a popular benchmark – small-scale turbulence indeed appeared to be hampered by large-scale dynamics. The ion transport level, however, turned out to be unrealistically high. By lowering the low-k drive in order to achieve levels which agree better with experimental findings, a tendency towards a scale separation between ion and electron heat transport has been observed for the first time. In contrast to its ion counterpart, the electron heat channel may thus exhibit substantial or even dominant high wave number contributions carried by ETG modes and short-wavelength TEMs. Therefore, the work presented in this thesis might help to understand residual electron heat fluxes in cases where the low-k drive becomes small compared to the ETG drive, as for instance in discharges with dominant electron heating, high β, or internal transport barriers. Furthermore, density and frequency spectra have been presented which might enable experimentalists to identify two-scale signatures.

First nonlocal investigations with GENE

An extensive verification effort has been performed for the newly developed global code. Along these lines, various benchmarks – as for instance Rosenbluth-Hinton tests, ρ^* scans, and direct comparisons with other gyrokinetic codes – have been passed successfully. GENE can thus be considered to be fully operational for nonlocal investigations. In terms of the comprehensiveness with respect to physical effects, it therefore represents by now one of the leading gyrokinetic codes worldwide. First results presented here have highlighted the importance of the choice of profile shapes when comparing local and global code results. In addition, the influence of the employed magnetic equilibrium model has been confirmed. Finally, the general operational functionality of the implemented source and sink terms has been demonstrated which represents an important step on the way to flux driven simulations.

6.2 Outlook

Coupled turbulence types on different scales

The prediction of significant electron heat fluxes originating from small scales even in the presence of large scale turbulence constitutes an important contribution to the discussion on the relevance of ETG driven modes in future fusion devices. Hence, further investigations including more complete physics, e.g. a realistic mass ratio or a realistic MHD equilibrium, are justified. However, an obvious obstacle within this context is the extremely challenging computational demand which can only be satisfied by state-of-the-art supercomputers. Additionally, a close cooperation with experimental groups working on the extension of their diagnostics into the high-k regime is desirable in order to facilitate comparisons with experimental data.

Nonlocal effects and further code development

The implementation of additional radial temperature, density, and magnetic geometry variations allows for the investigation of many new areas of interest which could not be addressed with GENE before. For instance, it is now possible to contribute to on-going discussions on local profile shearing [127, 128], avalanches [126], turbulence spreading [129], and the related discussion on the limitations of gyro-Bohm scaling, see e.g. Refs. [130, 128]. The further development of sources and sinks and the resulting possibility of performing flux-driven simulations may facilitate comparisons with experiments.

From the practical point of view, however, optimization of performance and parallelization are additional crucial issues. For instance, a modification of the velocity space representation or normalization in order to avoid the large number of grid points which is currently required, see Sec. 5.3, would probably result in a considerable improvement.

Furthermore, in order to perform simulations for small devices – i.e. large ρ^* – additional terms could be implemented, e.g. the $v_\parallel$ nonlinearity.

Coupled simulations

Another project which involves further macroscopic scales is the coupling of the GENE code with transport solvers, see e.g. Ref. [131]. The advantages are expected to be twofold. On one hand, several (local) flux tube simulations could be run in parallel at different radial positions. The results would be passed to the transport solver which would evolve the profiles and restart the local code with the updated temperatures and densities (along with the respective gradients) until a converged state is reached. Such a scenario would provide, for instance, an extended benchmark case for the global code. On the other hand, it is conceivable to employ the transport solver's ability to treat the

long-time evolution of what appears to be an equilibrium for the gyrokinetic codes. In this context, a transport solver could even be coupled to the global code which would then provide transport fluxes at predefined radial positions as soon as a quasi-stationary state is reached.

Appendix A

Implementation details of the gyrokinetic Vlasov-Maxwell system in GENE

As already mentioned in Sec. 2.2, Eq. (2.60) is not exactly the version of the gyrokinetic Vlasov Equation which is implemented in GENE . However, the modifications are only minor and will therefore be presented in this appendix. In a first step, Γ_σ shall be replaced by the modified distribution function and potential. Starting with the definitions of $\mathbf{\Gamma}_\sigma = \nabla F_{1\sigma} + \frac{F_{0\sigma}}{T_{0\sigma}} \nabla \left(q_\sigma \bar{\phi}_1 + \mu \bar{B}_{1\parallel} \right)$, $g_\sigma = F_{1\sigma} + \frac{q_\sigma}{c} \bar{A}_{1\parallel} \frac{v_\parallel}{T_{0\sigma}} F_{0\sigma}$, and $\xi_1 = \phi_1 - \frac{v_\parallel}{c} A_{1\parallel} + \frac{\mu}{q_\sigma} B_{1\parallel}$, it is easy to show that

$$\begin{aligned}\Gamma_\sigma =& \nabla g_{1\sigma} + \frac{q_\sigma}{T_{0\sigma}} F_{0\sigma} \nabla \bar{\xi}_1 - \\ & \frac{q_\sigma}{c} v_\parallel \bar{A}_{1\parallel} \frac{F_{0\sigma}}{T_{0\sigma}} \left[\frac{\nabla n_{0\sigma}}{n_{0\sigma}} + \frac{\nabla T_{0\sigma}}{T_{0\sigma}} \left(\frac{m_\sigma v_\parallel^2/2 + \mu B_0}{T_{0\sigma}} + \frac{1}{2} \right) - \frac{\nabla B_0}{B_0} \frac{\mu B_0}{T_{0\sigma}} \right].\end{aligned}$$

Further evaluation and normalization yields for the single components

$$\begin{aligned}\hat{\Gamma}_{\sigma,x} =& \partial_{\hat{x}} \hat{g}_{1\sigma} + \frac{\hat{q}_\sigma}{\hat{T}_{0\sigma}} \hat{F}_{0\sigma} \partial_{\hat{x}} \hat{\bar{\xi}}_1 + \frac{\rho_{\mathrm{ref}}}{L_{\mathrm{ref}}} \hat{v}_{T\sigma}(x_0) \hat{q}_\sigma \hat{v}_\parallel \hat{\bar{A}}_{1\parallel} \frac{\hat{F}_{0\sigma}}{\hat{T}_{0\sigma}} \left[\omega_n + \omega_T \left(\frac{\hat{v}_\parallel^2 + \hat{\mu} \hat{B}_0}{\hat{T}_{0\sigma}/\hat{T}_{0\sigma}(x_0)} - \frac{3}{2} \right) \right. \\ & \left. + \frac{\partial_{\hat{x}} \hat{B}_0}{\hat{B}_0} \frac{\hat{\mu} \hat{B}_0 T_{0\sigma}(x_0)}{\hat{T}_{0\sigma}} \right] = \partial_{\hat{x}} \hat{g}_{1\sigma} + \frac{\hat{q}_\sigma}{\hat{T}_{0\sigma}} \hat{F}_{0\sigma} \partial_{\hat{x}} \hat{\bar{\xi}}_1 + \mathcal{O}\left(\frac{\rho_{\mathrm{ref}}}{L_{\mathrm{ref}}} \right), \\ \hat{\Gamma}_{\sigma,y} =& \partial_{\hat{y}} \hat{g}_{1\sigma} + \frac{\hat{q}_\sigma}{\hat{T}_{0\sigma}} \hat{F}_{0\sigma} \partial_{\hat{y}} \hat{\bar{\xi}}_1, \\ \hat{\Gamma}_{\sigma,z} =& \partial_{\hat{z}} \hat{g}_{1\sigma} + \frac{\hat{q}_\sigma}{\hat{T}_{0\sigma}} \hat{F}_{0\sigma} \partial_{\hat{z}} \hat{\bar{\xi}}_1 + \frac{\hat{q}_\sigma}{\hat{T}_{0\sigma}} \hat{F}_{0\sigma} \hat{v}_{T\sigma}(x_0) \hat{v}_\parallel \hat{\mu} \hat{\bar{A}}_{1\parallel} \partial_{\hat{z}} \hat{B}_0 \frac{\hat{T}_{0\sigma}(x_0)}{\hat{T}_{0\sigma}}.\end{aligned}$$

Neglecting the term in $\Gamma_{\sigma,x}$ which is smaller by a factor $\frac{\rho_{\mathrm{ref}}}{L_{\mathrm{ref}}}$, Eq. (2.60) becomes

$$\begin{aligned}
\frac{\partial \hat{g}_{1\sigma}}{\partial \hat{t}} = &- \left\{ \frac{1}{\hat{\mathcal{C}}} \frac{\hat{B}_0}{\hat{B}^*_{0\parallel}} \left[\hat{\omega}_{n\sigma} + \hat{\omega}_{T\sigma} \left(\frac{\hat{v}_\parallel^2 + \hat{\mu}\hat{B}_0}{\hat{T}_{0\sigma}/\hat{T}_{0\sigma}(x_0)} - \frac{3}{2} \right) \right] \hat{F}_{0\sigma} \right. \\
&\left. + \frac{\hat{B}_0}{\hat{B}^*_{0\parallel}} \frac{\hat{T}_{0\sigma}(x_0)}{\hat{T}_{0\sigma}} \frac{\hat{\mu}\hat{B}_0 + 2\hat{v}_\parallel^2}{\hat{B}_0} \hat{K}_y \hat{F}_{0\sigma} + \frac{\hat{B}_0}{\hat{B}^*_{0\parallel}} \frac{T_{0\sigma}(x_0)}{\hat{T}_{0\sigma}} \frac{\hat{v}_\parallel^2}{\hat{\mathcal{C}}} \beta_{\mathrm{ref}} \frac{\hat{p_0}}{\hat{B}_0^2} \hat{\omega}_p \hat{F}_{0\sigma} \right\} \partial_{\hat{y}} \hat{\bar{\xi}}_1 \\
&- \frac{\hat{B}_0}{\hat{B}^*_{0\parallel}} \frac{\hat{T}_{0\sigma}(x_0)}{\hat{T}_{0\sigma}} \frac{\hat{\mu}\hat{B}_0 + 2\hat{v}_\parallel^2}{\hat{B}_0} \hat{F}_{0\sigma} \hat{K}_x \partial_{\hat{x}} \hat{\bar{\xi}}_1 \\
&- \frac{\hat{B}_0}{\hat{B}^*_{0\parallel}} \frac{\hat{T}_{0\sigma}(x_0)}{\hat{q}_\sigma} \frac{\hat{\mu}\hat{B}_0 + 2\hat{v}_\parallel^2}{\hat{B}_0} \hat{K}_x \partial_{\hat{x}} \hat{g}_{1\sigma} \\
&- \left\{ \frac{\hat{B}_0}{\hat{B}^*_{0\parallel}} \frac{\hat{T}_{0\sigma}(x_0)}{\hat{q}_\sigma} \frac{\hat{\mu}\hat{B}_0 + 2\hat{v}_\parallel^2}{\hat{B}_0} \hat{K}_y + \frac{\hat{B}_0}{\hat{B}^*_{0\parallel}} \frac{\hat{T}_{0\sigma}(x_0)}{\hat{q}_\sigma} \frac{\hat{v}_\parallel^2}{\hat{\mathcal{C}}} \beta_{\mathrm{ref}} \frac{\hat{p_0}}{\hat{B}_0^2} \hat{\omega}_p \right\} \partial_{\hat{y}} \hat{g}_{1\sigma} \\
&- \hat{v}_{T\sigma}(x_0) \frac{\hat{\mathcal{C}}}{J\hat{B}_0} \hat{v}_\parallel \left(\partial_{\hat{z}} \hat{F}_{1\sigma} + \frac{\hat{q}_\sigma}{\hat{T}_{0\sigma}} \hat{F}_{0\sigma} \partial_{\hat{z}} \hat{\bar{\phi}}_1 + \frac{\hat{T}_{0\sigma}(x_0)}{\hat{T}_{0\sigma}} \hat{F}_{0\sigma} \hat{\mu} \partial_{\hat{z}} \hat{\bar{B}}_{1\parallel} \right) \\
&+ \frac{\hat{v}_{T\sigma}(x_0)}{2} \frac{\hat{\mathcal{C}}}{\hat{J}\hat{B}_0} \hat{\mu} \partial_{\hat{z}} \hat{B}_0 \frac{\partial \hat{F}_{1\sigma}}{\partial \hat{v}_\parallel} + \frac{\hat{B}_0}{\hat{B}^*_{0\parallel}} \frac{1}{\hat{\mathcal{C}}} \left(-\partial_{\hat{x}} \hat{\bar{\xi}}_1 \partial_{\hat{y}} \hat{g}_{1\sigma} + \partial_{\hat{y}} \hat{\bar{\xi}}_1 \partial_{\hat{x}} \hat{g}_{1\sigma} \right) \\
&+ \frac{\hat{B}_0}{\hat{B}^*_{0\parallel}} \hat{F}_{0\sigma} \frac{\hat{T}_{0\sigma}(x_0)}{\hat{q}_\sigma} \frac{\hat{\mu}\hat{B}_0 + 2\hat{v}_\parallel^2}{\hat{B}_0} K_x \left[\hat{\omega}_{n\sigma} + \hat{\omega}_{T\sigma} \left(\frac{\hat{v}_\parallel^2 + \hat{\mu}\hat{B}_0}{\hat{T}_{0\sigma}/\hat{T}_{0\sigma}(x_0)} - \frac{3}{2} \right) \right]. \qquad \text{(A.1)}
\end{aligned}$$

Finally, the gyrokinetic Vlasov equation is presented in terms of the abbreviations employed in GENE in order to facilitate direct comparisons with the source code.

$$\begin{aligned}
\frac{\partial \hat{g}_\sigma}{\partial \hat{t}} = &\text{pdchibardy } \partial_{\hat{y}} \hat{\bar{\xi}}_1 + \text{pdchibardx } \partial_{\hat{x}} \hat{\bar{\xi}}_1 \\
&+ \text{pdg1dx } \partial_{\hat{x}} \hat{g}_{1\sigma} + \text{pdg1dy } \partial_{\hat{y}} \hat{g}_{1\sigma} \\
&+ \text{pdf1dz } \partial_{\hat{z}} \hat{F}_{1\sigma} + \text{pdphidz } \left(\partial_{\hat{z}} \hat{\bar{\phi}}_1 + \text{mu_Tjqj } \partial_{\hat{z}} \hat{\bar{B}}_{1\parallel} \right) \\
&+ \text{pnl } \left(-\partial_{\hat{x}} \hat{\bar{\xi}}_1 \partial_{\hat{y}} \hat{g}_{1\sigma} + \partial_{\hat{y}} \hat{\bar{\xi}}_1 \partial_{\hat{x}} \hat{g}_{1\sigma} \right) \\
&+ \text{trp } \frac{\partial \hat{F}_{1\sigma}}{\partial \hat{v}_\parallel} + \text{f0_contr} \qquad \text{(A.2)}
\end{aligned}$$

with the modified distribution function and field

$$\begin{aligned}
\hat{g}_{1\sigma} &= \hat{F}_{1\sigma} - \text{papbar } \hat{\bar{A}}_{1\parallel} \\
\hat{\bar{\xi}}_1 &= \hat{\bar{\phi}}_1 - \text{vTvpar } \hat{\bar{A}}_{1\parallel} + \text{mu_Tjqj } \hat{\bar{B}}_{1\parallel}, \qquad \text{(A.3)}
\end{aligned}$$

the following prefactors as implemented in GENE (revision 1106)

$$
\begin{aligned}
\text{pdchibardy} &= -\text{edr } - \text{curv qjTjF0 } K_y + \text{press qjTjF0} \\
\text{pdchibardx} &= -\text{curv qjTjF0 } K_x \\
\text{pdg1dx} &= -\text{curv } K_x \\
\text{pdg1dy} &= -\text{curv } K_y + \text{press} \\
\text{pdf1dz} &= -\hat{v}_{T\sigma}(x_0)\frac{\hat{\mathcal{C}}}{J\hat{B}_0}\hat{v}_{\parallel} \\
\text{pdphidz} &= \text{pdf1dz } \frac{\hat{q}_\sigma}{\hat{T}_{0\sigma}}\hat{F}_{0\sigma} \\
\text{mu\_Tjqj} &= \frac{\hat{T}_{0\sigma}(x_0)}{\hat{q}_\sigma}\hat{\mu} \\
\text{pnl} &= \frac{\hat{B}_0}{\hat{B}^*_{0\parallel}}\frac{1}{\hat{\mathcal{C}}} \\
\text{trp} &= \frac{\hat{v}_{T\sigma}(x_0)}{2}\frac{\hat{\mathcal{C}}}{J\hat{B}_0}\hat{\mu}\partial_{\hat{z}}\hat{B}_0 \\
\text{f0\_contr} &= \text{curv edr } K_x\frac{\hat{B}^*_{0\parallel}}{\hat{B}_0\hat{\mathcal{C}}} \\
\text{vTvpar} &= \sqrt{\frac{2\hat{T}_{0\sigma}(x_0)}{\hat{m}_\sigma}}\hat{v}_{\parallel} \\
\text{papbar} &= -\text{vTvpar } \frac{\hat{q}_\sigma}{\hat{T}_{0\sigma}}\hat{F}_{0\sigma}
\end{aligned}
\tag{A.4}
$$

and the additional abbreviations

$$
\begin{aligned}
\text{edr} &= \frac{1}{\hat{\mathcal{C}}}\frac{\hat{B}_0}{\hat{B}^*_{0\parallel}}\left[\omega_{n\sigma} + \omega_{T\sigma}\left(\frac{\hat{v}^2_{\parallel} + \hat{\mu}\hat{B}_0}{\hat{T}_{0\sigma}/\hat{T}_{0\sigma}(x_0)} - \frac{3}{2}\right)\right]\hat{F}_{0\sigma} \\
\text{curv} &= \frac{\hat{B}_0}{\hat{B}^*_{0\parallel}}\frac{\hat{T}_{0\sigma}(x_0)}{\hat{q}_\sigma}\frac{\hat{\mu}\hat{B}_0 + 2\hat{v}^2_{\parallel}}{\hat{B}_0} \\
\text{qjTjF0} &= \frac{\hat{q}_\sigma}{\hat{T}_{0\sigma}}\hat{F}_{0\sigma} \\
\text{press} &= \beta_{\text{ref}}\frac{\hat{B}_0}{\hat{B}^*_{0\parallel}}\frac{T_{0\sigma}(x_0)}{\hat{q}_\sigma}\frac{\hat{v}^2_{\parallel}}{\hat{\mathcal{C}}}\frac{\partial_{\hat{x}}\hat{p}_0}{\hat{B}^2_0}.
\end{aligned}
\tag{A.5}
$$

Appendix B

Geometry related issues

B.1 Volume and flux surface averages

Several physical quantities as, for instance, particle and heat transport levels are often compared by means of their volume or flux surface averages. This section therefore provides details on the corresponding calculations and furthermore contains a discussion on differences between the local and the global code version.

A volume average of an arbitrary function $f(\mathbf{x})$ is defined as

$$\langle f \rangle_V \equiv \frac{1}{V} \int_0^{L_x} \int_0^{L_y} \int_0^{L_z} f(\mathbf{x}) J(\mathbf{x}) \, \mathrm{d}x \mathrm{d}y \mathrm{d}z \tag{B.1}$$

where $\mathbf{x} = (x, y, z)$ and the flux tube volume is

$$V \equiv \int_0^{L_x} \int_0^{L_y} \int_0^{L_z} J(\mathbf{x}) \mathrm{d}x \mathrm{d}y \mathrm{d}z \tag{B.2}$$

with the Jacobian J taken from Eq. (2.38). Similarly, a flux surface average is constructed by

$$\langle f \rangle_{\mathrm{FS}} \equiv \frac{\partial}{\partial V} \int_V f(\mathbf{x}) \, \mathrm{d}V' = \frac{1}{A_{\mathrm{FS}}} \int f(\mathbf{x}) J(\mathbf{x}) \, \mathrm{d}y \mathrm{d}z \tag{B.3}$$

where the integration limits have been suppressed for the sake of readability and where $A_{\mathrm{FS}}(x) \equiv \int J(\mathbf{x}) \, \mathrm{d}y \mathrm{d}z$ as mentioned in Sec. 2.4.1. A simplification can be employed, if only axisymmetric devices are considered. Here, all geometry related quantities become independent of y and thus

$$\langle f \rangle_V = \frac{\int f(\mathbf{x}) J(x,z) \, \mathrm{d}x \mathrm{d}y \mathrm{d}z}{L_y \int J(x,z) \, \mathrm{d}x \mathrm{d}z} \qquad \text{and} \qquad \langle f \rangle_{\mathrm{FS}} = \frac{\int f(\mathbf{x}) J(x,z) \, \mathrm{d}y \mathrm{d}z}{L_y \int J(x,z) \, \mathrm{d}z}. \tag{B.4}$$

A discretization on a regular grid applied to all directions and a Fourier transformation in the y coordinate yield

$$\langle f \rangle_V = \frac{\sum_{x,z} f(x, k_y = 0, z) J(x,z)}{\sum_{x,z} J(x,z)} \quad \text{and} \quad \langle f \rangle_{\mathrm{FS}} = \frac{\sum_z f(x, k_y = 0, z) J(x,z)}{\sum_z J(x,z)}. \tag{B.5}$$

While both averages are closely related via $\langle f \rangle_V = \langle \langle f \rangle_{\mathrm{FS}}(x) \rangle_x$ in the local code where the Jacobian does not vary in the radial direction, they need to be carefully distinguished in the global code and in the corresponding post-processing.

For some applications, e.g. for interfaces to transport codes, the volume and flux surface area themselves are employed. They read in discretized form

$$V = \frac{L_x}{N_x} \sum_x A_{\mathrm{FS}} = \frac{L_x}{N_x} \frac{L_y 2\pi N_{\mathrm{pol}}}{N_z} \sum_x \sum_z J(x,z) \tag{B.6}$$

where L_z has been identified by the number of poloidal turns $N_{\mathrm{pol}} \in \mathbb{N}$ times 2π in the last step. Considering the normalization introduced in Sec. 2.2.3, the normalized volume is given in units of $\rho_{\mathrm{ref}}^2 L_{\mathrm{ref}}$ while the flux surface area is normalized to $\rho_{\mathrm{ref}} L_{\mathrm{ref}}$.

B.2 Diffusivities in arbitrary geometries

The diffusivities introduced in Sec. 3.6 have to be slightly modified if noncircular geometries or Shafranov shifts are considered. In theses cases, Eq. (3.88) has to generalized to

$$Q_\sigma^x = -n_{0\sigma} \chi_\sigma \nabla x \cdot \nabla T_{0\sigma} = -n_{0\sigma} \chi_\sigma \left| \nabla x \right|^2 \frac{\partial T_{0\sigma}}{\partial x}. \tag{B.7}$$

By furthermore assuming χ_σ to be constant on flux surfaces, one arrives at

$$\langle Q_\sigma^x \rangle_{\mathrm{FS}} = -n_{0\sigma} \chi_\sigma \langle g^{xx} \rangle_{\mathrm{FS}} \frac{\partial T_{0\sigma}}{\partial x} \quad \text{or} \quad \chi = \frac{\langle Q^x \rangle_{\mathrm{FS}}}{n_{0\sigma} T_{0\sigma} \omega_T \langle g^{xx} \rangle_{\mathrm{FS}}}, \tag{B.8}$$

respectively. The volume averaged diffusivity which is often employed in this work is then given by

$$\langle \chi \rangle_V = \left\langle \frac{\langle Q^x \rangle_{\mathrm{FS}}(x)}{n_{0\sigma}(x) T_{0\sigma}(x) \omega_T(x) \langle g^{xx} \rangle_{\mathrm{FS}}(x)} \right\rangle_V. \tag{B.9}$$

In the local code, it can be further simplified to

$$\langle \chi \rangle_V = \frac{\langle Q^x \rangle_{\mathrm{V}}}{n_{0\sigma} T_{0\sigma} \omega_T \langle g^{xx} \rangle_{\mathrm{FS}}}. \tag{B.10}$$

Note that in the global code, $n_{0\sigma}$, $T_{0\sigma}$ and ω_T are often corrected by the flux surface averaged part of the fluctuations, and that the same arguments naturally hold for the particle diffusivity D_σ.

Bibliography

[1] Energy Information Administration, *International Energy Outlook*, Technical Report DOE/EIA-0484(2009), U.S. Department of Energy, 2009.

[2] R. D. E. Atkinson and F. G. Houtermans, *Zur Frage der Aufbaumöglichkeit der Elemente in Sternen*, Z. Phys. **54**, 656 (1929).

[3] M. L. Oliphant, P. Harteck, and E. Rutherford, *Transmutation Effects observed with Heavy Hydrogen*, Nature **133**, 413 (1934).

[4] C. F. von Weizsäcker, Phys. Z. **38**, 176 (1937).

[5] H. A. Bethe, *Energy Production in Stars*, Phys. Rev. **55**, 434 (1939).

[6] J. Wesson, *Tokamaks*, Clarendon Press - Oxford, 2nd edition, 1997.

[7] ITER Organization, *ITER - the way to new energy*, 2009, `http://www.iter.org`.

[8] J. D. Lawson, *Some Criteria for a Power Producing Thermonuclear Reactor*, Proceedings of the Physical Society B **70**, 6 (1957).

[9] Max-Planck-Institut für Plasmaphysik, *ASDEX Upgrade fusion experiment [Brochure]*, 2006.

[10] A. A. Vlasov, *Reviews of Topical Problems: the Vibrational Properties of an Electron Gas*, Soviet Physics Uspekhi **10**, 721 (1968).

[11] F. F. Chen, *Introduction to Plasma Physics and Controlled Fusion: Plasma physics*, Springer, 2nd edition, 1984.

[12] K. Nishikawa and M. Wakatani, *Plasma Physics - Basic Theory with Fusion Applications*, Springer-Verlag, Berlin Heidelberg, 2nd edition, 1994.

[13] A. J. Brizard and T. S. Hahm, *Foundations of nonlinear gyrokinetic theory*, Reviews of Modern Physics **79**, 421 (2007).

[14] T. Dannert, *Gyrokinetische Simulation von Plasmaturbulenz mit gefangenen Teilchen und elektromagnetischen Effekten*, PhD thesis, Technische Universität München, 2005.

[15] J. R. Cary and R. G. Littlejohn, *Noncanonical Hamiltonian mechanics and its application to magnetic field line flow*, Annals of Physics **151**, 1 (1983).

[16] D. H. E. Dubin, J. A. Krommes, C. Oberman, and W. W. Lee, *Nonlinear gyrokinetic equations*, Physics of Fluids **26**, 3524 (1983).

[17] T. S. Hahm, W. W. Lee, and A. Brizard, *Nonlinear gyrokinetic theory for finite-beta plasmas*, Physics of Fluids **31**, 1940 (1988).

[18] T. S. Hahm, *Nonlinear gyrokinetic equations for tokamak microturbulence*, Physics of Fluids **31**, 2670 (1988).

[19] A. Brizard, *Nonlinear gyrokinetic Maxwell-Vlasov equations using magnetic coordinates*, Journal of Plasma Physics **41**, 541 (1989).

[20] R. G. Littlejohn, *Hamiltonian perturbation theory in noncanonical coordinates*, Journal of Mathematical Physics **23**, 742 (1982).

[21] J. D. Huba, *NRL (Naval Research Laboratory) plasma formulary*, 2007.

[22] H. Grad and H. Rubin, Proceedings of the Second United Nations International Conference on Peaceful Uses of Atomic Energy **31**, 190 (1958).

[23] V. D. Shafranov, *On Magnetohydrodynamical Equilibrium Configurations*, Soviet Journal of Experimental and Theoretical Physics **6**, 545 (1958).

[24] J. W. Connor, R. J. Hastie, and J. B. Taylor, *Shear, periodicity, and plasma ballooning modes*, Physical Review Letters **40**, 396 (1978).

[25] R. L. Miller, M. S. Chu, J. M. Greene, Y. R. Lin-Liu, and R. E. Waltz, *Noncircular, finite aspect ratio, local equilibrium model*, Physics of Plasmas **5**, 973 (1998).

[26] P. Xanthopoulos and F. Jenko, *Clebsch-type coordinates for nonlinear gyrokinetics in generic toroidal configurations*, Physics of Plasmas **13**, 092301 (2006).

[27] X. Lapillonne, S. Brunner, T. Dannert, S. Jolliet, A. Marinoni, L. Villard, T. Görler, F. Jenko, and F. Merz, *Clarifications to the limitations of the s-alpha equilibrium model for gyrokinetic computations of turbulence*, Physics of Plasmas **16**, 032308 (2009).

[28] Y. Idomura, S. Tokuda, and Y. Kishimoto, *Global gyrokinetic simulation of ion temperature gradient driven turbulence in plasmas using a canonical Maxwellian distribution*, Nuclear Fusion **43**, 234 (2003).

[29] L. Villard, S. J. Allfrey, A. Bottino, M. Brunetti, G. L. Falchetto, V. Grandgirard, R. Hatzky, J. Nührenberg, A. G. Peeters, O. Sauter, S. Sorge, and J. Vaclavik, *Full radius linear and nonlinear gyrokinetic simulations for tokamaks and stellarators: zonal flows, applied $E\times B$ flows, trapped electrons and finite beta*, Nuclear Fusion **44**, 172 (2004).

[30] J. C. Kniep, J.-N. G. Leboeuf, and V. K. Decyk, *Gyrokinetic particle-in-cell calculations of ion temperature gradient driven turbulence with parallel nonlinearity and strong flow corrections*, Computer Physics Communications **164**, 98 (2004).

[31] J. Candy, R. E. Waltz, S. E. Parker, and Y. Chen, *Relevance of the parallel nonlinearity in gyrokinetic simulations of tokamak plasmas*, Physics of Plasmas **13**, 074501 (2006).

[32] Y. Idomura, M. Ida, S. Tokuda, and L. Villard, *New conservative gyrokinetic full-f Vlasov code and its comparison to gyrokinetic δf particle-in-cell code*, Journal of Computational Physics **226**, 244 (2007).

[33] S. Jolliet, *Gyrokinetic particle-in-cell global simulations of ion-temperature-gradient and collisionless-trapped-electron-mode turbulence in tokamaks, PhD Thesis No. 4326*, PhD thesis, Ecole Polytechnique Fédérale de Lausanne, 2009.

[34] R. G. Littlejohn, *Hamiltonian formulation of guiding center motion*, Physics of Fluids **24**, 1730 (1981).

[35] W. D. D'haeseleer, W. N. G. Hitchon, J. D. Callen, and J. L. Shohet, *Flux Coordinates and Magnetic Field Structure. A Guide to a Fundamental Tool of Plasma Theory*, Springer-Verlag, New York, 1991.

[36] F. Merz, *Gyrokinetic Simulation of Multimode Plasma Turbulence*, PhD thesis, Westfälische Wilhelms-Universität Münster, 2008.

[37] F. Jenko, W. Dorland, M. Kotschenreuther, and B. N. Rogers, *Electron temperature gradient driven turbulence*, Physics of Plasmas **7**, 1904 (2000).

[38] T. Dannert and F. Jenko, *Gyrokinetic simulation of collisionless trapped-electron mode turbulence*, Physics of Plasmas **12**, 072309 (2005).

[39] H. Lederer, R. Hatzky, R. Tisma, A. Bottino, and F. Jenko, *Hyperscaling of plasma turbulence simulations in DEISA*, in *CLADE '07: Proceedings of the 5th IEEE workshop on Challenges of large applications in distributed environments*, pages 19–26, New York, NY, USA, 2007, ACM.

[40] M. Kammerer, F. Merz, and F. Jenko, *Exceptional points in linear gyrokinetics*, Physics of Plasmas **15**, 052102 (2008).

[41] M. J. Pueschel, *Electromagnetic Effects in Gyrokinetic Simulations of Plasma Turbulence*, PhD thesis, Westfälische Wilhelms-Universität Münster, 2009.

[42] F. Jenko and The GENE development team, *The GENE code*, 2009, `http://www.ipp.mpg.de/~fsj/gene`.

[43] A. M. Dimits, G. Bateman, M. A. Beer, B. I. Cohen, W. Dorland, G. W. Hammett, C. Kim, J. E. Kinsey, M. Kotschenreuther, A. H. Kritz, L. L. Lao, J. Mandrekas, W. M. Nevins, S. E. Parker, A. J. Redd, D. E. Shumaker, R. Sydora, and J. Weiland, *Comparisons and physics basis of tokamak transport models and turbulence simulations*, Physics of Plasmas **7**, 969 (2000).

[44] W. M. Nevins, J. Candy, S. Cowley, T. Dannert, A. Dimits, W. Dorland, C. Estrada-Mila, G. W. Hammett, F. Jenko, M. J. Pueschel, and D. E. Shumaker, *Characterizing electron temperature gradient turbulence via numerical simulation*, Physics of Plasmas **13**, 122306 (2006).

[45] H. Lütjens, A. Bondeson, and O. Sauter, *The CHEASE code for toroidal MHD equilibria*, Computer Physics Communications **97**, 219 (1996).

[46] P. Xanthopoulos, F. Merz, T. Görler, and F. Jenko, *Nonlinear Gyrokinetic Simulations of Ion-Temperature-Gradient Turbulence for the Optimized Wendelstein 7-X Stellarator*, Physical Review Letters **99**, 035002 (2007).

[47] K. V. Roberts and J. B. Taylor, *Gravitational Resistive Instability of an Incompressible Plasma in a Sheared Magnetic Field*, Physics of Fluids **8**, 315 (1965).

[48] S. C. Cowley, R. M. Kulsrud, and R. Sudan, *Considerations of ion-temperature-gradient-driven turbulence*, Physics of Fluids B **3**, 2767 (1991).

[49] M. A. Beer, *Gyrofluid Models of Turbulent Transport in Tokamaks*, PhD thesis, Princeton University, 1995.

[50] M. A. Beer, S. C. Cowley, and G. W. Hammett, *Field-aligned coordinates for nonlinear simulations of tokamak turbulence*, Physics of Plasmas **2**, 2687 (1995).

[51] B. Scott, *Global consistency for thin flux tube treatments of toroidal geometry*, Physics of Plasmas **5**, 2334 (1998).

[52] X. Lapillonne and S. Brunner, private communication, 2009.

[53] T. Dannert, private communication, 2008.

[54] S. Balay, K. Buschelman, W. D. Gropp, D. Kaushik, M. G. Knepley, L. C. McInnes, B. F. Smith, and H. Zhang, *PETSc Web page*, 2001, http://www.mcs.anl.gov/petsc.

[55] S. Balay, K. Buschelman, V. Eijkhout, W. D. Gropp, D. Kaushik, M. G. Knepley, L. C. McInnes, B. F. Smith, and H. Zhang, *PETSc Users Manual*, Technical Report ANL-95/11 - Revision 2.1.5, Argonne National Laboratory, 2004.

[56] S. Balay, W. D. Gropp, L. C. McInnes, and B. F. Smith, *Efficient Management of Parallelism in Object Oriented Numerical Software Libraries*, in *Modern Software Tools in Scientific Computing*, edited by E. Arge, A. M. Bruaset, and H. P. Langtangen, pages 163–202, Birkhäuser Press, 1997.

[57] V. Hernandez, J. E. Roman, and V. Vidal, *SLEPc: A Scalable and Flexible Toolkit for the Solution of Eigenvalue Problems*, ACM Transactions on Mathematical Software **31**, 351 (2005).

[58] V. Hernandez, J. E. Roman, E. Romero, A. Tomas, and V. Vidal, *SLEPc home page*, http://www.grycap.upv.es/slepc, 2009.

[59] M. Kammerer, *Betrachtung linearer Mikroinstabilitäten des gyrokinetischen Eigenwertproblems mit GENE*, Diploma thesis, Universität Ulm, 2008.

[60] J. E. Roman, M. Kammerer, F. Merz, and F. Jenko, *Fast Eigenvalue Calculations in a Massively Parallel Plasma Turbulence Code*, submitted for publication in 5th Special Issue of Parallel Computing on Parallel Matrix Algorithms and Applications, 2009.

[61] M. Frigo and S. G. Johnson, *The Design and Implementation of FFTW3*, Proceedings of the IEEE **93**, 216 (2005), Special issue on "Program Generation, Optimization, and Platform Adaptation".

[62] IBM Corporation, *Engineering and Scientific Subroutine Library (ESSL) and Parallel ESSL*, `http://publib.boulder.ibm.com/infocenter/clresctr/topic/com.ibm.cluster.essl.doc/esslbooks.html`, 1990-2008.

[63] Intel Corporation, *Intel®Math Kernel Library*, `www.intel.com/software/products/mkl/`, 2000-2008.

[64] X. Lapillonne, private communication, 2008.

[65] F. Jenko, *Numerische Modellierung von stoßfreier Driftwellenturbulenz*, PhD thesis, Technische Universität München, 1998.

[66] T. Görler and F. Jenko, *Scale Separation between Electron and Ion Thermal Transport*, Physical Review Letters **100**, 185002 (2008).

[67] T. Görler and F. Jenko, *Multiscale features of density and frequency spectra from nonlinear gyrokinetics*, Physics of Plasmas **15**, 102508 (2008).

[68] P. C. Liewer, *Measurements of microturbulence in tokamaks and comparisons with theories of turbulence and anomalous transport*, Nuclear Fusion **25**, 543 (1985).

[69] D. Told, F. Jenko, P. Xanthopoulos, L. D. Horton, E. Wolfrum, and ASDEX Upgrade Team, *Gyrokinetic microinstabilities in ASDEX Upgrade edge plasmas*, Physics of Plasmas **15**, 102306 (2008).

[70] B. W. Stallard et al., *Electron heat transport in improved confinement discharges in DIII-D*, Physics of Plasmas **6**, 1978 (1999).

[71] S. M. Kaye et al., *Confinement and local transport in the National Spherical Torus Experiment (NSTX)*, Nuclear Fusion **47**, 499 (2007).

[72] T. L. Rhodes, W. A. Peebles, M. A. van Zeeland, J. S. Degrassie, R. V. Bravenec, K. H. Burrell, J. C. Deboo, J. Lohr, C. C. Petty, X. V. Nguyen, E. J. Doyle, C. M. Greenfield, L. Zeng, and G. Wang, *Response of multiscale turbulence to electron cyclotron heating in the DIII-D tokamak*, Physics of Plasmas **14**, 056117 (2007).

[73] T. Zhang, X. Gao, Y. Li, and J. Zhao, *Energy confinement and high-k turbulence on HT-7 tokamak*, Physics Letters A **372**, 4705 (2008).

[74] J. W. Connor and H. R. Wilson, *REVIEW ARTICLE: A review of theories of the L-H transition*, Plasma Physics and Controlled Fusion **42**, 1 (2000).

[75] R. C. Wolf, *TOPICAL REVIEW: Internal transport barriers in tokamak plasmas*, Plasma Physics and Controlled Fusion **45**, 1 (2003).

[76] T. S. Hahm, P. H. Diamond, Z. Lin, G. Rewoldt, O. Gurcan, and S. Ethier, *On the dynamics of edge-core coupling*, Physics of Plasmas **12**, 090903 (2005).

[77] E. Mazzucato, D. R. Smith, R. E. Bell, S. M. Kaye, J. C. Hosea, B. P. Leblanc, J. R. Wilson, P. M. Ryan, C. W. Domier, N. C. Luhmann, Jr., H. Yuh, W. Lee, and H. Park, *Short-Scale Turbulent Fluctuations Driven by the Electron-Temperature Gradient in the National Spherical Torus Experiment*, Physical Review Letters **101**, 075001 (2008).

[78] W. Dorland, F. Jenko, M. Kotschenreuther, and B. N. Rogers, *Electron Temperature Gradient Turbulence*, Physical Review Letters **85**, 5579 (2000).

[79] F. Jenko and W. Dorland, *Prediction of Significant Tokamak Turbulence at Electron Gyroradius Scales*, Physical Review Letters **89**, 225001 (2002).

[80] Y. Idomura, *Self-organization in electron temperature gradient driven turbulence*, Physics of Plasmas **13**, 080701 (2006).

[81] N. Joiner, D. Applegate, S. C. Cowley, W. Dorland, and C. M. Roach, *Electron temperature gradient driven transport in a MAST H-mode plasma*, Plasma Physics and Controlled Fusion **48**, 685 (2006).

[82] A. Bottino, A. G. Peeters, R. Hatzky, S. Jolliet, B. F. McMillan, T. M. Tran, and L. Villard, *Nonlinear low noise particle-in-cell simulations of electron temperature gradient driven turbulence*, Physics of Plasmas **14**, 010701 (2007).

[83] J. Candy, R. E. Waltz, M. R. Fahey, and C. Holland, *The effect of ion-scale dynamics on electron-temperature-gradient turbulence*, Plasma Physics and Controlled Fusion **49**, 1209 (2007).

[84] F. Jenko, *On the Nature of ETG Turbulence and Cross-Scale Coupling*, J. Plasma Fusion Res. SERIES , 11 (2004).

[85] R. E. Waltz, J. Candy, and M. Fahey, *Coupled ion temperature gradient and trapped electron mode to electron temperature gradient mode gyrokinetic simulations*, Physics of Plasmas **14**, 056116 (2007).

[86] D. Strintzi and F. Jenko, *On the relation between secondary and modulational instabilities*, Physics of Plasmas **14**, 042305 (2007).

[87] H. L. F. von Helmholtz, *Ueber discontinuirliche Flüssigkeitsbewegungen*, Monatsbericht der Königlich-Preussischen Akademie der Wissenschaften zu Berlin **23**, 215 (1868).

[88] W. T. Kelvin, *Hydrokinetic solutions and observations*, Philosophical Magazine **42**, 362 (1871).

[89] B. N. Rogers, W. Dorland, and M. Kotschenreuther, *Generation and Stability of Zonal Flows in Ion-Temperature-Gradient Mode Turbulence*, Physical Review Letters **85**, 5336 (2000).

[90] A. Hasegawa and K. Mima, *Stationary spectrum of strong turbulence in magnetized nonuniform plasma*, Physical Review Letters **39**, 205 (1977).

[91] A. Hasegawa and K. Mima, *Pseudo-three-dimensional turbulence in magnetized nonuniform plasma*, Physics of Fluids **21**, 87 (1978).

[92] F. Jenko, *Streamer saturation: a dynamical systems approach*, Physics Letters A **351**, 417 (2006).

[93] M. J. Pueschel, T. Dannert, and F. Jenko, *On the role of numerical dissipation in Vlasov simulations of plasma microturbulence*, to be submitted to Comp. Phys. Commun. (2009).

[94] J. E. Kinsey, R. E. Waltz, and J. Candy, *The effect of safety factor and magnetic shear on turbulent transport in nonlinear gyrokinetic simulations*, Physics of Plasmas **13**, 022305 (2006).

[95] S.-I. Itoh and K. Itoh, *Statistical theory and transition in multiple-scale-length turbulence in plasmas*, Plasma Physics and Controlled Fusion **43**, 1055 (2001).

[96] S.-I. Itoh, A. Kitazawa, M. Yagi, and K. Itoh, *Bifurcation and phase diagram of turbulence constituted from three different scale-length modes* Bifurcation and phase diagram of turbulence constituted from three different scale-length modes*, Plasma Physics and Controlled Fusion **44**, 1311 (2002).

[97] K. Itoh, S.-I. Itoh, F. Spineanu, M. O. Vlad, and M. Kawasaki, *On transition in plasma turbulence with multiple scale lengths*, Plasma Physics and Controlled Fusion **45**, 911 (2003).

[98] F. Jenko and B. D. Scott, *Numerical computation of collisionless drift wave turbulence*, Physics of Plasmas **6**, 2418 (1999).

[99] D. R. Smith, E. Mazzucato, T. Munsat, H. Park, D. Johnson, L. Lin, C. W. Domier, M. Johnson, and N. C. Luhmann, *Microwave scattering system design for ρ_e scale turbulence measurements on NSTX*, Review of Scientific Instruments **75**, 3840 (2004).

[100] P. Hennequin, R. Sabot, C. Honoré, G. T. Hoang, X. Garbet, A. Truc, C. Fenzi, and A. Quéméneur, *Scaling laws of density fluctuations at high-k on Tore Supra*, Plasma Physics and Controlled Fusion **46**, B121 (2004).

[101] T. L. Rhodes, W. A. Peebles, X. Nguyen, M. A. Vanzeeland, J. S. Degrassie, E. J. Doyle, G. Wang, and L. Zeng, *Millimeter-wave backscatter diagnostic for the study of short scale length plasma fluctuations (invited)*, Review of Scientific Instruments **77**, 100000 (2006).

[102] C. Tröster, *Development of a flexible reflectometry system and its application to turbulence characterization in the ASDEX Upgrade tokamak*, PhD thesis, Ludwig-Maximilians-Universität München, 2008.

[103] F. Jenko and B. D. Scott, *Numerical computation of collisionless drift Alfvén turbulence*, Physics of Plasmas **6**, 2705 (1999).

[104] S. V. Henriksson, S. J. Janhunen, T. P. Kiviniemi, and J. A. Heikkinen, *Global spectral investigation of plasma turbulence in gyrokinetic simulations*, Physics of Plasmas **13**, 072303 (2006).

[105] F. Jenko and A. Kendl, *Radial and zonal modes in hyperfine-scale stellarator turbulence*, Physics of Plasmas **9**, 4103 (2002).

[106] A. Truc, A. Quéméneur, P. Hennequin, D. Grésillon, F. Gervais, C. Laviron, J. Olivain, S. K. Saha, and P. Devynck, *ALTAIR: An infrared laser scattering diagnostic on the TORE SUPRA tokamak*, Review of Scientific Instruments **63**, 3716 (1992).

[107] P. Hennequin, C. Honoré, A. Truc, A. Quéméneur, C. Fenzi-Bonizec, C. Bourdelle, X. Garbet, G. T. Hoang, and the Tore Supra team, *Fluctuation spectra and velocity profile from Doppler backscattering on Tore Supra*, Nuclear Fusion **46**, S771 (2006).

[108] P. Hennequin, *Scaling laws of density fluctuations in tokamak plasmas*, Comptes Rendus Physique **7**, 670 (2006).

[109] A. D. Gurchenko, E. Z. Gusakov, A. B. Altukhov, A. Y. Stepanov, L. A. Esipov, M. Y. Kantor, D. V. Kouprienko, V. V. Dyachenko, and S. I. Lashkul, *Observation of the ETG mode component of tokamak plasma turbulence by the UHR backscattering diagnostics*, Nuclear Fusion **47**, 245 (2007).

[110] G. G. Plunk, S. C. Cowley, A. A. Schekochihin, and T. Tatsuno, *Two dimensional magnetised plasma turbulence*, submitted to Journal of Fluid Mechanics (2009).

[111] A. V. Oppenheim and R. W. Schafer, *Zeitdiskrete Signalverarbeitung*, Oldenbourg, Muenchen, Wien, 3rd edition, 1999.

[112] T. L. Rhodes, private communication, 2007.

[113] S. Jolliet, A. Bottino, P. Angelino, R. Hatzky, T. Tran, B. McMillan, O. Sauter, K. Appert, Y. Idomura, and L. Villard, *A global collisionless PIC code in magnetic coordinates*, Computer Physics Communications **177**, 409 (2007).

[114] B. F. McMillan, S. Jolliet, T. M. Tran, L. Villard, A. Bottino, and P. Angelino, *Long global gyrokinetic simulations: Source terms and particle noise control*, Physics of Plasmas **15**, 052308 (2008).

[115] B. D. Scott, *Computation of turbulence in magnetically confined plasmas*, Plasma Physics and Controlled Fusion **48**, B277 (2006).

[116] N. Winsor, J. L. Johnson, and J. M. Dawson, *Geodesic Acoustic Waves in Hydromagnetic Systems*, Physics of Fluids **11**, 2448 (1968).

[117] M. N. Rosenbluth and F. L. Hinton, *Poloidal Flow Driven by Ion-Temperature-Gradient Turbulence in Tokamaks*, Physical Review Letters **80**, 724 (1998).

[118] F. L. Hinton and M. N. Rosenbluth, *Dynamics of axisymmetric and poloidal flows in tokamaks* , Plasma Physics and Controlled Fusion **41**, A653 (1999).

[119] H. Sugama and T.-H. Watanabe, *Collisionless damping of geodesic acoustic modes*, Journal of Plasma Physics **72**, 825 (2006).

[120] M. Fivaz, S. Brunner, G. de Ridder, O. Sauter, T. M. Tran, J. Vaclavik, L. Villard, and K. Appert, *Finite element approach to global gyrokinetic Particle-In-Cell simulations using magnetic coordinates*, Computer Physics Communications **111**, 27 (1998).

[121] L. Villard, private communication, 2009.

[122] G. L. Falchetto, B. D. Scott, P. Angelino, A. Bottino, T. Dannert, V. Grandgirard, S. Janhunen, F. Jenko, S. Jolliet, A. Kendl, B. F. McMillan, V. Naulin, A. H. Nielsen, M. Ottaviani, A. G. Peeters, M. J. Pueschel, D. Reiser, T. T. Ribeiro, and M. Romanelli, *The European turbulence code benchmarking effort: turbulence driven by thermal gradients in magnetically confined plasmas*, Plasma Physics and Controlled Fusion **50**, 124015 (2008).

[123] V. Grandgirard, Y. Sarazin, P. Angelino, A. Bottino, N. Crouseilles, G. Darmet, G. Dif-Pradalier, X. Garbet, P. Ghendrih, S. Jolliet, G. Latu, E. Sonnendrücker, and L. Villard, *Global full-f gyrokinetic simulations of plasma turbulence*, Plasma Physics and Controlled Fusion **49**, B173 (2007).

[124] V. Grandgirard, Y. Sarazin, X. Garbet, G. Dif-Pradalier, P. Ghendrih, N. Crouseilles, G. Latu, E. Sonnendrücker, N. Besse, and P. Bertrand, *Computing ITG turbulence with a full-f semi-Lagrangian code*, Communications in Nonlinear Science and Numerical Simulations **13**, 81 (2008).

[125] J. A. Heikkinen, S. J. Janhunen, T. P. Kiviniemi, and F. Ogando, *Full f gyrokinetic method for particle simulation of tokamak transport*, Journal of Computational Physics **227**, 5582 (2008).

[126] J. Candy and R. Waltz, *Anomalous Transport Scaling in the DIII-D Tokamak Matched by Supercomputer Simulation*, Physical Review Letters **91**, 045001 (2003).

[127] X. Garbet and R. E. Waltz, *Action at distance and Bohm scaling of turbulence in tokamaks*, Physics of Plasmas **3**, 1898 (1996).

[128] R. E. Waltz and J. Candy, *Heuristic theory of nonlocally broken gyro-Bohm scaling*, Physics of Plasmas **12**, 072303 (2005).

[129] T. S. Hahm, P. H. Diamond, Z. Lin, K. Itoh, and S.-I. Itoh, *Turbulence spreading into the linearly stable zone and transport scaling*, Plasma Physics and Controlled Fusion **46**, A323 (2004).

[130] J. Candy, R. E. Waltz, and W. Dorland, *The local limit of global gyrokinetic simulations*, Physics of Plasmas **11**, L25 (2004).

[131] M. A. Barnes, *Trinity: A Unified Treatment of Turbulence, Transport, and Heating in Magnetized Plasmas*, PhD thesis, University of Maryland, 2008.

List of publications

Publications in peer-reviewed journals

1. X. Lapillonne, S. Brunner, T. Dannert, S. Jolliet, A. Marinoni, L. Villard, T. Görler, F. Jenko and F. Merz,
   Clarifications to the limitations of the s-alpha equilibrium model for gyrokinetic computations of turbulence,
   Physics of Plasmas **16**, 032308 (2009)

2. T. Görler and F. Jenko,
   Multiscale features of density and frequency spectra from nonlinear gyrokinetics,
   Physics of Plasmas **15**, 102508 (2008)

3. T. Görler and F. Jenko,
   Scale Separation between Electron and Ion Thermal Transport,
   Physical Review Letters **100**, 185002 (2008)

4. P. Xanthopoulos, F. Merz, T. Görler, and F. Jenko,
   Nonlinear gyrokinetic simulations of ion-temperature-gradient turbulence for the optimized stellarator Wendelstein 7-X,
   Physical Review Letters **99**, 035002 (2007)

5. P. Cañizares Martínez, T. Görler, J. P. Paz, G. Morigi, and W. P. Schleich,
   Signatures of nonlocality in the first-order coherence of scattered light,
   Laser Physics **17**, 903 (2007)

Danksagung

An erster Stelle gebührt Herrn apl. Prof. Dr. Frank Jenko mein tiefer Dank. Er lieferte die Hinweise und stetige Ermutigung, die beiden dieser Arbeit zugrunde liegenden Themenkomplexe anzugehen. Neben einer hervorragenden Betreuung rechne ich ihm auch eine vielseitige Förderung, sei es durch die Entsendung zu internationalen Konferenzen und Fortbildungen als auch die Anleitung zur Anwerbung von Fördermitteln, hoch an. Desweiteren gilt mein Dank Prof. Dr. Peter Reineker und Prof. Dr. Steven Cowley, die sich freundlicherweise bereit erklärt haben, die Begutachtung dieser Arbeit zu übernehmen. Dr. Florian Merz möchte ich herzlich für die vielen Diskussionen und Erläuterungen, bspw. zu numerischen Problemstellungen und Parallelisierungstechniken, danken. Sie waren für das Gelingen dieser Arbeit ausgesprochen hilfreich. Ebenso bin ich Dr. Tilman Dannert zu Dank verpflichtet, der mir bei ersten Schritten mit Gene half und dem einige der Kernalgorithmen zur Einbindung nichtlokaler Effekte, auf denen diese Arbeit in großen Teilen beruht, zu verdanken sind. Die Entwicklung der globalen Erweiterung des Gene Codes wurde und wird in einer sehr harmonischen Zusammenarbeit mit dem CRPP, Lausanne, betrieben. Besonders hervorheben möchte ich hierbei Xavier Lapillonne, der bei der tatsächlichen Programmierung maßgeblich beteiligt war und auch nach hunderten von Mails und Telefonaten immer noch gerne zur Abstimmung weiterer Projekte bereit war. Ebenso gilt auch Dr. Stephan Brunner und Prof. Dr. Laurent Villard, die das Projekt von dieser Seite durch Rat und Tat unterstützt haben, mein tiefer Dank. Meinen Zimmerkollegen Dr. Moritz J. Püschel und Thilo Hauff danke ich für die vielen interessanten physikalischen Fragestellungen, aber auch für die ständige Erweiterung meines Horizonts durch gemeinsame Pausendiskussionen, sei es zum aktuellen politischen Geschehen, zu theologischen oder gesellschaftswissenschaftlichen Problematiken. In diesem Kontext möchte ich auch den verbleibenden Mitgliedern der Forschungsgruppe, namentlich Klaus Reuter, Matthias Kammerer, Daniel Told, Mirjam Schneller, Hauke Doerk-Bendig und Alexander Röder für die angenehme Atmosphäre und kollegiale Zusammenarbeit in den vergangenen Monaten oder Jahren danken. Dr. Pavlos Xanthopolous war mir bei der Einbindung realistischer Geometrien eine große Hilfe und hat diese mit seinem Tracer Code erst möglich gemacht. Prof. Dr. Terry Rhodes danke ich für die Bereitstellung eines entsprechenden Datensatzes für den DIII-D Tokamak.

Für die Bereitstellung von Rechenzeit und für die gelegentliche Hilfe bei Hard- und

Softwareprobleme bedanke ich mich Rechenzentrum Garching, hier insbesonders bei Herrn Reinhard Tisma. Desweiteren sollen Rechenzeitkontigente, die durch das Leibniz-Rechenzentrum der Bayerischen Akademie der Wissenschaften sowie durch das DEISA Konsortium (EU FP6 Projekte RI-508830 and RI-031513) und durch EUFORIA (EU FP7/2007-2013 Projekte Nr. 211804 und Nr. 222919) bereit gestellt wurden, dankend erwähnt werden.

Dem Max-Planck-Institut für Plasmaphysik und hier besonders dem Bereich Tokamaktheorie unter der Leitung von Frau Prof. Dr. Sibylle Günter sei herzlich für die Unterstützung und Bereitstellung der nötigen Infrastruktur für diese Arbeit gedankt.

Schließlich möchte ich auch die Personen, die das mühevolle Korrekturlesen dieser Arbeit übernommen haben, entsprechend honorieren. Hier haben mir Dr. Moritz J. Püschel, Dr. Florian Merz, Thilo Hauff, Daniel Told, Dr. Tilman Dannert und Xavier Lapillonne einen großen Dienst erwiesen.

Zuletzt gilt mein Dank meinen Eltern und Geschwistern, die mir während meiner gesamten Ausbildung immer ermunternd zur Seite standen und somit auch zum Gelingen dieser Arbeit beigetragen haben.